Measurements of Proton Electromagnetic Form Factors and Two-Photon Exchange in Elastic Electron-Proton Scattering

Mikhail Yurov
Tashkent, Uzbekistan

B.S.-M.S. US equivalent
Tashkent State University/
SANIGMI, 2001

A Dissertation presented to the Graduate Faculty of
the University of Virginia in Candidacy for the Degree of
Doctor of Philosophy

Department of Physics
University of Virginia
February, 2018

Abstract

Two experimental techniques, Rosenbluth separation and recoil polarization transfer, used to extract the proton's electromagnetic form factors ratio $G_{\mathrm{E_p}}/G_{\mathrm{M_p}}$, yield markedly different results. Modern theoretical calculations suggest that two-photon exchange is responsible for the observed discrepancy and that it is epsilon dependent.

Jefferson Lab (JLab) Experiment E05-017 was designed to measure the two-photon exchange contribution over a wide range of ε and Q^2. In contrast with the conventional Rosenbluth method, E05-017 detected the elastically scattered proton rather than the electron returning a much more precise extraction of the form factor ratios.

This thesis reports the preliminary results of the reduced cross sections extraction determined at 112 kinematic settings. The cross section measurements were used to calculate the $G_{\mathrm{E_p}}/G_{\mathrm{M_p}}$ ratio at sixteen values of Q^2 in the range from $0.40\,\mathrm{GeV}^2$ to $5.76\,\mathrm{GeV}^2$ significantly improving the available precision of unpolarized measurements in the low-to-modest and in the very high Q^2 range. In addition, new limits on the deviation from linearity in the Rosenbluth plot were determined at each Q^2, featuring highly detailed measurements with more than ten ε points at $Q^2 = 0.98\,\mathrm{GeV}^2$ and $2.29\,\mathrm{GeV}^2$.

Approved by:

Dissertation adviser
Prof. Day, Donal B.
Department of Physics

Committee Member
Prof. Thornton, Stephen T.
Department of Physics

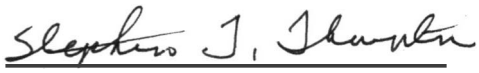

Committee Member
Prof. Liyanage, Nilanga K.
Department of Physics

GSAS representative
Prof. Keene, William C.
Department of Environmental Sciences

Дорогим маме и отцу

Acknowledgments

I would like to express my sincere gratitude to the many people whose efforts, help and support made this work possible. There is hardly a way to give all due credit to everyone who contributed, so if I have neglected to mention anyone, please forgive me.

In my education and training I was very fortunate to have Donal Day as my adviser; his continuous guidance and encouragement helped me to develop an understanding of the field and to gain confidence. In his desire to see me succeed, he provided me with unconditional support in difficult times and circumstances, way beyond that which one would expect from an academic adviser. Donal, I am very grateful for that. I would like to thank John Arrington, the spokesperson of Experiment E05-017, for his patience in guiding me through the process of data analysis with his encyclopedic knowledge of all the aspects of this experiment.

I would like to thank the members of the Rosen07 collaboration, JLab Hall C and Accelerator scientific and technical staffs whose enormous efforts made E05-017, E06-009 and E04-001 a success. In particular, I am very grateful to the students that worked on these experiments: Myriam Johnson, Vahe Mamyan, Ibrahim Albayrak, as well as my collaborators, Mark Jones, Patricia Solvignon and Brad Sawatzky, who helped me at the initial steps of my analysis.

This path would simply not have been started or concluded without the help of my friend and our group member Dustin Keller – thank you, Dustin. I was privileged to be introduced to and educated in the field of polarized targets by Don Craab whose body of knowledge and experience on the subject is absolutely invaluable – thank you, Don. I am also thankful for the kindness and support shown to me personally by Cass Sackett, Nilanga Liyanage, Suzie Garrett, Dawn Shifflett and Peter Cline throughout all of my years spent at the UVA Physics Department.

I really appreciate the time and feedback the examining members of my committee – Stephen Thornton, Nilanga Liyanage and William Keene – and also Jacob Pease have given me in thoroughly reviewing my thesis.

I owe much of my experimental knowledge to the people I worked with at JLab Hall B: Rustam Niyazov, Stepan Stepanyan, Valery Kubarovsky and Volker Burkert. Special thanks to Andrey Avanesov and Marina S. Avanesova and to my friends in Newport News for their continuous support and help in my adjusting to life in the US. I am very much thankful to my friend Dmitriy Nekrasov who singlehandedly started this entire journey. I would like to thank Vitaly Baturin for our useful discussions on detector developments and Wooyoung Kim for the opportunities given.

There are a lot of people back at home in Tashkent who influenced me tremendously and who carefully nurtured my interest in science. They remained dedicated to their work in difficult times and for that I am very grateful. I thank Biruni A. Fayzullaev, Vladimir A. Pazdzerskyi, Anatolyi A. Korzun, Nina I. Gurina and Lyudmila A. Pivkina. My thanks go to my closest friends and family.

Contents

Acronyms

CH_2 dihydridocarbon.

LD_2 liquid deuteron.

LH_2 liquid hydrogen.

ADC Analog-to-Digital Converter.

BCM Beam Current Monitors.

BLW Braun-Lenz-Wittmann.

BNA beam-normal-asymmetry.

BOX box.

BPM Beam Position Monitor.

BSY Beam Switch Yard.

CAMAC Computer-Aided Measurement And Control.

CDT computer dead-time.

CEA Cambridge Electron Accelerator.

CEBAF Continuous Electron Beam Accelerator Facility.

CHL Central Helium Liquefier.

CLAS CEBAF Large Acceptance Spectrometer.

CODA CEBAF On-line Data Acquisition.

COZ Chernyak-Ogloblin-Zhitnitsky.

DAQ Data Acquisition system.

DC drift chamber.

DESY German Electron Synchrotron.

DNP dynamical nuclear polarization.

DORIS Double-Ring Storage.

EDT electronic dead-time.

ElBrem electron bremsstrahlung.

ElSE electron self-energy.

ELT electronic live-time.

ElVC electron vertex correction.

EPICS Experimental and Physics Industrial Control System.

ESR End Station Refrigerator.

GC gas Cherenkov.

GEM gas electron multiplier.

GPD generalized parton distributions.

GS Gari-Stefanis.

HAPPEX Hall A Proton Parity Experiment.

HERA Hadron-Electron Ring Accelerator.

HERMES DESY fixed-target experiment to explore spin.

Het heterotic.

HMS High Momentum Spectrometer.

IR infrared.

JLab Jefferson Lab.

LT longitudinal-transverse separation.

MAMI Mainz Microtron.

MC Monte Carlo.

MIT-Bates MIT Bates Linear Accelerator Center.

MWPC multi-wire proportional chamber.

NIM Nuclear Instrumentation Module.

NMR nuclear magnetic resonance.

PAW Physics Analysis Workstation.

PID particle identification.

PMT photo-multiplier tube.

pQCD perturbative quantum chromodynamics.

PrBrem proton bremsstrahlung.

PREX The Lead Radius Experiment.

PrSE proton self-energy.

PrVC proton vertex correction.

PT polarization transfer.

PV parity violating.

QCD quantum chromodynamics.

QCDSF lattice QCD calculations.

QED quantum electrodynamics.

QWEAK The Weak Charge of the Proton Experiment.

RCS real compton scattering.

ROC Read-Out Controller.

SLAC Stanford Linear Accelerator Center.

SOS Short Orbit Spectrometer.

SRF superconducting radio-frequency.

SSA single spin asymmetry.

TDC Time-To-Digital Converter.

TNA target-normal-asymmetry.

TPE two-photon exchange.

VEPP-3 Novosibirsk Electron-Positron Storage Ring.

VME Versa Module Europa bus.

VP vacuum polarization.

XBOX crossed-box.

List of Figures

List of Tables

1 Introduction

1.1 Overview

The investigation of the complex underlying structure of the proton has been a focal point of nuclear and particle physics since the pioneering experiments of O. Stern in 1933 [67] and R. Hofstadter in 1953 [68]. The discovery of the anomalous magnetic moment gave an initial indication of the proton's composite nature while Hofstadter's results provided the first clear evidence that it could not be described as a point-like Dirac particle. The following decades of experimental and theoretical work led to the formulation of quantum chromodynamics (QCD), a quantum field theory of the strong interactions, which is believed to govern interactions between quarks and gluons. The growing array of data from both leptonic and hadronic scattering experiments of increasingly higher energies has been used to rigorously test QCD, leading to the modern quark-parton description of the nucleon. While perturbative techniques used in QCD have excellent predictive power at high energies, they cannot be applied in the moderate-to-low range of the four-momentum transfer squared Q^2. The Q^2 dependence of the strong coupling constant,

$$\alpha_{\mathrm{s}}(Q^2) \propto \frac{1}{\ln(Q^2/\Lambda^2_{\mathrm{QCD}})}, \tag{1.1}$$

significantly complicates calculations when the four-momentum transfer is of the same order as Λ_{QCD}, the QCD renormalization scaling factor. The consequence is that for a wide scope of hadronic physics phenomena in this range of energies the calculations cannot be conducted in terms of the fundamental parameters of the QCD Lagrangian and have to rely on phenomenological models or functions whose parameters are constrained by experimental data. One of the examples that falls into this category is the Q^2 dependence of the electromagnetic form factors of the nucleon.

The electric form factor, G_{E}, and the magnetic form factor, G_{M}, are fundamental quantities that encapsulate the internal structure of the nucleon and are related to

the spatial distribution of its charge and magnetization densities. Their investigations, initiated by Hofstadter and his team at the Stanford University High Energy Physics Laboratory, have a long history, and a rich body of experiments were conducted to better understand and explain global features of the form factors. Elastic electron scattering was and continues to be the primary experimental tool in the form factors studies. These measurements made it possible to make several important observations, such as proton form factor scaling and ability to represent $G_{\mathrm{E}}^{\mathrm{p}}$ and $G_{\mathrm{M}}^{\mathrm{p}}$ by a simple dipole form, but by the end of 1980s, the progress in these studies significantly slowed down. Intrinsic limitations of the unpolarized measurements, the prevailing type of experiments at the time, imposed serious restrictions on the precision achievable in both the low and high Q^2 domains.

The evolution of experimental facilities in the 1990s, such as development of high intensity polarized electron beams, recoil polarimeters and polarized targets, allowed a dramatic improvement in the precision of the data and a resurgence of interest in the studies of the form factors. While the experiments exploiting polarization observables aimed at getting improved data quality, their results came as a surprise to the nuclear community, revealing a significant discrepancy with the G_{E} and G_{M} extraction based on unpolarized cross sections. The apparent disagreement between unpolarized and polarized measurements triggered a serious reevaluation of previously collected data and both theoretical and experimental efforts to resolve the inconsistency.

The progress of the last two decades indicated, with convincing evidence, that the discrepancy may be explained in terms of the two-photon exchange (TPE) contribution. Previous elastic electron scattering experiments were analyzed assuming an exchange of a single virtual photon – the Born approximation. A number of improved calculations were performed in the last few years to estimate the previously neglected TPE effects. However, despite several theoretical approaches being successful in resolving most of the observed disagreement, further improvements on the scope and the quality of experimental data are necessary for direct verification of these models.

As a part of this broad program, an experiment focused on making high precision measurements of unpolarized cross sections was performed to map out the kinematic dependence of TPE effects in a wide range of Q^2 values. The description of the experimental goals, techniques and procedures, as well as preliminary experimental results is the subject of this document.

The content of this thesis is organized as follows. This chapter continues with the formalism of elastic electron scattering and several important definitions of the form factors. Sections 1.3 through 1.5 present an overview and experimental status of the conventional and improved techniques used in unpolarized and polarized scattering measurements. Chapter 2 discusses how TPE contribution can be probed directly and indirectly through several observables and shows the scope of currently available data on each presented observable. The second part of Chapter 2 outlines the effect of the inclusion of the higher order terms, such as two-photon exchange, on scattering formalism and gives a summary of available TPE calculations. The introductory overview of Chapter 3 lays out the motivational background for the

experiment which is also partially covered in previous chapters and gives a general description of the experimental run and data collection. Sections 3.2 through 3.6 provide details on the accelerator's essential elements and operation as well as an overview of the basic experimental hall equipment. Some results of the standard measurements that characterize equipment performance and which are part of the typical data flow are also included in these sections. Chapter 4 covers analysis of this experiment and is devoted to the discussion of the full data processing from initial event reconstruction to the extracted cross sections. This combines calibration procedures, analysis of the specific runs, and calculations of the detector inefficiencies and various corrections. The Monte Carlo (MC) simulation which is an essential part of the analysis strategy and the cross section extraction are described in Sections 4.6 and 4.7. The most important part of the analysis procedure for this experiment is the estimate of systematic uncertainties which is covered in Section 4.8. Chapter 5 presents preliminary results of this experiment and provide an outlook for future work.

1.2 Electron scattering

The advantage of exploiting an electromagnetic probe lies in the fact that the lepton is a structureless point-like particle and thus extracted observables reflect the underlying composition of the target rather than both the probe and the target as is the case in hadron-hadron collisions. In addition, electromagnetic interactions are extremely well understood within the theory of quantum electrodynamics (QED) so lepton-nucleon, and in particular elastic electron-proton, scattering experiments provide the cleanest information on the proton form factors.

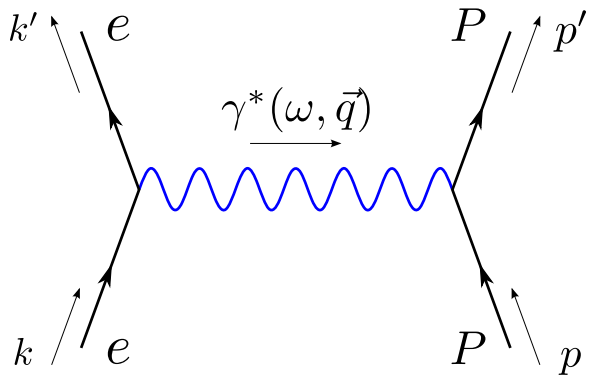

Figure 1.1: One-photon-exchange Feynman diagram as a lowest order term in elastic electron-proton scattering.

In the electron-proton (ep) scattering process the interaction occurs *via* exchange of one or more virtual photons. The calculations in the Born approximation take into account the lowest order process only, as depicted by the diagram shown in Fig. 1.1. The kinematics of elastic scattering,

$$e(k_\mu) + P(p_\mu) \rightarrow e(k'_\mu) + P(p'_\mu), \tag{1.2}$$

for which the proton remains in its ground state, is represented by several commonly used parameters. The incident electron has a four-momentum $k = k(E, \vec{k})$ while the target proton is initially at rest with four-momentum $p = p(M_\mathrm{p}, 0)$. The four-momentum transfer $q = q(\omega, \vec{q})$ is carried by a single virtual photon γ^*. The final state quantities for electron and proton are k' and p' respectively which gives the momentum transfer as

$$q = k - k' = p' - p. \tag{1.3}$$

At the energies of interest, the electron mass can be safely neglected since $E \gg m_\mathrm{e}$. In this case, the Lorentz invariant quantity $Q^2 \equiv -q^2 > 0$, or four-momentum transfer squared, in the laboratory frame is given by

$$Q^2 = 4EE' \sin^2 \frac{\theta_\mathrm{e}}{2}, \tag{1.4}$$

where E and E' are initial and final electron energies and θ_e is the electron scattering angle. The cross section is typically defined in terms of Q^2 and dimensionless quantities

$$\tau = \frac{Q^2}{4M_\mathrm{p}^2} \quad \text{and} \quad \varepsilon = \left(1 + 2(1+\tau)\tan^2 \frac{\theta_\mathrm{e}}{2}\right)^{-1}, \tag{1.5}$$

where the τ is a kinematic variable defined by the four-momentum transfer squared and the ε is the virtual photon polarization parameter. In the Born approximation, the invariant transition amplitude for elastic ep scattering $\mathcal{M}_{1\gamma}$, where the 1γ index signifies the exchange of a single virtual photon, can be expressed as

$$\mathcal{M}_{1\gamma} = -\frac{e^2}{q^2} j_\mu J^\mu, \tag{1.6}$$

where j_μ and J^μ are electron and proton electromagnetic currents respectively and e is the electric charge. These currents can be formulated in terms of the electron $u(k)$ and proton $v(p)$ spinors as follows:

$$j_\mu = \bar{u}(k')\gamma_\mu u(k), \quad J^\mu = \bar{v}(p')\Gamma^\mu v(p). \tag{1.7}$$

The internal proton structure is parametrized within $\Gamma^\mu(q)$ by introducing two functions F_1 and F_2 known as the Dirac and Pauli form factors respectively:

$$\Gamma^\mu(q) = \gamma^\mu F_1(Q^2) + \frac{i\sigma^{\mu\nu} q_\nu}{2M_\mathrm{p}} \kappa F_2(Q^2) \tag{1.8}$$

where κ is the anomalous magnetic moment in units of the nuclear magneton, μ_N. The Dirac and Pauli form factors are functions of four-momentum transfer Q^2 alone and are the only terms allowed in the Born approximation. Following these definitions, we can write the elastic *ep* differential cross section in the lab frame as

$$\frac{d\sigma}{d\Omega} = \sigma_{ns}\left[\left(F_1^2 + \frac{\kappa^2 Q^2}{2M_p^2}F_2^2\right) + \frac{Q^2}{2M_p^2}(F_1 + \kappa F_2)^2 \tan^2\frac{\theta_e}{2}\right] \tag{1.9}$$

where σ_{ns} is the Mott cross section modified to account for proton recoil effects. The Mott cross section, σ_{Mott}, describes the scattering of a spin $\frac{1}{2}$ electron by a spin-less proton and is given by

$$\sigma_{ns} = \sigma_{Mott}\frac{E'}{E} = \frac{\alpha^2\cos^2(\theta/2)}{4E^2\sin^4(\theta/2)}\frac{E'}{E}. \tag{1.10}$$

In practice, the cross section is more easily analyzed when it is rewritten in terms the Sachs form factors $G_{E_p}(Q^2)$ and $G_{M_p}(Q^2)$ [69, 70] . They can be expressed as linear combinations of the Dirac and Pauli form factors as

$$G_{E_p}(Q^2) = F_1^2 - \kappa\tau F_2^2, \quad G_{M_p}(Q^2) = F_1^2 + \kappa F_2^2. \tag{1.11}$$

Substituting these back in Eq. 1.9 and taking into account Eq. 1.5 results in

$$\frac{d\sigma}{d\Omega} = \frac{d\sigma}{d\Omega}_{ns}\frac{1}{1+\tau}\left(G_{E_p}^2(Q^2) + \frac{\tau}{\varepsilon}G_{M_p}^2(Q^2)\right). \tag{1.12}$$

In this form the cross section is no longer dependent on the mixed term and is expressed by the G_{E_p} and G_{M_p} quadratures only. In the static limit, $Q^2 \to 0$, the Sachs form factors reduce to the charge and magnetic moment of the proton in units of the electron charge and of the nuclear magneton.

Eq. 1.12 is known as Rosenbluth formula [71]. The associated technique, the Rosenbluth separation method, was used as a standard procedure for extraction of the proton's electromagnetic form factors over several decades.

1.3 Rosenbluth separation

The basis for the Rosenbluth separation method lies in the linear dependence of the cross section in parameter ε. The cleanest form of this dependence is obtained by defining reduced cross section, σ_R, based on Eq. 1.12

$$\sigma_R = \frac{d\sigma}{d\Omega}\frac{(1+\tau)\varepsilon}{\sigma_{ns}} = \tau G_{M_p}^2 + \varepsilon G_{E_p}^2. \tag{1.13}$$

The form factors extraction is performed by analyzing σ_R at several ε points of fixed Q^2. Experimentally, the reduced cross section is measured by varying the electron scattering angle while adjusting the incident beam energy such that Q^2 remains constant as ε varies. The form factors values are typically obtained from the linear fit to reduced cross section measurements vs ε which yields $G^2_{E_p}$ as the slope, and $\tau G^2_{M_p}$ as the intercept.

The immediate observation from Eq. 1.13 reflects the fact that the Rosenbluth separation method has reduced sensitivity to $G^2_{E_p}$ at higher Q^2 values. This limitation is due to the τ ($\propto Q^2$) parameter becoming large as Q^2 increases such that cross section predominantly measures the $G^2_{M_p}$ contribution. The opposite behavior is true for the extraction of $G^2_{M_p}$ at very small Q^2 where the cross section is dominated by the electric form factor except for the region where $\varepsilon \to 0$. It should also be noted that the Rosenbluth separation method is only sensitive to the form factors quadratures and thus cannot be used to determine the signs of the form factor.

Despite these important limitations, the Rosenbluth technique provided high precision data for $G^2_{E_p}$ up to $\sim 2\,\mathrm{GeV}^2$, and $G^2_{M_p}$ up to $\sim 30\,\mathrm{GeV}^2$. The classic Rosenbluth approach, where the cross section is measured by detecting the scattered electron (electron Rosenbluth), is the major source of our knowledge on proton form factors. The global elastic *ep* cross section database expanded [2–11, 13, 14, 72–78] from the early 1960s to the most recent measurements published in 2010 [78]. The overall experimental and theoretical status of the form factors studies has been reported in multiple review papers [1, 17, 79–84], many of which were stimulated by the observed discrepancy with polarization method data. In addition, several [15, 16, 24–26, 45] global fits and reanalysis of the proton electromagnetic factors were performed allowing for relative renormalization of the cross section points and taking into account historically diverse radiative correction procedures for separate data sets.

A selected list of G_{E_p} and G_{M_p} measurements is presented in Fig. 1.2a and Fig. 1.2b. One of the first observations, especially in the early measurements with a limited Q^2 reach, was that both proton factors can be reasonably well approximated by a dipole form factor, which is used as a normalization term in Fig. 1.2,

$$G_D = \left(1 + \frac{Q^2}{0.71}\right)^{-2}. \tag{1.14}$$

The limitations of the electron Rosenbluth in the extraction of G_{E_p} become apparent above $Q^2 \sim 2\,\mathrm{GeV}^2$. Two Stanford Linear Accelerator Center (SLAC) experiments [9, 10] , and later an experiment at JLab [11], extended the G_{E_p} precision and the upper range of Q^2, however, they yielded noticeably different results in the region above $3\,\mathrm{GeV}^2$. Contrary to this behavior, the results of G_{M_p} extraction indicate excellent internal consistency through the different data sets. Several experiments [13, 14] that probed G_{M_p} at very high Q^2 did not perform a conventional Rosenbluth separation; G_{M_p} values were derived under the assumption that $\mu_p G_{E_p}/G_{M_p} = 1$. These results showed a clear deviation of the proton magnetic form factor from the simple dipole form.

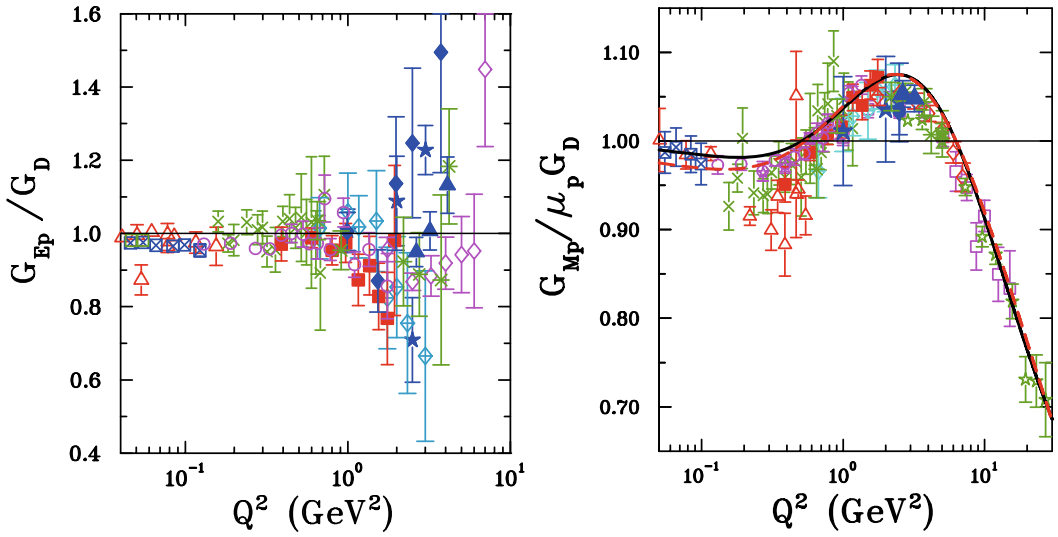

(a) World data on G_{E_p}/G_D as a function of Q^2.

(b) World data on $G_{M_p}/\mu_p G_D$ as a function of Q^2.

Figure 1.2: Selected list of experimental results on the Rosenbluth extraction of the proton electromagnetic form factors: open triangle (red) [1], multiplication sign (green) [2], open circle (magenta) [3], filled diamond (blue) [4], filled square (red) [5], crossed diamond (cyan) [6], crossed square (blue) [7], open square (green) [8], filled star (blue) [9], open diamond (magenta) [10], asterisk (green) [11], filled triangle (blue) [12], open square (magenta) [13], open star (green) [14]. The solid and dashed line fits are performed by [15] and [16]. *Figure source: Ref.* [17].

Apart from [3, 5, 6] measurements that suggested a decrease of G_{E_p} with increasing Q^2, proton form factors ratio obtained via electron Rosenbluth method have approximately been consistent with the concept of *scaling*, the empirical relation

$$\mu_p G_{E_p}/G_{M_p} \approx 1. \tag{1.15}$$

The low Q^2 domain, which is important for the proton charge radius studies, was recently investigated at Mainz Microtron (MAMI) [45]. About 1400 elastic cross sections were measured with outstanding precision in the $0.003 \leq Q^2 \leq 1\,\mathrm{GeV}^2$ range. The elastic scattering measurements presented in this thesis overlap with MAMI's data set in the $0.4 \leqslant Q^2 \leqslant 1\,\mathrm{GeV}^2$ region and further explore form factors at much higher Q^2 values, up to $5.7\,\mathrm{GeV}^2$.

1.4 Recoil polarization

The possibility of accessing information on electromagnetic form factors through spin polarization observables was first discussed in 1960s. The corresponding formalism was developed in the number of initial and following papers [85–89] suggesting several types of the experiments using a longitudinally polarized electron beam and a polarized target. However, the required experimental facilities that would provide sufficiently high figures of merit became available only in the middle of the 1990s.

The recoil polarization, or polarization transfer (PT), method exploits a longitudinally polarized electron beam with an unpolarized target and measures the polarization components of the struck proton. The polarization of the recoil proton is determined through secondary re-scattering of the proton with a *recoil polarimeter*. In the single photon approximation the proton polarization component, normal to the scattering plane, is zero. The in-plane longitudinal and transverse components, P_l and P_t, have the following relationships with form factors

$$I_\mathrm{o} P_\mathrm{l} = \frac{E+E'}{M_\mathrm{p}} \sqrt{\tau(1+\tau)} G^2_{\mathrm{M_p}}(Q^2) \tan^2(\theta_\mathrm{e}/2), \tag{1.16}$$

$$I_\mathrm{o} P_\mathrm{t} = -2\sqrt{\tau(1+\tau)} G_{\mathrm{E_p}}(Q^2) G_{\mathrm{M_p}}(Q^2) \tan(\theta_\mathrm{e}/2), \tag{1.17}$$

where I_o is defined as

$$I_\mathrm{o} = G^2_{\mathrm{E_p}}(Q^2) + \frac{\tau}{\varepsilon} G^2_{\mathrm{M_p}}(Q^2). \tag{1.18}$$

Comparison of Eq. 1.16 and Eq. 1.17 shows that form factor ratio can be directly obtained by measuring the ratio of polarization components P_l and P_t

$$\frac{G_{\mathrm{E_p}}}{G_{\mathrm{M_p}}} = \frac{P_\mathrm{t}}{P_\mathrm{l}} \frac{E+E'}{2M_\mathrm{p}} \tan\left(\frac{\theta_\mathrm{e}}{2}\right). \tag{1.19}$$

The obvious limitation of the PT method is that it does not allow extraction of the individual form factors and measures their ratio only. However, for the ratio measurements it offers several experimental advantages over the Rosenbluth separation technique. In the typical PT experiment the recoil polarimeter measures the struck proton's azimuthal angular distribution after its re-scattering in a secondary target. This allows determination of both polarization components simultaneously which means that only one measurement is necessary for a given Q^2. In addition, the PT ratio extraction does not require the knowledge of the electron beam polarization or of the analyzing power of the recoil polarimeter. Combined, these factors result in strongly decreased systematic uncertainties. In the region of large Q^2 where the magnetic form factor G_M dominates cross section measurements, the recoil polarization method provides notably more precise determination of the form factors ratio.

A broad array of experimental results [18–23, 57, 65, 66, 90–96] determining the $G_{\mathrm{E_p}}/G_{\mathrm{M_p}}$ ratio has been accumulated mostly within the last two decades. Fig. 1.3 compares a representative selection of low and high Q^2 measurements from both cross section and polarization transfer experiments. The most important conclusion from the series of JLab's experiments was the sharp and almost linear monotonic decrease of the ratio $\mu_\mathrm{p} G_{\mathrm{E_p}}/G_{\mathrm{M_p}}$ above $Q^2 \approx 1\,\mathrm{GeV}^2$, for the first time clearly indicating the difference in the Q^2 dependence of the form factors $G_{\mathrm{E_p}}$ and $G_{\mathrm{M_p}}$.

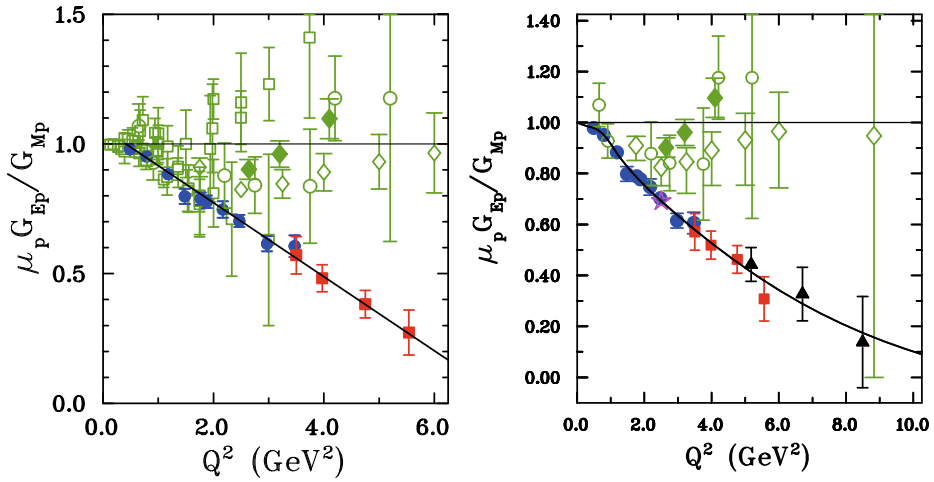

Figure 1.3: Selected list of experimental results on $\mu_p G_{E_p}/G_{M_p}$ extraction from Rosenbluth separation (green) and polarization transfer measurements: filled circle (blue) [18, 19], filled square (red) [20](left), [21](right), filled star (magenta) [22], filled triangle (black) [23]. Left: detailed view of the small Q^2 region, fit to the data [20]. Right: large Q^2 measurements; 7 parameter fit, polynomial over polynomial, constrained to 1 at $Q^2 = 0$. *Figure source: Ref.* [17].

It is worth mentioning that there is another class of the experiments exploiting spin observables, which is sensitive to the the form factor ratio in a similar fashion. In this double-polarization method, the asymmetry between positive and negative helicity states of the incoming electron on a polarized nucleon target is measured for elastic scattering. The measured asymmetry, A_{meas}, is given in terms of the physics asymmetry, A, by $A_{\text{meas}} = P_{\text{beam}} P_{\text{target}} A$, where

$$A = -\frac{2\sqrt{\tau(1+\tau)}\tan(\theta_e/2)}{\frac{G_E^2}{G_M^2} + \frac{\tau}{\varepsilon}} \left[\sin\theta^* \cos\phi^* \frac{G_E}{G_M} + \sqrt{\tau[1+(1+\tau)\tan^2(\theta_e/2)]}\cos\theta^* \right]. \tag{1.20}$$

The direction of the target polarization vector is defined by polar and azimuthal angles θ^* and ϕ^* with z pointing in the direction of momentum transfer q and y normal to the scattering plane. The optimal G_E extraction is achieved by orienting the target polarization perpendicular to the momentum transfer vector and parallel to the scattering plane. The measurements [97, 98] of the beam-target asymmetry are prone to different systematic effects when compared to either the Rosenbluth technique or the polarization transfer technique and thus offer an independent verification of the form factors ratio.

1.5 Proton Rosenbluth

As a first response to the surprising violation of the form factor scaling, $\mu_p G_{E_p}/G_{M_p} \approx 1$, in polarization transfer measurements, the previous Rosenbluth results were put under close scrutiny. It should be noted that formerly commonly accepted scaling

behavior was an approximate experimental observation. It was supported by several global analyses of the conventional Rosenbluth results [9, 24]. A good empirical fit to the world data was achieved by Bosted [24], who used an inverse polynomial in Q to describe form factors in the range of $0.0 < Q^2 < 30.0\,\mathrm{GeV}^2$,

$$G_{\mathrm{E_p}}(Q^2) = \frac{1}{1 + 0.62Q + 0.68Q^2 + 2.80Q^3 + 0.83Q^4}, \tag{1.21}$$

$$\frac{G_{\mathrm{M_p}}(Q^2)}{\mu_{\mathrm{p}}} = \frac{1}{1 + 0.35Q + 2.44Q^2 + 0.50Q^3 + 1.20Q^4 + 0.32Q^5}. \tag{1.22}$$

However, these analysis were performed before PT results were available and questioned the validity of the cross section measurements. An exhaustive reanalysis of the world cross section data-set was performed by Arrington [25, 26] that aimed to reveal any inconsistency in the Rosenbluth method which would explain observed disagreement. While the reanalysis method was similar to the one presented in [9] it included several important modifications: the cross section database was extended to include results which were not available for Ref. [9] analysis, updated radiative corrections were applied for some of the early measurements, and some normalization uncertainties were recalculated. The major conclusion of this work was that the existing cross section measurements show a good consistency between all different data sets. The extracted value of the form factors ratio supported the results of the previous global Rosenbluth analysis. Various scenarios, where one or more data-sets are excluded from the global fit, were used to check the stability of the global fit along with the variation of the relative normalization of different data-sets. These modifications did not produce changes in the $\mu_{\mathrm{p}} G_{\mathrm{E_p}}/G_{\mathrm{M_p}}$ significant enough to account for the discrepancy with polarization measurements. Fig. 1.4 summarizes results of the global Rosenbluth fits along with recoil polarization fit.

Despite the fact that no inconsistencies were found in cross section measurements, their results exhibit significant scatter with increasingly large uncertainties for $Q^2 > 1\,\mathrm{GeV}^2$ where the standard Rosenbluth extraction of $G_{\mathrm{E_p}}$ is notoriously hard. From this perspective, an additional independent experimental validation of the Rosenbluth method was required to check if some undiscovered systematic error can bring cross section data in accord with polarization results.

To address this issue an experiment with an improved Rosenbluth technique was conducted in Hall A at JLab [12]. In this experiment (E01-001) the struck proton was detected instead of the scattered electron, whereas nearly all previous Rosenbluth separations were performed with electron detection. There are several advantages to the extraction of the elastic scattering cross section through observation of the outgoing proton:

- much weaker variation of the cross section's ε dependence than for the electron detection experiments (Fig. 1.5a),

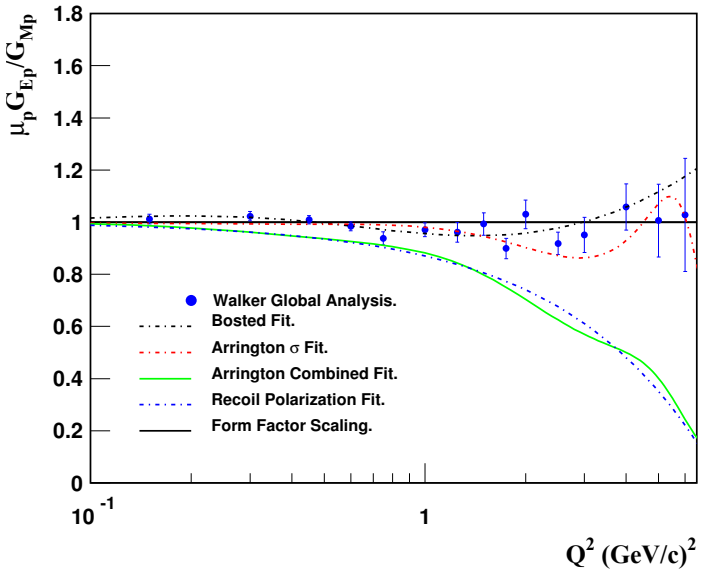

Figure 1.4: Selected list of global fits of the form factors ratio for both techniques as analyzed by [9, 24–26]. More details can be found in [27]. *Figure source: Ref.* [27].

- access to kinematics corresponding to smaller electron scattering angles (larger ε) and extension of the small-ε range due to increased cross section,
- constant proton momentum compared to the rapid changes in the electron momentum with ε (Fig. 1.5),
- smaller sensitivity to kinematical offsets (Fig. 1.6).

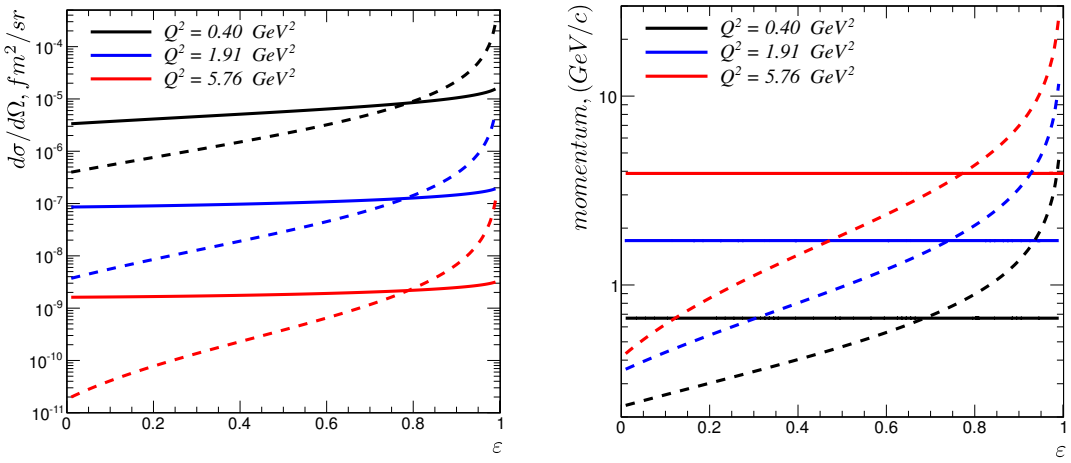

(a) The cross section ε dependence

(b) The momentum ε dependence

Figure 1.5: Experimental benefits of the detection of the recoil proton (solid) over the scattered electron (dashed) for three selected Q^2 values.

Fig. 1.5a shows ε dependence of both $d\sigma/d\Omega_{\text{proton}}$ and $d\sigma/d\Omega_{\text{electron}}$ cross sections for small, moderate, and large values of Q^2. Variations of the electron cross sections across the ε range constitute several orders of magnitude for all shown Q^2.

The corresponding proton cross section changes are considerable at low Q^2 (factor of $\sim$ 2 in the measured ε range) but at higher Q^2 they become small to negligible. Experimentally, it means that the corresponding rate dependent corrections and uncertainties will have considerably reduced effect on the extracted cross sections in the proton case. Furthermore, a rapidly dropping electron cross section at small ε (backward electron angles) imposes a limitation on the achievable statistical accuracy for the given angular acceptance of the spectrometer while the proton counting rates are high. On the other hand, the cross section at very forward, down to $\sim 8°$, electron angles can be measured which would typically be inaccessible in the electron runs due to the geometrical constraints of the spectrometer. These improvements in the angular coverage increases the measurable ε range, a parameter which is crucial for Rosenbluth linearity tests and, hence, validity of the Born approximation.

In Fig. 1.5b the magnitude of the scattered electron momentum as a function of ε is compared to the momentum of the proton (constant at selected Q^2). Proton detection allows the spectrometer magnets' current to be set to the same value for all spectrometer angles which eliminates small variations in the spectrometer optics unavoidable in the electron runs. Overall, this minimizes the effect of all momentum-dependent corrections such as detector efficiency, multiple scattering, and particle identification.

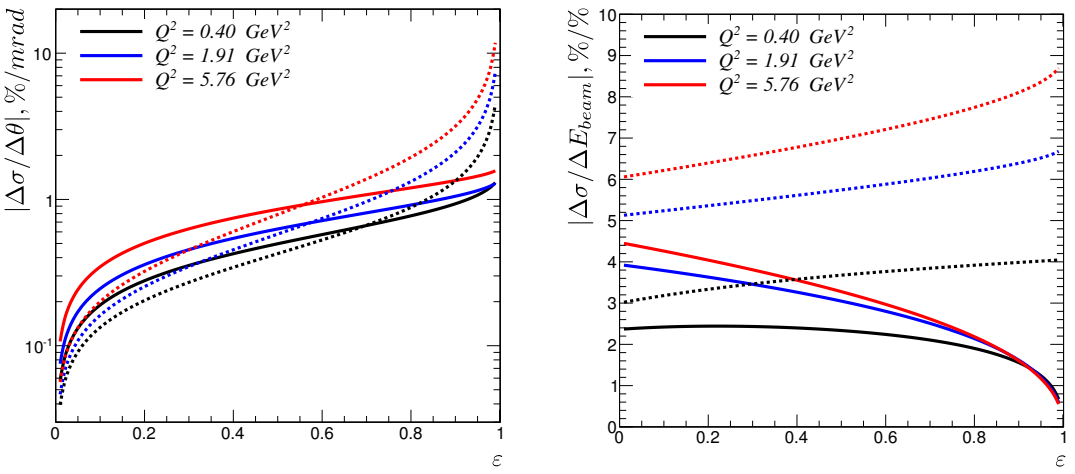

(a) The ε dependence of the cross section variance with respect to the small change in the scattering angle.

(b) The ε dependence of the cross section variance with respect to the small change in the incident beam energy.

Figure 1.6: Sensitivity to the kinematical offsets in case of the detection of the recoil proton (solid) and the scattered electron (dashed) for three selected Q^2 values.

Sensitivity of the cross section measurements to the kinematical settings, such as spectrometer angle or the beam energy, dictates how much final results are affected by their uncertainty. Fig. 1.6a depicts the cross section derivative with respect to the scattering angle for the relevant particle as a function of ε. It quotes the corresponding change of the cross section for a 1.0 mrad change in the scattering angle. In the ε region where angular sensitivity is the dominant source of uncertainty, the

variation of the cross section for electron is a factor of $2-5$ larger than that for the proton. For $\varepsilon \lesssim 0.6$ the proton's cross section angular variations become larger, however, for this kinematics they have smaller amplitude and are less critical for overall uncertainty.

Similar calculations for the beam energy sensitivity are shown in Fig. 1.6b. The results indicate variations for a 1% change in the incoming beam energy. Again, the proton detection offers an advantage over conventional electron runs by reducing variation for all kinematics. Thus, accuracy of the JLab beam energy measurements of $\delta E_{\rm beam}/E_{\rm beam} \approx 2 \times 10^{-4}$ translates into $\approx 0.2\%$ cross section uncertainty for the proton detection.

In addition, the radiative corrections in case of the proton are on average smaller by a factor of ~ 2. In both cases radiative corrections result in a linear dependence on ε and a similar maximum size. However, at Q^2, where the size of corrections is comparable to the Rosenbluth slope that is determined by $G_{\rm E_p}$, the difference in correcting slopes becomes particularly important. One of the examples, where corrections are larger when detecting the proton, is the proton absorption correction. Proton absorption may introduce insignificant ε dependence as the amount of the material seen by a struck proton depends on the proton scattering angle.

The combined impact of improvements in Hall A E01-011 "Super-Rosenbluth" experiment at JLab led to the substantial reduction of the ε dependent systematic errors in $G_{\rm E_p}/G_{\rm M_p}$ extraction compared to the conventional (e,e') experiments. The results of the experiment [12] are given by a solid green diamonds on Fig. 1.3. The $G_{\rm E_p}/G_{\rm M_p}$ ratio was measured at $Q^2 = 2.64, 3.10$ and $4.60\,{\rm GeV}^2$ and was found to be consistent with previous Rosenbluth data. Since (e,e') and (e,p) are prone to different systematics, this result appeared to exclude the possibility that neglected sources of error, in either data set, are responsible for the disagreement with polarization transfer results.

The success of the proton Rosenbluth E01-011 measurements motivated further exploration of the elastic scattering with this improved technique. It continued with a new experiment, E05-017, that was performed in Hall C at JLab, analysis of which is presented in this thesis. The only other experiment which measured both the momentum and the angle of the outgoing proton was performed at the Saskatchewan Accelerator Laboratory in Canada [73]. It was limited to very small values of Q^2 with the electron beam energy not exceeding 130 MeV and was focused on the extraction of the proton charge radius.

2

Two-photon exchange

2.1 Experimental status

Persisting disagreement between cross section and polarization transfer measurements outlined in the previous sections indicated that a more fundamental issue exists with either of the presented techniques suggesting incompletely understood physics as the origin for the observed inconsistency. Several groups (see Sec. 2.2) simultaneously suggested that typically neglected corrections involving hard two-photon-exchange (TPE) processes can largely account for the discrepancy. The corresponding results and general formalism of these improved calculations will be briefly discussed in this chapter. Since the calculation of the hard TPE contribution is sensitive to the internal structure of the nucleon, it necessarily introduces model dependence and can only be included into the cross section approximately. While these corrections were omitted in both methods their effects on the observables in each measurement technique and on the values of the extracted form factors are different. In case of the polarization measurements the expectation is that the radiative corrections in general, including TPE effects, should be very small as they operate with observables defined through the cross section ratios. By contrast, the Rosenbluth form factors extraction is very sensitive to the corrections that introduce angular dependence. While the TPE contribution is merely at the level of several percent these modifications generate strong ε dependence which, at sufficiently large Q^2, becomes comparable or exceeds the $\sigma_{\mathrm{R}}(\varepsilon)$ slope produced by $G_{\mathrm{E_p}}$. Thus, the impact that TPE corrections have in Rosenbluth method is significantly magnified. Theoretical and experimental progress in studying TPE effects have been the subject of several past and very recent reviews [42, 52, 56]. The first $G_{\mathrm{E_p}}$ and $G_{\mathrm{M_p}}$ extraction including explicit two-photon exchange corrections were performed by Arrington [59]. There are several experimental approaches that can be used to probe the size and ε dependence of TPE effects and, thus, to provide necessary constraints on the existing theoretical methodologies of TPE calculations. The real and imaginary part of the TPE amplitudes manifest themselves differently in observables for both unpolarized and polarized measurements. The $G_{\mathrm{E}}/G_{\mathrm{M}}$ extraction is

affected by the real part of the amplitude which modifies unpolarized σ_{R} and P_{t}, P_{l} components of the polarization transfer technique. The imaginary part of the amplitude corresponds to the non-zero values of the normal asymmetries which are forbidden in one-photon exchange approximation.

2.1.1 Charge-dependent lepton scattering

The cleanest experimental signature of TPE mechanism in unpolarized scattering is provided by comparing electron-proton and positron-proton cross sections. The interference term between one- and two-photon exchange amplitudes is sensitive to the sign of the lepton charge. This gives an opportunity to isolate the real part of hard two-photon exchange contribution by measuring the ratio of e^+p and e^-p cross sections. There is another calculable charge-odd term contributing to the ratio which is related to the lepton-proton bremsstrahlung amplitude interference. The ratio itself is typically written as

$$R = \frac{\sigma(e^+p)}{\sigma(e^-p)} \approx \frac{1 + \delta_{\mathrm{even}} - \delta_{2\gamma} - \delta_{\mathrm{brem}}}{1 + \delta_{\mathrm{even}} + \delta_{2\gamma} + \delta_{\mathrm{brem}}} \tag{2.1}$$

where δ_{even} is the charge-even radiative correction factor while $\delta_{2\gamma}$ and δ_{brem} are the TPE and bremsstrahlung interference contributions respectively. In the standard analysis, the experimental ratio R is modified with calculations of δ_{even} and δ_{brem} contributions. Then the TPE contribution is extracted as

$$R_{2\gamma} = 1 - 2\delta_{2\gamma}. \tag{2.2}$$

Experimentally challenging measurements of $R_{2\gamma}$ are generally limited to the moderate Q^2 or larger values of ε where the cross section is large enough to make the usage of the low intensity positron beams statistically feasible. Several experiments on e^+p and e^-p comparison were conducted in the 1960s [28–34]. The most recent results were obtained from three modern experiments at VEPP-3 (Novosibirsk), CLAS (Hall B, JLab), and OLYMPUS (DESY) [36–39, 43]. The constraints on TPE contribution provided by the early lepton scattering tests were reexamined by J. Arrington [35] to verify if their size was adequate to account for Rosenbluth-polarization discrepancy. The combined linear fit to the ε dependence of measurements below $2\,\mathrm{GeV}^2$ yielded a slope of $-(5.7 \pm 1.8)\,\%$ (Fig. 2.1). A $2.8\,\%$ TPE contribution to the Rosenbluth extraction due to this slope accounts for half that needed to resolve the disagreement between polarization transfer and Rosenbluth data at high Q^2.

A new set of measurements from VEPP-3, CLAS, and OLYMPUS, each described below, provided a much better precision on $R_{2\gamma}$ extraction but were, in general, limited to $Q^2 < 2\,\mathrm{GeV}^2$ range.

At the VEPP-3 storage ring alternating electron and positron beams were directed upon internal ^{1}H gaseous target [36]. The experiment used non-magnetic

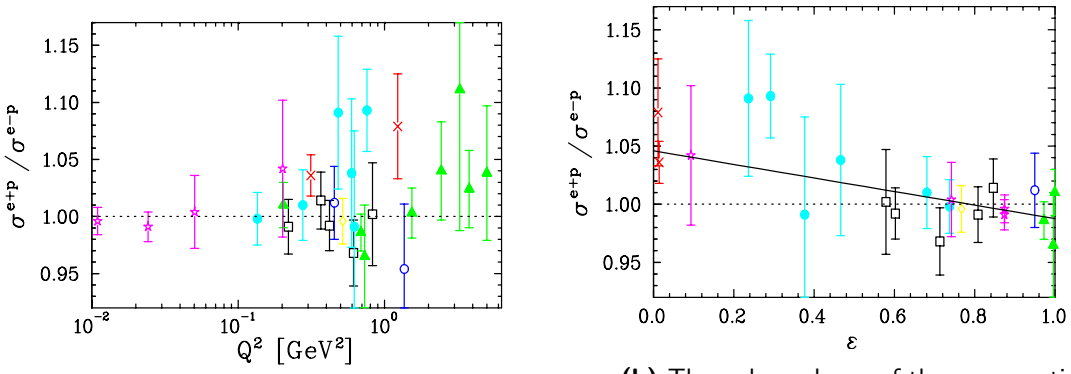

(a) The Q^2 dependence of the cross section ratio, $R{=}\sigma_{e+}/\sigma_{e-}$.

(b) The ε dependence of the cross section ratio, $R{=}\sigma_{e+}/\sigma_{e-}$. Black line is a linear fit for the combined data set below 2 GeV^2.

Figure 2.1: Selected list of experimental results on lepton scattering comparison: black squares [28], red crosses [29], green solid triangles [30], blue hollow circles [31], yellow diamonds [32], cyan filled circles [33], magenta stars [34]. *Figure source: Ref.* [35].

spectrometers to detect the scattered lepton and the recoil proton in coincidence. The data taking period was split in two parts which ran at 1.6 GeV and 1.0 GeV beam energies respectively. The measurements at very forward kinematics ($\varepsilon > 0.9$), where the hard TPE effects are expected to be small, were used as luminosity normalization points. The VEPP-3 results are shown in Fig. 2.2 and Fig. 2.3 along with data obtained from CLAS measurements.

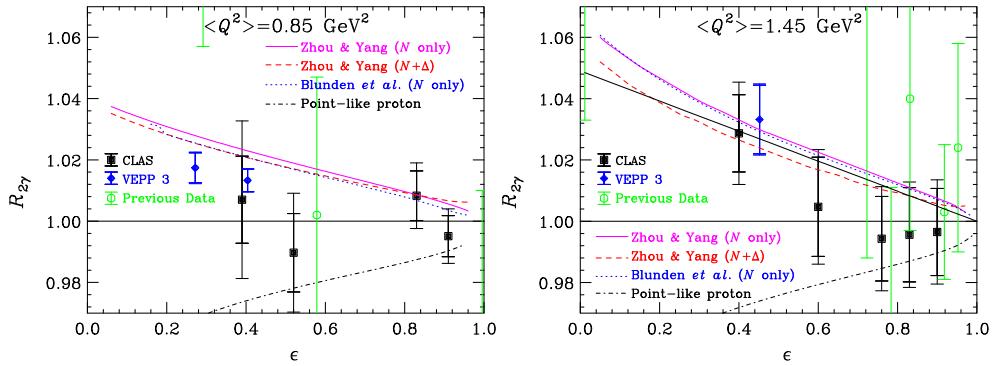

Figure 2.2: Combined results of VEPP-3 (Novosibirsk) [36] and CLAS (JLab) [37–39] experiments for extraction of $R_{2\gamma}$ as function of ε. Theoretical curves: magenta solid and red dashed [40], blue dotted [41], black dot-dashed [42]. *Figure source: Ref.* [39].

For measurements at CLAS [37–39], a mixed lepton beam was produced by two stages of conversion of the initial 5.6 GeV electron beam. First, a gold radiator was used to generate a bremsstrahlung photon beam which was then collimated while the initial electron beam was diverted to the beam dump. Electron-positron pairs were created by passing photons through a converter. The e^+e^- beam was then horizontally separated by a chicane magnet, guided around a tungsten block used to stop photons, and directed towards a 30 cm long liquid hydrogen target. Overdetermined elastic kinematics for the detected scattered lepton and proton allowed

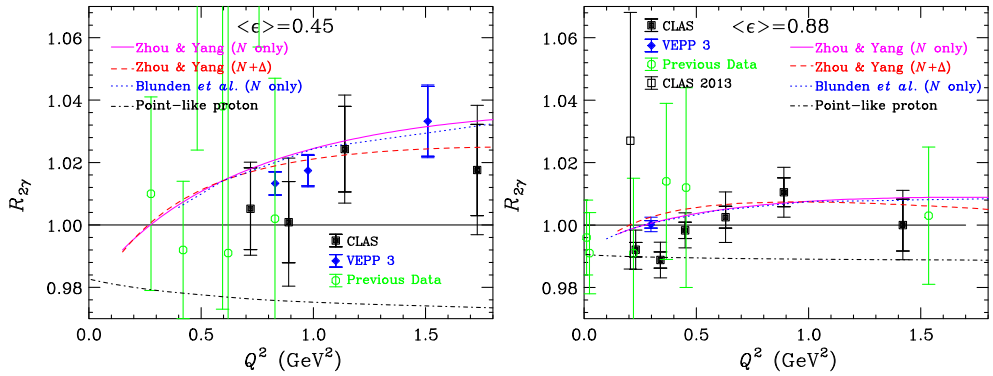

Figure 2.3: Combined results of VEPP-3 (Novosibirsk) [36] and CLAS (JLab) [37–39] experiments for extraction of $R_{2\gamma}$ as function of Q^2. Theoretical curves: magenta solid and red dashed [40], blue dotted [41], black dot-dashed [42]. *Figure source: Ref.* [39].

reconstruction of the incident lepton energy. Since it was impossible to measure absolute luminosity, the extraction of $R_{2\gamma}$ relied on the fact that electrons and protons were produced in equal amounts. The acceptance related systematic uncertainties for oppositely charged leptons were controlled by periodically switching the polarity of the CLAS torus magnet and beamline chicane. CLAS data had quite broad kinematical coverage in the Q^2–ε plane but, since for certain beam energies range statistics were limited, the results were quoted for bin-averaged values of Q^2 and ε.

The OLYMPUS experiment [43] exploited alternating monoenergetic lepton beams from the DORIS storage ring with a windowless internal ^{1}H gaseous target. The coincidence events of an elastically scattered lepton-proton pair were detected in the toroidal magnetic spectrometer with the angular acceptance of $20^\circ < \theta < 80^\circ$, $-15^\circ < \phi < 15^\circ$. The absolute and relative (between beam species) integrated luminosity values were determined in several independent ways. Beside the slow control information including beam current and position monitors, two independent detector systems were constructed for this task, symmetric Møller/Bhabha calorimeters and two telescopes of interleaved gas electron multiplier (GEM) detectors and multi-wire proportional chamber (MWPC). The OLYMPUS data analysis heavily relied on a comprehensive Monte Carlo simulation of the experiment which included effects of $e^\pm$ acceptance differences, radiative corrections, luminosity, and reconstruction efficiency and resolution. The final results on $R_{2\gamma}$ were quoted for several radiative correction prescriptions. Fig. 2.4 depicts ε dependence of $R_{2\gamma}$ for Mo and Tsai convention of radiative corrections to all orders.

Overall, the modern experiments produced significantly more precise results than the earlier experiments, however, the direct comparison of VEPP-3, CLAS, and OLYMPUS data is complicated by the fact that only few measurements were performed at the same kinematics. All three data sets show a modest increase in $R_{2\gamma}$ to $2\,\% - 3\,\%$ for $\varepsilon < 0.5$, especially at larger Q^2. While the results were in reasonable agreement, the OLYMPUS data were systematically less than unity at high ε values. The moderate Q^2 dependence was more clearly pronounced for VEPP-3 data set. Although the estimates of $R_{2\gamma}$ from these experiments exclude a *no-*

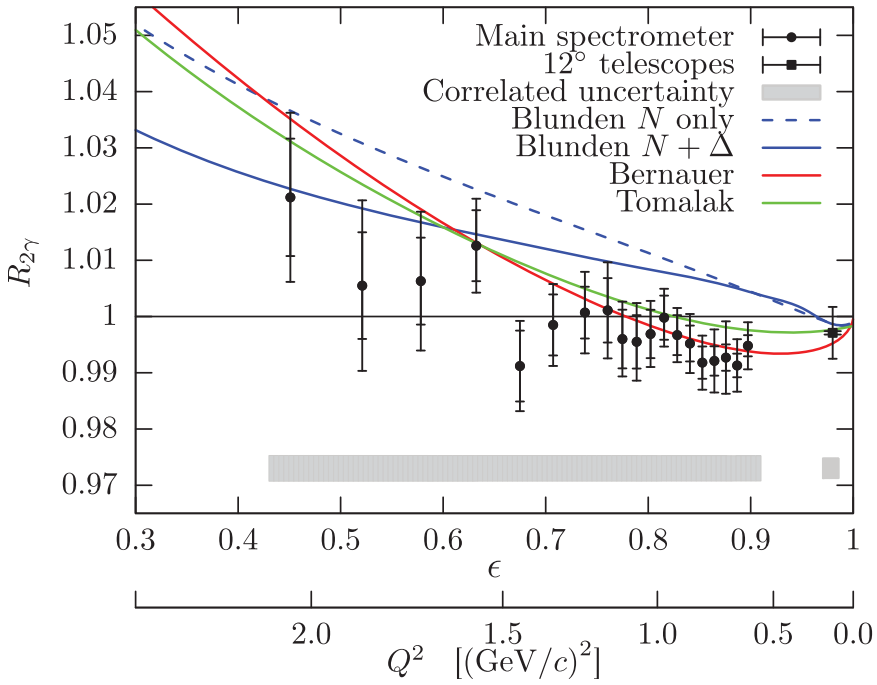

Figure 2.4: Results of OLYMPUS (DESY) [43] experiment for extraction of $R_{2\gamma}$ as function of ε (note, however, that ε bins correspond to a correlated variation over Q^2). Theoretical curves: Blunden [41, 44], Bernauer [45], Tomalak [46]. *Figure source: Ref.* [43].

hard TPE effect (Sec. 2.2) hypothesis at greater than the 95% confidence level [52], there is a clear deficiency of experimental constraints at higher Q^2 and, more importantly, at small ε values.

2.1.2 Spin dependent observables

As mentioned above, the polarization observables are sensitive to both the real and imaginary part of the hard TPE amplitudes. The presence of TPE effects in the electron-proton scattering experiments exploiting spin degrees freedom can be verified by observing:

(i) the ε dependence of the recoil proton polarization components P_{l}, P_{t} and their ratio R in PT measurements configuration with a longitudinally polarized electron beam and unpolarized target;

(ii) the induced component of the recoil proton polarization, P_{n}, normal to the scattering plane in PT measurements configuration with a electron longitudinally polarized beam and unpolarized target;

(iii) the single spin asymmetry (SSA) with an unpolarized electron beam and target polarized perpendicular to the scattering plane, also referred to as target-normal-asymmetry (TNA) or A_{n};

(iv) the SSA with an electron beam polarized perpendicular to the scattering plane and unpolarized target, also known as beam-normal-asymmetry (BNA) or B_n.

The terms of the real part of TPE amplitudes that contribute to P_l, P_t and R in item (i) result in the ε dependence which vanishes under the one-photon-exchange approximation where G_{E_p}, G_{M_p} are real functions of Q^2 only. These assumptions were tested during the JLab experiment $GE_p(2\gamma)$ [22] where the ratios R and P_l/P_l^{Born} were measured separately at a fixed $Q^2 = 2.5\,GeV^2$ over a wide ε range. The elastic events were produced by scattering a longitudinally polarized electron beam from a 20 cm liquid hydrogen target. The electrons were measured in a large acceptance lead-glass electromagnetic calorimeter. The Hall C High Momentum Spectrometer (HMS) was used to detect protons. The polarization components of the proton were measured in the Focal Plane Polarimeter (recoil polarimeter). The polarized recoil protons undergo a secondary rescattering off carbon or hydrogen nucleus in the two 55 cm thick dihydridocarbon (CH_2) blocks which induces an azimuthal asymmetry in the angular distribution of the scattered protons. This asymmetry was measured by pairs of drift chambers which followed each of CH_2 blocks. The results of the experiment are shown in Fig. 2.5.

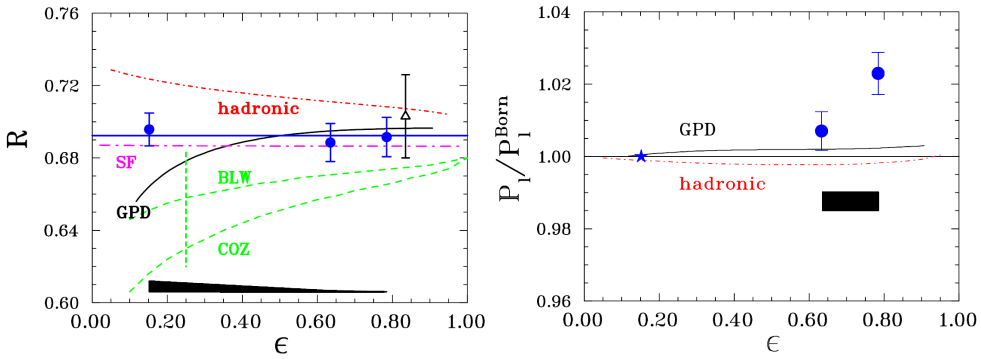

Figure 2.5: Results of $GE_p2\gamma$ (JLab) experiment: filled circles [22], open triangle [19]. Left: R (see item (i)) extraction as a function of ε, black band is the point-to-point systematic uncertainty. Right: P_l/P_l^{Born} (see item (i)) extraction as a function of ε, black band is the point-to-point systematic uncertainty. Theoretical curves (for acronym definitions see Sec. 2.2): red dot-dashed [41], solid black [47], dashed green [48], magenta dot-dashed [49]. *Figure source: Ref.* [22]

The polarization ratio does not indicate an ε dependence within experimental errors and is consistent with Born approximation over the range $0.15 \lesssim \varepsilon \lesssim 0.8$. In contrast, the results on P_l/P_l^{Born} agree with a *no-hard TPE* effect hypothesis only for moderate values of ε but indicate a $\approx 2\,\%$, up to 4.5 standard deviations, enhancement at the larger ε value.

The observables listed in the items (ii)–(iv) are sensitive to the imaginary part of the TPE amplitude. The non-zero value of the induced proton polarization or indicated asymmetries would provide a clear evidence for TPE presence. However, the results of such measurements cannot be directly used to reconcile Rosenbluth-PT disagreement since the form factors depend on the real part of the amplitude.

Since various notations for target- (A, A_n, A_y) and beam-normal (A_n, $A_\perp$, B_n) single spin asymmetries were used in literature, the nomenclature from [56] were used here with $A_n(B_n)$ for target(beam) SSA respectively.

Several experiments [50, 99–101] were conducted in the late 1960s aimed to measure possible recoil proton polarization P_n, item (i). The combined results cover the Q^2 range from 0.3 to 1.9 GeV^2. The main elements of experimental arrangements were similar to the ones described above for PT measurements. No evidence for induced normal polarization of the recoil proton were found within experimental uncertainties. A summary of the results is shown in Fig. 2.6.

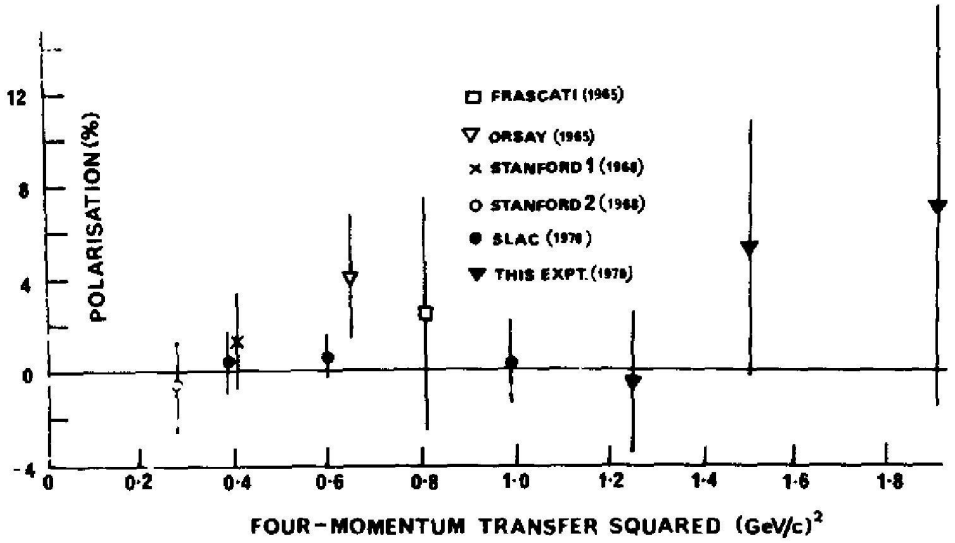

Figure 2.6: Selected list of experimental results on measurements of the normal component of the recoil proton polarization, P_n as a function of Q^2. *Figure source: Ref.* [50]

The TNA outlined in the item (iii) have been studied in a very limited number of experiments [102–106] performed at Cambridge Electron Accelerator (CEA) and SLAC and recently [106] by HERMES collaboration at DESY. The only results for dedicated TPE search in elastic scattering was obtained by Powell [105] where the TNA was measured for $Q^2 = 0.38, 0.59, 0.98$ GeV^2. The electrons which elastically scattered from the polarized proton target were detected in 20 GeV magnetic spectrometer in End Station A at SLAC. A frozen mixture of the 95 % butanol and 5 % water was used as target material and polarization was achieved through the process of dynamical nuclear polarization (DNP). In DNP the target's polarization direction reversal is achieved by changing the frequency of the microwave field irradiating the target. To minimize systematic uncertainties, spin-flip procedures were conducted once every 3 minutes with a weighted average polarization of ~ 20 %. The final result's uncertainty were found to be dominated by the statistical errors. Within the total quoted uncertainties, the results for measured TNA were found to be statistically indistinguishable from zero. The three experiments [102–104] measured TNA in a search for violation of the time invariance in the inelastic scattering processes. Their results did not indicate any sizable asymmetries. HERMES col-

laboration [106] focused on exploring TPE effects in the deep-inelastic region under the assumption of the time reversal invariance and parity conservation. The TNA were measured with electron and positron beams and a transversely polarized gaseous hydrogen target internal to the HERA storage ring. No asymmetry signal was found within experimental uncertainties. The only non-zero TNA were observed [107, 108] for quasi-elastic and inelastic scattering experiments on a normally polarized gaseous ^{3}He target which was used as an approximation for a polarized neutron.

The technological advancements and perfection of the experimental methods along with the ability to produce transversely polarized electron beams made it feasible to measure small single spin asymmetries noted in the item (iv). These improvements were originally achieved for measurement of the parity violating (PV) asymmetries, $A_{\rm PV}$, with the pioneering experiments performed at MIT-Bates by SAMPLE collaboration. The initial experiments, which employed a longitudinally polarized electron beam, was followed by the measurement [109] of the BNA with transversely polarized 200 MeV electrons incident on a 40 cm long liquid hydrogen target. This measurement was performed at a backward electron scattering angle of 146.1° and $Q^2 = 0.1\,\mathrm{GeV}^2$ indicating, for the first time, nonzero BNA value of $B_{\rm n} = (-15.4 \pm 5.4)$ ppm. Since then, several collaborations performed $B_{\rm n}$ measurements [110–116] in various Q^2 ranges and for both forward and backward scattering angles. In addition to the elastic electron scattering from the liquid hydrogen target, HAPPEX/PREX [114] and QWEAK [115] (preliminary) collaborations scattered electrons from a number of nuclear targets (^{4}He, ^{12}C, ^{208}Pb). A representative sample of measurement results is shown in Table 2.1.

Collaboration	$Q^2[GeV^2]$	$B_{\rm n}[ppm]$
MIT-Bates SAMPLE [109]	0.100	-15.40 ± 5.40
MAMI A4 [110]	0.106	$-8.59 \pm 0.89_{stat} \pm 0.75_{syst}$
MAMI A4 [110]	0.230	$-8.52 \pm 2.31_{stat} \pm 0.87_{syst}$
JLab G0 [111]	0.150	$-4.06 \pm 0.99_{stat} \pm 0.63_{syst}$
JLab G0 [111]	0.250	$-4.82 \pm 1.87_{stat} \pm 0.98_{syst}$
JLab G0 [113]	0.220	-176.50 ± 9.40
JLab G0 [113]	0.630	-21.00 ± 24.00
JLab HAPPEX/PREX [114]	0.099	-6.80 ± 1.54
MAMI A4 [116]	0.350	$-99.55 \pm 6.73_{stat} \pm 4.63_{syst}$

Table 2.1: Selected list of experimental results on measurements of the beam normal single spin asymmetry, $B_{\rm n}$, with ^{1}H targets only. Although, the non-zero $B_{\rm n}$ results cannot be directly related to the form factors discrepancy since it is sensitive to the imaginary part of the TPE amplitude, they give an important verification of the TPE effects presence.

2.1.3 Unpolarized scattering

The unpolarized elastic scattering experiments with a single beam species (either electron or positron) can offer yet another approach to validate the presence of TPE effects and to test predictions of available theoretical models. With neither

beam or target being polarized, the size and ε-dependence of TPE contribution can reveal itself through:

(i) the linearity violation of the standard Rosenbluth plot,

(ii) the precise measurements of the discrepancy between Rosenbluth and polarization transfer data.

The Born approximation requires the ε dependence of the reduced cross section, σ_{R}, to be linear as shown in the Eq. 1.13. Thus, any observation of non-linearities that is not covered in the standard radiative correction procedure would provide an experimental signature of effects beyond single photon exchange approximation, item (i). If $\delta_{2\gamma}$ represents the contribution of TPE effects, or more specifically the real part of the $1\gamma \otimes 2\gamma$ interference term, then the measured cross section can be written as

$$\sigma_{\mathrm{R}}^{\mathrm{meas}} = \sigma_{\mathrm{R}}(1 + \delta_{2\gamma}), \tag{2.3}$$

where σ_{R} is given by Eq. 1.13. In this case any ε dependence of $\delta_{2\gamma}$ would result in the appearance, at a minimum, of the ε^2 term in $\sigma_{\mathrm{R}}^{\mathrm{meas}}$. A simple linear parametrization [52] of TPE term, as $\delta_{2\gamma} = A(1-\varepsilon)$, gives

$$\sigma_{\mathrm{R}}^{\mathrm{meas}} \approx \varepsilon^2[-AG_{\mathrm{E_p}}^2] + \varepsilon[(1+A)G_{\mathrm{E_p}}^2 - A\tau G_{\mathrm{M_p}}^2] + (1+A)\tau G_{\mathrm{M_p}}^2. \tag{2.4}$$

Eq. 2.4 shows the difficulty of experimental verification of non-linearity – the size of the quadratic term contribution remains relatively small. At larger Q^2 values where the TPE corrections are expected to be considerable, the contribution from $G_{\mathrm{E_p}}$ to the reduced cross section becomes small. The opposite behavior is true at small Q^2 where the $G_{\mathrm{E_p}}$ term dominates the cross section but TPE effects are small. In order to quantify the deviation from linearity in Rosenbluth measurements Tvaskis and Arrington [42, 51] suggested using a second-order degree polynomial fit of the form:

$$\sigma_{\mathrm{R}}^{\mathrm{meas}} = P_0[1 + P_1(\varepsilon - 0.5) + P_2(\varepsilon - 0.5)^2], \tag{2.5}$$

so that the parameter P_2 and its uncertainty δP_2 provide a simple figure of merit for such measurements and set limits on ε^2 term. In the form of Eq. 2.5, P_2 represents a fractional curvature contribution to the cross section. In addition, the expansion is done around $\varepsilon = 0.5$, such that the nonlinear term is measured with respect to the average cross section. This approach does not impose the expected constraint that TPE effects should vanish as $\varepsilon \to 1$; however, it minimizes uncertainties for the data sets with a limited coverage at the extremes of ε. Initially, the fitting procedure was performed by Qattan and Arrington [27, 42] for the data sets of the best conventional Rosenbluth separation from SLAC experiment NE11 [10]

and of the Super-Rosenbluth measurement from JLab E01-001 experiment [12]. The fitting results for two similar Q^2 settings are shown in Fig. 2.7. Both experiments show the curvature parameter P_2 to be consistent with zero while Super-Rosenbluth measurements improve the limits by more than a factor of 2, from $\delta P_2^{\text{NE11}} = 10\,\%$ to $\delta P_2^{\text{E01-001}} = 4.4\,\%$.

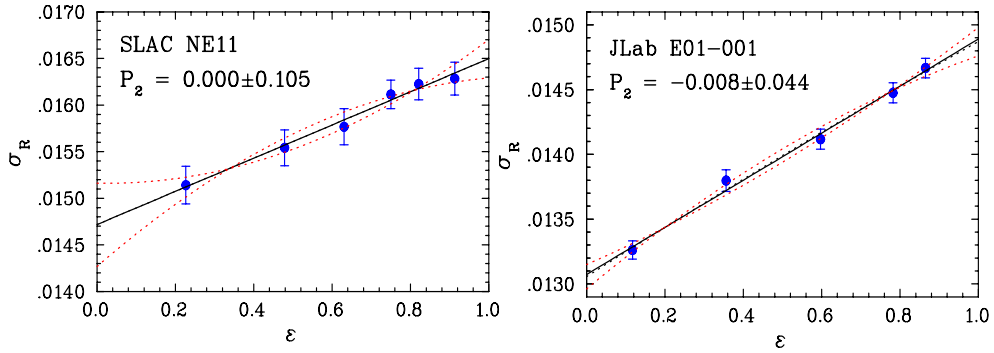

Figure 2.7: Estimates of the deviation from linearity in the Rosenbluth plot. Left: SLAC NE1 experimental data at $2.5\,\text{GeV}^2$ [10]. Right: JLab E01-001 experimental data at $2.64\,\text{GeV}^2$ [12]. The black solid line is a linear fit, the dashed red lines corresponds to $\pm 1\sigma_{P_2}$ variations around the central value of the curvature parameter P_2. *Figure source: Ref.* [42].

A global model-independent search [51] for non-linearities, which included both elastic and inelastic scattering (resonance and deep-inelastic regimes), concluded that the combined data set of σ_{R} is consistent with a *linear* ε dependence: the absence of the second-order term. The results of this analysis are given in Fig. 2.8. The global average value of P_2 was found to be $\langle P_2 \rangle = 0.019 \pm 0.027$ for elastic scattering data (red dotted line in Fig. 2.8) and $\langle P_2 \rangle = -0.060 \pm 0.042$ ($\langle P_2 \rangle = -0.012 \pm 0.071$) for the resonance (deep-inelastic) regions respectively. However, the majority of the points in the low Q^2 domain lack the sensitivity to discriminate nonlinear effects and the only significant limits at $2 < Q^2 < 4\,\text{GeV}^2$ are set by precision Super-Rosenbluth measurements [12]. Analogous analyses of the nonlinear contribution parametrization of *ep* [117, 118] and *ed* [119] elastic scattering produced similar negligibly small non-linearities.

While the δP_2 results presented in Fig. 2.8 provide reasonable constraints on P_2 they do not fully reflect the sensitivity of the measurements. There is a very limited number of precise measurements for $\varepsilon < 0.2$ available in the global database which significantly restricts experimental sensitivity to non-linearities that occur only at low ε. Besides the apparent need of improving Rosenbluth precision, in order to maximize resolving power of non-linearity tests, it is important to expand the ε range of the measurements such that both extremes of ε are covered. Furthermore, it is also necessary to increase the number of ε points at selected Q^2 and, thus, establish a clear reference of the linear region for discriminating against ε^2 contribution.

To address these concerns, E05-017 (Sec. 3.1) conducted highly detailed ε scans for two Q^2 settings at $Q^2 = 0.98\,\text{GeV}^2$ and at $Q^2 = 2.29\,\text{GeV}^2$. The majority of other Q^2 settings include measurements with ε well below 0.2. In general, special

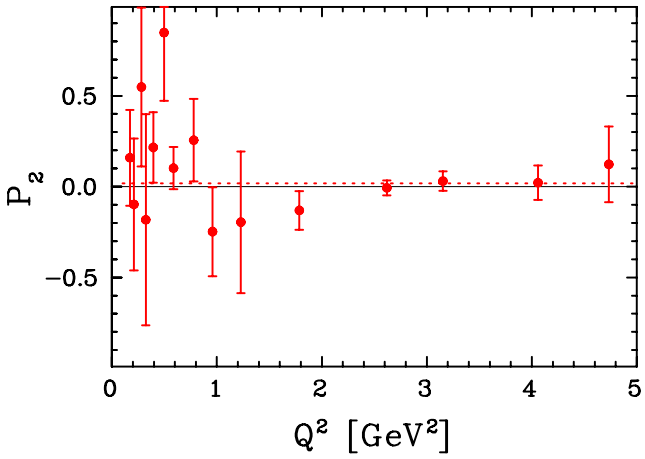

Figure 2.8: The Q^2 dependence of the curvature parameter P_2 from the global analysis of nonlinear effects in Rosenbluth measurements [51]. The red dotted line represents the global average. *Figure source: Ref.* [42].

care was taken to increase the sensitivity of linearity tests by increasing the number of ε points which were spaced almost uniformly between maximum possible values on both ends of the ε range.

Another way in which unpolarized elastic scattering can be utilized to quantitatively probe the size of TPE corrections is to make improved measurements of the discrepancy between the Rosenbluth and polarization transfer methods over a wide kinematic range, as was outlined in item (ii). Unlike the observations of nonlinearity or the other methods covered in previous sections, this approach does not provide an experimental signature of the TPE presence; instead it probes TPE corrections indirectly and relies on several assumptions. Since it is based on the comparison of the form factors ratio deduced from PT measurements, its validity depends on whether the polarization transfer method indeed represents Born form factors and whether the TPE is the only mechanism responsible for disagreement. The limitations of this approach include the extent by which TPE modifies PT results, the experimental uncertainties in PT measurements and the degree of how much linear extrapolation of the PT based slope to $\varepsilon \to 1$ is affected by a possible non-linear behavior of the cross section. The approximate size of the required TPE corrections can be schematically demonstrated as shown in Fig. 2.9 where the results of Super-Rosenbluth separation E01-011 [12] are plotted for two Q^2 settings along with a linear fit (blue line).

The red dashed line indicates the ε dependence as expected from the global analysis of the polarization transfer measurements parametrized here by a simple form:

$$\mu_{\mathrm{p}} G_{\mathrm{E}}/G_{\mathrm{M}} = (1.0 - 0.135(Q^2 - 0.24)). \tag{2.6}$$

The PT measurements can constrain only the value of the slope and have to be normalized to match the Rosenbluth extraction at $\varepsilon = 1.0$ where the TPE contribution is supposed to vanish. Assuming that the TPE modifications on $\mu_{\mathrm{p}} G_{\mathrm{E}}/G_{\mathrm{M}}$ in

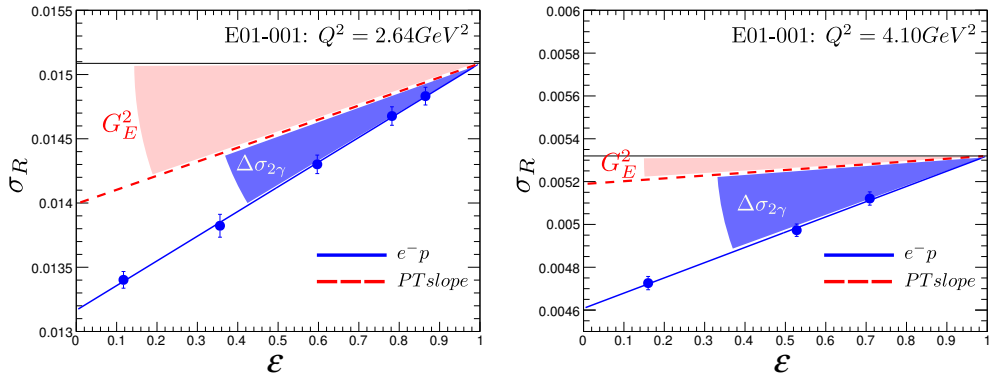

Figure 2.9: The ε dependence of the reduced cross section at $Q^2 = 2.64\,\mathrm{GeV}^2$ (left) and $Q^2 = 4.10\,\mathrm{GeV}^2$ (right). The blue solid circles is Super-Rosendluth E01-001 data [12]. The blue solid line is the Rosenbluth linear fit. The dashed red line is the slope prediction from parametrization (see details in the text) of the global PT data. The blue and red filled sectors illustrate the size of possible contribution to the slope from the TPE (G_E) respectively.

PT measurements are small, i.e. the PT form factors ratio corresponds to the Born approximation, then the ε dependence depicted by the red dashed line is related to the contribution from the electric form factor. If TPE effects are solely responsible for inconsistency, the part of the slope shown as a blue filled sector would represent constraints on the size of the corresponding correction. This yields about half of the observed ε dependence at $Q^2 = 2.64\,\mathrm{GeV}^2$ and $\sim 85\,\%$ at $Q^2 = 4.10\,\mathrm{GeV}^2$. It means that for $Q^2 > 4\,\mathrm{GeV}^2$ the ε dependence is almost entirely due to the TPE and precise elastic cross section measurements allow for a clean separation of G_M and TPE with G_E acting as small correcting factor.

Despite the aforementioned limitations, precise measurements of the discrepancy between Rosenbluth separation and polarization transfer methods is the only currently available tool to put estimates on TPE corrections above $2\,\mathrm{GeV}^2$. The kinematical reach of the direct TPE measurements, $R_{2\gamma}$, with electron and positron beams described in the previous sections is dictated by the luminosity of existing positron facilities. Fig. 2.10 shows kinematic limitations of recent $e^{\pm}p$ measurements. The JLab $GE_\mathrm{p}(2\gamma)$ polarization transfer TPE search [22] was performed at $Q^2 = 2.5\,\mathrm{GeV}^2$.

While Rosenbluth-polarization transfer comparison provides a means for TPE amplitudes extraction and several analyses of this type are already available [120–127], the resulting uncertainties in TPE amplitudes are currently dominated by the large uncertainties in the Rosenbluth measurements of $\mu_\mathrm{p} G_\mathrm{E}/G_\mathrm{M}$, especially at high Q^2. Since global analyses have to typically combine multiple experimental data that had access to a different ε kinematics, the final $\mu_\mathrm{p} G_\mathrm{E}/G_\mathrm{M}$ uncertainties are dependent on relative normalization among the data sets which may lead to a strongly correlated systematic shifts between small and large ε measurements. In the large $Q^2 > 2\,\mathrm{GeV}^2$ region E05-017 offers the advantage of a single extraction over the entire Q^2 range compared to the world's body of high-Q^2 measurements. In the small Q^2 range E05-017 again covers a wide array of Q^2 settings with an excellent ε span including the region $1 \lesssim Q^2 \lesssim 2\,\mathrm{GeV}^2$, where previous tests of

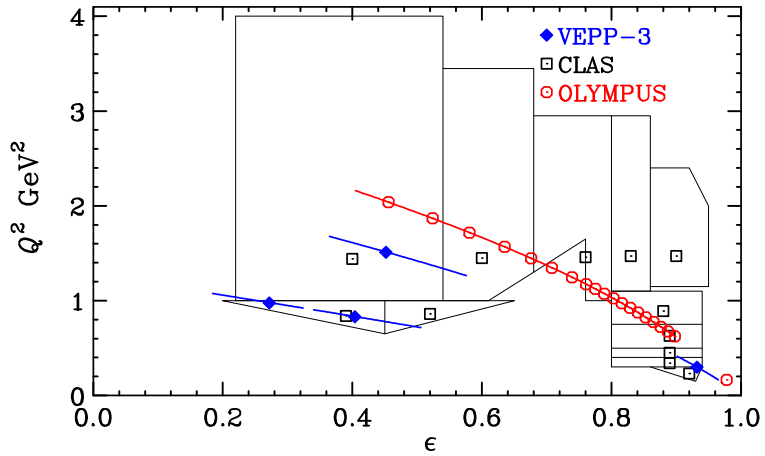

Figure 2.10: Kinematic coverage in the Q^2-ε plane for three recent TPE experiments [36–39, 43] comparing the e^+p and e^-p cross sections. VEPP-3 and OLYMPUS used monoenergetic beams while CLAS ran with a range of beam energies and had bins summed over in both Q^2 and ε. *Figure source: Ref.* [52].

discrepancy were inconclusive (see Sec. 3.1).

2.2 Theoretical status

Early approaches [128–136] to calculate TPE effects performed in the 1950s and 1960s, well before the observed form factors discrepancy, were in agreement with the expectation that their size should be of the order $\mathcal{O}(\alpha = e^2/(4\pi))$ with respect to a single photon exchange approximation and were also in agreement with results of $e^{\pm}p$ scattering experiments of that period (Fig. 2.1). In general, the Rosenbluth form factors extraction requires a number of corrections of order e^2 relative to the Born approximation to be applied to the measured reduced cross section such that it follows the form of Eq. 1.13. These corrections, also known as radiative corrections, have been routinely used in practically all single-arm Rosenbluth measurements. Through several decades, their calculation evolved from the work of Mo and Tsai [137–139], which is often referred to as the standard radiative corrections, to inclusion of additional terms for SLAC measurements [9, 10] and more recent calculations of Maximon and Tjon [140] and others [53, 141–143].

The processes that are accounted for in the corrections include diagrams with exchange of additional virtual photon and emission of a real photon in bremsstrahlung radiation which corresponds to inelastic scattering (see Fig. 2.11). In addition, the radiative correction terms are further categorized into "soft" and "hard" parts. The "soft" terms correspond to the condition when momentum carried by one of the virtual photons is vanishingly small, i.e. this photon does not resolve hadronic structure so the proton is treated as a point-like object. The "hard" terms require understanding of the underlying proton structure and, thus, become model-dependent. The standard radiative corrections [137,139], which cover essentially all diagrams on Fig. 2.11 are quite significant – at large Q^2 they generate ε dependence comparable

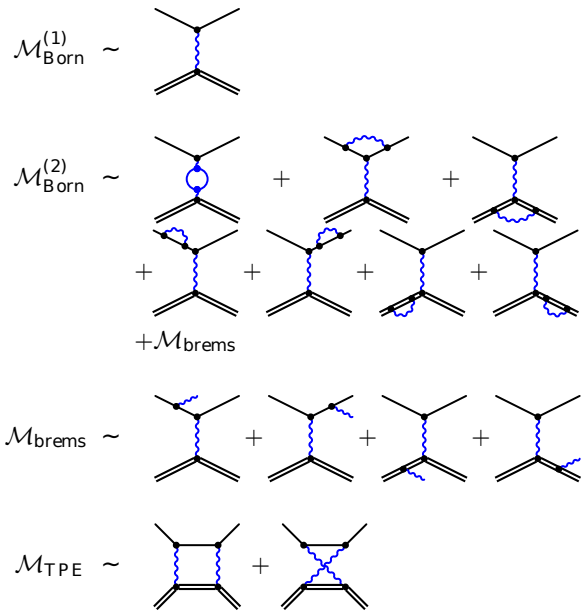

Figure 2.11: Feynman diagrams beyond the leading order. First row: elastic electron scattering. Second row: vacuum polarization (VP), electron vertex correction (ElVC) and proton vertex correction (PrVC). Third row: electron self-energy (ElSE) and proton self-energy (PrSE). Forth row: inelastic diagrams for electron bremsstrahlung (ElBrem) and proton bremsstrahlung (PrBrem). Fifth row: box (BOX) and crossed-box (XBOX) TPE diagrams. *Figure source: Ref.* [53].

in size to the slope that comes from G_{E} contribution; however, they only incorporate terms which are independent of hadron structure. In particular, the TPE contributions when both photons are hard were neglected due to insufficient knowledge of the intermediate hadronic state. The general properties of several radiative correction treatments were covered by Arrington in Ref. [42]. The modification of the reduced cross section from Eq. 1.13 under radiative corrections can be written [42] as:

$$\sigma_{\text{R}} = \sigma^0_{\text{R}}(1 + \delta^{\text{soft}}_{\text{virt}} + \delta^{\text{hard}}_{\text{virt}} + \delta_{\text{brem}}). \tag{2.7}$$

The $\delta^{\text{soft}}_{\text{virt}}$ corresponds to the dominant factorizable term proportional to the Born amplitude through a purely kinematical factor $f(Q^2, \varepsilon)$ and $\delta^{\text{hard}}_{\text{virt}}$ is non-factorizable hard term:

$$\mathcal{M}_{\text{1-loop}} = f(Q^2, \varepsilon)\mathcal{M}_{1\gamma} + \mathcal{M}_{\text{hard}}, \tag{2.8}$$

where $\mathcal{M}_{\text{1-loop}}$ represents all one-loop virtual corrections while $\mathcal{M}_{1\gamma}$ and $\mathcal{M}_{\text{hard}}$ are Born and hard non-factorizable amplitudes respectively, such that

$$\delta^{\text{soft}}_{\text{virt}} = 2f(Q^2, \varepsilon) \quad \text{and} \quad \delta^{\text{hard}}_{\text{virt}} = \frac{2\Re e\{\mathcal{M}^*_{1\gamma}\mathcal{M}^2_{\text{hard}}\}}{|\mathcal{M}_{1\gamma}|^2}. \tag{2.9}$$

Furthermore, both δ_{brem} and $\delta_{\text{virt}}^{\text{soft}}$, except for VP, ElSE, and PrSE (see Fig. 2.11 for notation), contain infrared (IR) divergent and IR finite terms. The corresponding IR divergent parts of inelastic δ_{brem} and the terms of δ_{virt} cancel each other exactly. Historically, the majority of analyses on elastic cross section extraction implemented radiative corrections of Mo and Tsai (MoT) which means that the soft IR divergent parts of the full TPE amplitudes are included. Since that became a standard procedure, the modern discussion of TPE effects focuses only on the "hard",

$$\delta_{2\gamma} = \delta_{\text{full}} - \delta_{\text{MoT}}^{\text{IR}}, \tag{2.10}$$

part of BOX and XBOX diagrams.

More recent Rosenbluth measurements [45, 78] use an improved version of radiative procedures offered by Maximon and Tjon (MTj). Their three important additions include: (a) an evaluation of the soft bremsstrahlung cross section without any approximation, (b) a partial approximation removal in the evaluation of the soft TPE contribution, (c) no soft photon approximation for PrVC treatment which generated only weak ε dependence and can be neglected in form factor disagreement studies. Since the updated prescription for radiative corrections treatment partially redefines what constitutes the soft, model independent, part of TPE it is useful to understand the difference in the ε dependence between these two treatments. The detailed comparison of the form $(\delta_{\text{MoT}}^{\text{IR}} + \delta_{\text{MoT}}^{\text{brem}}) - (\delta_{\text{MTj}}^{\text{IR}} + \delta_{\text{MTj}}^{\text{brem}})$ can be found in [42]. The radiative procedures used in this thesis for analysis of E05-017 are those of Walker and Ent [9, 141].

2.2.1 Generalized formalism

Over the past two decades the investigation of the hard $\delta_{2\gamma}$ properties and determination whether it can fully or partially reconcile form factors obtained from polarized and unpolarized elastic scattering data resulted in significant progress in theoretical calculations. One of the first steps in this direction was the development [144] of the general description of elastic scattering reaction (1.2). When considering all helicity (h, h', λ, λ') combinations,

$$e(k,h) + P(p,\lambda) \rightarrow e(k',h') + P(p',\lambda'), \tag{2.11}$$

a total of sixteen amplitudes are possible in the expansion of the scattering matrix. An additional requirement of parity conservation and time-reversal invariance reduces the number of independent helicity amplitudes to 8 and further to 6 respectively. To provide a general parametrization of elastic ep scattering amplitude, Guichon and Vanderhaeghen [144] introduced three complex generalized form factors

$$T = \frac{e^2}{Q^2}\bar{u}_{\text{e}}(k',h')\gamma_\mu u_{\text{e}}(k,h) \times \bar{u}_{\text{p}}(p',\lambda')\left(\tilde{G}_{\text{M}}\gamma^\mu - \tilde{F}_2\frac{P^\mu}{M_{\text{p}}} + \tilde{F}_3\frac{\gamma\cdot K P^\mu}{M_{\text{p}}^2}\right)u_{\text{p}}(p,\lambda), \tag{2.12}$$

where $\tilde{G}_{\rm M}$, $\tilde{F}_2$, $\tilde{F}_3$ are the complex functions of ε and Q^2 and with K, P defined as

$$K = \frac{k+k'}{2}, \quad P = \frac{p+p'}{2}, \quad \nu = K \cdot P. \tag{2.13}$$

The generalized notation was chosen such that it naturally reduces to the usual proton electromagnetic form factor $G_{\rm E}$ and $G_{\rm M}$ under one-photon exchange approximation. $\tilde{G}_{\rm E}$ is defined as $\tilde{G}_{\rm E} \equiv \tilde{G}_{\rm M} - (1+\tau)\tilde{F}_2$ such that

$$\begin{aligned}
\tilde{G}_{\rm E}(Q^2,\varepsilon) &= G_{\rm E}(Q^2) + \delta\tilde{G}_{\rm E}(Q^2,\varepsilon), \\
\tilde{G}_{\rm M}(Q^2,\varepsilon) &= G_{\rm M}(Q^2) + \delta\tilde{G}_{\rm M}(Q^2,\varepsilon), \\
\tilde{F}_3(Q^2,\varepsilon) &\equiv \delta\tilde{F}_3(Q^2,\varepsilon).
\end{aligned} \tag{2.14}$$

The complex amplitudes $\delta\tilde{G}_{\rm E}$, $\delta\tilde{G}_{\rm M}$ and $\delta\tilde{F}_3$ contain information on the processes beyond the Born approximation. The derivation procedure for corresponding changes in the expressions for the observables of interest can be found in [145]. The summary of the results on how unpolarized and polarized scattering observables are modified is given by

$$\sigma_{\rm R}^{2\gamma} = G_{\rm M}^2 + \frac{\varepsilon}{\tau}G_{\rm E}^2 + \frac{2\varepsilon}{\tau}G_{\rm E}\Re e\left(\delta\tilde{G}_{\rm E} + \frac{\nu}{M_{\rm p}^2}\tilde{F}_3\right) + 2G_{\rm M}\Re e\left(\delta\tilde{G}_{\rm M} + \frac{\varepsilon\nu}{M_{\rm p}^2}\tilde{F}_3\right) + \mathcal{O}(e^4) \tag{2.15}$$

for the reduced cross section, while the transverse, longitudinal, and normal components of the polarization of the recoil proton are presented as [145]

$$\begin{aligned}
P_{\rm t}^{2\gamma} &= -h\sqrt{\frac{\varepsilon(1-\varepsilon)}{\tau}}\frac{1}{\sigma_{\rm R}}\left[G_{\rm E}G_{\rm M} + G_{\rm M}\Re e\left(\delta\tilde{G}_{\rm E} + \frac{\nu}{M_{\rm p}^2}\tilde{F}_3\right) + G_{\rm E}\Re e(\delta\tilde{G}_{\rm M}) + \mathcal{O}(e^4)\right], \\
P_{\rm l}^{2\gamma} &= h\sqrt{1-\varepsilon^2}\frac{1}{\sigma_{\rm R}}\left[G_{\rm M}^2 + 2G_{\rm M}\Re e\left(\delta\tilde{G}_{\rm M} + \frac{\varepsilon}{1+\varepsilon}\frac{\nu}{M_{\rm p}^2}\tilde{F}_3\right) + \mathcal{O}(e^4)\right], \\
P_{\rm n}^{2\gamma} &= h\sqrt{\frac{2\varepsilon(1+\varepsilon)}{\tau}}\frac{1}{\sigma_{\rm R}}\left[-G_{\rm M}\Im m\left(\delta\tilde{G}_{\rm E} + \frac{\nu}{M_{\rm p}^2}\tilde{F}_3\right) + G_{\rm E}\Im m\left(\delta\tilde{G}_{\rm M} + \frac{2\varepsilon}{1+\varepsilon}\frac{\nu}{M_{\rm p}^2}\tilde{F}_3\right) + \mathcal{O}(e^4)\right], \\
R^{2\gamma} &= -\sqrt{\frac{\tau(1+\varepsilon)}{2\varepsilon}}\frac{P_{\rm t}}{P_{\rm l}} \\
&= R\left[1 - \frac{\Re e(\delta\tilde{G}_{\rm M})}{G_{\rm M}} + \frac{1}{R}\frac{\Re e(\delta\tilde{G}_{\rm E})}{G_{\rm E}} + \frac{\nu\Re e(\tilde{F}_3)}{M_{\rm p}^2}\left(\frac{1}{G_{\rm E}} - \frac{2\varepsilon}{G_{\rm M}(1+\varepsilon)}\right)\right] + \mathcal{O}(e^4),
\end{aligned} \tag{2.16}$$

where $h = \pm 1/2$ is the helicity of the electron and $R = G_{\rm E}/G_{\rm M}$ is the $R_{\rm Born}$.

Albeit the generalized form factors include contributions from all other higher order terms, they are typically referred to as two-photon exchange corrections. Another useful convention is to express their real part relative to the magnetic form factor as dimensionless quantities:

$$Y_{\rm M}(Q^2,\varepsilon) \equiv \Re e\left(\frac{\delta\tilde{G}_{\rm M}}{G_{\rm M}}\right), \quad Y_{\rm E}(Q^2,\varepsilon) \equiv \Re e\left(\frac{\delta\tilde{G}_{\rm E}}{G_{\rm M}}\right), \quad Y_3(Q^2,\varepsilon) \equiv \frac{\nu}{M_{\rm p}^2}\Re e\left(\frac{\delta\tilde{F}_3}{G_{\rm M}}\right). \tag{2.17}$$

In this notation Eq. 2.15 and 2.16, observables of the Rosenbluth and polarization transfer (PT) methods, transforms into

$$\frac{\sigma_{\rm R}^{2\gamma}}{G_{\rm M}^2} = 1 + \frac{\varepsilon}{\tau}\left[R^2 + 2Y_3(\tau+R) + 2Y_{\rm E}R\right] + 2Y_{\rm M} + \mathcal{O}(e^4), \tag{2.18}$$

$$R_{\rm PT}^{2\gamma} = R + Y_3\left(1 - R\frac{2\varepsilon}{1+\varepsilon}\right) + Y_{\rm E} - Y_{\rm M}R + \mathcal{O}(e^4). \tag{2.19}$$

From this perspective, it becomes more transparent that the $\mu_{\rm p}G_{\rm E_p}/G_{\rm M_p}$ ratio, as it is measured with either Rosenbluth or polarization transfer methods, does not return the true form factor ratio. Instead, the slope measured with the Rosenbluth separation, or longitudinal-transverse separation (LT), technique (ignoring possible ε dependence of $Y_{\rm M}$) yields

$$\left(R_{\rm LT}^{2\gamma}\right)^2 = R^2 + 2Y_3(\tau+R) + 2Y_{\rm E}R, \tag{2.20}$$

while an overall addition, $\Delta\sigma_{\rm R}^{2\gamma} = \sigma_{\rm R}^{2\gamma} - \sigma_{\rm R}^{\rm Born}$, to the measured cross section is given by

$$\frac{\Delta\sigma_{\rm R}^{2\gamma}}{G_{\rm M}^2} \approx \frac{1}{\tau}\left[2\varepsilon Y_3(\tau+R) + 2\varepsilon Y_{\rm E}R + 2\tau Y_{\rm M}\right]. \tag{2.21}$$

As it was outlined in the items (i) and (ii) of Sec. 2.1.3, the purpose of the E05-017 run was (a) to provide precision data on $\left(R_{\rm LT}^{2\gamma}\right)^2$ over a wide Q^2 range so that the meaningful separation of the TPE amplitudes is possible by analyzing the difference between $\left(R_{\rm LT}^{2\gamma}\right)^2$ and $\left(R_{\rm PT}^{2\gamma}\right)^2$, and (b) to set much tighter limits on non-linearity of the reduced cross section and, thus, to restrict the scope of assumptions on ε dependence of $Y_{\rm M}$, $Y_{\rm E}$ and Y_3 that are used for their extraction.

The investigation of the ε dependence of the spin-dependent observables $R_{\rm PT}^{2\gamma}$ and, separately, $P_{\rm l}^{2\gamma}$ (see item (i) of Sec. 2.1.2) offers additional independent constraints on TPE amplitudes. The $P_{\rm l}^{2\gamma}$ is typically expressed with respect to its Born value as [145]

$$\frac{P_l^{2\gamma}}{P_l^{\mathrm{Born}}} = 1 - \frac{2\varepsilon}{1+\frac{\varepsilon}{\tau}R^2}\left(Y_3\left[\frac{\varepsilon}{1+\varepsilon}\left(1-\frac{R^2}{\tau}\right)+\frac{R}{\tau}\right]+\frac{R}{\tau}\left[Y_{\mathrm{E}}-RY_{\mathrm{M}}\right]\right) \tag{2.22}$$

A quick comparison of Eq. 2.18, 2.19 and 2.22 show that TPE contribution (omitting the terms proportional to R) to $\sigma_{\mathrm{R}}^{2\gamma}$ and $R_{\mathrm{PT}}^{2\gamma}$ are of the order of $\varepsilon Y_3 + Y_{\mathrm{M}}$ and $Y_3 + Y_{\mathrm{E}}$ respectively while $P_l^{2\gamma}/P_l^{\mathrm{Born}}$ is dominated by the Y_3 term.

In the case of the $e^{\pm}p \to e^{\pm}p$ cross section comparison summarized in Sec. 2.1.1, the corresponding expression, Eq. 2.18, for positron-proton scattering would change sign in front of the TPE amplitude terms and, hence, would provide important TPE constraint.

However, due to the limitations of the existing cross section (insufficient quality at large Q^2), polarization transfer (restricted mostly to ε =0.75 to 0.9), and positron-proton (available up to a moderate $Q^2 \approx 2\,\mathrm{GeV}^2$ only, sensitive to the correction to account for bremsstrahlung interference term changing sign similarly to TPE) data a range of assumptions about behavior of the corresponding terms have to be made in order to perform phenomenological TPE extraction [120–127] of this type. The most recent discussion of the various approaches that were taken for Y_{M}, Y_{E} and Y_3 phenomenological extraction by several different groups can be found in [127].

Finally, the $P_n^{2\gamma}$ from Eq. 2.16 probes the imaginary part of TPE amplitudes. Since neither of $\left(R_{\mathrm{LT}}^{2\gamma}\right)^2$ and $\left(R_{\mathrm{PT}}^{2\gamma}\right)^2$ includes imaginary TPE contribution terms, the $P_n^{2\gamma}$ measurements would not be directly relevant for the form factor discrepancy investigation. However, recent advancements in dispersive methods [46, 146–148], which allow one to obtain the real part of the amplitude from the imaginary, provide a necessary link for usage of $P_n^{2\gamma}$ data as yet another input for TPE studies. The $P_n^{2\gamma}$ measurements is equivalent [149], through the time-reversal invariance, to the measurement of the A_n or target SSA (see items (ii) and (iii) of Sec. 2.1.2). Surprisingly, no modern data exist on target normal asymmetries for elastic scattering with the polarized proton target and no dedicated experiments have been proposed for TNA measurements.

2.2.2 Hadronic calculations

In a parallel effort, the hadronic model was used to evaluate two-photon exchange contributions to elastic electron-proton scattering cross sections by Blunden [41, 54]. The total TPE amplitude part of the $\mathcal{M}_{\mathrm{hard}}$, Eq. 2.8, was computed [42] as

$$\mathcal{M}_{2\gamma} = \mathcal{M}_{\mathrm{box}} + \mathcal{M}_{\mathrm{xbox}}. \tag{2.23}$$

The BOX (XBOX) amplitude, Fig. 2.12, is then given by

$$\mathcal{M}_{2\gamma}^{\mathrm{box(xbox)}} = -ie^4 \int \frac{d^4q_1}{(2\pi)^4} L_{\mu\nu}^{\mathrm{box(xbox)}} H_{\mathrm{R}}^{\mu\nu} \Delta_{\mathrm{F}}(q_1,\lambda)\Delta_{\mathrm{F}}(q_2,\lambda), \tag{2.24}$$

where the leptonic tensors are

$$L^{\text{box}}_{\mu\nu} = \bar{u}_{\text{e}}(k')\gamma_\mu S_{\text{F}}(k-q_1, m_{\text{e}})\gamma_\nu u_{\text{e}}(k), \quad L^{\text{xbox}}_{\mu\nu} = \bar{u}_{\text{e}}(k')\gamma_\mu S_{\text{F}}(k-q_2, m_{\text{e}})\gamma_\nu u_{\text{e}}(k). \tag{2.25}$$

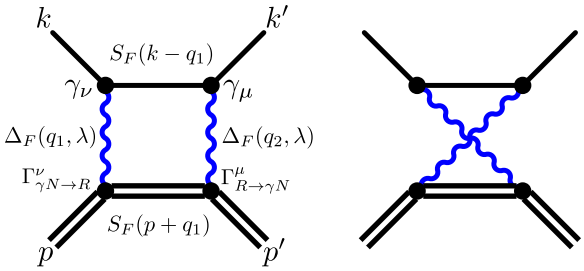

Figure 2.12: Left: direct box diagram. Right: crossed box diagram.

The hadronic tensor for an intermediate hadronic state R of invariant mass M_{R} can be written as

$$H^{\mu\nu}_{\text{R}} = \bar{u}_{\text{p}}(p')\Gamma^\mu_{\text{R}\to\gamma\text{N}}(p+q_1, -q_2)S_{\text{F}}(p+q_1, M_{\text{R}})\Gamma^\nu_{\gamma\text{N}\to\text{R}}(p+q_1, q_1)u_{\text{N}}(p). \tag{2.26}$$

The initial calculations were performed keeping just the elastic nucleon as an intermediate state R that dominates the TPE corrections at low to moderate Q^2. In this case, the electromagnetic current operator Γ^μ is parametrized by phenomenological form factors 1.8. The electron and photon propagators are

$$S_{\text{F}}(k, m) = \frac{\not{k} + m}{k^2 - m^2 + i\epsilon}, \quad \Delta_{\text{F}}(k, \lambda) = \frac{1}{k^2 - \lambda^2 + i\epsilon} \tag{2.27}$$

The first results of a series of papers on hadronic calculations, shown in Fig 2.13, produced the ε-dependent slope of the proper size and sign to at least partially reconciles the discrepancy. The overall effect was the most pronounced at $\varepsilon < 0.4$ leading to significant deviation from linearity with increasing Q^2.

These results were later extended [44] to include inelastic contribution, such as $\Delta(1232)$ resonance, in the intermediate state. The three form factors, $g_{\text{i}}(Q^2)$, required to describe $\gamma N \to \Delta$ ($\Delta \to \gamma N$) vertices were parametrized by the dipole form with a dipole mass of $\Lambda_\Delta = 0.84\,\text{GeV}$ [42]. Intended to extend validity of the hadronic approach to a larger Q^2, the Δ TPE correction produced the relative slope of the ε dependence opposite to that of the nucleon and, hence, reduced the N state TPE contribution to some extent. Recently, the estimates of the Δ resonance contribution were revisited and were improved mostly by investigating the effect of various $g_{\text{i}}(Q^2)$ parametrizations. The details of corresponding results can be found in [40, 150, 151]. The influence of the higher-mass resonance states contribution was also investigated in the work of Kondratyuk and Blunden [55]. The

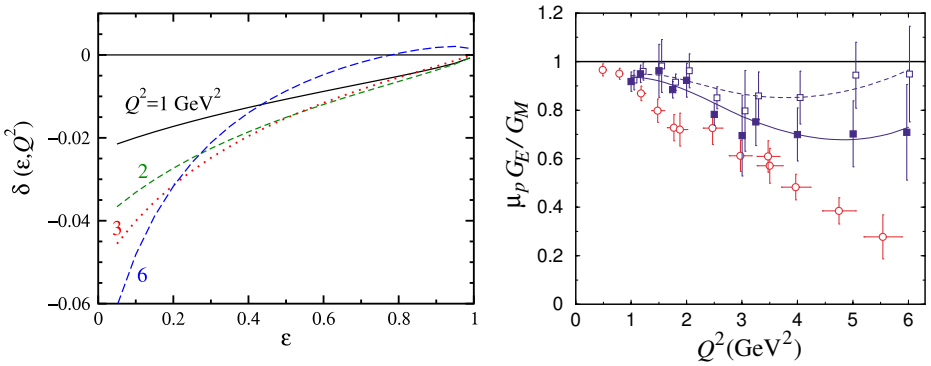

Figure 2.13: Left: the ε dependence of the difference between full TPE correction to the elastic cross section and MoT prescription as discussed in text (Eq. 2.10). *Figure source: Ref.* [42]. Right: form factor ratio plotted as a function of Q^2. The hollow squares [25] is the Rosenbluth data along with Arrington global fit. The hollow circles is the polarization transfer data [18]. The solid squares is the TPE corrected [54] Rosenbluth results. *Figure source: Ref.* [54].

total TPE correction effect to the elastic cross section from the sum of the most important hadron resonances as intermediate states [42],

$$\delta_{2\gamma} = \delta^{\mathrm{N}} + \delta^{\Delta} + \delta^{\mathrm{D}_{13}} + \delta^{\mathrm{D}_{33}} + \delta^{\mathrm{P}_{11}} + \delta^{\mathrm{S}_{11}} + \delta^{\mathrm{S}_{31}}, \tag{2.28}$$

is shown in Fig. 2.14.

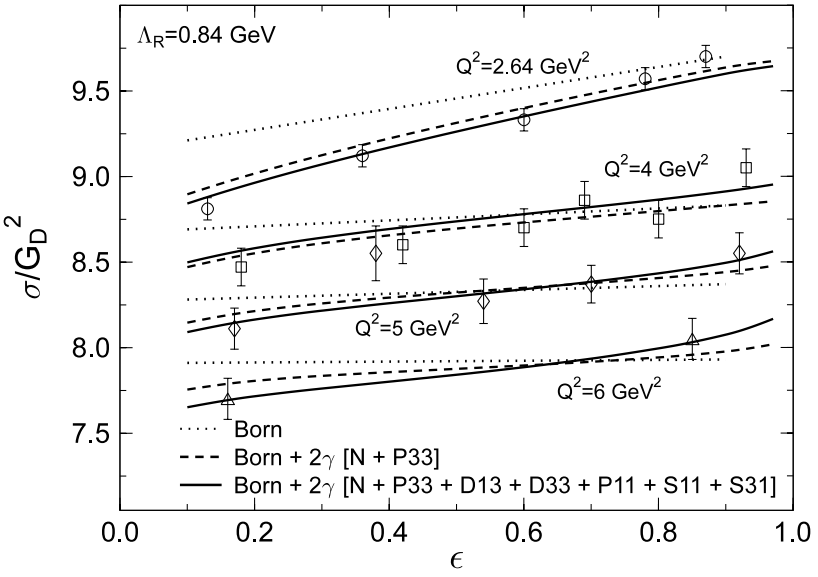

Figure 2.14: Reduced cross section normalized by the dipole shape form factor squared as a function of ε. The Δ resonance and, separately, the sum of Eq. 2.28 resonances influence is indicated by the corresponding curves. *Figure source: Ref.* [55].

2.2.3 Partonic calculations

In the high Q^2 regime, where the implementation of intermediate states beyond the resonance region in hadronic calculations becomes impractical, several groups studied the TPE effects under a partonic approach. In this approach developed by [47, 152] the TPE amplitudes were related to the generalized parton distributions (GPD). The elastic scattering was considered through the so-called handbag process, Fig. 2.15, assuming the dominance of both photons' interaction with a single quark.

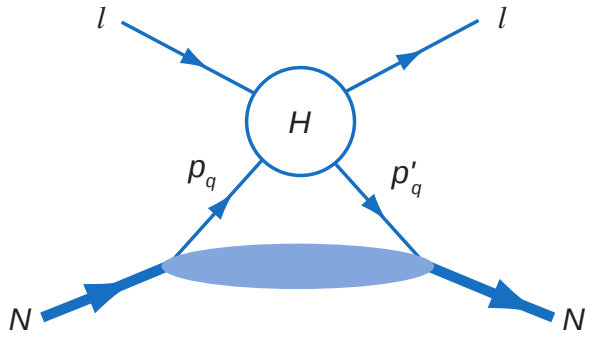

Figure 2.15: Handbag Feynman diagram representing elastic scattering at large Q^2. Single quark is emitted (p_q) and reabsorbed (p'_q) by the nucleon blob represented by GPDs. H indicates partonic scattering process. *Figure source: Ref.* [56].

The scattering amplitude H shown in Fig. 2.15 constitutes the electron scattering off of a quark of flavor q, $e(k) + q(p_q) \rightarrow e(k') + q(p'_q)$, and includes the TPE BOX and XBOX diagrams similar to the ones from Fig. 2.12 only with the proton replaced by the point-like quark. This electron-quark scattering amplitude is separated into a soft and hard parts and their corresponding real and imaginary components is then calculated. The soft part is defined as a situation where the four-momentum carried by one of the photons is zero and was shown to contain an IR divergent term. The treatment of this partonic subprocess, which is essentially scattering on a spin 1/2 Dirac particle calculated before [153, 154], is followed by applying GPD formalism to describe emission and reabsorption of the quark by the nucleon, as shown in the lower part of diagram in Fig. 2.15. Besides the handbag mechanism, there are other contributing processes where photons interact with different quarks. They have to be included to properly reproduce the IR divergent terms. The combined IR contribution from these processes along with the IR term from the soft part of handbag diagram was shown to have the same results as the soft part calculations in the hadronic model discussed above and to get canceled with contributions arising from the emission of the real soft photon by the electron or proton, i.e. bremsstrahlung radiative corrections. However, the hard parts of the process when photons couple to a different quarks, the cat's ears diagram, were neglected. The hard TPE contributions to generalized form factors, Eq. 2.14, are obtained as [47]

$$\delta\tilde{G}_{\rm E}^{\rm hard} = -\left(\frac{1+\varepsilon}{2\varepsilon}\right)(A-C) + \sqrt{\frac{1+\varepsilon}{2\varepsilon}}B,$$
$$\delta\tilde{G}_{\rm M}^{\rm hard} = C,$$
$$\tilde{F}_3^{\rm hard} = \frac{M_{\rm p}^2}{\nu}\frac{1+\varepsilon}{2\varepsilon}(A-C), \tag{2.29}$$

with

$$A = \int_{-1}^{1}\frac{dx}{x}\frac{\left[(\hat{s}-\hat{u})\tilde{f}_1^{\rm hard} - \hat{s}\hat{u}\tilde{f}_3\right]}{(s-u)}\sum_q e_{\rm q}^2\left(H^{\rm q}+E^{\rm q}\right),$$
$$B = \int_{-1}^{1}\frac{dx}{x}\frac{\left[(\hat{s}-\hat{u})\tilde{f}_1^{\rm hard} - \hat{s}\hat{u}\tilde{f}_3\right]}{(s-u)}\sum_q e_{\rm q}^2\left(H^{\rm q}-\tau E^{\rm q}\right),$$
$$C = \int_{-1}^{1}\frac{dx}{x}\tilde{f}_1^{\rm hard}{\rm sgn}(x)\sum_q e_{\rm q}^2\tilde{H}^{\rm q}, \tag{2.30}$$

where $\tilde{f}_1^{\rm hard}$ and $\tilde{f}_3$ are partonic amplitudes. The details of kinematic definitions can be found in [47]. The $H^{\rm q}$, $E^{\rm q}$ and $\tilde{H}^{\rm q}$ are the GPDs for a quark of flavor q in the proton.
Two different GPD models were used to estimate integrals in Eq. 2.30: a Gaussian parametrization and modified Regge parametrization. The corresponding cross section including the GPD based two-photon corrections can be written as:

$$\sigma_{\rm R} = \sigma_{\rm R}^{\rm hard} + \sigma_{\rm R}^{\rm soft}, \tag{2.31}$$

where

$$\sigma_{\rm R}^{\rm hard} = (1+\varepsilon)G_{\rm M}\Re e(A) + \sqrt{2\varepsilon(1+\varepsilon)}\frac{1}{\tau}G_{\rm E}\Re e(B) + (1-\varepsilon)G_{\rm M}\Re e(C),$$
$$\sigma_{\rm R}^{\rm soft} = \sigma_{\rm R}^{1\gamma}(1+\delta_{\rm soft}^{2\gamma}+\delta_{\rm brem}^{\rm ep}). \tag{2.32}$$

The results of these calculations for both GPD models are shown in Fig. 2.16. The straight line approximates $\sigma_{\rm R}^{1\gamma}$ behavior and is produced by using the polarization transfer measurements of $G_{\rm E}/G_{\rm M}$. The modification of this prediction from polarization transfer results introduced with the GPDs based TPE corrections are shown by the curved lines. The observed change of the slope agrees with the experimental data of the Rosenbluth extraction. In addition, the TPE correction generated non-linearity in the ε dependence growing with increasing Q^2. The effect of the TPE corrections on the form factors ratio is shown in Fig. 2.17. The results are presented for the Gaussian GPD model only. The modified Regge GPD model, omitted for clarity, gives similar results of partial reconciliation of the Rosenbluth and polarization transfer methods disagreement.

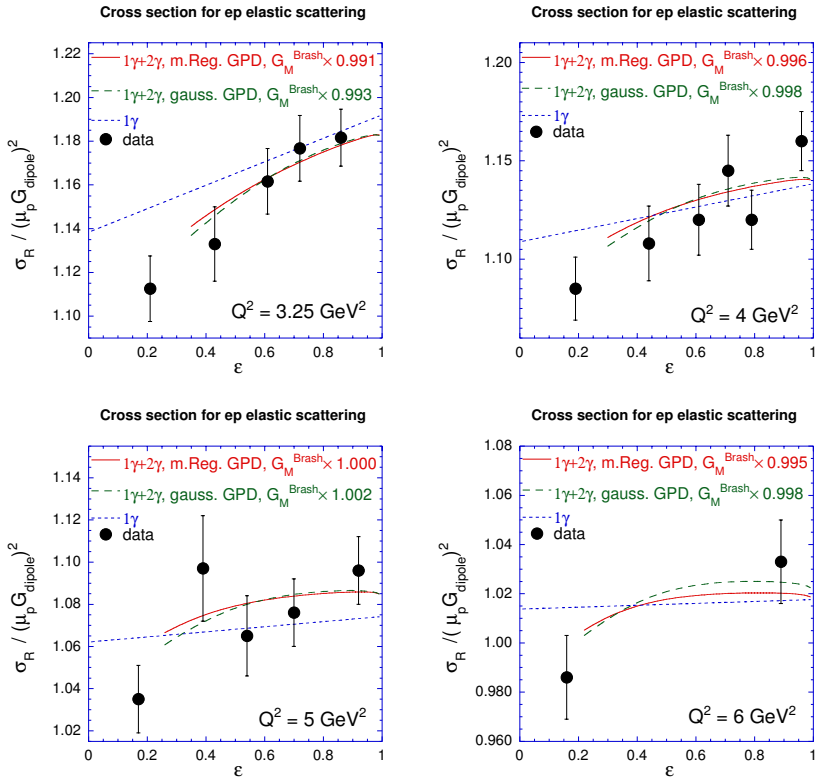

Figure 2.16: Reduced cross section normalized by the dipole form factor squared as a function of ε plotted for four Q^2 values. The black solid circles is the Rosenbluth measurements [10]. The blue dotted line is the Rosenbluth slope prediction based on G_E/G_M measurements [18, 57]. The solid red curve is the σ_R calculation using the modified Regge GPD. The dashed green curve is the σ_R calculation using the Gaussian GPD. *Figure source: Ref.* [47].

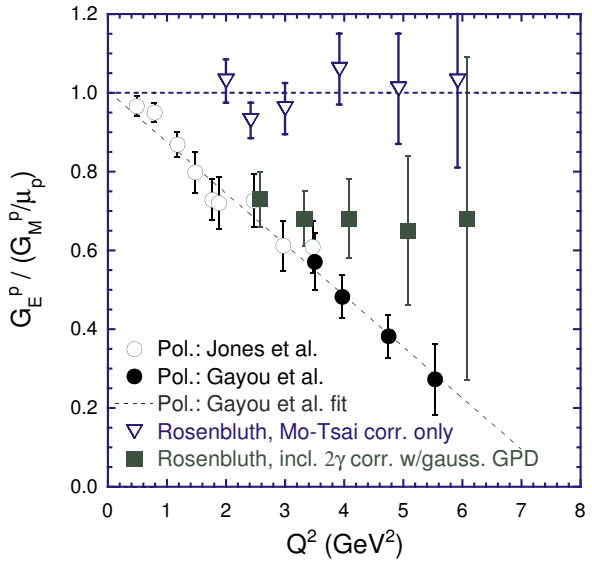

Figure 2.17: Form factors ration as a function of Q^2. Circles: polarization transfer data [18, 57]. Triangles: Rosenbluth data [25] with standard radiative corrections only. Squares: TPE corrected Rosenbluth measurements [10]. *Figure source: Ref.* [47].

2.2.4 Perturbative calculations

The extension of the TPE studies to even higher four-momentum transfer regions was considered within the framework of perturbative quantum chromodynamics (pQCD). Two pQCD based complimentary approaches, [58] and [48, 155, 156], were developed which estimated TPE corrections to σ_{R} for $Q^2 = 2.5\,\mathrm{GeV}^2 - 30\,\mathrm{GeV}^2$.

In the analysis of Borisyuk and Kobushkin [58], it is argued that the diagram considered in the partonic model in which both photons are coupled to the same quark (Fig. 2.18(c)) represents subleading order in α_{s} since the transferred momentum has to be redistributed through the exchange of two hard gluons. In general, the one-photon exchange approximation is described by seven diagrams shown in Fig. 2.18(a) and the amplitudes scale as $\alpha\alpha_{\mathrm{s}}^2/Q^6$.

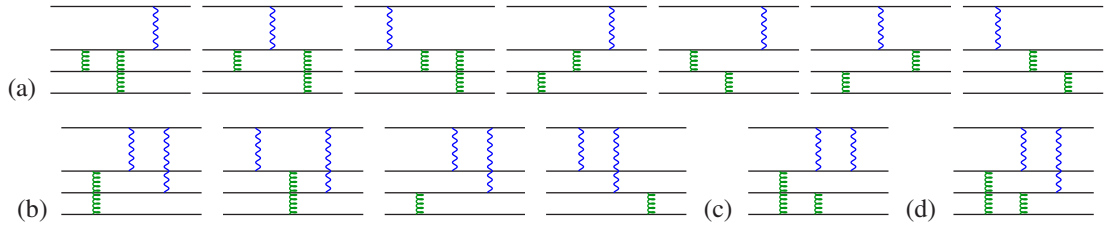

Figure 2.18: Feynman diagrams representing elastic scattering in pQCD approach: (a) one-photon exchange ($\alpha\alpha_{\mathrm{s}}^2/Q^6$); leading order TPE ($\alpha^2\alpha_{\mathrm{s}}/Q^6$); (c,d) subleading order TPE ($\alpha^2\alpha_{\mathrm{s}}^2/Q^6$). *Figure source: Ref.* [58].

The Fig. 2.18(b) shows the diagrams in the leading-order pQCD contribution to the TPE amplitude, $\sim \alpha^2\alpha_{\mathrm{s}}/Q^6$, where the photons are connected to different quarks while requiring the exchange of one gluon only. It indicates that the suppression of TPE relative to the Born amplitude is of the order of $\alpha/\alpha_{\mathrm{s}}$ which is significantly larger than the commonly assumed factor of α.

For large Q^2, the cross section was considered to be dominated by the terms proportional to the generalized magnetic form factor $\delta\tilde{G}_{\mathrm{M}}$

$$\sigma_{\mathrm{R}} \approx \frac{Q^2}{4M_{\mathrm{p}}^2} G_{\mathrm{M}}^2 \left(1 + 2\Re e \frac{\delta\tilde{G}_{\mathrm{M}}}{G_{\mathrm{M}}}\right). \tag{2.33}$$

Assuming that the nucleon is composed of three collinearly moving quarks with momenta $x_{\mathrm{i}}p$, where $0 < x_{\mathrm{i}} < 1$ and $\sum_{\mathrm{i}=1}^{3} x_{\mathrm{i}} = 1$, the amplitude of the process is given by [58]

$$\mathcal{M} = \langle \phi(y_{\mathrm{i}}) \left| T(y_{\mathrm{i}}, x_{\mathrm{i}},) \right| \phi(x_{\mathrm{i}}) \rangle \,, \tag{2.34}$$

where $\phi(x_{\mathrm{i}})$ ($\phi(y_{\mathrm{i}})$) is the initial (final) quark distribution amplitude and T is the hard scattering amplitude at the quark level. Several models for distribution amplitude have been used for numerical calculations: Chernyak-Ogloblin-Zhitnitsky

(COZ), Gari-Stefanis (GS), and heterotic (Het) (see [58] for details). The TPE amplitude $\delta\tilde{G}_{\rm M}/G_{\rm M}$ calculated with COZ wave function was estimated to grow logarithmically with Q^2. The results are shown in Fig. 2.19 for two ε values. The ε dependence of the amplitude was found to be approximately linear with the relative value of TPE amplitude reaching 3.5 % at $Q^2 \approx 30\,\mathrm{GeV}^2$, the maximal Q^2 currently investigated. At $Q^2 \sim 3\,\mathrm{GeV}^2$ the pQCD results approximately match with hadronic calculations shown by the dashed curves in Fig. 2.19.

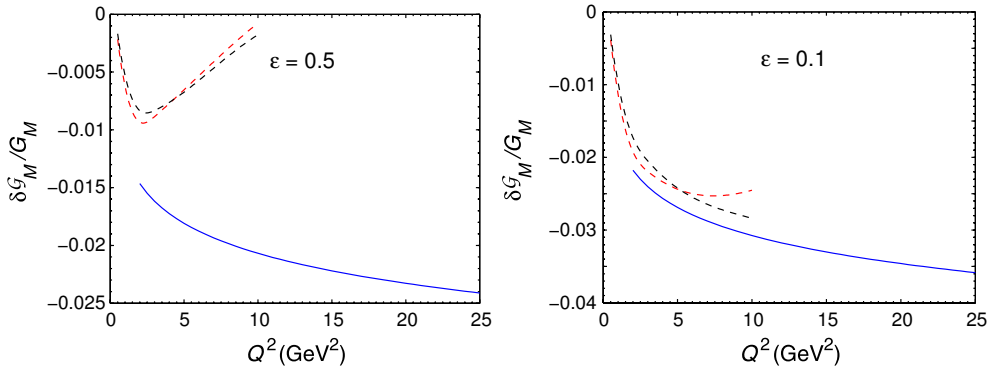

Figure 2.19: The Q^2 dependence of the TPE amplitude $\delta\tilde{G}_{\rm M}/G_{\rm M}$ for $\varepsilon = 0.5$ (left) and $\varepsilon = 0.1$ (right). The blue curve is pQCD (COZ) calculations [58]. The dashed curves is hadronic calculations: dipole parametrization (red), [59] (black). *Figure source: Ref.* [58].

Alternative pQCD calculations of TPE corrections were performed by Kivel and Vanderhaeghen [48, 155, 156]. Similarly to Borisyuk and Kobushkin, they concluded that the leading TPE is driven by processes involving one hard gluon exchange. At high Q^2, this behavior led to $1/Q^4$ dependence for $\delta\tilde{G}_{\rm M}$ and $\nu\tilde{F}_3/M_{\rm p}^2$ while $\tilde{F}_2$ (see Eq. 2.12) is suppressed as $1/Q^6$. Unlike the results of [58], the calculations in [48] estimated the absolute TPE correction relative to the phenomenological one-photon exchange amplitude. In order to perform calculation COZ and Braun-Lenz-Wittmann (BLW) models were used along with lattice QCD calculations (QCDSF) for comparison (see [48] for details). The TPE effects on $\sigma_{\rm R}$ were calculated for several Q^2 values and are shown in Fig. 2.20. The biggest effect was observed within the COZ model with non-linearities only occurring as $\varepsilon \to 1$. This work has been extended in [155, 156] to include a new soft spectator terms in the framework of soft-collinear effective theory.

2.2.5 Summary of calculations

The difficulty of TPE calculations has been recently tackled from various fronts. Significant progress was achieved by different groups that explored the details of TPE corrections using models valid over different range of Q^2. The effects of TPE corrections outlined in previous sections for hadronic, partonic and pQCD approaches were mostly considered for $\sigma_{\rm R}$ and the form factors ratio which is most relevant for the E05-017 analysis. The analogous calculations were performed for observables related to the spin dependent measurements and experiments on e^+p/e^-p ratios.

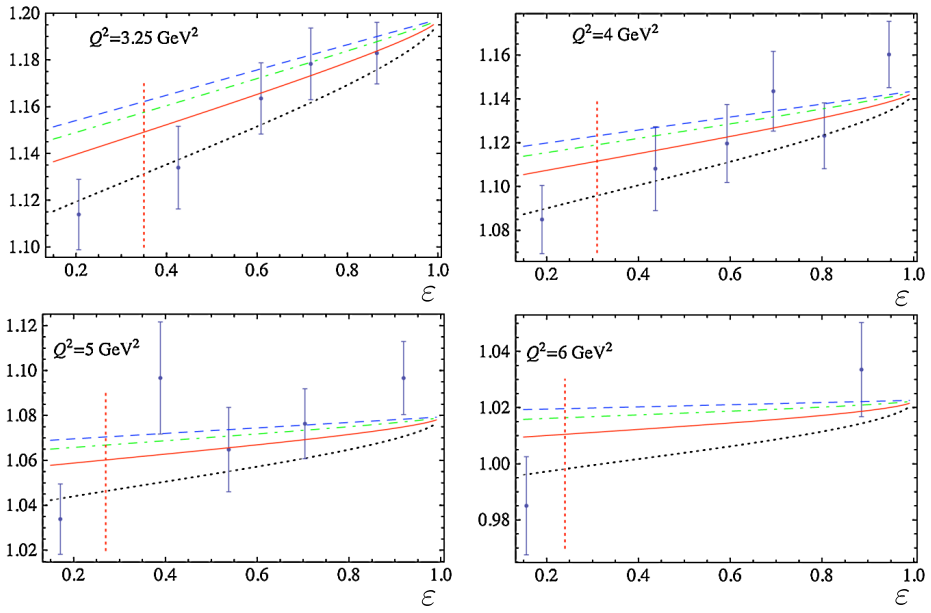

Figure 2.20: Reduced cross section normalized by the dipole form factor squared as a function of ε plotted for four Q^2 values. The blue dashed line is the Rosenbluth slope prediction based on G_E/G_M measurements [18, 19, 57]. The pQCD based calculations of TPE are plotted as (see [48] for details): COZ (dotted black), BLW (solid red), and QCDSF (dash-dotted green). *Figure source: Ref.* [48].

Several examples of these calculations are shown in Fig. 2.2, 2.3 and Fig. 2.4 for the electron-positron scattering cross section comparison and in Fig. 2.5 for the ε dependence studies of polarization observables.

In addition, several other methods such as dispersive methods [46, 146–148] and structure function calculations [49] were used to estimate TPE contributions.

Despite substantial improvements, the calculated TPE corrections do not fully eliminate the G_E/G_M discrepancy; matching hadronic models with high Q^2 QCD based calculations remains problematic and their predictions are quantitatively different. Nearly all available models indicate sizable non-linearities in the ε dependence of σ_R, however, predictions for both the magnitude and the ε range of non-linearities are quite different in different approaches.

3 Experiment

3.1 Overview

Experiment E05-017 was a series of proton Rosenbluth (or Super-Rosenbluth) measurements performed over a wide range of Q^2 values at Thomas Jefferson National Laboratory (JLab) in experimental Hall C of the Continuous Electron Beam Accelerator Facility (CEBAF). After success of the first JLab Super-Rosenbluth experiment, E01-001, E05-017 was proposed [157] to search for an indication of non-linearities in the ε dependence of the cross section by maximizing the range and reaching extremes of ε (Sec. 2.1.3 and 2.2.1). Another goal of the experiment was precise extraction of the proton form factors ratio for $0.4 \leqslant Q^2 \leqslant 5.6\,\mathrm{GeV}^2$.

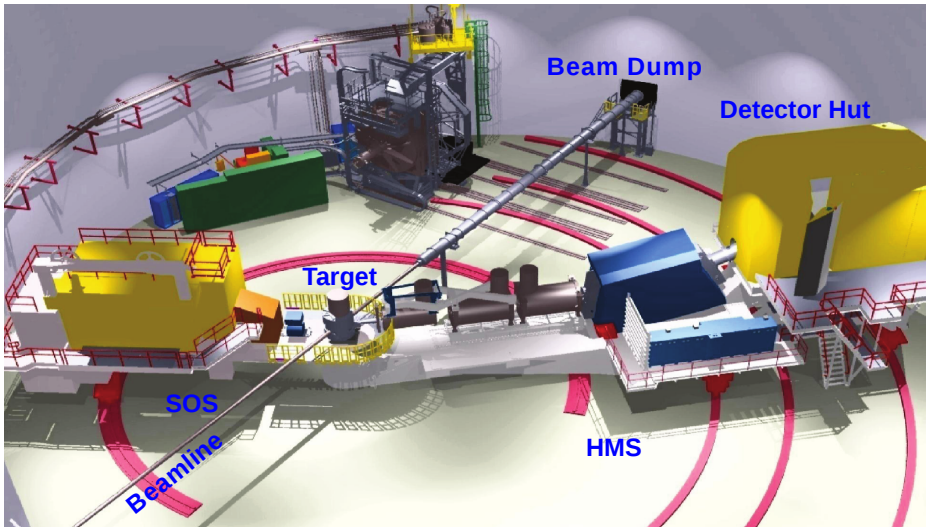

Figure 3.1: The experimental Hall C schematic diagram.

While the main objective of the E01-001 run was verification of the Rosenbluth-polarization transfer discrepancy, E05-017 focused on precise measurement of this disagreement covering much broader kinematics. The experiment described here

accessed both much smaller Q^2 values, where the previous examination of discrepancy was insufficient, and much higher Q^2, where the inconsistency is largest and the contribution to the Rosenbluth slope from electric form factor is very small. Special attention was paid to maximize sensitivity of the Rosenbluth extraction to non-linearity measurements. In particular, at $Q^2 = 0.983\,\mathrm{GeV}^2$ ($Q^2 = 2.28\,\mathrm{GeV}^2$) 13(10) ε points respectively were measured providing highly detailed tests of non-linearities.

Experimental Hall C is equipped with a movable spectrometer on each side of the beamline, various beamline diagnostic devices and a beam dump, and cryogenic target system located at the pivot point of both spectrometers. The schematic layout of the Hall C is shown on Fig. 3.1. An incident unpolarized electron beam was directed on a 4-cm-long unpolarized liquid hydrogen target. Struck protons were inclusively detected in the Hall C High Momentum Spectrometer (HMS). The Hall C Short Orbit Spectrometer (SOS) was planned to be used for coincidence measurements, where both elastically scattered electron and proton are detected. However, SOS was not available during the run time.

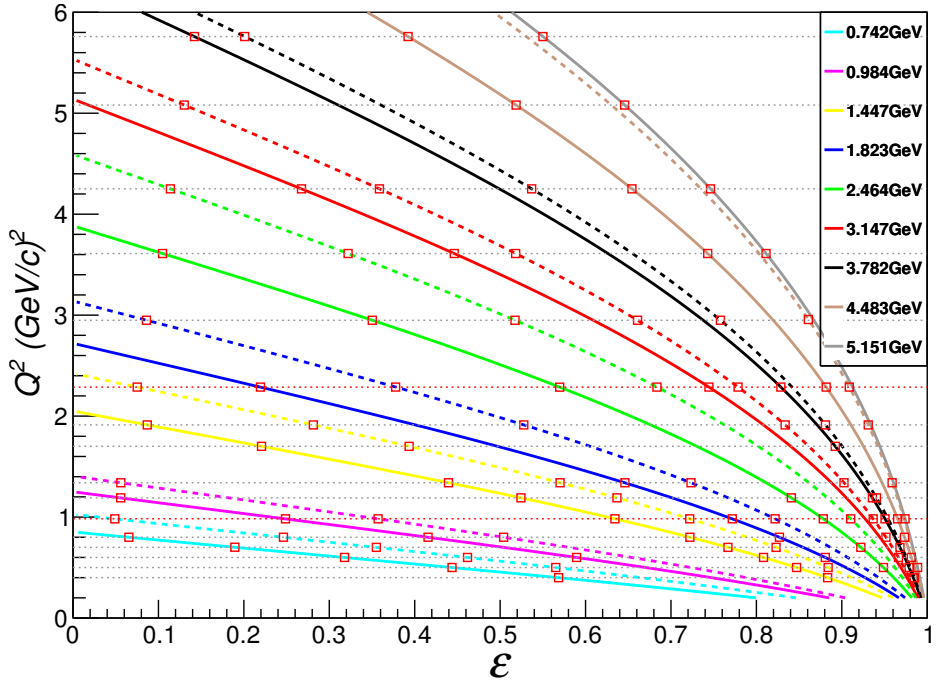

Figure 3.2: The E05-017 nominal kinematic coverage. The solid and dashed lines are constant beam energy settings.

By varying the incident electron beam energy and the HMS central angle the cross section was measured at a total of 102 (112) kinematic settings at 16 different values for Q^2 (Table 3.1). The accelerator schedule had to be optimized to satisfy the running conditions for all three experimental halls; therefore, there were a periods of data-taking where the HMS had to be moved to the next position before the necessary statistics for the current kinematic setting was acquired. Once the accelerator's schedule made it possible to complete the data collection for that point,

the HMS was repositioned to the appropriate spectrometer angle. For several settings, the HMS repositioning resulted in a slightly different angle as compared to the original setting. The data analysis treated these settings separately, such that the number of initial 102 nominal settings increased to 112 (Table 3.1). Fig. 3.2 shows entire nominal kinematic coverage of E05-017 that required 17 different settings of the beam energy and HMS central angle ranging from 10.5° to 66.7°. In addition, to estimate background contribution from the target endcaps, data with an empty aluminum target were taken at each kinematic setting. For the purpose of this analysis, kinematic settings were classified by the beam energy and HMS central angle values and are shown in Table 3.1.

Two other Hall C experiments, E06-009 and E04-001, were performed in the same run period as E05-017. Therefore, most calibration and reconstruction procedures were performed for the entire data set of all three experiments.

3.2 Accelerator

The CEBAF at JLab is designed [158] to provide high current (up to 200 µA) high polarization (up to 85 %) continuous electron beam simultaneously for three end stations (Hall A, B and C). Each experimental Hall can receive the electron beam with different values of the beam current and different but related values of the beam energy of up to 6 GeV. JLab has just completed an upgrade: the maximum beam energy is now 12 GeV and a fourth end station, experimental Hall D, has been built.

The accelerator complex, shown on Fig. 3.3, consists of an injector, North and South linear accelerators (linacs), recirculation arcs, a Beam Switch Yard (BSY) and Central Helium Liquefier (CHL). The electrons are produced by excitation of a strained GaAs photocathode with circularly polarized photons created by the laser source with a wavelength of 780 nm. During three-hall operation, three separate lasers - one for each hall - are used to generate three interlaced electron beams at a repetition rate of 499 MHz. The 499 MHz frequency of the electron train is subharmonic of the fundamental accelerator operating frequency of 1497 MHz.

The injector subsystems allow for the preparation of short stable bunch lengths and the pre-acceleration of electrons to ≈ 50 MeV. The linac portions of the CEBAF beam line is composed of a series of 5-cell superconducting radio-frequency (SRF) niobium cavities designed to operate at the accelerator fundamental frequency. SRF cavities form a larger linac element called the cryomodule. Each cryomodule holds 8 cavities submerged in a bath of liquid helium from the CHL and maintained at a temperature of 2 K. A total of twenty cryomodules are grouped together in each linac. The North and South linacs are joined into the complete recirculating beamline by two 180° bending arcs, sets of steering and focusing dipole and quadruple magnets. The beam can be accelerated to a maximum of five recirculation passes. The electrons leaving the injector are already highly relativistic and their velocity is nearly independent of their energy difference, thus, electron bunches with different energies travel at the same spatial location. However, when

#	$E(MeV)$	$\theta(^\circ)$	$p(MeV)$	#	$E(MeV)$	$\theta(^\circ)$	$p(MeV)$	#	$E(MeV)$	$\theta(^\circ)$	$p(MeV)$
1	0.742	12.906	0.991	39	1.824	37.291	1.360	77	3.782	38.486	1.942
2	0.742	22.715	0.917	40	1.824	44.917	1.121	78	3.782	44.610	1.588
3	0.742	30.195	0.838	41	1.824	49.300	0.991	79	3.782	51.165	1.262
4	0.742	36.972	0.756	42	1.824	54.670	0.838	80	3.782	54.331	1.121
5	0.742	43.638	0.667	43	2.056	10.518	2.328	81	3.782	59.462	0.916
6	0.850	10.498	1.121	44	2.056	24.015	1.942	82	3.782	63.898	0.756
7	0.850	10.505*	1.121	45	2.056	30.474	1.718	83	3.782	66.510	0.667
8	0.850	25.091	0.991	46	2.056	40.139	1.360	84	3.923	12.262	3.896
9	0.850	30.988	0.916	47	2.056	47.138	1.121	85	3.923	23.595	3.063
10	0.850	36.575	0.838	48	2.462	10.518	2.704	86	3.923	33.233	2.328
11	0.850	42.093	0.756	49	2.462	21.102	2.328	87	3.923	42.818	1.718
12	0.984	11.155	1.262	50	2.462	29.920	1.942	88	3.923	51.481	1.262
13	0.984	24.270	1.121	51	2.462	46.024	1.262	89	3.923	66.698	0.667
14	0.984	32.862	0.991	52	2.462	49.790	1.121	90	4.482	17.652	3.896
15	0.984	41.844	0.838	53	2.462	55.755	0.916	91	4.482	17.655*	3.896
16	1.076	10.799	1.360	54	2.462	60.840	0.756	92	4.482	21.630	3.523
17	1.076	29.078	1.121	55	2.850	10.641	3.063	93	4.482	21.634*	3.523
18	1.076	36.392	0.991	56	2.850	18.983	2.704	94	4.482	26.573	3.063
19	1.447	12.360	1.718	57	2.850	26.203	2.328	95	4.482	30.615	2.704
20	1.447	19.698	1.588	58	2.850	33.523	1.942	96	4.482	40.644	1.942
21	1.447	29.965	1.360	59	2.850	51.630	1.121	97	4.482	55.600	1.121
22	1.447	33.969	1.262	60	3.147	16.279	3.063	98	4.482	58.645	0.991
23	1.447	39.578	1.121	61	3.147	22.570	2.704	99	4.482	62.504	0.838
24	1.447	44.779	0.991	62	3.147	35.465	1.942	100	5.052	36.862	2.332
25	1.447	47.790	0.916	63	3.362	10.619	3.523	101	5.052	41.946	1.942
26	1.447	50.981	0.838	64	3.362	10.620*	3.523	102	5.052	45.431	1.718
27	1.447	54.420	0.756	65	3.362	18.929	3.063	103	5.052	51.516	1.360
28	1.447	58.193	0.667	66	3.362	18.938*	3.063	104	5.151	21.383	3.896
29	1.657	10.505	1.942	67	3.362	24.473	2.704	105	5.151	21.387*	3.896
30	1.657	21.866	1.718	68	3.362	30.300	2.328	106	5.151	21.389*	3.896
31	1.657	26.570	1.588	69	3.362	36.659	1.942	107	5.151	24.715	3.523
32	1.657	26.573*	1.588	70	3.362	40.805	1.718	108	5.151	29.071	3.063
33	1.657	34.630	1.360	71	3.362	47.820	1.360	109	5.151	29.075*	3.063
34	1.657	38.017	1.262	72	3.362	53.299	1.121	110	5.151	32.761	2.704
35	1.657	42.922	1.121	73	3.362	56.641	0.991	111	5.151	56.490	1.121
36	1.657	50.337	0.916	74	3.362	60.830	0.838	112	5.151	65.364	0.756
37	1.657	56.440	0.756	75	3.782	10.553	3.896				
38	1.824	18.098	1.942	76	3.782	10.570*	3.896				

Table 3.1: List of the nominal E05-017 kinematic settings. For several kinematic settings (marked with *) the HMS had to be moved before the necessary statistics was acquired. Once the accelerator's schedule made it possible to finish the data-taking for that particular point, the HMS was repositioned to the spectrometer angle that was slightly different from the original setting. Therefore, for analysis purposes those settings were treated as separate points, thus increasing the total number from initial 102 to 112 settings.

electrons leave the accelerating section they have to be separated according to their momentum and directed to one of the 5 (4) unique paths in the east (west) arc with magnetic fields set to transport specific beam energy. At the exit of the bending arc, the beam is recombined before it enters the next linac. Once the desired

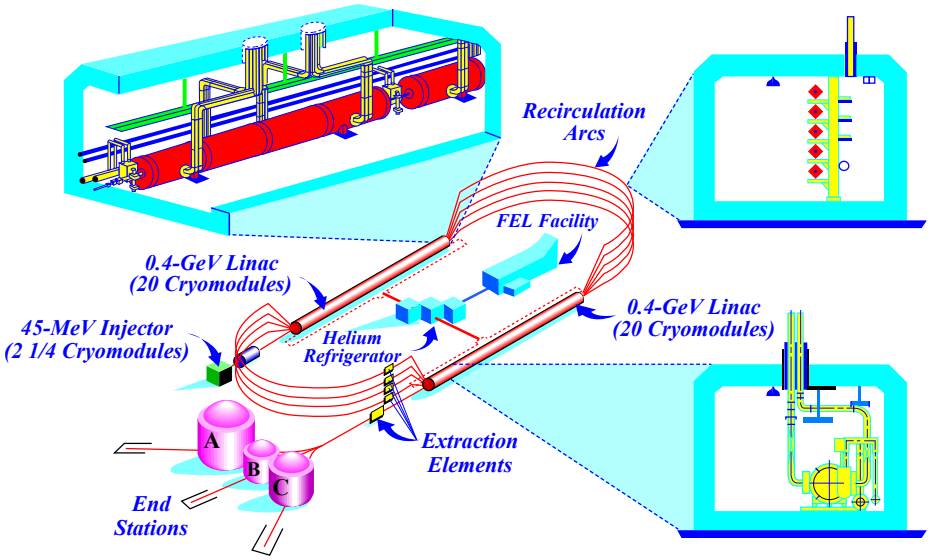

Figure 3.3: The CEBAF schematic diagram.

beam energy is reached, the BSY, located at the end of the South linac, separates and redirects the beam to the individual experimental Hall.

The single linac energy (before the upgrate) can be set between 200 MeV and 600 MeV with the total beam energy available for the experimental Hall given by

$$E_{\text{beam}} = (2n + \alpha)E_{\text{l}}, \tag{3.1}$$

where n is the number of recirculation passes, $\alpha = E_{\text{injector}}/E_{\text{l}} = 0.1125$, E_{l} is the linac energy.

For E05-017, CEBAF supplied Hall C with an unpolarized electron beam with energies in the range $0.742 \leqslant E_{\text{beam}} \leqslant 5.150$ GeV at beam currents up to 100 µA.

3.3 Hall C beamline

The Hall C part of the beamline, shown on Fig. 3.4, starts from the BSY where initial deflection from the straight orbit is provided. It then further steers and focuses the beam in a 34.3° arc towards the target scattering chamber and eventually to the beam dump. Beam bending and focusing is performed by the set of 8 dipoles, 12 quadrupoles and 8 sextupoles. To fully characterize electron beam properties the beamline is equipped with several instruments to measure the profile and position, energy, polarization, and current of the beam.

3.3.1 Beam position measurements

There are two types of devices that provide beam position and profile measurements. The superharp, a wire scanner, performs very precise but destructive measurements [159] and cannot be used for continuous monitoring simultaneously with

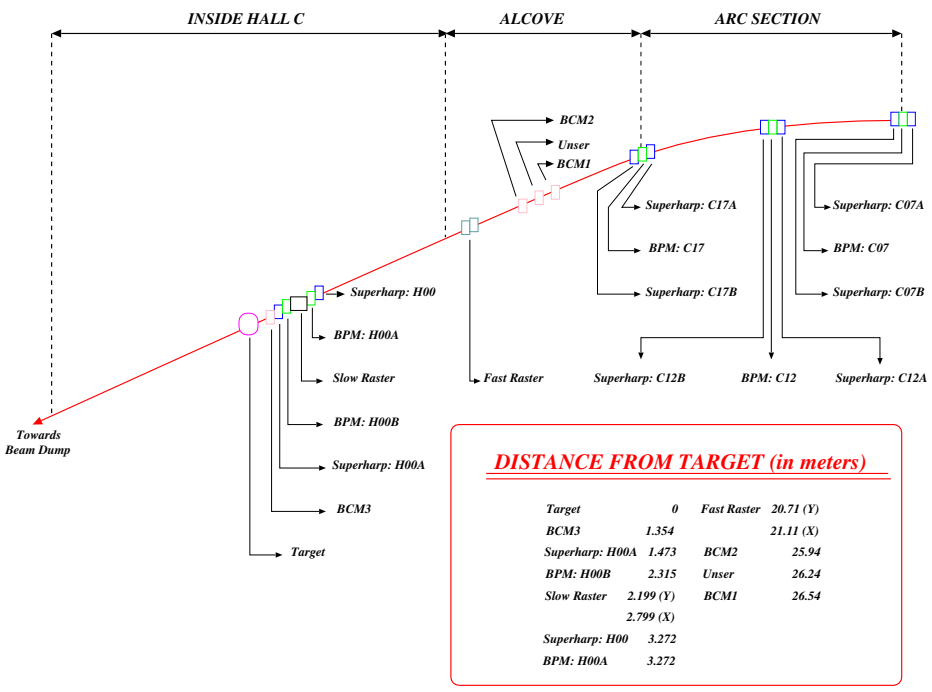

Figure 3.4: The Hall C beamline schematic diagram.

data taking. The Beam Position Monitor (BPM), a resonating RF cavity with antennae inside, is a less precise non-invasive measurement device [160] which is used to record relative X, Y position of the beam during the run time. The schematic location of the superharps and BPMs along the Hall C beamline is shown on Fig. 3.4.

The superharp consists of a movable frame with three 22 µm diameter tungsten wires, two vertical and one horizontal. The device sits on a heavy granite table which vibrationally decouples the superharp from the rest of the beamline elements. Stepper motors move the frame in and out of the beam while position encoder measures the ladder position. Each wire is connected to the Analog-to-Digital Converter (ADC) which picks up the current signal when the beam crosses the wire. In addition to the wire current profile, resulting γ-rays bremsstrahlung radiation profile is measured with a photo-multiplier tube (PMT). The wire current and PMT readings along with the encoder information allow extremely precise determination of the beam position.

A BPM consists of 4 open-ended thin-wire antenna array rotated by 45° around the beam axis. Each antenna is tuned to 1/3 of the accelerator operating frequency. When the beam passes through the cavity each antenna generates a signal which is proportional to the distance between the beam and antenna positions. In order to determine the relative position of the beam with respect to the central axis of the beamline the standard difference-over-sum technique is used. For absolute BPM position calibration these data have to be compared with superharp measurements.

3.3.2 Beam current measurements

The beam current is measured by a set of Beam Current Monitors (BCM). A BCM is a stainless steel cylindrical wave guide with the beam traveling along the axis of the cylinder. The cavity dimensions are designed such that the resonant modes can be excited in the presence of the beam. The corresponding signal detected in the wire loop antenna is proportional to the beam current. For a specific excitation mode the signal is almost independent of the beam position and the electron bunch length. The antenna output voltage is sent to a voltage-to-frequency converter and read out by a scaler. The BCM cavity gain slowly drifts over time and has to be calibrated against another beam current measuring device, a parametric DC current converter (Unser monitor). The Unser [161] uses a set of toroidal cores as a current sensitive element and has very stable gain. However, it is quite sensitive to thermal fluctuations and other physical conditions which affect its zero offset. For this reason it is impractical to use it as a continuous monitor for the accumulated charge. BCM gain calibration has to be performed periodically during the experiment. A set of special runs is required in order to get calibration data. The response of the Unser and the BCMs is measured at a series of beam currents that cover the range of $10\,\mu A - 100\,\mu A$ with $10\,\mu A$ step. Each current setting is normally of 1.5-2 minutes in duration with alternating beam on and beam off periods. The beam off periods are necessary for determining the Unser and BCMs offsets. A standard Hall C calibration routine is used to calculate the beam current for each beam-on period using the measured Unser offset and gain.

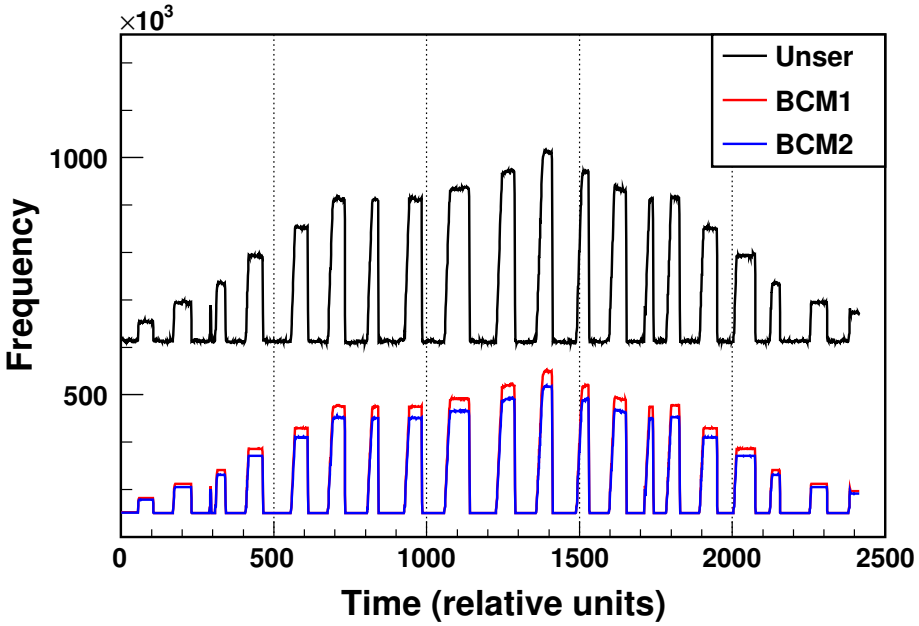

Figure 3.5: An example of the BCM and Unser monitor response to the up-down scan of the electron beam current. *Figure source: Ref.* [60].

The BCMs were calibrated a total of four times during the run period. Fig. 3.5 and 3.6 show the integrated beam current measurements in two second intervals as

well as the gain and offset stability for two BCMs over the period of two months.

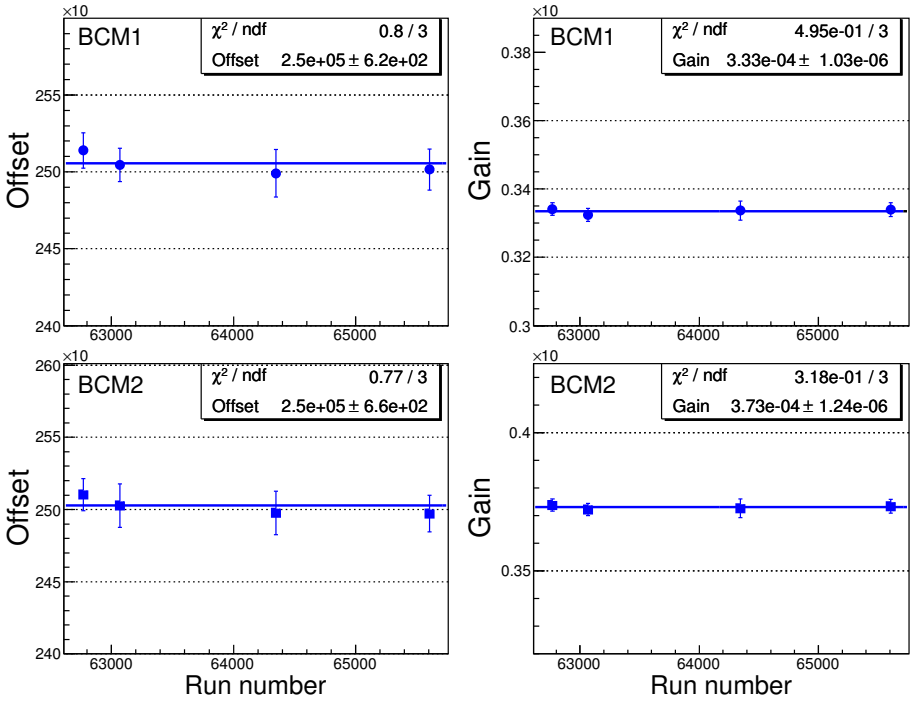

Figure 3.6: Four sets of beam current monitors calibration performed over the period of 2 months. *Figure source: Ref.* [60]

3.3.3 Beam energy measurements

Several methods have been developed for electron beam energy measurements which can be categorized in two groups. In the first group [162], the transport arc portion of the beamline is used as a magnetic analyzer to obtain the beam energy. Both the accelerator East arc and the Hall C arc can be used for the measurements of this type. The measurements of the other group are independent of the knowledge of the bending magnetic fields and rely on scattering kinematic beam energy determination [163].

The nominal beam energy values can be determined from the settings of the East arc magnets; however, the actual values used for the event reconstruction are obtained from more precise Hall C arc measurements. Special procedures required for the measurements do not allow monitoring the absolute beam energy continuously. First, the arc optics has to be changed from achromatic to dispersive mode so the field map is defined by the dipole magnets only. One of the dipole magnets was precisely calibrated and the others are assumed to have the same field map. The Hall C arc has 3 pairs of the superharps (Sec. 3.3.1) located at the beginning, middle, and the end of the arc. With the accurate position and direction information from the superharps, the current of the bending magnets is adjusted such that the beam is steered through the central ray of the magnets in the arc. Once the magnetic field integral, $\int Bdl$, is determined from the current in the dipoles, the beam

energy can be calculated from:

$$E_{\text{beam}} \simeq p = \frac{e}{\theta_{\text{arc}}} \int Bdl, \tag{3.2}$$

where e is the electron charge and θ_{arc} is the arc bending angle. The error analysis showed that the accuracy of these absolute beam energy measurements is $\approx 2 \times 10^{-4}$ [163]. After the beam measurements are completed the arc is tuned to regular achromatic mode. During the data-taking period the relative beam energy measurement can be monitored with the information provided by BPMs. With the focusing magnets turned on and with the limited accuracy of BPM measurements, the precision of the absolute measurements would be significantly reduced; however, the uncertainty of the relative beam energy measurements is only $\approx (2-3) \times 10^{-4}$.

For the seventeen beam energy settings of E05-017, sixteen Hall C arc beam energy measurements were conducted. The summary of the measurement results are shown in Table 3.2. For $E_{\text{beam}} = 5.052\,\text{GeV}$ accelerator East arc nominal value was used instead since the Hall C arc measurements were not conducted for this setting. The data taking at $E_{\text{beam}} = 1.656\,\text{GeV}$ was split in two parts and Hall C arc measurements were performed for the first part only but the linac energy, E_{l}, had not been changed in between.

Run period	$E(MeV)$	$\sigma_{\text{E}}(MeV)$
62645 - 62872	2056.26	0.53
62873 - 62913	5052.00	-
62914 - 63093	3361.79	0.85
63094 - 63157	1823.57	0.46
63158 - 63280	4482.39	1.12
63281 - 63323	1076.18	0.27
63324 - 63416	5150.52	1.29

Run period	$E(MeV)$	$\sigma_{\text{E}}(MeV)$
64186 - 64361	1656.65	0.41
64362 - 64451	850.44	0.21
64452 - 64484	1656.65	0.41
64485 - 64660	2462.11	0.62
64661 - 64738	984.42	0.25
64739 - 64888	3782.34	0.95
64889 - 65031	2849.91	0.71
65032 - 65159	3922.59	0.98
65160 - 65207	3147.09	0.79
65208 - 65341	742.26	0.19
65342 - 65475	1446.81	0.36

Table 3.2: E05-017 (part 1 and 2) Hall C arc beam energy measurements. Run periods for E06-009 and E04-001 are omitted.

3.3.4 Beam raster

The electron beam energy deposition through ionization losses to the cryogenic target can be significant enough to exceed the cooling capacity of the target system. In this case local liquid overheating is possible with consequent target boiling (bubble formation) and hence target density and luminosity fluctuations. Beam rastering [164] is used to minimize local heat load by effectively increasing the beam spot size. The Hall C fast raster system located 25 m upstream from the target provides high scanning velocity, linear and homogeneous raster density distribution. It consists of two steering magnets that deflect the beam in vertical and horizontal directions. The frequency (24.96 kHz and 25.08 kHz) and the waveform (triangle) of

the driving magnets are chosen such that the raster forms a rectangularly shaped pattern on the target. The size of the raster pattern during the E05-017 run was ±1 mm in both directions.

3.4 Target

The Hall C target system is located at the spectrometer pivot close to the center of the Hall. The actual targets are installed on the ladder inside a cylindrical aluminum vacuum enclosure called the scattering chamber. The scattering chamber exit window on the HMS side is made of 0.4 mm thick aluminum. The target ladder is connected to a bellows, and a lifter mechanism moves vertically in the scattering chamber and allows insertion of the intended target material into the beam. The lifter is controlled by a stepper motor and provides relatively quick (a few minutes), accurate, and reproducible target positioning at the beam height. From the top to the bottom, the target ladder shown on Fig. 3.7 hosts liquid cryogenic targets, optics calibration targets, blank targets, and solid targets.

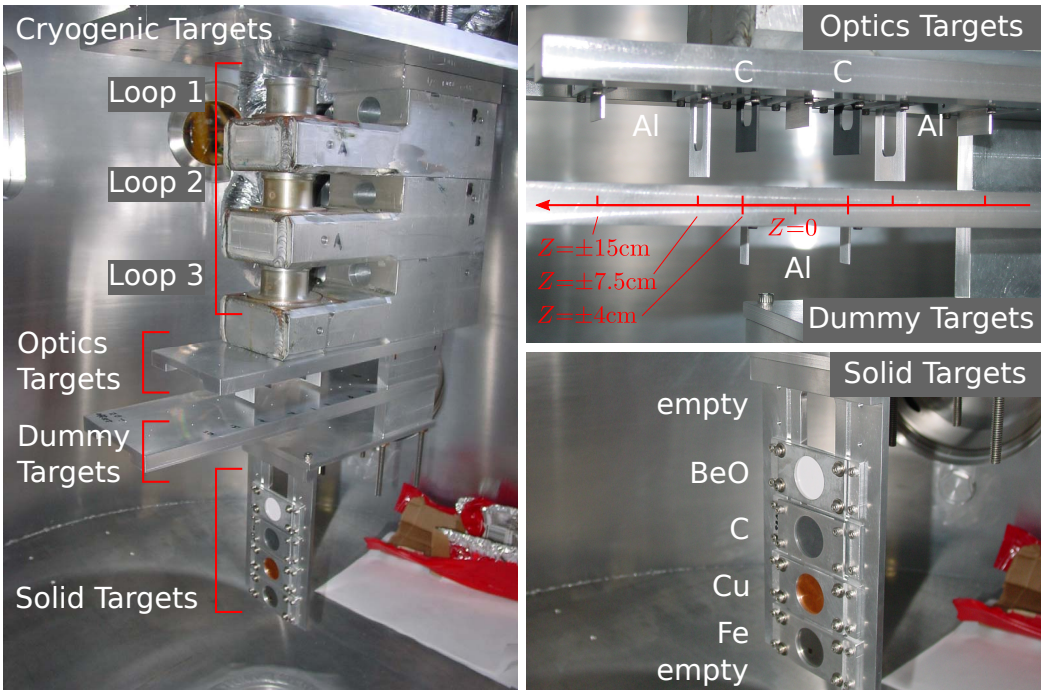

Figure 3.7: The Hall C target system. Left: entire target ladder (during E05-017 Loop1 was filled with LH_2). Top right: optics targets include Al foils at $Z = \pm 15\,\mathrm{cm}$, $\pm 7.5\,\mathrm{cm}$, $0\,\mathrm{cm}$, as well as C targets at $Z = \pm 4\,\mathrm{cm}$; dummy target include two Al foils at $Z = \pm 4\,\mathrm{cm}$. Bottom right: solid targets.

The cryogenic part of the ladder has three separate loops for the cryogenic liquid circulation with each loop attached to the cylindrical target cell. Only the top, loop 1, cell was filled with liquid hydrogen (LH_2) and used during the E05-017 experiment. The LH_2 cell is made of thin aluminum whose dimensions are given in Table 3.3. The cell axis is oriented vertically, such that the curved side of the target

is exposed to the incoming electron beam. Re-circulation elements of the loop (see Fig. 3.8) include a fan, heat exchangers, and a high power heater. A circulating fan continuously moves LH_2 through the cell and heat exchangers which are cooled with the flow of the target coolant (Helium) to 15 K. The nominal operational values of target pressure and temperature (23 psia and 19 K respectively) were monitored at several locations of the loop. The proportional-integral-derivative loop-controlled heater is used to maintain the constant heat load on the target when the beam current changes.

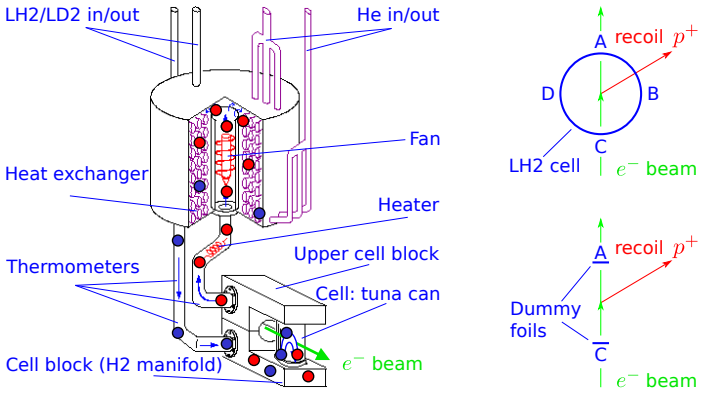

Figure 3.8: Left: the diagram of the cryogenic liquid circulation inside of the target loop. The tuna can is a short right cylinder with the cylinder axis oriented vertically. Top (bottom) right: LH_2 (Dummy) target orientation relative to the incoming electron beam. Four letters indicate locations of the target wall thickness measurements shown in Table 3.3.

Target	LH_2 Loop1	Dummy
Alloy	Al7075-T6	Al6061-T6
A(mm)	0.1384 ± 0.0013	0.944 ± 0.013
B(mm)	0.1359 ± 0.0013	
C(mm)	0.1270 ± 0.0013	0.984 ± 0.013
D(mm)	0.1308 ± 0.0013	
OD(mm)	40.1300 ± 0.0013	
Z position(cm)	0.0	± 2.0
Encoder(arb units)	32 344 713	18 588 297

Table 3.3: The Hall C target survey data. Target wall thickness is given at each of the 4 letter positions shown in Fig. 3.8. OD stands for outer diameter.

Scattering from the aluminum cell of the LH_2 target is the source of the background which is hard to simulate in terms of the recoil proton kinematics. The contribution of this background was measured at each kinematic setting by detecting protons scattered off of the blank ("dummy") target. The blank target is emulated by two 0.8 cm wide aluminum foils installed perpendicular to the beamline at ± 2 cm of the target center. The foils (see Table 3.3) were made thicker than the actual target walls to minimize the required beam time for these measurements (see also Sec. 4.7.2).

Among the solid targets, the Carbon (C) target was used for calibration purposes.

3.5 Spectrometer

The HMS is a set of the superconducting magnets and a detector package (see Fig. 3.9) installed on a common carriage. The motor-driven carriage rotates around a rigidly fixed central bearing system along the tracks secured on the floor. The carriage pivot is concentric with the target central line and rotation is limited to a 10.5° forward HMS central angle by the beam pipe and transverse size of the HMS.

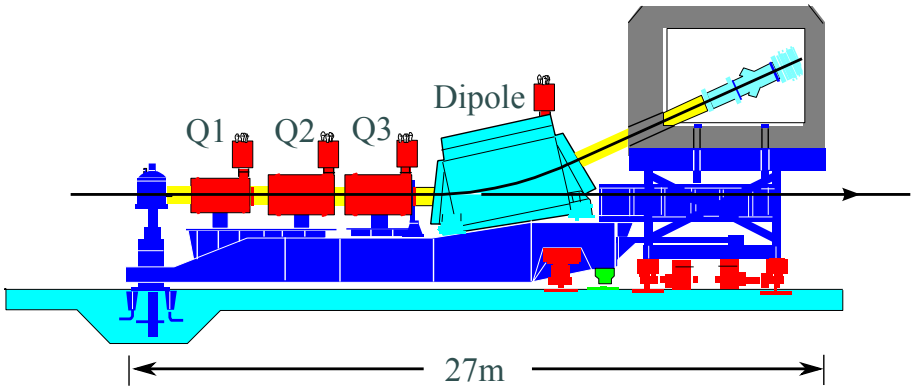

Figure 3.9: The HMS side view schematic diagram.

The HMS magnets comprise a QQQD focusing configuration. All magnets are cooled to 4 K with liquid Helium supplied by the End Station Refrigerator (ESR). The dipole magnet works as a magnetic analyzer and sets a dispersive field in the vertical direction. The dipole central ray bending angle is 25° with 12.06 m radius. While the field of the dipole magnet defines HMS central momentum, the quadrupoles determine HMS acceptance and focusing properties. Quadrupoles Q1 and Q3 provide focusing in the vertical plane, whereas Q2 is responsible for focusing in the non-dispersive plane. Basic HMS properties are given in Table 3.4. The magnetic field in the quadrupoles is set by current and a nuclear magnetic resonance (NMR) probe is used for the dipole settings.

The front of the first quadrupole is equipped with a collimator box, which holds a sieve slit, two octagonal collimators of different size, and one blank space. An array of small holes in the sieve slit is used to conduct HMS optics studies and octagonal apertures define the solid angle acceptance of the HMS.

3.6 Detector

The HMS detector package (see Fig. 3.10) is installed in a radiation-shielded detector hut and is used to identify and characterize scattered charged particles entering the hut through the dipole exit. The detector package can be interchangeably exploited as an electron and hadron detector. The trajectory of the particle is

Parameter	HMS specification
Maximum central momentum	7.4 GeV/c
Momentum acceptance	±10 %
Momentum resolution	< 0.1 %
Solid angle	6.7 msr
Scattering angle acceptance	±40.0 mrad
Out-of-plane angle acceptance	±80.0 mrad
Extended target acceptance	10.0 cm
In plane angle resolution	0.4 mrad
Out of plane angle resolution	0.9 mrad
Useful target length	10.0 cm
Vertex Reconstruction Accuracy	2.0 mm

Table 3.4: HMS nominal characteristics.

provided by a pair of wire drift chamber (DC) DC1 and DC2. Two sets of scintillator hodoscopes (S1, S2) are responsible for the main triggering and time-of-flight (TOF) measurements. Aerogel and gas Cherenkov detectors are used for particle identification. The last element is a segmented electromagnetic lead-glass calorimeter which provides energy measurements. The calorimeter and Cherenkov detector were not used during E05-017. However, the Cherenkov detector is located in front of the scintillator plane S2 and thus its contribution to the proton absorption has to be properly estimated.

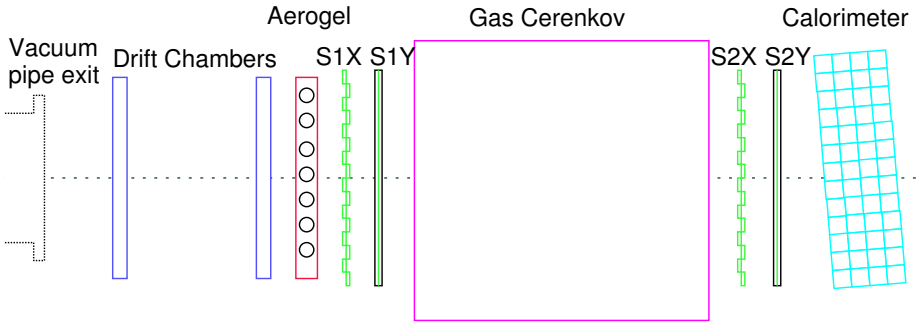

Figure 3.10: The HMS detector package side view schematic diagram.

3.6.1 Drift Chambers

The track position in the drift chamber is determined to high accuracy by measuring the drift time of the electrons released in the ionization process, when the charged particle passes through the gas atoms in the chamber. The wires in the chamber form a "drift cell" in which electrons drift towards the sense wire in the potential created by the field wires held at negative high voltage. The high voltages are adjusted to create nearly circular equipotential contours so that the drift time depends on the track's distance to the sense wire only. As the field gets stronger in

the vicinity of the sense wire an avalanche of secondary electrons is formed and is picked up as a negative pulse on the wire. The signal is then amplified, discriminated, and sent to the Time-To-Digital Converter (TDC). The TDCs measure the time difference between the wire and the trigger signals and the hit position is then determined by the tracking software based on the known electron drift velocity.

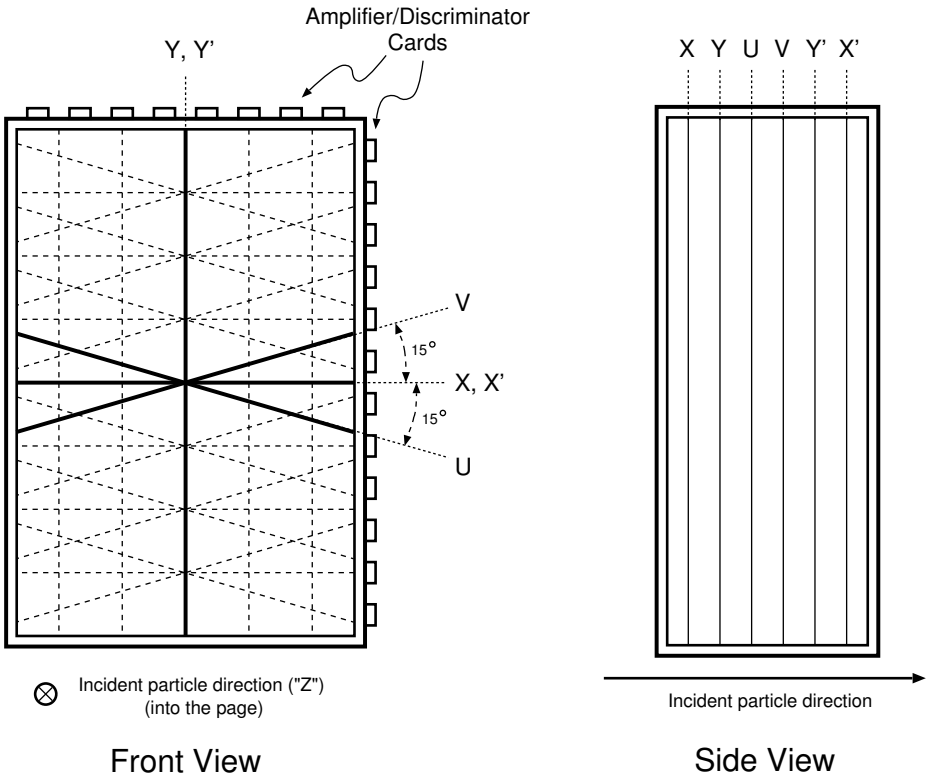

Figure 3.11: The Drift Chamber schematic diagram.

Both DC1 and DC2 have identical design (see Fig. 3.11). The sensitive area of each chamber is approximately 113 cm (dispersive) by 52 cm (transverse). The distance between the centers of the chambers is 81.2 cm. The orientation of the sense wires in each drift chamber forms 6 planes (x, y, u, v, x', y') spaced 1.8 cm apart. The x' (y') plane is shifted from the x (y) plane by 0.5 cm (half the wire spacing of 1 cm). The u and v planes are rotated by $\pm 15^\circ$ with respect to the x plane. The redundancy is used to resolve left-right ambiguity of the track position with respect to the wire. The 25 µm diameter gold-plated tungsten and 150 µm diameter gold-plated copper beryllium are used for the sense and field wires respectively. The gas mixing system supplies the chamber with argon and ethane in equal (by weight) amounts.

With the combined information from six planes, the final position resolution is approximately 280 µm per plane. The drift chamber track position together with the knowledge of the HMS optics allow for the reconstruction of the particle trajectory, reaction vertex and momentum at the target.

3.6.2 Hodoscope

The passage of charged particles through specific types of the luminescent materials causes scintillations as molecules are first excited and then relax to their lower-energy states, thereby re-emitting light. By detecting these scintillations with PMTs at several spatial locations the TOF of the particle can be measured. The HMS has a total of four scintillator planes paired in two horizontal-vertical (X-Y) hodoscopes. Another important function of the hodoscopes is to provide the event triggering for detector read-out.

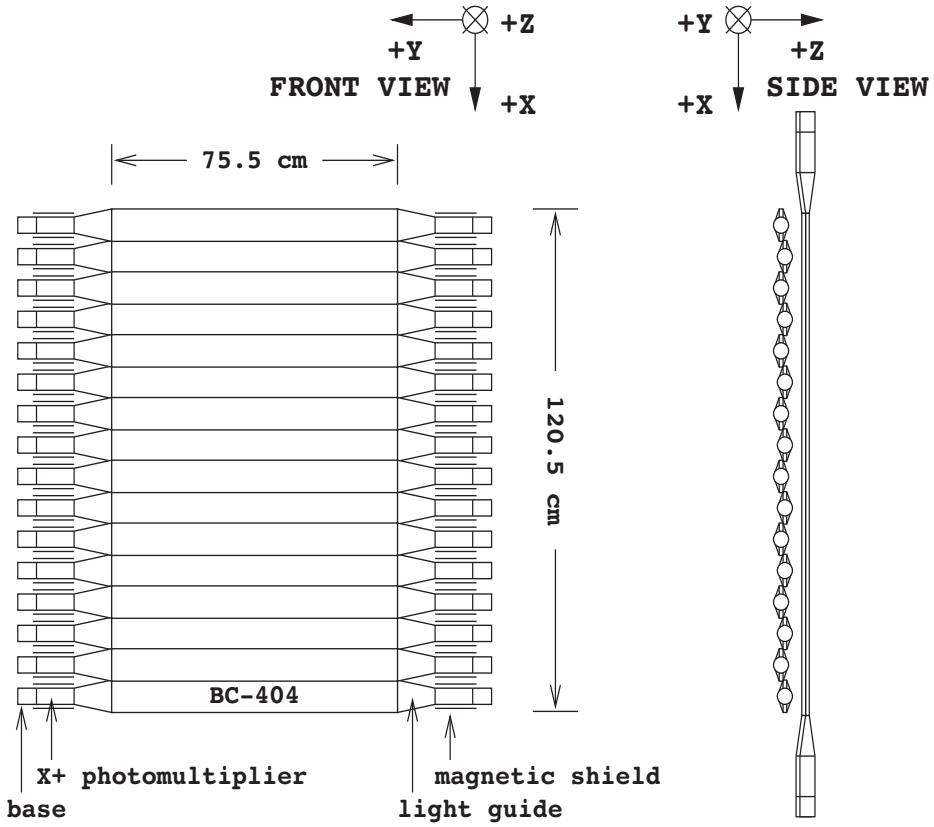

Figure 3.12: The Hodoscope schematic diagram.

The individual hodoscope element is a BC404 scintillator strip wrapped in aluminum foil and two layers of tedlar with lucite light guides and the PMTs attached on the both ends of the strip. Each X plane (see Fig. 3.12) consists of sixteen 75.5 cm long scintillator paddles while each Y plane has ten 120.5 cm long elements. All scintillators are 1 cm thick and 8 cm wide paddles installed with approximately 0.5 cm overlap in the beam direction to avoid gaps in the active area. The light can propagate towards the light guide and PMT directly or through the total internal reflection from the scintillator surface. After a splitter, 1/3 of the PMT signal amplitude is digitized in an ADC and another 2/3 is discriminated for the TDC read-out, scalers, and the logic module which forms the trigger.

The first stage of the hodoscope logic generates the OR signal of all discriminated PMTs responses from one side of a given plane ($S1X_+$=$S1X1_+$ OR $S1X2_+$

... OR $S1X16_+$). These two signals from each side of the plane are combined with logical AND ($S1X = S1X_+$ AND $S1X_-$) to produce 4 plane signals $S1X$, $S1Y$, $S2X$, and $S2Y$. Additionally, two more signals are formed for each hodoscope, ($S1$=$S1X$ OR $S1Y$) and ($S2$=$S2X$ OR $S2Y$). On the next stage two logical signals, called $STOF$ and $SCIN$, are generated to be used as a part of the main trigger. The $STOF$ is produced for the coincidence between $S1$ and $S2$ which ensures a minimum requirement for a good TOF measurement. The $SCIN$ is more restrictive than the $STOF$ and requires a coincidence of the three out of four $S1X$, $S1Y$, $S2X$, and $S2Y$ signals.

3.6.3 Aerogel Cherenkov

Cherenkov detectors are ubiquitous in nuclear physics scattering experiments. They perform critical particle identification as they take advantage of the fact that charged particles moving faster than the speed of light in a medium emit radiation. When installed in a momentum spectrometer they discriminate between particles of the same momentum but different masses. The emission threshold is satisfied when the particle velocity in the medium exceeds the speed of the light in that medium with the angle of emission given by

$$\cos\theta_{\mathrm{C}} = \frac{1}{\beta n}, \tag{3.3}$$

where β is the particle velocity in the medium and n is the medium index of refraction. The ability to control emission by choosing the material with the appropriate index of refraction is exploited in the threshold Cherenkov detectors for particle identification in the given momentum range of the particle.

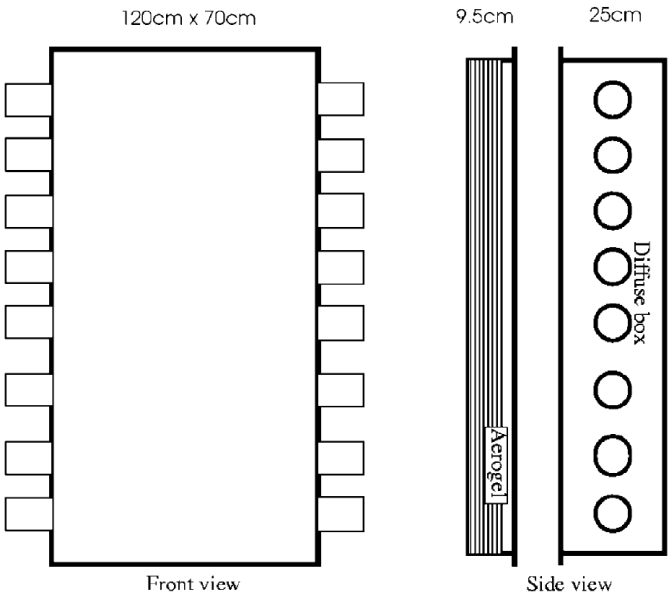

Figure 3.13: The Aerogel Cherenkov schematic diagram.

The radiator material used in the Hall C aerogel Cherenkov detector (see Fig. 3.13) has an index of refraction of 1.015 which meets the threshold condition for positively charged pions with momentum above $\approx 0.803\,\text{GeV}$. Thus, it could be used as a veto detector for almost all kinematic settings of E05-017 since the analogous condition for the protons would require proton momentum to be above $\approx 5.396\,\text{GeV}$. Over 650 aerogel tiles are stuck together in an aerogel tray to form a 9 cm thick radiator. The tray is attached to a diffusion light box where the Cherenkov light is detected by 16 Photonis XP4572B 5 inches PMTs. The sensitive area of the detector is about $(120 \times 70)\,\text{cm}^2$.

3.6.4 Data Acquisition

The information flow produced by the detector package, target system and beamline equipment is handled by the Hall C Data Acquisition system (DAQ). The DAQ includes Fastbus/VME/CAMAC crates as well as JLab custom built and Nuclear Instrumentation Module (NIM) electronics modules. The ADC, TDC and scaler boards residing in the Fastbus and VME crates are managed by the Read-Out Controller (ROC), a CPU unit controlling the crate. The individual ROC communicates with the Trigger Supervisor which generates triggers to initiate the ROC read-out. The software package, CEBAF On-line Data Acquisition (CODA), developed by the JLab DAQ group is primarily responsible for building the physical event from ROC's data fragments, incorporating all corresponding information and writing it to the disk. The raw ADC and TDC detector hit values and certain beamline quantities (beam position, raster) are recorded on the event-by-event basis and form the so-called CODA physics event. The read-out of the HMS hardware scalers is performed asynchronously with the main trigger and is injected into the data stream every two seconds. The slow control variables, such as the accelerator settings, target parameters, and others, are handled by the Experimental and Physics Industrial Control System (EPICS). The EPICS event is triggered by CODA and is written to the common data file every 30 seconds.

The hardware-based decision to accept the physics event is provided by the Hall C trigger electronics. Several trigger schemes have been developed (see Fig. 3.14) to allow flexible particle selection and background rejection. There are two types of triggers for the HMS configured to detect electrons called ELREAL and PION (see Fig.). The ELREAL can be produced in two ways by either requiring the presence of SCIN/STOF, gas Cherenkov and calorimeter first layer signals or the presence of the tighter hodoscope signal SCIN and higher threshold calorimeter signals. The redundancy is implemented to improve electron trigger efficiency. Selection of the charged pions is provided by the PION trigger defined as a hodoscope SCIN signal vetoed by the gas Cherenkov signal. When both the HMS and SOS spectrometers are operational and detection of the coincidence events is necessary, the COIN trigger is used which ensures arrival of the single arm triggers within a tight time window ($30\,\text{ns} - 100\,\text{ns}$). A special circuit allows for each type of the trigger to be prescaled to satisfy the needs of the experiment. To acquire ADC pedestal positions for calibration purposes, the 1000 "Pedestal" triggers are generated at the start of

each run by a pulser signal.

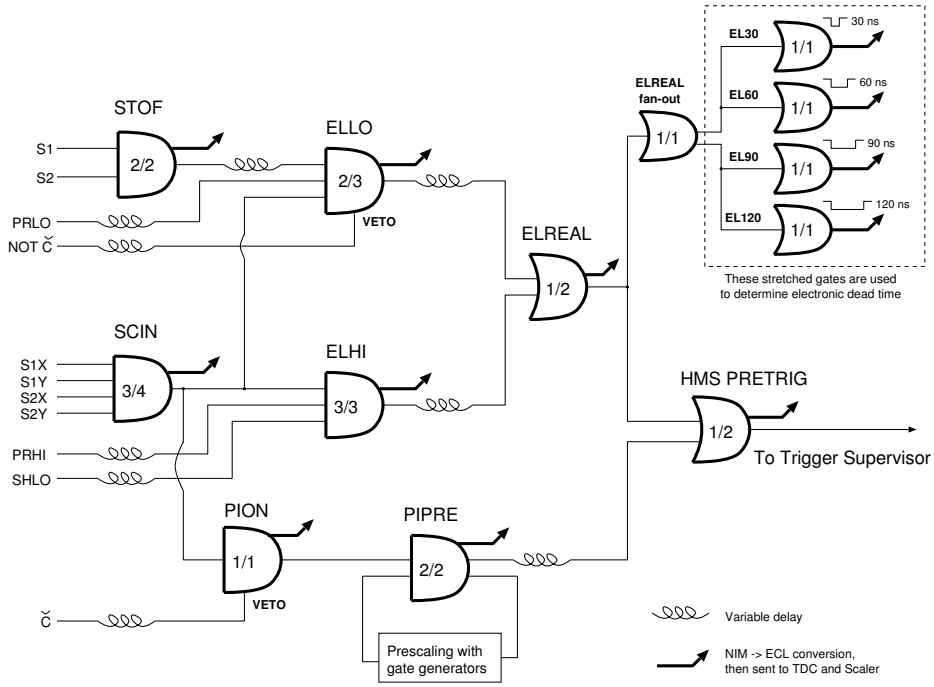

Figure 3.14: The HMS trigger logic schematic diagram.

To select proton events in the HMS during E05-017, a combination of the hodoscope STOF and SCIN triggers was used. In the beginning of the experiment the STOF was chosen as being possibly more efficient because its trigger condition was more relaxed. It was then found that for some kinematics it generates many triggers with only two planes fired suggesting noticeable background contamination. The trigger scheme was switched to the SCIN condition requiring hits in three out of four hodoscope planes.

4 Analysis

4.1 Overview

The analysis process concerns itself with translating the "raw" data, detector ADC and TDC values, into observables necessary to achieve experimental goals. For this experiment the analysis was split in three separate stages: (1) reconstruction of the physical event, (2) isolation of elastic events from the background and calculation of the elastic cross section, and (3) extraction of the form factor ratios along with an estimations of the constraints on nonlinear behavior of the ε dependence of σ_{R} .

The information recorded during the experiment by the DAQ system is divided into "runs", the data taken at one beam energy and spectrometer angle setting for the period of $15 - 30$ minutes ($2\,\mathrm{M} - 2.5\,\mathrm{M}$ triggers). A single kinematic setting, thereby, comprises several runs taken to acquire proposed statistics and to perform auxiliary studies with Al and C targets. In order to reconstruct physical quantities (Sec. 4.2), such as four-momentum of the scattered particle, from the ADC and TDC values, each detector element is calibrated and the data are then processed on the run-by-run basis with a standard Hall C data analysis software using the calibration database. The reconstructed quantities include the position of the interaction vertex, momentum, direction and the time-of-flight of the particle, as well as the quantities related to luminosity measurements such as beam charge and target density.

Once the reconstructed data is available, the counting rates can be determined through the careful selection of elastic scattering events. The combined counting rates relates to the cross section as

$$N_{\mathrm{tot}}^{\mathrm{data}} = N_{\mathrm{bgrd}}^{\mathrm{data}} + \iint \mathcal{L} \frac{d^2\sigma_{\mathrm{R}}}{dE' d\Omega} (\Delta E' \Delta\Omega) \epsilon A(E', \theta), \tag{4.1}$$

where N^{bgrd} is the number of background events, $\mathcal{L}$ is integrated luminosity, ϵ is the total detection efficiency, and $A(E', \theta)$ is the acceptance of the detector package. While the luminosity and efficiency are deduced from specialized measurements, the

complex dependence of the acceptance on the spectrometer geometry, target configuration and kinematics of the event, typically, requires a Monte Carlo (MC) simulation (Sec. 4.6) for its determination. Thus, it is more practical to use the *MC ratio* method for cross section extraction. In the MC ratio method, the number of the measured elastic events is compared to the results of the complete MC simulation, which includes all aspects of the experimental setup, multiple scattering, external energy losses, and radiative corrections,

$$N_{\rm elas}^{\rm MC} = \iint \mathcal{L} \frac{d^2\sigma_{\rm R}^{\rm MC}}{dE'd\Omega}(\Delta E'\Delta\Omega)A^{\rm MC}(E',\theta). \tag{4.2}$$

The cross section is then obtained by taking a ratio of Eq. 4.1 and 4.2, i.e. it is extracted as a deviation from the model cross section $\sigma_{\rm R}^{\rm MC}$:

$$\sigma_{\rm R} = \sigma_{\rm R}^{\rm MC}\frac{Y^{\rm data}(E',\theta)}{Y^{\rm MC}(E',\theta)}, \tag{4.3}$$

where $Y^{\rm data}$ ($Y^{\rm MC}$) is the measured (simulated) normalized yield and it is assumed that the MC simulation properly reproduces acceptance, such that $A(E',\theta) = A^{\rm MC}(E',\theta)$. The measured normalized yield is calculated as

$$Y^{\rm data} = \frac{N_{\rm tot}^{\rm data} - N_{\rm bgrd}^{\rm data}}{Q\epsilon}, \tag{4.4}$$

with Q denoting the measured beam charge integrated over one run time period. In the actual analysis, the numerator of Eq. 4.4 is represented by the corresponding distribution which splits the spectrometer acceptance of a single setting measurement in either momentum or scattering angle bins. Since E05-017 exploits the benefits of proton detection (Sec. 1.5) with over-determined elastic kinematics (both the momentum and the scattering angle of the proton are measured), it is, in fact, useful to define the following quantities

$$\delta p = p^{\rm meas} - p^{\rm calc}(\theta^{\rm meas}), \quad \delta\theta = \theta^{\rm meas} - \theta^{\rm calc}(p^{\rm meas}), \tag{4.5}$$

where $p^{\rm meas}$ ($\theta^{\rm meas}$) is the measured momentum (scattering angle) of the recoil proton detected in HMS. The $p^{\rm calc}$ ($\theta^{\rm calc}$) is the momentum (angle) calculated based on the measurements of the angle (momentum) from the same event. The calculation assumes fixed two-body elastic kinematics and gives the corresponding values as

$$p^{\rm calc} = \frac{2E(EM_{\rm p} + M_{\rm p}^2)\cos(\theta^{\rm meas})}{(E+M_{\rm p})^2 - E^2\cos^2(\theta^{\rm meas})}, \quad \cos(\theta^{\rm calc}) = \frac{(E+M_{\rm p})(E_{\rm p}+M_{\rm p})}{Ep^{\rm meas}}, \tag{4.6}$$

where E is the beam energy, $M_{\rm p}$ is the proton mass, and $E_{\rm p}$ is the energy of the scattered proton. The δp ($\delta\theta$) histograms are then normalized by the denominator of Eq. 4.4 value which is referred to as effective charge:

$$Q^{\text{eff}} = Q\epsilon = Q\epsilon_{\text{DAQ}}\epsilon_{\text{cor}}\epsilon_{\text{PID}}, \tag{4.7}$$

$$\epsilon_{\text{DAQ}} = \frac{1}{c_{\text{PS}}}(1 - c_{\text{EDT}})(1 - c_{\text{CDT}})\epsilon_{\text{DC}}\epsilon_{\text{trig}}, \tag{4.8}$$

$$\epsilon_{\text{cor}} = c_{\text{absn}}c_{\text{trgB}}c_{\text{trgL}}c_{\beta=0}. \tag{4.9}$$

The ϵ term represents a combined set of corrections and efficiencies which can be further categorized as ϵ_{DAQ}, ϵ_{cor}, and ϵ_{PID}. The ϵ_{DAQ} takes into account the efficiencies of the track reconstruction and DAQ performance. It includes electronic dead-time (EDT) and computer dead-time (CDT) (c_{EDT}, c_{CDT}), trigger and HMS DC efficiencies (ϵ_{DC}, ϵ_{trig}), and a prescaling factor (Sec. 4.3). The ϵ_{cor} is the product of a number of corrections applied to properly account for events that were lost (Sec. 4.4). These corrections include the fraction of the protons absorbed along the trajectory to the detector package (c_{absn}), luminosity fluctuations due to the LH_2 target boiling (c_{trgB}), target length variations due to the beam position instability (c_{trgL}), and the fraction of events with a valid reconstructed track but with missing TOF, β of the particle, information ($c_{\beta=0}$). The ϵ_{PID} is efficiency related to the particle identification procedure (Sec. 4.5).

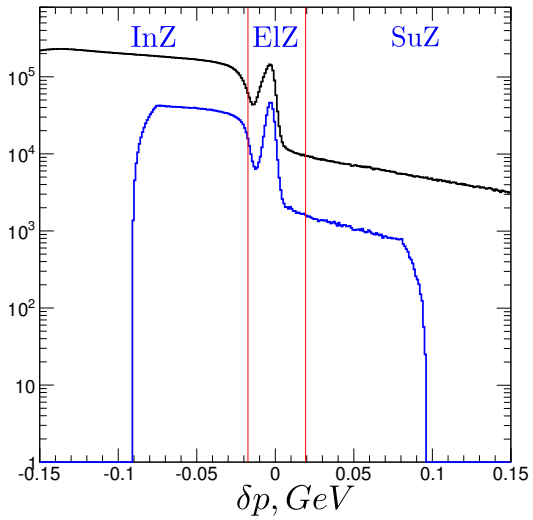

Figure 4.1: Sample δp distribution for $Q^2 = 1.91\,\text{GeV}^2$ and $\theta_{\text{HMS}} = 12.36°$: unsuppressed (black), acceptance cuts (Sec. 4.7.1) applied (blue), exemplary elastic cuts (vertical red lines). The δp histogram is shown to facilitate explanation for analysis procedures only. The $\delta\theta$ distribution (Eq. 4.5) is used for the actual cross section extraction (see details in the text).

A sample δp distribution is shown by the black line in Fig. 4.1. The form of Eq. 4.5 defines the main features of the δp histogram. The prominent elastic peak is centered around $\delta p = 0$ with a width predominantly determined by the HMS momentum and angular resolution. The left (negative) part of the elastic peak displays a broadening due to radiative effects. This radiative elastic tail extends farther to the negative part of the spectrum and is hidden under a wide inelastic shoulder. The momentum of inelastic events is smaller than the one expected for elastically

scattered protons. Conversely, events on the other (positive) side of the histogram constitute the so-called "super-elastic" zone with the proton momentum exceeding the one expected from elastic kinematics. The boundary of the inelastic (InZ) and super-elastic (SuZ) background zones, the total number of the background events and the extent to which it overlaps with the elastic zone (ElZ) strongly depends on kinematic settings and, consequently, affects cross section extraction.

The separation of the elastic events from various sources of the background is performed in two steps. First, all detected protons are differentiated from the other particle types (deuteron, triton, charge pion). This task, referred to as particle identification, is accomplished by imposing a certain selection criteria, or "cuts", on the time-of-flight information deduced from the hodoscope measurements (Sec. 4.5). In the second step, elastically scattered protons are distinguished from quasi-elastic and inelastic events. The quasi-elastic scattering reactions, $\mathrm{Al}(e,p)$, occur in the aluminum target cell windows and produce a flat homogeneous background in the δp ($\delta\theta$) distribution. Its contribution extends under the elastic peak but fully dominates the spectrum only in the super-elastic zone, typically defined as a region 5σ above the mean position of the elastic peak. Simulating quasi-elastic scattering contribution is problematic, especially in terms of the recoil proton kinematics. Therefore, to estimate the quasi-elastic background, extensive measurements with a dummy target were made at each of the kinematic settings (Sec. 4.7). In addition to being a source of quasi-elastic background, the upstream aluminum target window acts as a radiator capable of producing hard bremsstrahlung photons at or near the full beam energy. The bremsstrahlung photons, which propagate through the LH_2 target material, initiate reactions of neutral pion photoproduction ($\gamma p \rightarrow \pi^0 p$) and Compton scattering ($\gamma p \rightarrow \gamma p$). The π^0 photoproduction constitutes the prevalent fraction of events that populates the inelastic zone in Fig. 4.1. The momentum difference between elastically scattered proton and the proton resulting from $\gamma p \rightarrow \pi^0 p$ scattering indicates a threshold condition for π^0 photoproduction which is reflected by a characteristic dip on the left side of δp distribution in Fig. 4.1. The dip is prominent for certain kinematic settings only, where the HMS resolution is adequate for the corresponding momentum difference and the neutral pion count is sufficiently high. In the case of the Compton scattering, the kinematics of the reaction is identical to elastic scattering due to the zero mass of the scattered photon. The only distinction from the elastically scattered proton would be given by the energy difference between primary electron beam and radiated bremsstrahlung photons. Although the Compton scattering background can stretch out up to the point of $\delta p = 0$, its contribution is quite insignificant since the Compton cross section relative to the photoproduction cross section (for kinematics covered during E05-017) never exceeds $\sim 5\,\%$ (Sec. 4.6.2). To allow separation of the elastic peak from inelastic processes in the overlapping region, the MC simulation of both the $\gamma p \rightarrow \pi^0 p$ and $\gamma p \rightarrow \gamma p$ processes has been performed for each Q^2 and ε setting.

Once each component is retrieved, either through MC simulation ($ep \rightarrow ep$, $\gamma p \rightarrow \pi^0 p$ and $\gamma p \rightarrow \gamma p$) or through direct measurements ($\mathrm{Al}(e,p)$), the analysis focuses on combining them to reconstruct observed spectra. The MC simulation has

to be tuned in order to properly reproduce the resolution observed in the spectrometer (Sec. 4.7.4). The δp distribution obtained with the dummy target has to be accurately scaled to account for effects related to the thickness difference between the dummy aluminum foils and the actual target endcaps. The simulated elastic scattering and background ingredients are then subject to the process of iterative fitting to the measured spectrum. This method is used to minimize effects of any mismatch in the peak widths or tails. After that part is concluded, the number of elastic events is determined within a δp window around the elastic peak (Fig. 4.1 vertical lines) and the ratio entering Eq. 4.3 is calculated to extract the desired cross section.

The $\delta\theta$ distribution, equivalent to the δp spectrum, was used in the actual analysis, since the width of the elastic peak in the angular representation is more consistent for different ε settings. Thus, a single elastic cut can be used for the selected Q^2 point which, in turn, minimizes the ε dependence of related systematic uncertainty.

4.2 Event reconstruction

During the experiment, the entire data flow is recorded using a particular CODA format which specifies several event types, such as the physics, scaler, EPICS, and pedestal events associated with a relevant trigger. A standalone software packages are used to perform calibration of the detector elements and the beamline equipment. Calibration results are written in the database as a set of appropriate constants. The standard Hall C data analysis software, ENGINE, starts with parsing CODA event information, importing calibration constants and reading the so-called "detector map" which matches the ROC channel addresses with a physical location of the detector element. The ENGINE then invokes execution of several subroutines which process and reconstruct data from the corresponding detector. Reconstruction results are written in the form of Physics Analysis Workstation (PAW) ntuples and several report files [163]. In contrast to Experiments E06-009 and E04-001 of the same run period where the HMS was used for electron detection with the gas Cherenkov (GC) and calorimeter active, for the E05-017 reconstruction, the ntuples were filled only with information reconstructed from the drift chambers (DC), hodoscope and aerogel Cherenkov detectors, while the GC and the calorimeter reconstruction was disabled. The reconstruction at the detector level is followed by transporting particle trajectories back to the interaction vertex.

There are several coordinate systems used to facilitate reconstruction calculations. The laboratory frame is defined at the center of the target such that the $z_{\rm lab}$ axis is horizontal with a positive $\hat{z}_{\rm lab}$ pointing downstream along the beamline direction. The $x_{\rm lab}$ axis points vertically downward. The $y_{\rm lab}$ axis points to the left in the horizontal direction and completes this right-handed coordinate system such that the HMS (SOS) is located at $\phi = 270^\circ$ ($\phi = 90^\circ$). The target coordinate system, $(\hat{x}_{\rm trg}, \hat{y}_{\rm trg}, \hat{z}_{\rm trg})$, is rigidly fixed at the HMS and rotates with the spectrometer relative to the lab frame. The positive $\hat{z}_{\rm trg}$ direction points along the central ray

(optical axis) of the spectrometer in the horizontal plane and is rotated by θ_{HMS} with respect to the lab z_{lab} axis. The target system x_{trg} axis coincides with the lab x_{lab} axis while the y_{trg} axis completes it to form a right-handed coordinate frame. The coordinate system adopted for the detector hut is centered at the *focal plane* which is defined to be the plane perpendicular to the HMS central ray and equidistant from the two drift chambers [163]. The z_{fp} axis still points along the HMS optical axis but since the spectrometer central ray followed the 25° dipole bend it is rotated upward in the vertical direction with respect to $\hat{z}_{\text{trg}}$. The positive $\hat{x}_{\text{fp}}$ ($\hat{y}_{\text{fp}}$) points in the dispersive (non-dispersive) direction of increasing momentum. Finally, there is another coordinate system associated with the beamline. It is used to calculate several quantities such as raster-dependent beam position on the target. It is a left-handed coordinate system specified as $\hat{z}_{\text{b}} = \hat{z}_{\text{lab}}$, $\hat{x}_{\text{b}} = -\hat{y}_{\text{lab}}$, and $\hat{y}_{\text{b}} = -\hat{x}_{\text{lab}}$.

4.2.1 HMS DC tracking

The HMS tracking algorithm allows reconstruction of the proton trajectory at the focal plane based on TDC hits detected in the drift chambers. The multi-hit TDC with 0.5 ns per count resolution can record up to eight hits per event in a single wire. Initially, a loose TDC cut is applied to remove a background which is not related to the trigger track. For this run period, to suppress accidental events which may cause the failure of the tracking algorithm, the TDC window was narrowed from the typical 1800-3300 TDC channels to 2400-2900 TDC channels [60]. Once the total number of hits is determined, events with an insufficient or with an excessive number of hits are discarded. The pattern recognition procedure identifies the hit clusters, *space points*, which are defined as all possible intersections of non-parallel wires with a good hit. The relative distance squared for all available space point pairs is then calculated and is compared to the user-defined value. The space points that satisfy this condition are grouped together. For each hit a drift time is determined with respect to the delayed "start time" reconstructed from the hodoscope and by taking into account cable lengths and signal propagation times.

After initial drift time information is available and the groups of space points are identified, the reconstruction procedure continues with fitting a "stub", a mini-track determined from the hits of one chamber. Stub fitting relies on the drift distance obtained from the measured drift time. Since proton trajectories are nearly perpendicular to the wire plane, it is safe to assume that the distance of the closest approach traveled by liberated electrons lies in the wire plane. The distribution of the drift distances, averaged over all cells, is expected to be uniform when performing time-to-distance conversion. A time-to-distance map (Fig. 4.2) is generated for each wire plane by analyzing about 2×10^5 events. The drift distance is then evaluated as

$$D(t) = D_0 \frac{\int_{t_{\text{min}}}^{t} F(\tau) d\tau}{\int_{t_{\text{min}}}^{t_{\text{max}}} F(\tau) d\tau}, \tag{4.10}$$

where D_0 is the maximum 5 mm drift distance defined by the DC cell size and $F(\tau)$ is the measured drift time distribution function.

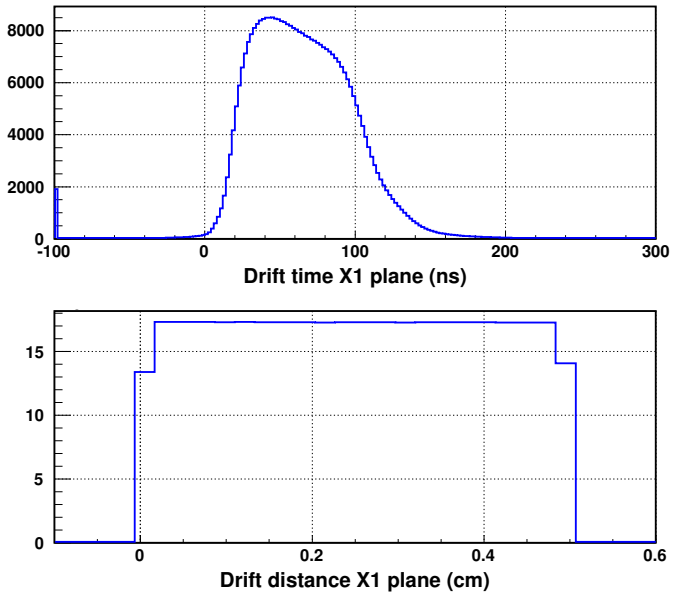

Figure 4.2: HMS drift time and HMS drift distance distributions for DC plane X1. *Figure source: Ref.* [60].

However, only the absolute value of the distance between the track and the wire can be extracted from time-to-distance conversion. The full track reconstruction is still hindered by so-called left-right ambiguity, i.e. the possibility for the track to pass the wire on one or on another side. The ambiguity is resolved by iteratively performing a stub fitting for all (2^6) possible left-right combinations. The number of combinations and, consequently, the CPU run-time can be reduced by adopting certain approximations. The stub fit with the smallest χ^2 is selected for further processing. The stubs from both chambers are then combined together by again cycling through all possible combinations, linking and fitting them to a full track. The straight line fit parameters along with the corresponding χ^2 value are recorded as a focal plane quantities: coordinates ($x_{\rm fp}$, $y_{\rm fp}$) and slopes ($x'_{\rm fp} = dx_{\rm fp}/dz_{\rm fp}$, $y'_{\rm fp} = dy_{\rm fp}/dz_{\rm fp}$).

For the E05-015 reconstruction procedure, the assumption was made that only one particle passes through the drift chambers per event so that a single best track has to be selected from the number of complete candidate tracks. Selection of the best track candidate requires transporting the tracks back to the interaction vertex through the spectrometer optics. A number of quantities, such as vertex coordinates and the proton direction, are then computed in the target coordinate system and are subjected to the series of cuts which determine the selection of the final track.

4.2.2 HMS optics

After obtaining the focal plane ($x_{\rm fp}$, $y_{\rm fp}$, $x'_{\rm fp}$, $y'_{\rm fp}$) coordinates, the subsequent task is the reconstruction of the proton four-momentum vector and its position at the target. These quantities are expressed as the ($x_{\rm trg}, y_{\rm trg}, z_{\rm trg} = z_{\rm lab} = 0$) vertex coordinates, the tangents of the out-of-plane and in-plane angles ($x'_{\rm trg}, y'_{\rm trg}$), and the deviation from the central HMS momentum, $\Delta_{\rm p} = (p^{\rm meas} - p_{\rm HMS})/p_{\rm HMS}$. The correspondence between the focal plane and target values requires precise knowledge of the HMS optical properties which are described by the HMS transport matrix. In general, these calculations constitute an under-determined problem since the number of measured parameters ($x_{\rm fp}$, $y_{\rm fp}$, $x'_{\rm fp}$, $y'_{\rm fp}$) is smaller than the number of unknowns ($x_{\rm trg}$, $x'_{\rm trg}$, $y_{\rm trg}$, $y'_{\rm trg}$, $\Delta_{\rm p}$). Since the vertical beam position on the target is controlled by the raster and is determined on a per-event basis from the raster signal, a reasonable approximation can be made that the reaction vertical vertex position $x_{\rm trg}$ at $z_{\rm lab} = 0$ is determined by the average beam position as measured by the BPM, with event-by-event correction for the raster offset. The other four quantities in the target coordinate system are reconstructed as a Taylor-series expansion of the focal plane coordinates through the transformations

$$m^i_{\rm trg} = \sum_{j,k,l,m}^{N} M^i_{jklm} (x_{\rm fp})^j, (y_{\rm fp})^k, (x'_{\rm fp})^l, (y'_{\rm fp})^m, \tag{4.11}$$

$$\text{for}(1 \leqslant j + k + l + m \leqslant N), \tag{4.12}$$

where $m_{\rm trg} = (x'_{\rm trg}, y_{\rm trg}, y'_{\rm trg}, \Delta_{\rm p})$ and M^i_{jklm} denotes a reconstruction matrix element. The calculation of the matrix elements M^i_{jklm} is based on iterative fitting procedure and is normally performed up to the fifth order on the data obtained from the "optics runs". The initial fitting coefficients are provided by a software package called COSY [165], which represents a sufficiently accurate model of the spectrometer optics. The optics runs used for coefficients calibration are a series of dedicated runs conducted with a special collimator, a sieve slit, installed before the optical elements of the spectrometer and a thin carbon target. The sieve slit collimator has an array of holes of 0.508 cm (0.254 cm for the central hole) diameter with a position well-known from the survey. So, the comparison of the angular distributions can be made from the sieve slit data between the reconstructed and known values. Certain mismatches in the reconstructed data [61] were revealed during the sieve slit studies and when comparing data to the MC simulation. The offsets from expected values were found in both $x'_{\rm trg}$ and $y'_{\rm trg}$ distributions. The $y'_{\rm trg}$ mismatch was attributed to a small, 0.45 mm, relative shift of DC1 with respect to DC2 in $y_{\rm fp}$ direction (Fig. 4.3). Similar studies were performed for $x'_{\rm trg}$ and, consequently, $\Delta_{\rm p}$ offsets by comparing relevant distributions from data and MC (Fig. 4.4). The $x'_{\rm trg}$ shift was found to be related to the vertical beam position offset, $\delta y_{\rm b} \approx -1.5$ mm with corresponding momentum change of $\Delta_{\rm p} = \Delta_{\rm p} + \delta y_{\rm b} \cdot 0.13$.

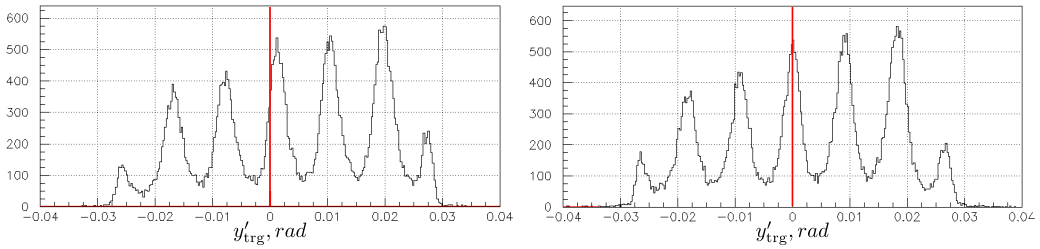

Figure 4.3: The y'_{trg} distribution for the sieve slit run with peaks corresponding to the horizontal collimator's holes. The effect of applying DC relative shift correction on the position of the central peak is shown: before (left) and after (right) correction. *Figure source: Ref.* [61].

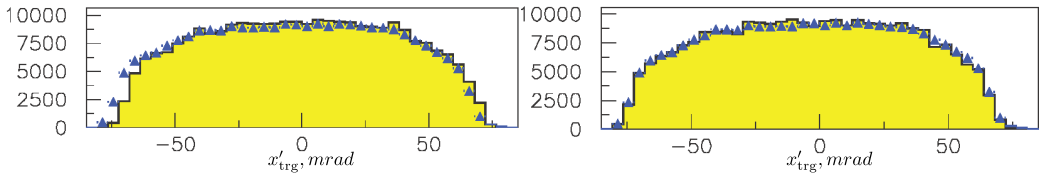

Figure 4.4: The x'_{trg} distribution for the data (yellow) and MC simulation (blue). The effect of applying beam position offset δy_{b} correction on the shape of the distribution is shown: before (left) and after (right) correction. *Figure source: Ref.* [61].

4.2.3 Time-of-flight measurements

As previously discussed in Sec. 3.6.2, the hodoscope signals form an event trigger and are used to calculate the TOF of the particle crucial for particle identification (PID) studies reviewed in Sec. 4.5. Another important hodoscope function is to set initial time for the drift distance measurements in DC. The hodoscope event reconstruction produces the following information: the DC start time as the time projected back to the focal plane $z_{\mathrm{fp}} = 0$, the particle's velocity ($\beta = v/c$) calculated from the time-of-flight between hodoscope front and back planes, the energy deposition for each plane (dE/dx) as the amplitude of the PMT signal. After calculation of the track-independent quantities, the timing calculations are revisited once the tracking analysis is ready.

Timing reconstruction starts from converting the output of the common-start high resolution TDCs of $\sim$ 25.9 ps per TDC count resolution to nanoseconds. An overall offset due to the delay differences between channels is then removed and the time is determined with respect to an arbitrarily chosen PMTs. The time walk correction (see Ref. [163] for detailed description of the hodoscope timing corrections) is applied to account for uncertainty caused by the time difference at which simultaneous signals of unequal amplitudes reach the threshold condition set by a discriminator. To minimize this uncertainty a special procedure was carried out to gain-match individual PMTs by adjusting PMT high voltages such that the consistent pulse height is obtained as a response to a radioactive source.

Timing variation effects of the light propagation from the hit location to the PMT window associated with the scintillator refraction index and geometry as well as the light-guide characteristics also has to be included in the corrections. Initially, when the track's parameters are not yet available, the hit position can be evalu-

ated by the time difference between the "+" and "-" end PMTs of the paddle and, therefore, a good signal on both ends is required. The average time is projected back to the focal plane assuming that $x'_{\rm fp} = y'_{\rm fp} = 0$ and $p = p_{\rm HMS}$ for subsequent tracking calculations. After the focal plane quantities of the particle are reconstructed, the track can be projected onto hodoscope planes and the hit position precision can be significantly improved. The timing analysis is then repeated. In addition, the path length between scintillators is determined with consequent TOF and β calculations. Finally, the dE/dx is a by-product of the timing correction calcilations which is no directly related to the TOF reconstruction. However, it is used in the main analysis (Sec. 4.5) and was evaluated as the geometric mean of the ADC signals from both PMTs of the paddle.

All correction parameters (cable lengths offset, time walk correction, light propagation through the scintillator) required for the hodoscope timing information reconstruction are determined during calibration procedure [62]. The standalone calibration software package uses a data event file with a relatively clean sample of the protons. The proton events were prepared by suppressing charged pion content by using the aerogel Cherenkov information and deuteron content by using preliminary TOF cuts (Sec. 4.5). One set of calibration results constitutes three parameters for each hodoscope PMT. The calibration constants' quality depends significantly on the proton momentum. In order to take this into account a separate hodoscope calibration was performed for three Q^2 regions: $Q^2 \leqslant 0.98\,{\rm GeV}^2$, $1.19\,{\rm GeV}^2 \leqslant Q^2 \leqslant 1.70\,{\rm GeV}^2$, $Q^2 \geqslant 1.91\,{\rm GeV}^2$. In addition, calibration was repeated for each region after a configuration change for the E06-009 and E04-001 runs with a total of six different sets of calibration constants for the E05-017 run period. The relative improvement of the TOF resolution after a new set of calibration constants obtained is shown in Fig. 4.5 for $\delta\beta$ distribution which is defined as

$$\delta\beta = \beta^{\rm meas} - \frac{p_{\rm p}}{E_{\rm p}} \tag{4.13}$$

where $\beta^{\rm meas}$ is the particle's β as measured by the hodoscope, $p_{\rm p}$ and $E_{\rm p}$ are reconstructed momentum and energy assuming that detected particle is proton.

4.2.4 Aerogel Cherenkov response

The aerogel Cherenkov is typically used to discriminate protons and positively charge pions over a range of momenta where only π^+ are fast enough to give a signal. As such, its response can be used as a veto signal in the offline analysis. Therefore, for the aerogel reconstruction it was only necessary to translate each PMT signal amplitude measured by ADC into the number photo-electrons, $N_{\rm pe}^{\rm aero}$, observed in a given event. The sum of the photo-electrons detected from all PMTs on "+" ("-") side of the detector as well as the total sum is calculated. The total sum is assigned zero if the sums on both sides individually are less than 0.5 pe. In certain cases, when the individual PMT signal is large enough to cause ADC overflow (ADC count is greater than 8192) the corresponding aerogel hit is assigned $N_{\rm pe}^{\rm aero} = 100$.

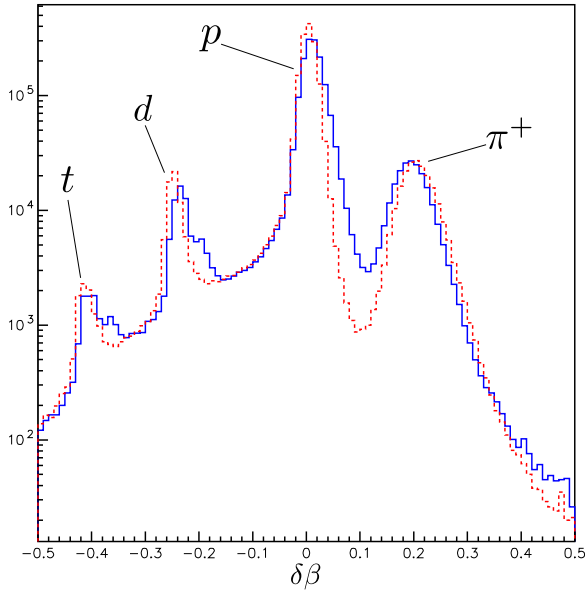

Figure 4.5: The $\delta\beta$ distribution for $p_{\mathrm{HMS}} = 1.36\,\mathrm{GeV}$. The resolution improvement is shown before (blue) and after (red) hodoscope calibration. The observed peaks correspond to protons, deuterons, tritons and π^+. *Figure source: Ref.* [62].

For the aerogel calibration, a raw ADC histogram is filled for each PMT. Positions of the pedestal and single photo-electron peaks are determined through the appropriate fitting procedure. A sample ADC spectrum is shown in Fig. 4.6. As for the hodoscope calibration, two sets of calibration constants were obtained for the E05-017 run period (before and after configuration change).

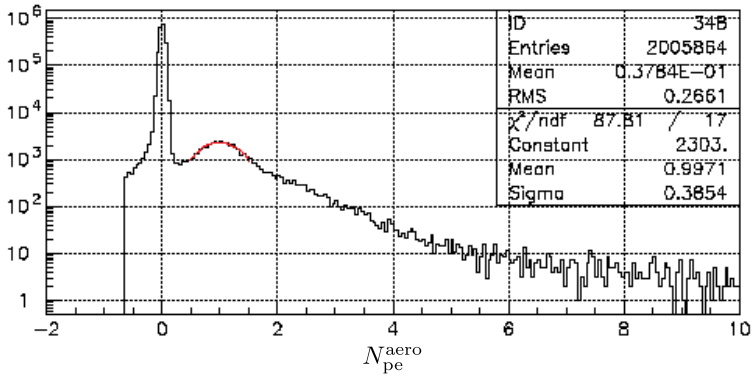

Figure 4.6: A sample $N_{\mathrm{pe}}^{\mathrm{aero}}$ distribution (black) is shown for one of the PMTs on the "-" side of the aerogel Cherenkov detector. The Gaussian fit to the single photo-electron peak is indicated by the red line. *Figure source: Ref.* [62].

It has to be noted that, for several kinematic settings the calibration procedure was complicated by a very low π^+ count rate. So, the usage of the aerogel information was restricted to hodoscope calibration (Sec. 4.2.3) and particle identification studies (Sec. 4.5).

4.3 Efficiencies

4.3.1 DAQ

There are several correction factors introduced to account for intrinsic limitations of the DAQ system performance. The finite electronics processing time sets an upper limit on the trigger rate that can be recorded during data taking. The associated event losses and event rate reduction are characterized by (a) electronic dead-time (or live-time), (b) computer dead-time (or live-time), (c) prescale factor.

The hodoscope discriminators and logic modules produce the output signals of an adjustable width. If another event occurs while the previous output signal remains active, it will be ignored. The probability of finding several events within a fixed time interval is given by a Poisson distribution [163]

$$P(n) = \frac{(Rt)^n e^{-Rt}}{n!}, \tag{4.14}$$

where R is the average event rate and n is the number of events. For relatively small event rates and a narrow gate widths generated by the logic module, the probability of observing zero events within the gate duration, τ, would be given by $P(0) = e^{-R\tau} \approx 1 - R\tau$. The fraction of the measured events, or the electronic live-time (ELT) $c_{\rm ELT} = 1 - c_{\rm EDT}$, is equal to the probability that the events are separated by the time larger than the gate width:

$$c_{\rm ELT} = \frac{N_{\rm meas}}{N_{\rm tot}} \approx 1 - R\tau. \tag{4.15}$$

In practice, in order to determine $N_{\rm tot}$ and consequently the electronic dead-time correction for the E05-017 run, four copies of the SCIN trigger (see Fig. 3.14) were generated with different widths ($\tau = 50\,$ns, 100 ns, 150 ns, 200 ns) which were used to increment a corresponding scaler (N_{50}, N_{100}, N_{150}, N_{200}). The $N_{\rm tot}$ can be then found by a linear extrapolation to $\tau = 0$ (Fig. 4.7). The actual electronic dead-time is calculated, as a part of the reconstruction procedure, based on information from two scalers only as follows

$$c_{\rm EDT} = \frac{(N_{100} - N_{150})}{N_{100}} \frac{\tau}{50}. \tag{4.16}$$

During the experiment, the gate widths of individual modules were set to $\sim 50\,$ns but the effective gate width is larger due to an overlap between the signals at the logic modules forming the SCIN trigger. It was determined to be approximately $\tau = 60\,$ns. The $c_{\rm EDT}$ is calculated on the run-by-run basis and is applied as a correction through Eq. 4.7. During this experiment, the typical SCIN trigger rates for on the LH_2 target did not exceed 45 kHz, resulting in $c_{\rm EDT} < 0.3\,\%$. Only for a few runs on the aluminum target, where the beam current was increased to reduce the running time, the peak rates were on the level of 100 kHz with $c_{\rm EDT} \sim 0.8\,\%$.

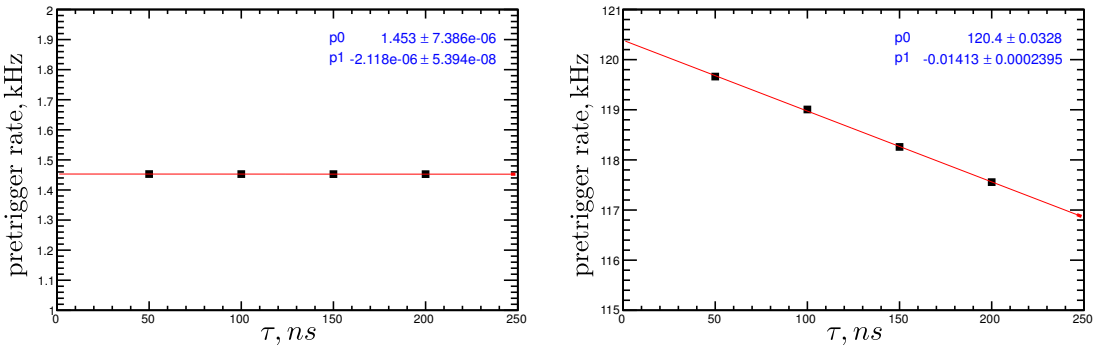

Figure 4.7: The rates of the pretrigger signal corresponding to the different gate widths are plotted as a function of the gate width: left (right) - low (high) rate run.

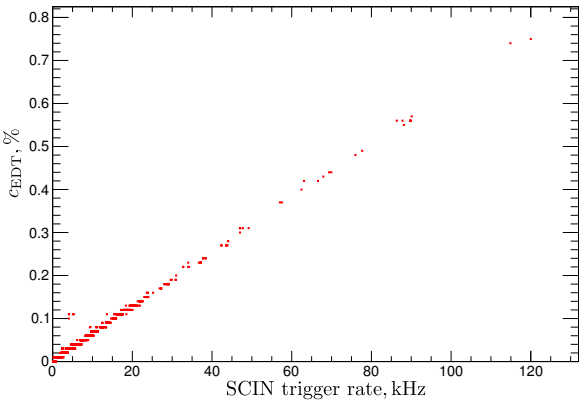

Figure 4.8: The electronic dead-time is plotted as a function of the SCIN trigger rate.

A more significant loss of information occurs due to the DAQ computer being busy processing a previous event and thus being unable to accept new triggers. The factors affecting the computer dead-time include the trigger rate, the digitization time of the ADC and TDC modules, ROCs memory readout time, the total size of the event and the network bandwidth available for data transfer. The typical processing time for one event is on the order of a few hundreds of microseconds. For particularly high rates, the computer dead-time can be reduced by prescaling which allows for a more even sampling of the triggers in time. The prescaling factor, c_{PS}, is set at the trigger supervisor level and signifies that only one in every c_{PS} events is accepted.

The computer dead-time is monitored continuously and is calculated for each run by comparing the number of SCIN triggers to the number of triggers accepted by the trigger supervisor. The computer dead-times that were observed during this experiment are shown in Fig. 4.9 as a function of the incoming pretrigger rate along with the prescale setting used for each run.

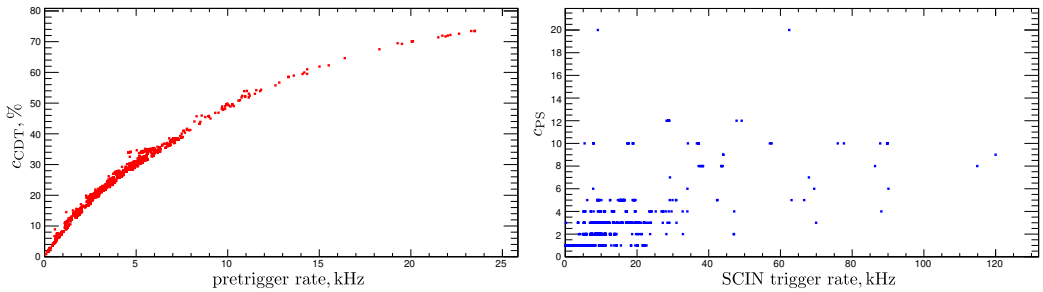

Figure 4.9: Left: the computer dead-time is plotted as a function of the pretrigger trigger rate (after accounting for the prescaling factor). Right: the prescale settings are plotted as a function of the SCIN trigger rate.

4.3.2 Hodoscope

The inefficiency of the detectors which are used to form a trigger signal may also lead to event losses. Since for this run the only relevant trigger was formed based on the hodoscope response, the trigger loss correction factor ϵ_{trig} is determined by the hodoscope paddle inefficiency. The evaluation of a single paddle performance is done by selecting the tracks that pointed to the middle of the paddle ($\pm 2\,\text{cm}$ around the center of the scintillator) and verifying if the PMTs on both ends of the paddle had a signal. The number of the actual and expected hits is then summed over for each plane and the efficiency of the hodoscope single plane is calculated as their ratio.

The combined SCIN trigger efficiency is obtained by summing over all permutations in which the trigger can be formed

$$\epsilon_{\text{trig}} = \prod_{i=1,4} \epsilon_i + \sum_{j=1,4} (1-\epsilon_j) \prod_{i \neq j} \epsilon_i, \tag{4.17}$$

where i and j are the plane numbers and $\epsilon_{i,j}$ is the hodoscope plane efficiency determined as described above. The trigger condition of firing three out of four planes ensures that trigger efficiency remains high, $\epsilon_{\text{trig}} > 99.4\,\%$. The trigger efficiency observed during this experiment is shown in Fig. 4.10. The blue points, with efficiency values lower than what is expected for the standard operation, correspond to the runs for which the high voltage of several paddle PMTs in each X hodoscope plane were turned off. This was done for two kinematic settings (#64 and #75 of Table 3.1) with high inelastic background rates. The disabled paddles are physically located in a region of the spectrometer which detects smaller momentum particles, matching inelastic scattering only. Thus, the procedure imposed a "hardware" cut on the inelastic background, reduced the dead-time and increased the fraction of elastic events for these runs.

The dependence of the trigger efficiency, excluding the runs with suppressed inelastic background, on the SCIN trigger rate is shown in Fig. 4.11. The lower values of ϵ_{trig} at SCIN rate $< 10\,\text{kHz}$ were attributed to the unsatisfactory measurements of the trigger efficiency in the presence of the significant inelastic background

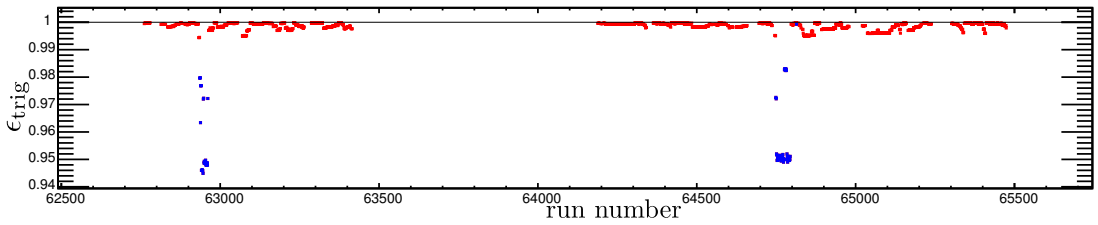

Figure 4.10: The ϵ_{trig} is plotted as a function of run number. The blue points correspond to the run with several PMTs disabled to suppress inelastic background for two high Q^2 and small θ_{HMS} kinematics.

near the edge of the acceptance. For this region the trigger efficiency was assigned a value of $\epsilon_{\text{trig}} = 0.999$ with a conservative uncertainty of 0.1 %.

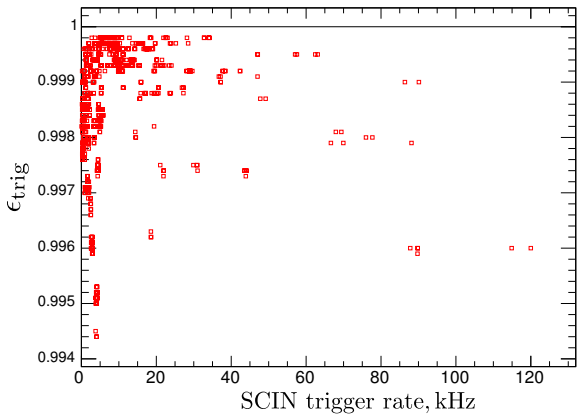

Figure 4.11: The ϵ_{trig} is plotted as a function of SCIN trigger rate. The runs that had several PMTs switched off are excluded.

4.3.3 Tracking

There are several factors that might cause a failure of the tracking reconstruction algorithm described in Sec. 4.2.1. The associated inefficiency arises when an otherwise legitimate track has an insufficient or an excessive number of hits in the drift chambers. The former leads to an unresolved left-right ambiguity while the later may result in the inclusion of unrelated hits in the track-fitting procedure. In addition, at high rates, the increasing probability of simultaneously having two or more good tracks leads to an inability to properly reconstruct either.

The tracking efficiency is determined as the ratio of the number of events for which at least one track was reconstructed and identified as "valid" to the number of events identified as valid:

$$\epsilon_{\text{DC}} = \frac{N_{\text{valid+track}}}{N_{\text{valid}}}. \tag{4.18}$$

A number of conditions has to be satisfied in order to increment N_{valid}. First, the calculations are performed only for events that populate the central fiducial region of the hodoscope, specified as the region of 4-13 (X planes) by 4-7 (Y planes) hodoscope paddles. At least two hits have to be found in each chamber while one of the chambers is required to have at least four hits. The upper bound on the number of hits in each chamber was set to be 25. All four hodoscope planes in the fiducial area must have signals. The hodoscope part of the algorithm is also expected to calculate the track-independent TOF of the particle, i.e. to perform the first stage of the hodoscope data reconstruction where the position of the hit along the paddles is determined using the timing information only with the requirement to have a signal in both PMTs of the paddle.

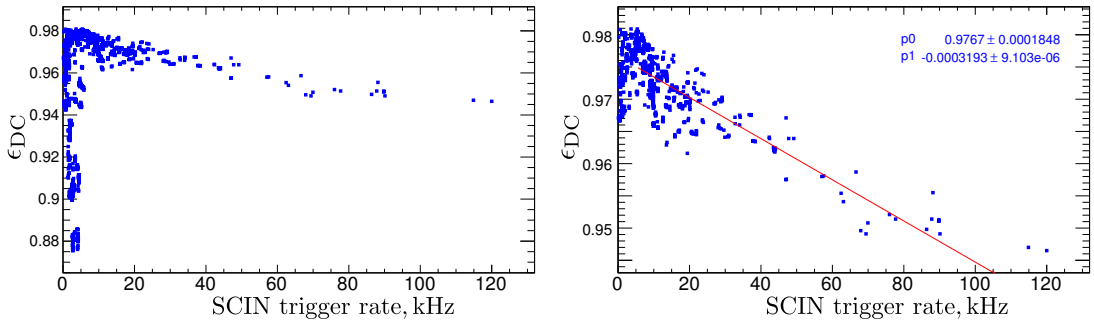

Figure 4.12: The ϵ_{DC} is plotted as a function of SCIN trigger rate (left). The runs with high fraction of the background at the edge of acceptance and switched off PMTs are excluded (right). The red line is the linear fit for ϵ_{DC} parametrization.

As in the case of the trigger efficiency, the small values, < 0.96, of the tracking efficiency (Fig. 4.12 left) correspond to the measurements with the high fraction of background rates and disabled hodoscope paddles. A cut was applied to eliminate those runs prior to performing a linear fit to parametrize ϵ_{DC} dependence on the SCIN trigger rate. The ϵ_{DC} spread around fit parametrization is shown in Fig. 4.13.

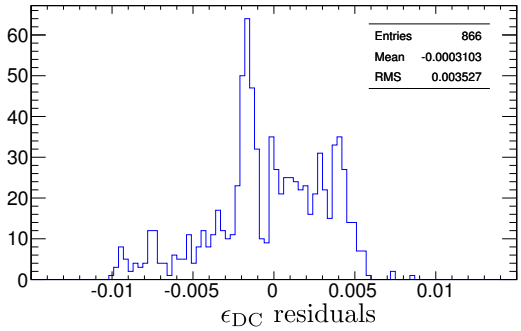

Figure 4.13: The residuals between the ϵ_{DC} values and the linear fit shown in Fig. 4.12 (left).

4.4 Corrections

4.4.1 Target boiling

Reduction of the LH_2 density is possible if the excessive amount of heat load to the target from the electron beam causes local target boiling. The physics of target boiling is complex and depends on the target cell configuration, fast raster settings, target fan speed, etc. However, the bulk effect and desired correction can be deduced from the analysis of the "luminosity scan", a set of dedicated runs with increasing electron beam intensity, I^{beam}, typically from 10 µA to 100 µA, directed at LH_2 and C targets. A total of five luminosity scans, including the liquid deuteron (LD_2) target, were conducted during the run period, while two scans (A and B) with the maximum current range and with LH_2 and C data collected at the same kinematic settings were selected for the E05-017 target boiling correction analysis. All luminosity scans were taken with the HMS tuned to detect scattered electrons. For each run, the electron-normalized yield was determined by analyzing the rates, N, for several types of trigger scalers

$$Y = \frac{N}{Q(1 - c_{\text{EDT}})\epsilon_{\text{trig}}}. \tag{4.19}$$

The yield dependence on beam current was investigated with respect to the yield at the minimum value of the current for a given luminosity run. The current dependence is expected to be linear; however, small offsets in the BCM calibration as well as the events originating from the target endcaps and cosmic rays may introduce $\sim 1/I^{\text{beam}}$ terms to the dependence. The results of the luminosity scan with a solid carbon target, which is immune to the boiling effects, can be used to eliminate BCM offset contribution. So, the ratio of the LH_2 to the C target runs output provide a better estimate of the yield-current slope

$$R_{\text{boil}}(I^{\text{beam}}) = \frac{Y_{\text{LH}_2}(I^{\text{beam}})/Y_{\text{LH}_2}(I^{\text{beam}}_{\text{min}})}{Y_{\text{C}}(I^{\text{beam}})/Y_{\text{C}}(I^{\text{beam}}_{\text{min}})} \tag{4.20}$$

Parametrization of the target density dependence on the beam current is given by

$$\rho_{\text{trg}}(I^{\text{beam}}) = \rho_{\text{trg}}(0)(1 - c_{\text{boil}} I^{\text{beam}}), \tag{4.21}$$

$$c_{\text{trgB}} = \frac{\rho_{\text{trg}}(I^{\text{beam}})}{\rho_{\text{trg}}(0)} = 1 - c_{\text{boil}} I^{\text{beam}}. \tag{4.22}$$

where c_{boil} is determined from the slope parameter of the linear fit to $R_{\text{boil}}(I^{\text{beam}})$ and is, typically, quoted as a relative density change per 100 µA.

The initial dependence for each scan and target configuration along with the fitting procedure is illustrated in Fig. 4.14. The trigger signals (SCIN, PRE50, EL-REAL) used to increment the associated scaler are defined in Sec. 3.6.4. The slope

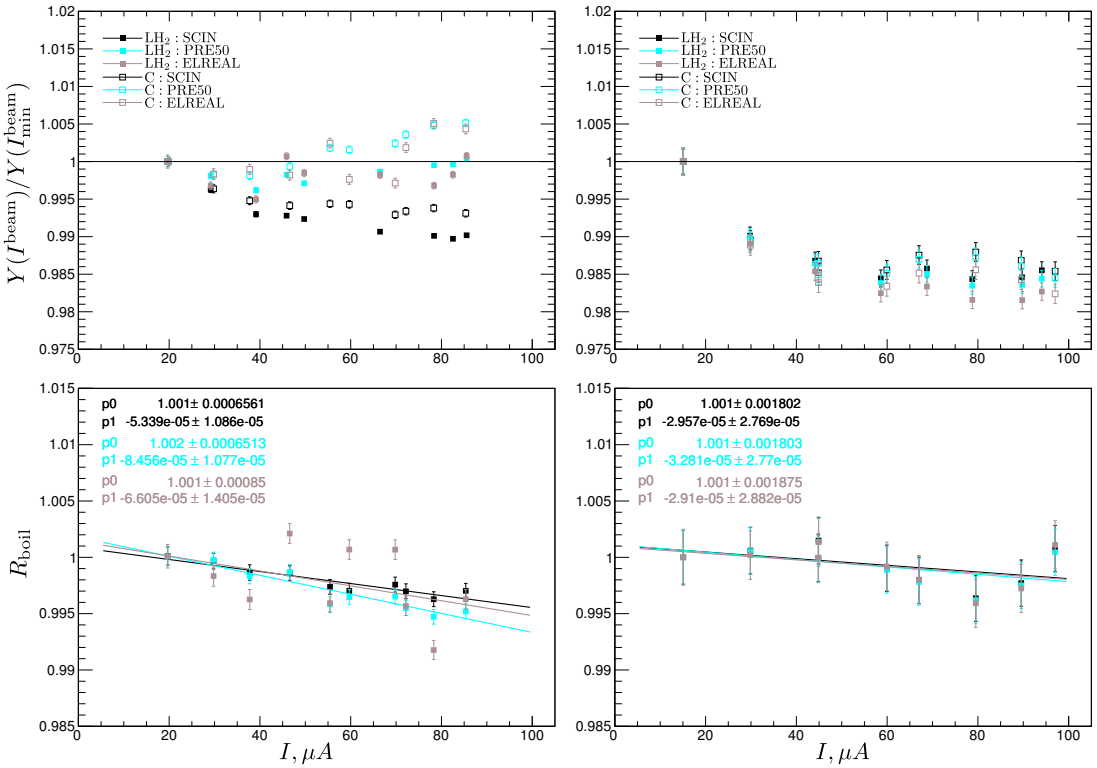

Figure 4.14: Target boiling correction studies are shown for luminosity scan A (left column) and B (right column). The top row demonstrates normalized yields as defined by Eq. 4.19 calculated with respect to the yield determined at $I^{\text{beam}}_{\text{min}}$ plotted as a function of electron beam current. Bottom row plots R_{boil} as defined by Eq. 4.20 along with corresponding linear fits. Color code represents the type of the trigger used to calculate event rate for LH_2 (solid squares) and C (hollow squares) targets.

extraction results exhibit quite significant scatter from approximately 0.3 %/100 µA to 0.85 %/100 µA. In addition, the luminosity scan B does not indicate expected linear behavior. Since, it is impossible to separate electrons scattering from the aluminum target windows in the analysis of scaler rates, the slope results are most likely underestimated. A similar analysis was performed in Ref. [60, 61], with the distinction that the yield calculation was based on the reconstructed tracks count with more restrictive software cuts, rather than hardware trigger conditions. The corresponding results of $\sim$ 1.7 %/100 µA and $\sim$ 0.2 %/100 µA were obtained for A and B luminosity scans respectively. A combined estimate, (0.9 ± 0.5) %/100 µA, of the slope for the E05-017 run period was accepted as a final result.

4.4.2 Target length

The axis of the cylindrical target cell (Fig. 3.8 of Sec. 3.4) has vertical orientation such that the target cell cross section in the horizontal plane would be given as depicted in Fig. 4.15. It is clear that if the beam position has an offset (x_{b}) from the target center in the horizontal direction ($\hat{x}_{\text{b}}$) then the effective target thickness, as seen by incoming electrons, would decrease as

$$L_{\text{eff}} = 2\sqrt{r_{\text{trg}}^2 - x_{\text{b}}^2}, \tag{4.23}$$

where r_{trg} is the internal radius of the target cell and x_{b} is beam position coordinate as measured in the beamline coordinate system.

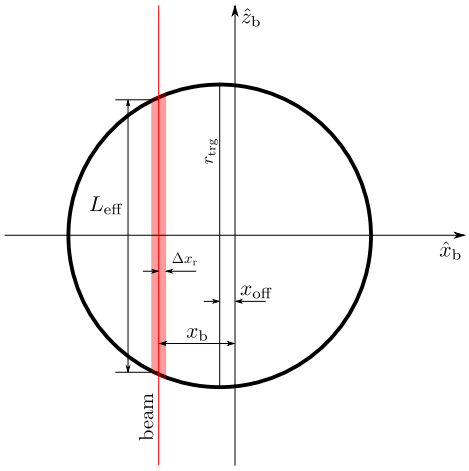

Figure 4.15: Schematic view (not to scale) of the target cell cross section in the horizontal plane. The beam path is offset from the target center by $x_{\text{b}} - x_{\text{off}}$. The raster pattern of the size $\pm\Delta x_{\text{r}}$ is indicated by the shaded area. The actual thickness as seen by the beam is given by L_{eff}.

The appropriate correction is required to account for a change in luminosity due to the beam position displacements during the run time. The correction also has to take into account the horizontal raster beam spread. The BPM electronics do not have a capability to record the beam position at the driving frequency of the raster magnet (over 20 kHz) and produces a raster averaged signal. The target length correction is given by

$$c_{\text{trgL}} = \frac{L_{\text{eff}}}{L_0} = \frac{2\int_{x_{\text{b}}-\Delta x_{\text{r}}}^{x_{\text{b}}+\Delta x_{\text{r}}} \sqrt{r_{\text{trg}}^2 - x^2}dx}{2\Delta x_{\text{r}} L_0}, \tag{4.24}$$

where $L_0 = 2r_{\text{trg}}$ is the target cell internal diameter (Table 3.3), x_{b} is the current value of the beam position, and Δx_{r} is the size of the raster in horizontal direction.

Another factor affecting displacement of the beam from the target center is the horizontal offset, x_{off}, of the target position itself. The target ladder offset is largely caused by thermal contraction when the target is filled with cryogenic liquid and by a small shift due to the vacuum chamber evacuation. A number of special runs, "position scan", measured the electron yield for several different settings of x_{b} (Ref. [60, 61]). The yield dependence on x_{b} is then fitted to a function:

$$f(x_{\text{b}}) = p_0\sqrt{p_2^2 - (x_{\text{b}} - p_1)}, \tag{4.25}$$

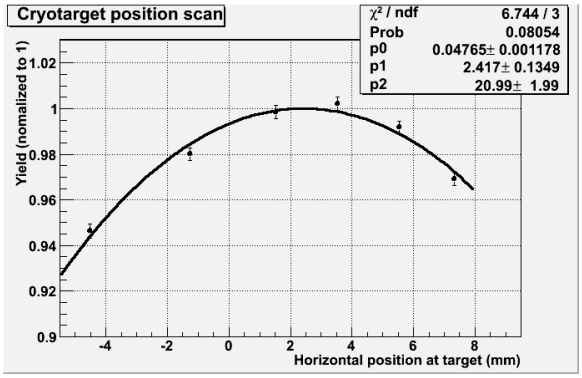

Figure 4.16: Normalized electron yield is plotted as a function of x_{b}. *Figure source: Ref.* [60, 61].

where $p_1 = x_{\mathrm{off}}$. The x_{b} was determined from BPM$_{textA}$ and BPM$_{textC}$ measurements projected on the target. Fitting results are shown in Fig. 4.16.

Once the x_{off} value is known, the beam position is locked such that the $(x_{\mathrm{b}} - x_{\mathrm{off}})$ value positions the beam at the center of the target. However, occasional drifts away from the center occur and have to be corrected for by c_{trgL}. For c_{trgL} analysis, the x_{b} at the target is calculated from BPM$_{textA}$ and BPM$_{textC}$ measurements for each EPICS event. The effective length L_{eff} is then calculated according to Eq. 4.24 by taking into account raster averaging and x_{off}. Finally, the target length correction is extracted for the effective length averaged over one run. The c_{trgL} results are presented in Fig. 4.17. For the majority of the runs, the impact of the target length correction is negligible at $< 0.02\,\%$ level, excluding a group of runs with a correction factor up to $\sim 0.05\,\%$. The c_{trgL} correction is applied as described in Eq. 4.7 on run-by-run basis.

4.4.3 Tracks with missing TOF

In the second stage of the hodoscope timing analysis (Sec. 4.2), when the tracking information is already available, the reconstruction algorithm recalculates the scintillator hit time only for the paddles that are pointed to by the projected track or for the directly adjacent ones. However, the nuclear reactions or multiple scattering processes, taking place in the first hodoscope layer or in the DC wire, may significantly deflect particle trajectory. While the deflection leads to the absence of scintillator hits (for two or more hodoscope layers) along the particle path, the SCIN trigger condition nonetheless has to be met. For events with no hits in either front or back planes, the β of the particle is assigned a value of zero.

The correction for the fraction of elastic events lost due to the missing TOF information can be calculated as $c_{\beta=0} = 1 - (N_{\beta=0}/N_{\beta!=0})$. The $\delta\theta$ distribution, analogous to the one shown in Fig. 4.1, is used to estimate the fraction for inelastic, elastic and super-elastic zones by determining the number of β=0 and β!=0 events in each zone respectively. The results are presented in Fig. 4.18 for each Q^2 and HMS central angle setting. In general, about $2\,\%$ ($2\,\%$ reference is shown by the red line) of the events have TOF information missing. The low Q^2 data are more affected by

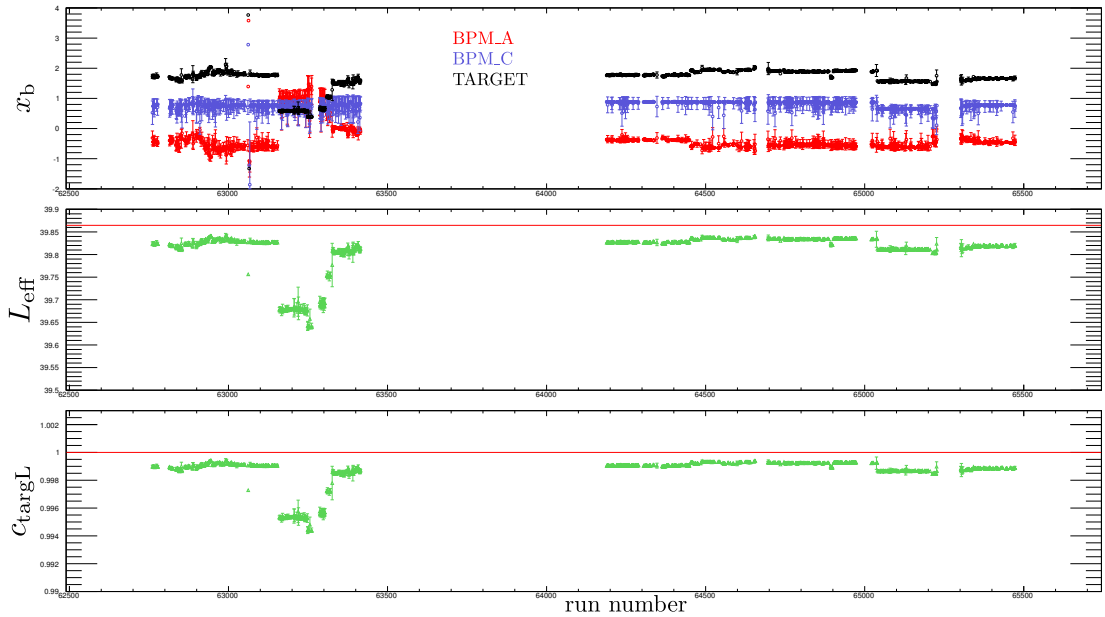

Figure 4.17: Several steps of c_{trgL} analysis procedure. The horizontal beam position (top), effective length (middle), and the target length correction (bottom) are plotted as a function of the run number. The x_b values are also run averaged for clarity. The red line in the middle plot corresponds to the inner diameter of the target cell.

multiple scattering, while the high Q^2 data are exposed to a larger background at the edges of the acceptance. Only moderate ε dependence was observed, predominantly, at the small HMS central angles.

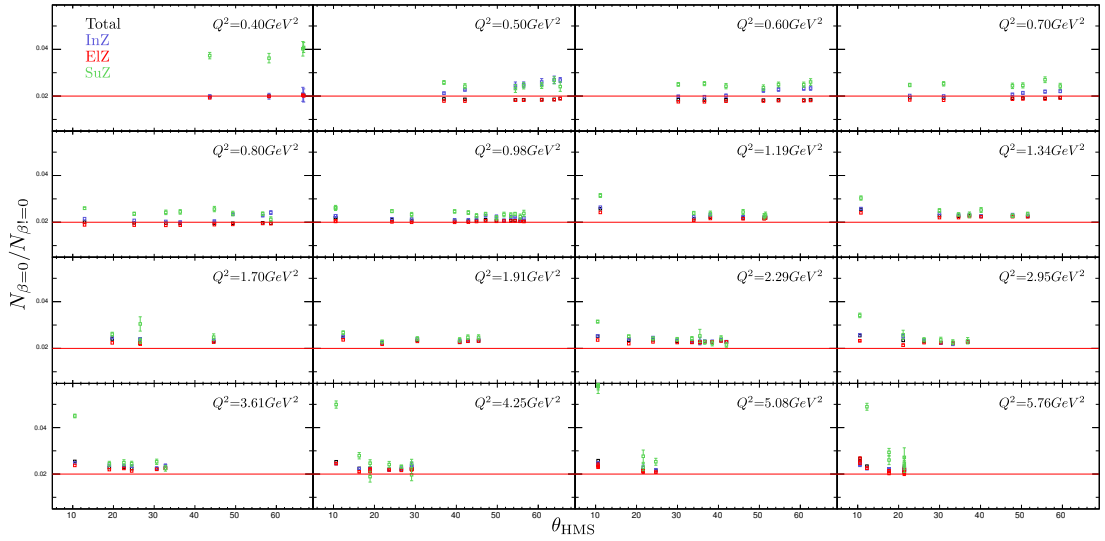

Figure 4.18: The fraction of events with missing TOF information is plotted as a function of θ_{HMS}. Each plot corresponds to a separate Q^2 setting. The fraction of the lost events is calculated for total (black) integral of $\delta\theta$ distribution as well as for events in inelastic (blue), elastic (red), and super-elastic (green) zones. The red line represents a 2 % reference point.

The most noticeable angular dependence observed at large Q^2 was primarily at-

tributed to the increased number of the background events which were not suppressed by the elastic $\delta\theta$ cut. Excluding these high Q^2 and low ε points, the ε dependence was averaged over by a zero order polynomial fit at each Q^2. The averaged values resulting from the fitting procedure were plotted as a function of the HMS central momentum p_{HMS} and piece-wise parametrized by two polynomial functions of the fourth ($p_{\text{HMS}} < 1.63\,\text{GeV}$) and the first ($p_{\text{HMS}} \geqslant 1.63\,\text{GeV}$) order accordingly. The respective dependence and fitting results are demonstrated in Fig. 4.19. The $c_{\beta=0}$ correction is calculated according to the fitting parametrization and is applied based on p_{HMS}.

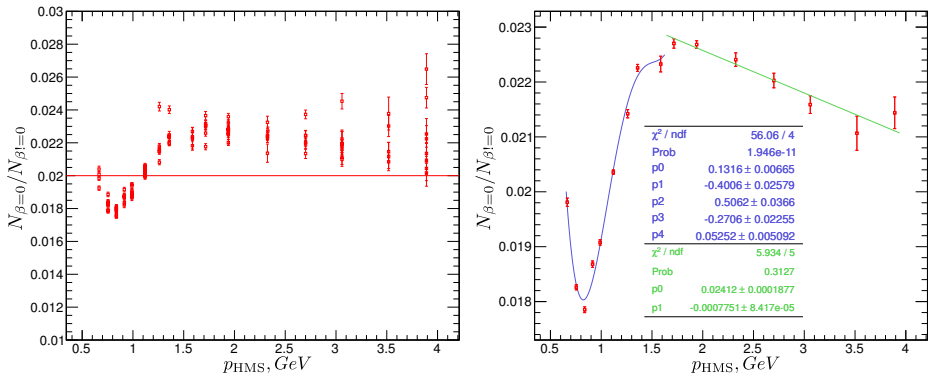

Figure 4.19: The fraction of elastic events with missing TOF information is plotted as a function of p_{HMS}. The left plot represents the combined results for each θ_{HMS} setting. The right plot shows the θ_{HMS} averaged fraction with the corresponding parametrization (see text for details).

4.4.4 Proton absorption

The proton absorption, which is not considered in the MC simulation, has to be applied as an additional correction factor in order to properly account for the scattered protons undergoing nuclear interactions along its trajectory. In order to trigger an event, the proton has to reach at least the third hodoscope plane while propagating through the material contained in the target, the spectrometer, and the detector hut.

Two approaches in the estimation of the proton absorption correction, c_{absn}, are described in Ref. [27, 62]. By including each sort of the material contributing to the absorption, the c_{absn} can be found as

$$c_{\text{absn}} = 1 - \prod_{i}^{n} e^{-X_i/\bar{\lambda}_i}, \tag{4.26}$$

where the second term is referred to as a proton transmission coefficient. It is characterized by the product of the thickness and the density of each absorber, X_i, and the effective absorption length (mean free path), $\bar{\lambda}_i$. The difference between the approaches used in Ref. [27, 62] is associated with $\bar{\lambda}_i$ treatment which is, for a single material, defined as

$$\lambda_{\rm act} = \frac{2\lambda_{\rm T}\lambda_{\rm I}}{(\lambda_{\rm T}+\lambda_{\rm I})},$$
$$\lambda_{\rm avg} = \frac{\lambda_{\rm T}+\lambda_{\rm I}}{2}. \tag{4.27}$$

The $\lambda_{\rm T}$ ($\lambda_{\rm I}$) is the mean free path between nuclear (inelastic) collisions. Two estimates (Eq. 4.27) were used since the elastic contribution to the absorption cannot be fully separated.

Material	X, [g/cm^2]	$\lambda_{\rm T}$, [g/cm^2]	$\lambda_{\rm I}$, [g/cm^2]	$X/\lambda_{\rm avg}$	$X/\lambda_{\rm act}$
LH_2 Target	1.44×10^{-1}	4.33×10^{1}	5.08×10^{1}	3.07×10^{-3}	3.09×10^{-3}
Al Target wall	3.70×10^{-2}	7.06×10^{1}	1.06×10^{2}	4.19×10^{-4}	4.36×10^{-4}
Al Chamber Window	1.10×10^{-1}	7.06×10^{1}	1.06×10^{2}	1.24×10^{-3}	1.29×10^{-3}
Air	1.82×10^{-2}	6.20×10^{1}	9.00×10^{1}	2.39×10^{-4}	2.47×10^{-4}
Kevlar Mag. Entrance	2.82×10^{-2}	7.00×10^{1}	7.00×10^{1}	4.03×10^{-4}	4.03×10^{-4}
Mylar Mag. Entrance	1.77×10^{-2}	6.25×10^{1}	8.57×10^{1}	2.38×10^{-4}	2.44×10^{-4}
Al Mag Exit	7.54×10^{-2}	7.06×10^{1}	1.06×10^{2}	8.52×10^{-4}	8.89×10^{-4}
Air	3.10×10^{-1}	6.20×10^{1}	9.00×10^{1}	4.08×10^{-3}	4.22×10^{-3}
Mylar Wire Chamber Ent.	3.53×10^{-3}	6.25×10^{1}	8.57×10^{1}	4.76×10^{-5}	4.88×10^{-5}
Sense Wires	9.46×10^{-5}	1.10×10^{2}	1.85×10^{2}	6.41×10^{-7}	6.84×10^{-7}
Field Wires	9.56×10^{-4}	6.98×10^{1}	1.08×10^{2}	1.08×10^{-5}	1.13×10^{-5}
W.C. Gas	2.77×10^{-3}	6.86×10^{1}	1.01×10^{2}	3.26×10^{-5}	3.39×10^{-5}
Mylar W.C. Exit	3.53×10^{-3}	6.25×10^{1}	8.57×10^{1}	4.76×10^{-5}	4.88×10^{-5}
Al Aerogel Ent.	4.05×10^{-1}	7.06×10^{1}	1.06×10^{2}	4.58×10^{-3}	4.77×10^{-3}
Aerogel	6.43×10^{-1}	6.55×10^{1}	9.57×10^{1}	7.97×10^{-3}	8.26×10^{-3}
Al Aerogel Exit	2.70×10^{-1}	7.06×10^{1}	1.06×10^{2}	3.05×10^{-3}	3.18×10^{-3}
Polystyrene Scintilators	2.20×10^{0}	5.84×10^{1}	8.20×10^{1}	3.13×10^{-2}	3.22×10^{-2}
Al Cherenkov Ent.	2.74×10^{-1}	7.06×10^{1}	1.06×10^{2}	3.10×10^{-3}	3.23×10^{-3}
Cherenkov Mirror Support	1.00×10^{-1}	7.00×10^{1}	7.00×10^{1}	1.43×10^{-3}	1.43×10^{-3}
$SiO_2$2 Cherenkov Mirror	6.60×10^{-1}	6.52×10^{1}	9.78×10^{1}	8.10×10^{-3}	8.44×10^{-3}
Al Cherenkov Exit	2.74×10^{-1}	7.06×10^{1}	1.06×10^{2}	3.10×10^{-3}	3.23×10^{-3}
Polystyrene Scintilators	2.75×10^{-1}	5.84×10^{1}	8.20×10^{1}	3.91×10^{-3}	4.03×10^{-3}
Sum				7.72×10^{-2}	7.98×10^{-2}
Transmission				9.26×10^{-1}	9.23×10^{-1}
Absorption				7.40×10^{-2}	7.70×10^{-2}

Table 4.1: The proton absorber characteristics. *Table source: Ref.* [62].

Table 4.1 lists the proton absorbers' properties which are relevant to the configuration of this experiment.

4.5 Particle identification

One of the major steps in selecting elastically scattered protons is the separation of the protons of interest from other positively charged particles, such as deuterons (d), tritons (t) and pions (π^+), entering the spectrometer. Several types of measurements done during the E05-017 run possess the necessary discriminating properties

required for particle identification (PID). The primary PID was provided by the particle's time-of-flight (TOF) measured between the scintillator planes of the hodoscope. In addition, the energy deposited in the first hodoscope plane, dE/dx, and the number of photo-electrons, $N_{\rm pe}^{\rm aero}$, produced in the aerogel Cherenkov's PMTs can be used to further clean up the proton sample.

The reconstruction software package was configured to output particle velocity, β, as a result of TOF measurements. However, in the final analysis the actual time expressed in nanoseconds was used as the corresponding TOF spectra had more consistent peak widths for different particle types and as a function of Q^2. The resulting TOF spectrum was calculated and analyzed as

$$TOF = \frac{k}{\beta} \quad \text{and} \quad k = \frac{L}{c}\sqrt{1 + (x'_{\rm fp})^2 + (y'_{\rm fp})^2}, \tag{4.28}$$

$$\delta_{\rm TOF} = TOF - k\sqrt{1 + (M_{\rm p}/P_{\rm meas})^2}, \tag{4.29}$$

where $L = 220.99\,{\rm cm}$ is the distance between the hodoscope planes, c is the speed of light in ${\rm cm\,ns^{-1}}$, $x'_{\rm fp}(y'_{\rm fp})$ is the out(in)-plane angle of the track and $P_{\rm meas}$ is the measured momentum of the track. Thus, $\delta_{\rm TOF}$ represents the difference between the measured TOF and the TOF which would be obtained for a proton of a given momentum. The example of the typical $\delta_{\rm TOF}$ distribution is shown in Fig. 4.20 for two Q^2 with protons forming a peak around zero while faster (slower) moving π^+ (d, t) appearing at the left (right) side of the spectrum. The characteristic TOF shape of individual peaks arises from several factors, such as a slightly different orientation of the tracks with respect to the hodoscope plane, energy losses and multiple scattering, which produce a long tail on one side and a rapidly falling edge on the other.

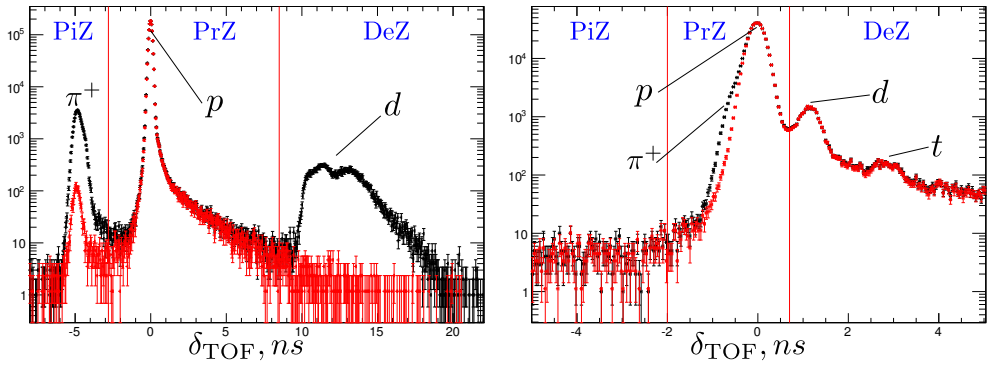

Figure 4.20: The $\delta_{\rm TOF}$ (defined in Eq. 4.29) distribution for $Q^2 = 0.50\,{\rm GeV^2}$ (left) and $Q^2 = 3.61\,{\rm GeV^2}$ (right): $\delta_{\rm TOF}$ full (black); $\delta_{\rm TOF}$ with d (left) and π^+ (right) suppressed (red). The vertical red lines represent the corresponding $\delta_{\rm TOF}$ proton cut.

The evaluation of the PID efficiency requires a determination of the reliable TOF lineshape for each particle type which has to be obtained from the data. In general, the lineshape depends on kinematic settings ε and Q^2. In the case of the proton, the ε-dependence is expected to be small since at a fixed Q^2 proton momentum

remains constant and corresponding TOF distributions should be the same at different angles. This small, but not negligible, ε dependence is due to the fact that the size of the background at very forward and backward angles varies significantly. The Q^2 dependence manifests itself in weakly changing widths and tail-to-peak ratios of δ_{TOF} spectra. The most visible aspect of the Q^2 dependence is the shrinking timing offsets between the peaks as Q^2 increases which is evident in Fig. 4.20. The highly asymmetric form of the TOF distribution and drastically different source and shape of the background on both sides of the proton peak demanded a separate evaluation of the efficiency on the left (right) π^+ (d, t) side. Respectively, the δ_{TOF} proton cut splits the distribution into three zones: the π^+ zone, the proton zone, and the deuteron zone. The deuteron zone should be understood as a combined deuteron and triton contribution. The correction that is required for the number of events within the proton zone is given by

$$\epsilon_{\mathrm{PID}} = \frac{(1-\epsilon^{\mathrm{L}}_{\mathrm{TOF}})(1-\epsilon^{\mathrm{R}}_{\mathrm{TOF}})}{(1-c_{\pi^+})(1-c_d)} \tag{4.30}$$

where $\epsilon^{\mathrm{L}}_{\mathrm{TOF}}$ ($\epsilon^{\mathrm{R}}_{\mathrm{TOF}}$) is the π^+ (d) side proton TOF cut inefficiency and c_{π^+} (c_d) is the charged pion (deuteron) contamination. The $\epsilon^{\mathrm{L}}_{\mathrm{TOF}}$ ($\epsilon^{\mathrm{R}}_{\mathrm{TOF}}$) represents the fraction of the total proton count loss due to the TOF cut on the left (right) side of the proton peak. The charged pion (deuteron) contamination defines the fraction of events, with respect to the proton peak, leaking into the proton zone from corresponding peak tails on the left (right). While the full δ_{TOF} distribution (black line in Fig. 4.20) is integrated for the cross section extraction, the $\epsilon^{\mathrm{L}}_{\mathrm{TOF}}$, $\epsilon^{\mathrm{R}}_{\mathrm{TOF}}$, c_{π^+}, c_d are evaluated by using the lineshape ($\delta^{\mathrm{prot}}_{\mathrm{TOF}}$, $\delta^{\mathrm{pipl}}_{\mathrm{TOF}}$, $\delta^{\mathrm{deut}}_{\mathrm{TOF}}$) of the relevant particle as follows

$$\epsilon^{\mathrm{L}}_{\mathrm{TOF}} = \frac{N^{\mathrm{PiZ}}_{\mathrm{prot}}(\delta^{\mathrm{prot}}_{\mathrm{TOF}})}{N^{\mathrm{PrZ}}_{\mathrm{prot}}(\delta^{\mathrm{prot}}_{\mathrm{TOF}})}, \quad \epsilon^{\mathrm{R}}_{\mathrm{TOF}} = \frac{N^{\mathrm{DeZ}}_{\mathrm{prot}}(\delta^{\mathrm{prot}}_{\mathrm{TOF}})}{N^{\mathrm{PrZ}}_{\mathrm{prot}}(\delta^{\mathrm{prot}}_{\mathrm{TOF}})}, \tag{4.31}$$

$$c_{\pi^+} = \frac{N^{\mathrm{PrZ}}_{\mathrm{pipl}}(\delta^{\mathrm{pipl}}_{\mathrm{TOF}})}{N^{\mathrm{PrZ}}_{\mathrm{prot}}(\delta^{\mathrm{full}}_{\mathrm{TOF}})}, \quad c_d = \frac{N^{\mathrm{PrZ}}_{\mathrm{deut}}(\delta^{\mathrm{deut}}_{\mathrm{TOF}})}{N^{\mathrm{PrZ}}_{\mathrm{prot}}(\delta^{\mathrm{full}}_{\mathrm{TOF}})}, \tag{4.32}$$

where $N^{\mathrm{PrZ}}_{\mathrm{prot}}$ ($N^{\mathrm{PiZ}}_{\mathrm{prot}}$, $N^{\mathrm{DeZ}}_{\mathrm{prot}}$) is the number of protons in the proton (π^+, d) zone and $N^{\mathrm{PrZ}}_{\mathrm{pipl}}$ ($N^{\mathrm{PrZ}}_{\mathrm{deut}}$) is the number of charged pions (deuterons) in the proton zone. The corresponding lineshapes ($\delta^{\mathrm{prot}}_{\mathrm{TOF}}$, $\delta^{\mathrm{pipl}}_{\mathrm{TOF}}$, $\delta^{\mathrm{deut}}_{\mathrm{TOF}}$) were obtained by applying certain sets of "profile" cuts (dE/dx, $N^{\mathrm{aero}}_{\mathrm{pe}}$, target vertex, elastic) to provide a clean p, π^+, d samples and were investigated under various scenarios to check reproducibility and to estimate associated systematic uncertainty. The true lineshape was assumed to be independent of these cuts.

The purpose of the PID studies was to estimate the efficiency of the δ_{TOF} proton cut, shown in Fig. 4.20 by two vertical lines, as well as to calculate the amount of π^+, d and t contamination in the proton sample. In addition, these studies allowed

the optimization of the δ_{TOF} cut such that the compromise between the minimum inefficiency and the minimum contamination was found. It should be noted that, since the minimization of overall uncertainties is the priority of this experiment, the profile cuts implemented to obtain clean lineshapes were not used in the main analysis since they would introduce systematic uncertainty that would be hard to estimate.

4.5.1 Proton TOF cut inefficiency

The main challenge of extracting a clean proton TOF lineshape is the identification of profile cuts that would be appropriate to suppress the background (deuterons or charged pions) at a given Q^2. Since the profile cut efficiency changes depending on the type of the background and kinematic setting, besides separately treating $\epsilon^{\mathrm{L}}_{\mathrm{TOF}}$ and $\epsilon^{\mathrm{R}}_{\mathrm{TOF}}$, it was necessary to apply different sets of profile cuts at different Q^2 values. Once the proper set of profile cuts was determined the corresponding inefficiency was calculated according to Eq. 4.31. In several instances where the profile cuts were not able to completely remove the background events, the corresponding tail of the proton lineshape was approximated by the exponential fit performed on the sidebands around the background peak. The stability of the resulting clean proton sample shape was tested under several scenarios. The summary of the final profile cuts used in the analysis is presented in Table 4.2 and Table 4.3.

Zone	Q^2, [GeV^2]	Profile cut	N_{prot} estimation method
PiZ	0.40-1.34	AERO+DEDX+ELAS$^{\mathrm{h}}$	histogram integral + sideband fit
	1.70-5.76		histogram integral
DeZ	0.40-4.25	AERO+DEDX	histogram integral
	5.08-5.76	AERO+DEDX+ZTAR	

Table 4.2: Combination of profile cuts used to define the clean proton lineshape in the charged pion and deuteron zones.

The "AERO" cut, or $N^{\mathrm{aero}}_{\mathrm{pe}} = 0$, signifies no signal in aerogel Cherenkov condition specific to protons, deuterons, and tritons and is used to suppress fast moving π^+s. However, at low Q^2 the momentum of the charged pions was insufficient to pass the threshold condition (Eq. 3.3) so the $N^{\mathrm{aero}}_{\mathrm{pe}}$ cut only partially eliminated π^+ background. For this Q^2 range (see Table 4.2), the residual background peak in the π^+ zone had to be replaced by the sideband fit before $N^{\mathrm{PiZ}}_{\mathrm{prot}}$ can be estimated. Although the AERO cut has no effect on deuteron removal, it was also used for calculation of $\epsilon^{\mathrm{R}}_{\mathrm{TOF}}$ to restrict the amount of π^+ contributing to $N^{\mathrm{PrZ}}_{\mathrm{prot}}$.

The track's energy deposition in the scintillator, dE/dx, exhibit excellent properties as a particle signature, especially at low Q^2. The dE/dx is presented by the geometric average of the ADC signals detected by PMTs on both ends of the scintillator strip. The corresponding "DEDX" cut was efficient in rejecting the majority of deuterons (charged pions) up to $Q^2 \approx 4.25\,\mathrm{GeV}^2$ ($Q^2 \approx 2.29\,\mathrm{GeV}^2$). Above $Q^2 \approx 5.00\,\mathrm{GeV}^2$ the proton dE/dx distribution become almost indistinguish-

Q^2, [GeV^2]	AERO, [p.e.]	DEDX, [ADC]	ELAS$^{\mathrm{h}}$	ZTAR, [cm]
0.40		410< dE/dx <560		
0.50		340< dE/dx <530		
0.60		310< dE/dx <480		
0.70		280< dE/dx <455		
0.80		270< dE/dx <430		
0.98		265< dE/dx <380		
1.19		245< dE/dx <350		
1.34	$-0.1< N_{\mathrm{pe}}^{\mathrm{aero}} <0.1$	230< dE/dx <310	$\left\|\delta\theta^{\mathrm{el}} - \delta\theta_{\mathrm{m}}^{\mathrm{el}}\right\| < 3\sigma$	$\left\|z^{\mathrm{trg}} - z_{\mathrm{m}}^{\mathrm{trg}}\right\| <1.3$
1.70		220< dE/dx <270		
1.91		200< dE/dx <255		
2.29		200< dE/dx <230		
2.95		175< dE/dx <215		
3.61		170< dE/dx <205		
4.25		165< dE/dx <200		
5.08		160< dE/dx <220		
5.76		160< dE/dx <220		

Table 4.3: Definition of profile cuts of Table 4.2 ($\delta\theta^{\mathrm{el}} = \delta\theta^{\mathrm{el}}(Q^2, \varepsilon)$, $z^{\mathrm{trg}} = z^{\mathrm{trg}}(Q^2, \varepsilon)$).

able from the background energy deposition. The DEDX cut was used in conjunction with the AERO cut to define the proton lineshape on both sides of the proton peak.

Two additional cuts, "ELAS$^{\mathrm{h}}$" and "ZTAR", were used to further suppress the background in the kinematic range where AERO and DEDX cuts were insufficient. The ELAS$^{\mathrm{h}}$, hard elastic cut, was defined as $\pm 3\sigma$ region around the mean position of elastic peak in $\delta\theta$ distribution. The ELAS$^{\mathrm{h}}$ should be distinguished from the elastic cut used for cross section extraction. The purpose of this cut is to maximally reduce the number of inelastic and superelastic events contributing to the TOF spectrum while maintaining high statistic for elastic protons. The charged pions and deuterons are fairly evenly distributed across the $\delta\theta$ histogram and fully extend under elastic peak so the efficiency of ELAS$^{\mathrm{h}}$ is limited. Similarly, the target vertex cut, "ZTAR" can be used to remove events coming from the target cell's aluminum windows. The z coordinate of the track vertex in the lab frame itself is defined through the target system vertex coordinate, y_{trg}, as $z = y_{\mathrm{trg}}/\sin(\theta)$. As a compromise between preserving elastic statistics and the necessity of moving away from the target endcaps, the central region of target with a length of 2.6 cm were chosen as a ZTAR cut. Deuterons cannot be produced in an ep scattering reaction and, thus, can only originate from the electron scattering from the aluminum of the target window. Therefore, ZTAR is mostly effective for the removal of deuterons. Since π^+ are produced in both aluminum and hydrogen, the cost of statistics reduction outweighs the benefits of using ZTAR for charged pion suppression.

Separation of the particles with cuts discussed above is shown in Fig. 4.21 for two Q^2. The left column shows the logarithm of $N_{\mathrm{pe}}^{\mathrm{aero}}$ plotted versus energy deposition, dE/dx. A small offset was added to $N_{\mathrm{pe}}^{\mathrm{aero}}$ to clearly indicate the number of events at $N_{\mathrm{pe}}^{\mathrm{aero}} = 0$, which corresponds to ~ -4 on the logarithmic scale. The majority of protons and deuterons have $N_{\mathrm{pe}}^{\mathrm{aero}} = 0$ with a small non-zero tail. At $Q^2 =$

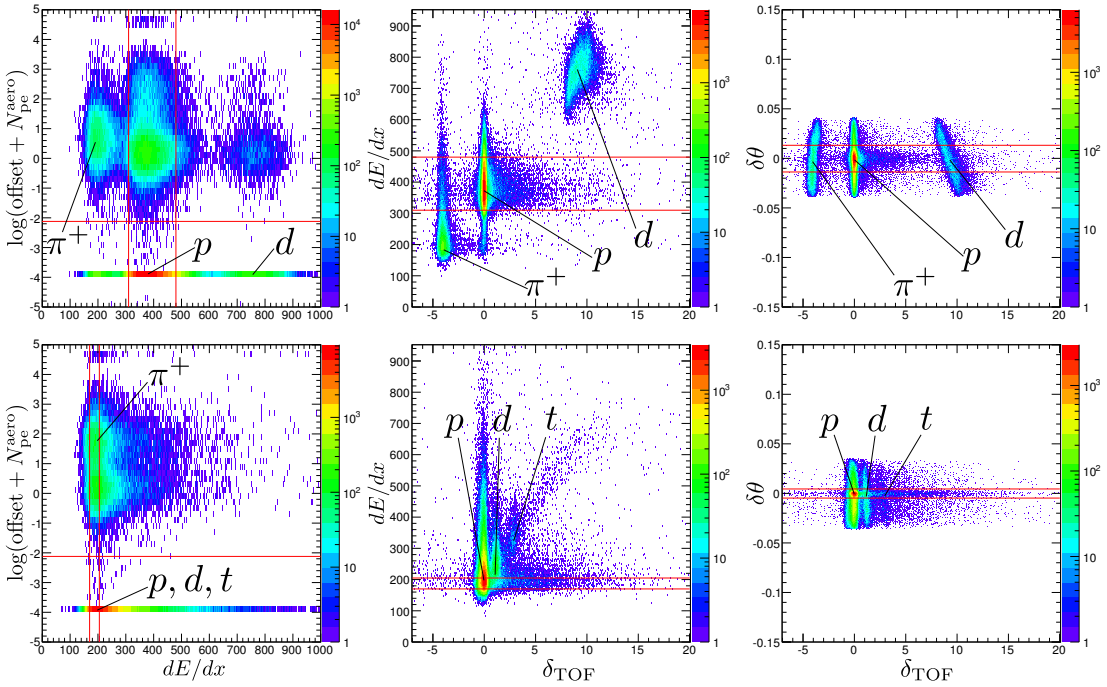

Figure 4.21: Profile cuts performance is shown for $Q^2 = 0.60\,\mathrm{GeV}^2$, $\theta_{\mathrm{HMS}} = 50.98°$ (top) and $Q^2 = 3.61\,\mathrm{GeV}^2$, $\theta_{\mathrm{HMS}} = 32.76°$ (bottom). DEDX (vertical red) and the upper boundary (horizontal red) of the AERO cut are shown in the left column. DEDX (ELAS$^{\mathrm{h}}$) cut is shown in the middle (right) column.

$0.60\,\mathrm{GeV}^2$, only $\sim 50\,\%$ of π^+ generated a signal in the aerogel Cherenkov which indicates that detector efficiency was limited for these kinematics. The π^+ contamination studies showed that π^+ aerogel detection efficiency significantly improves as Q^2 increases. Contrary to this behavior, dE/dx separation ability decreased with increased Q^2. The middle column of Fig. 4.21 demonstrates the dE/dx correlation with δ_{TOF}. At $Q^2 = 3.61\,\mathrm{GeV}^2$, the DEDX cut partially eliminates deuterons while π^+'s values of dE/dx are almost identical to those of the proton. Finally, the last column plots $\delta\theta$ as a function of δ_{TOF} and illustrates the amount of the background removed by the ELAS$^{\mathrm{h}}$ cut.

An example of the proton shape obtained with profile cuts is given in Fig 4.22. The left plot depicts the full unsuppressed δ_{TOF} spectrum for several θ_{HMS} settings at the same Q^2 normalized such that the $\pm 3\sigma$ integral of the proton peak is the same for all distributions. It has to be noted that at a fixed Q^2 the size of the background peaks is ε dependent. This trend is particularly pronounced in case of the π^+ contribution with the number of charged pion events decreasing as the spectrometer angle decreases (see Fig 4.22 left). For the clean proton lineshape, shown on the right, the ε dependence is mostly removed. However, a certain mismatch remains in the tail's contour at $\delta_{\mathrm{TOF}} < -2\,\mathrm{ns}$ and $\delta_{\mathrm{TOF}} > 4\,\mathrm{ns}$, specifically, notable for small spectrometer angles $\theta_{\mathrm{HMS}} = 12.36°$ and $\theta_{\mathrm{HMS}} = 21.87°$.

Using the clean proton spectra shown in Fig. 4.22 (right), the proton TOF cut inefficiency was calculated for each kinematic setting according to Eq. 4.31. The

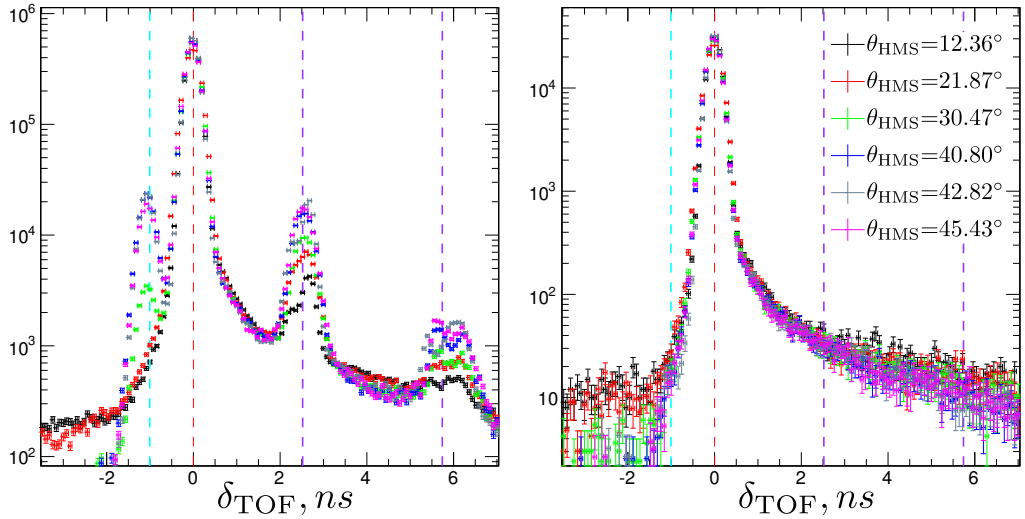

Figure 4.22: Normalized (at the proton peak) δ_{TOF} distribution is shown for several ε settings at $Q^2 = 1.91\,\mathrm{GeV}^2$: full (left), clean proton lineshape (right) obtained with AERO, DEDX, ELAS$^{\mathrm{h}}$ cuts. Dashed colored lines indicate expected positions, from left to right, of π^+, proton, deuteron, and triton peaks. Positions are calculated based on P_{meas} and the corresponding mass of the particle.

final inefficiency was obtained for a set of cuts discussed in Sec. 4.5.4.

4.5.2 Charged pion contamination

The placement of the exemplary TOF cuts in Fig. 4.20 shows that the tails of both charged pion and deuteron peaks can contribute to the number of counts in the proton zone. The evaluation of this contribution is complicated by a strong Q^2 dependence of the lineshape extraction, i.e. peaks move closer together and eventually merge as Q^2 increases, and by a limited background statistics for certain kinematics, in which case the background tails are poorly defined and are hard to measure. The following strategy was used to overcome these difficulties:

(a) extract π^+ lineshape by performing the subtraction $\delta^{\mathrm{pipl}}_{\mathrm{TOF}} = \delta^{\mathrm{full}}_{\mathrm{TOF}} - \delta^{\mathrm{prot}}_{\mathrm{TOF}}$ (where $\delta^{\mathrm{pipl}}_{\mathrm{TOF}}$ is the clean positively charged pion distribution) with the clean proton $\delta^{\mathrm{prot}}_{\mathrm{TOF}}$ normalized to match proton peak integral in $\delta^{\mathrm{full}}_{\mathrm{TOF}}$ distribution;

(b) use π^+ lineshape to estimate the total number of π^+ events, $N^{\mathrm{Tot}}_{\mathrm{pipl}}$;

(c) estimate $N^{\mathrm{PrZ}}_{\mathrm{pipl}}$ (Eq. 4.32) as the fraction that end up in the proton zone of the total number of π^+ events.

In order to address item (a), the proton shape was estimated similarly to the procedure discussed in Sec. 4.5.1. However, in this case care should be taken to preserve high statistics in the clean δ_{TOF} distribution. Overly aggressive profile cuts may remove a large fraction of the protons resulting in a high scaling factor when matching $\delta^{\mathrm{full}}_{\mathrm{TOF}}$ and $\delta^{\mathrm{prot}}_{\mathrm{TOF}}$ spectra. So, even the small distortion of the rapidly falling

Zone	Q^2, [GeV^2]	Profile cut
PiZ	0.40-1.34	AERO+DEDX+ELAS^h
	1.70-5.76	AERO

Table 4.4: Combination of profile cuts used to define clean proton lineshape for π^+ contamination studies.

proton edge will significantly impact the extracted $\delta^{\text{pipl}}_{\text{TOF}}$ shape and charged pion count. The definitions of the profile cuts used are given in Table 4.4.

The example of the normalized $\delta^{\text{prot}}_{\text{TOF}}$ spectrum that corresponds to the cuts from Table 4.4 is shown by the red symbols in Fig. 4.20. The results of the respective subtraction procedure is given in Fig. 4.23. The $N^{\text{Tot}}_{\text{pipl}}$ was determined by integrating a Gaussian fit (Fig. 4.23 red line) to the $\delta^{\text{pipl}}_{\text{TOF}}$ distribution in the $\pm 5\sigma$ range (item (b)). For the small π^+ count kinematics with no visible π^+ peak, the histogram integral was estimated instead in the $\sim \pm 5\sigma$ region around the expected, for this Q^2, charged pion peak position.

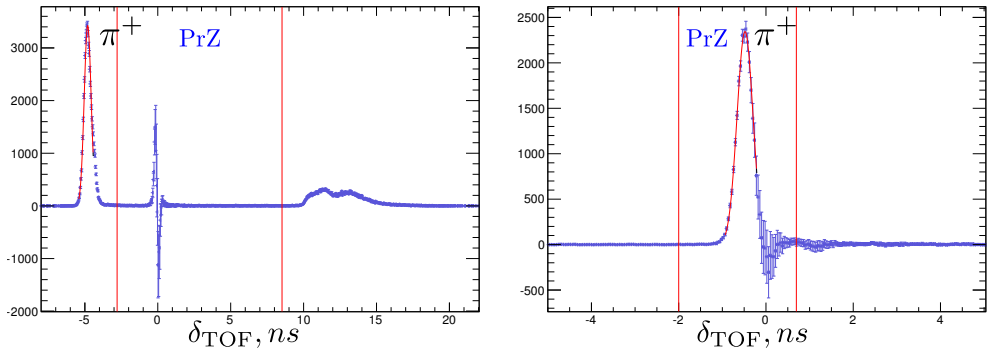

Figure 4.23: The $\delta^{\text{pipl}}_{\text{TOF}} = \delta^{\text{full}}_{\text{TOF}} - \delta^{\text{prot}}_{\text{TOF}}$ distribution (subtraction of the spectrum shown by red symbols from distribution indicated by black symbols in Fig. 4.20) for $Q^2 = 0.50\,\text{GeV}^2$ (left) and $Q^2 = 3.61\,\text{GeV}^2$ (right): $\delta^{\text{pipl}}_{\text{TOF}}$ spectrum (blue); gaussian fit to $\delta^{\text{pipl}}_{\text{TOF}}$ (red).

As clearly seen in Fig. 4.20 (left red symbols), there is a residual π^+ peak remaining in the $\delta^{\text{prot}}_{\text{TOF}}$ distribution due to unsatisfactory performance of the AERO cut resulting in π^+ over-subtraction. Therefore, the $N^{\text{Tot}}_{\text{pipl}}$ had to be corrected to properly account for the total number of charged pions. As the visible residual peaks were observed up to $Q^2 = 1.91\,\text{GeV}^2$, the correction of the form

$$f^{\text{corr}}_{\text{aero}} = \frac{N^{\text{PiZ}}_{\text{pipl}}(\delta^{\text{pipl}}_{\text{TOF}})}{N^{\text{PiZ}}_{\text{pipl}}(\delta^{\text{full}}_{\text{TOF}})}, \tag{4.33}$$

with $N^{\text{PiZ}}_{\text{pipl}}$ given by the Gaussian fit integral, was applied to $N^{\text{Tot}}_{\text{pipl}}$ for the low-to-middle Q^2 span.

Prior to the procedure of PID optimization, initial estimates of the π^+ contamination were performed by applying the TOF cut such that the main portion of the π^+ peak would be outside of the cut region (Fig. 4.23 left). Then, the true π^+

contamination is given by expression 4.32, where $N_{\rm pipl}^{\rm PrZ}$ is the tail fraction of $N_{\rm pipl}^{\rm Tot}$ that is leaking into the proton zone. As mentioned above, the direct evaluation of $N_{\rm pipl}^{\rm PrZ}$ from the $\delta_{\rm TOF}^{\rm pipl}$ distribution is often problematic since even small imperfections of the proton TOF shape lead to significant fluctuations, specifically in the tail region (Fig. 4.23 at $0.2< \delta_{\rm TOF} <-0.2$ ns). An alternative calculation of the tail fraction can be made by making the relatively presumptive assumption that the π^+ lineshape can be modeled after that of the proton. The π^+ shape is most distorted and is visibly wider, Fig. 4.20 (left black), at small Q^2, in large part, due to the variation with particle momentum (or θ) which can be seen in the upper right plot of Fig. 4.21. Fortunately, at these settings peaks are well separated, contamination is minimal and a more conservative estimate of the tail fraction was made. As Q^2 increases the widths of the peaks become more consistent (Fig. 4.22 left) and can be safely approximated by the proton lineshape. The proton model-lineshape is defined in Table 4.2. Taking into account the assumption discussed above, the charged pion contamination can be estimated as

$$c_{\pi^+} = \frac{N_{\rm pipl}^{\rm PrZ}(\delta_{\rm TOF}^{\rm pipl})}{N_{\rm prot}^{\rm PrZ}(\delta_{\rm TOF}^{\rm full})} \approx \frac{1}{N_{\rm prot}^{\rm PrZ}(\delta_{\rm TOF}^{\rm full})} \left(\frac{N_{\rm pipl}^{\rm Tot}}{1 - f_{\rm aero}^{\rm corr}} \right) f_{\rm tail} f_{\rm elas}, \tag{4.34}$$

where $f_{\rm tail}$ is the $\delta_{\rm TOF}^{\rm pipl}$ tail fraction and $f_{\rm elas}$ is the fraction of π^+ events in the proton zone removed by the final elastic cut. By using the proton lineshape as a model for π^+ distribution, the $f_{\rm tail}$ is calculated as

$$f_{\rm tail} = \frac{N_{\rm model}^{\rm tail}}{N_{\rm model}^{\rm main}}, \tag{4.35}$$

where $N_{\rm model}^{\rm tail}$ and $N_{\rm model}^{\rm main}$ are the number of events in the tail and the main peak of the model distribution respectively. The distance between the center of the π^+ peak and position of the corresponding TOF cut has to be calculated to find the beginning of the tail zone for the model spectrum. It includes conservative estimates for the π^+ peak momentum dependence which effectively moves the TOF cut closer to the center of the peak. The number of events in the tail is computed as a histogram integral while the number of events in the main peak is evaluated precisely as in the case of $N_{\rm pipl}^{\rm Tot}$ ($\pm 5\sigma$ integral of the Gaussian fit).

Reduction of the π^+ contamination by the elastic cut can be evaluated if the relevant $\delta\theta$ distribution for charged pions can be reconstructed from data. It was found that it is reliably approximated by the $\delta\theta$ spectrum measured for the aluminum (dummy) target. The $f_{\rm elas}$ is then given as

$$f_{\rm elas} = \frac{N_{\rm alum}^{\rm elastic}}{N_{\rm alum}^{\rm total}}, \tag{4.36}$$

where $N_{\rm alum}^{\rm elastic}$ is the number of events within the elastic window and $N_{\rm alum}^{\rm total}$ is the total number of events.

4.5.3 Deuteron contamination

The same general steps were taken to calculate deuteron contamination impact but there are several important distinctions in comparison with c_{π^+} estimates. A different set of profile cuts defines the proton lineshape for the subtraction procedure which is shown in Table 4.5. The ELAS$^{\text{s}}$ (soft) cut is the relaxed version of the ELAS$^{\text{h}}$ (hard) for the purpose of preserving proton statistics.

Zone	Q^2, [GeV^2]	Profile cut
DeZ	0.40-4.25	DEDX
	5.08-5.76	DEDX+ELAS$^{\text{s}}$

Table 4.5: Combination of profile cuts used to define clean proton lineshape for deuteron contamination studies.

As previously discussed, the deuterons are solely produced inside the target window material, so the primary difference with charged pion contamination arises from the fact that deuteron contamination is almost completely eliminated during the dummy target subtraction process. Clean $\delta^{\text{deut}}_{\text{TOF}}$ distributions normalized by accumulated effective charge were obtained from LH_2 and dummy target data following procedures outlined in previous section. To calculate the amount of residual deuterons the dummy (aluminum) $\delta^{\text{deut}}_{\text{TOF}}$ spectrum was subtracted from $\delta^{\text{deut}}_{\text{TOF}}$ for liquid hydrogen as

$$\begin{aligned}
\delta^{\text{deut}}_{\text{TOF}}(\text{lhyd}) &= \delta^{\text{full}}_{\text{TOF}}(\text{lhyd}) - \delta^{\text{prot}}_{\text{TOF}}(\text{lhyd}),\\
\delta^{\text{deut}}_{\text{TOF}}(\text{alum}) &= \delta^{\text{full}}_{\text{TOF}}(\text{alum}) - \delta^{\text{prot}}_{\text{TOF}}(\text{alum}),\\
\delta^{\text{deut}}_{\text{TOF}}(\text{residual}) &= \delta^{\text{deut}}_{\text{TOF}}(\text{lhyd}) - k\delta^{\text{deut}}_{\text{TOF}}(\text{alum}),
\end{aligned} \tag{4.37}$$

where k is the dummy subtraction scaling coefficient discussed in Section 4.8.

The main stages of this procedure are depicted in Fig. 4.24. The total number of deuteron events, $N^{\text{Tot}}_{\text{deut}}$, was estimated based on the clean deuteron spectrum (Fig. 4.24 right, magenta) as a histogram integral around $\sim \pm 5\sigma$ of the deuteron peak (Fig. 4.24 left, solid vertical lines).

In addition to the excellent deuteron suppression by the dummy subtraction procedure, the left edge (smaller δ_{TOF} values) of the deuteron peak is expected to fall sharply, similar to the behavior of the proton peak. Therefore, in contrast to the π^+ contamination, the deuteron tail contributes less to the counts in the proton zone. So, if the TOF cut falls in the region below the left boundary of the deuteron region, the deuteron contamination was considered to be essentially zero ($f_{\text{tail}} = 0$). The residual distribution (Fig. 4.24 right, gray) was used to calculate the final deuteron contamination according to

$$c_d = \frac{N^{\text{PrZ}}_{\text{deut}}(\delta^{\text{deut}}_{\text{TOF}})}{N^{\text{PrZ}}_{\text{prot}}(\delta^{\text{full}}_{\text{TOF}})} \approx \frac{1}{N^{\text{PrZ}}_{\text{prot}}(\delta^{\text{full}}_{\text{TOF}})} N^{\text{Tot}}_{\text{deut}} f_{\text{tail}} f_{\text{elas}}. \tag{4.38}$$

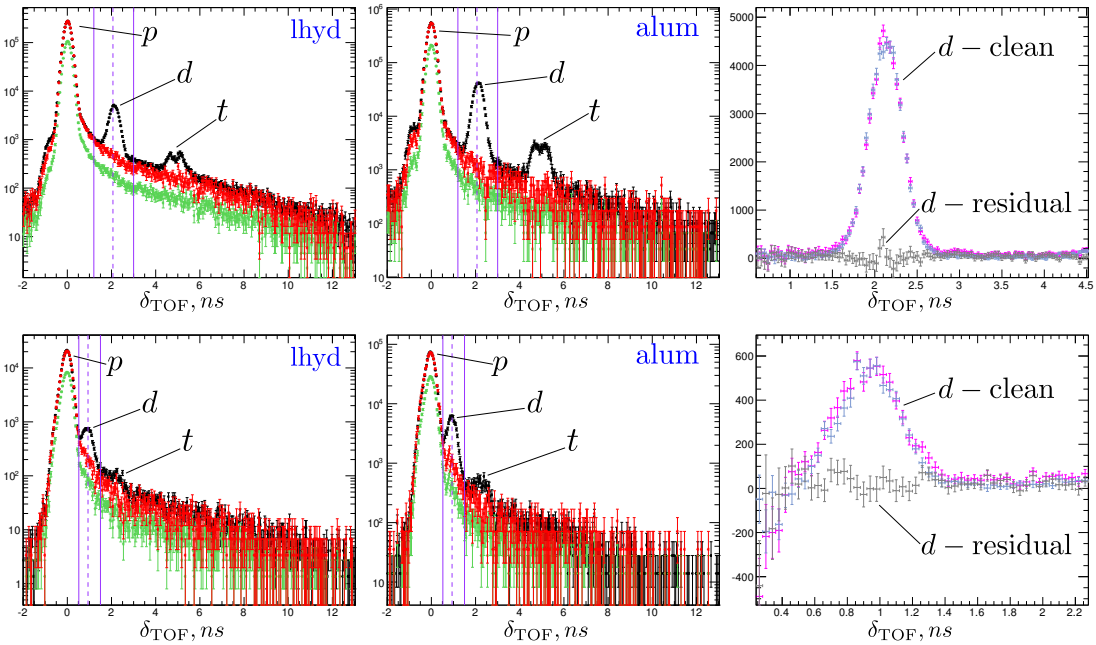

Figure 4.24: The evaluation procedure for the total number of deuteron events is shown for $Q^2 = 2.29\,\mathrm{GeV}^2$, $\theta_{\mathrm{HMS}} = 24.02°$ (top) and $Q^2 = 4.25\,\mathrm{GeV}^2$, $\theta_{\mathrm{HMS}} = 29.07°$ (bottom). The $\delta^{\mathrm{full}}_{\mathrm{TOF}}$ (black), $\delta^{\mathrm{prot}}_{\mathrm{TOF}}$ (green), and $\delta^{\mathrm{prot}}_{\mathrm{TOF}}$ scaled for deuteron extraction (red) spectra obtained with LH_2 (dummy) target data are shown in the left (middle) column. Clean deuteron distributions (zoomed in at the deuteron peak), as extracted with LH_2 (magenta) and scaled dummy (light blue) data, are shown in the right column. The gray histogram represents the dummy subtracted deuteron distribution, $\delta^{\mathrm{deut}}_{\mathrm{TOF}}(\mathrm{residual})$. The vertical solid lines define the deuteron peak region for $N^{\mathrm{Tot}}_{\mathrm{deut}}$ evaluation. The dashed colored line indicates the expected position of the deuteron peak.

4.5.4 TOF cuts optimization

To optimize particle identification results, proton inefficiency and contamination values were studied while the varying position of the TOF cuts with a scatter over variations used to estimate systematic uncertainties. The values of $\epsilon^{\mathrm{L}}_{\mathrm{TOF}}$, c_{π^+} and several intermediate quantities were calculated in $[-6,\,0]$ ns ($[-4,\,0]$ ns), depending on the Q^2 setting, interval with a step size of 0.1 ns. For the deuteron side quantities, the Q^2 variations of the interval were from 0.0 ns to 5 ns, 13 ns and 25 ns respectively. The TOF cut was varied on one side at a time while keeping the other side TOF cut position fixed. In addition, corresponding statistical and systematic uncertainties related to the sensitivity of the cut position were determined at each step. For a given TOF cut position, the systematic uncertainty of the inefficiency (contamination) calculation was defined as RMS scatter of the three (five) neighboring points with respect to the central value as

$$\Delta y = \sqrt{[(y_{\mathrm{i}} - y_{\mathrm{i\text{-}1}})^2 + (y_{\mathrm{i}} - y_{\mathrm{i+1}})^2]/3}, \tag{4.39}$$

where y is the quantity of interest and i denotes the current cut position.

The results of the cut variation procedure are demonstrated in Fig. 4.25. In order

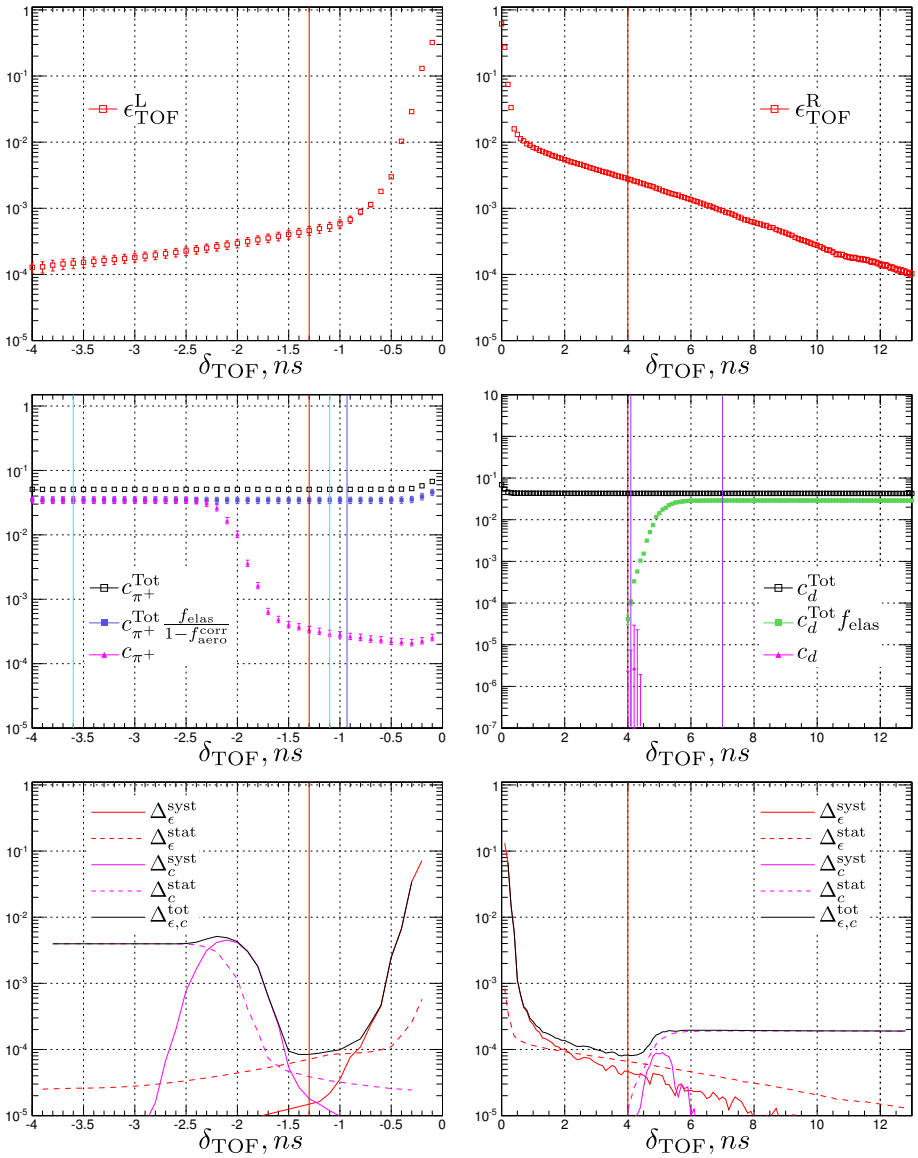

Figure 4.25: Example of the TOF cuts optimization studies is shown for $Q^2 = 0.98\,\mathrm{GeV}^2$, $\theta_{\mathrm{HMS}} = 56.49^\circ$. The left (right) column illustrates calculations on the π^+ (deuteron) side. The top row shows proton inefficiency as a function of the TOF cut position (step size $0.1\,\mathrm{ns}$). The middle row shows total (black) and final contamination (magenta). Intermediate steps are also included: $c^{\mathrm{Tot}}_{\pi^+}$ corrected for AERO cut (Eq. 4.33) inefficiency and elastic fraction (Eq. 4.36) (green); c^{Tot}_{d} corrected for elastic fraction (Eq. 4.36) (blue). The bottom row shows statistical, systematic and combined uncertainty for each calculated component. The vertical red line shows the final TOF cut position. The vertical cyan (purple) lines show the π^+ (deuteron) region.

to determine the optimal TOF cut position, the factors taken into consideration were extended to:

(a) minimization of combined uncertainty,

(b) choosing a single cut for the entire set of ε points at given, Q^2 to avoid ε dependent systematic effects,

(c) minimization of the proton inefficiency,

(d) minimization of the contamination.

Q^2, [GeV^2]	PID^s, [ns]
0.40	(−3.00, 13.50)
0.50	(−2.80, 8.50)
0.60	(−2.30, 7.10)
0.70	(−2.00, 6.00)
0.80	(−1.60, 5.24)
0.98	(−1.30, 4.00)
1.19	(−1.00, 3.24)
1.34	(−0.80, 2.80)

Q^2, [GeV^2]	PID^s, [ns]
1.70	(−0.66, 2.24)
1.91	(−0.62, 8.00)
2.29	(−2.00, 8.00)
2.95	(−2.00, 8.00)
3.61	(−2.00, 8.00)
4.25	(−2.00, 8.00)
5.08	(−2.00, 8.00)
5.76	(−2.00, 8.00)

Table 4.6: List of δ_{TOF} cuts, PID^s, used to define proton zone.

A final set of soft δ_{TOF} cuts, "PID^s", listed in Table 4.6 was identified for each Q^2 value. At $Q^2 = 2.29\,\text{GeV}^2$ ($Q^2 = 1.91\,\text{GeV}^2$) the proton zone on the left (right) side was extended to fully include the corresponding π^+ (deuteron) peak. Each component of the PID efficiency was recalculated for the δ_{TOF} cuts given in Table 4.6. Results summary for each kinematic setting is plotted as a function of Q^2 in Fig 4.26.

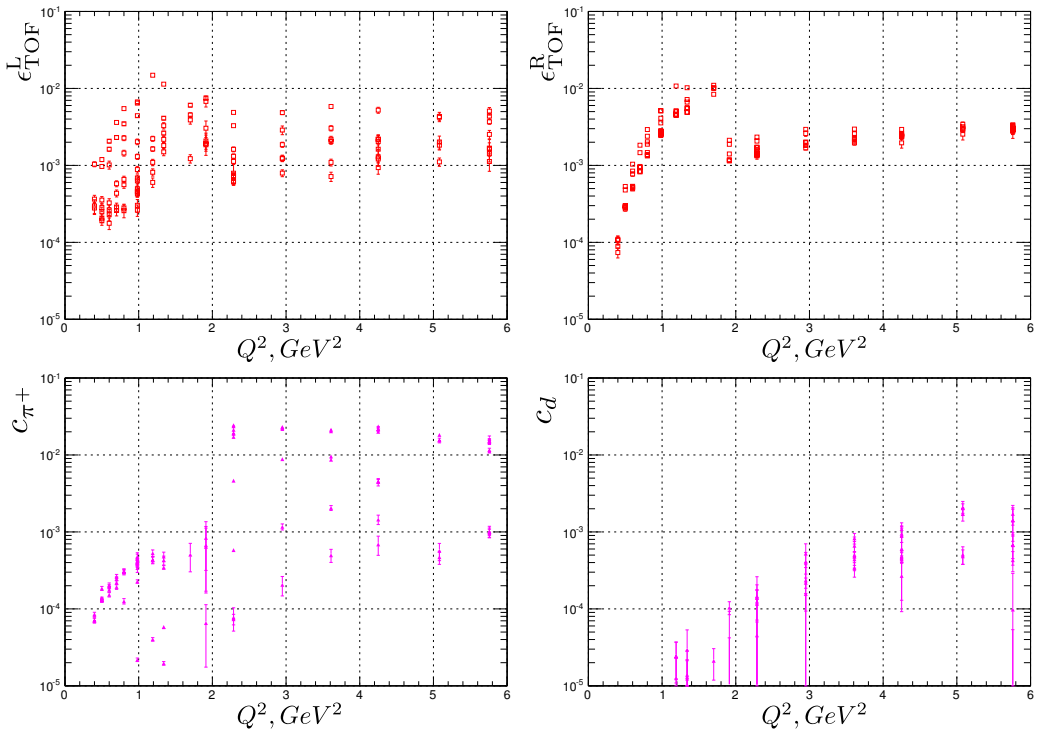

Figure 4.26: PID study results for PID^s cuts defined in Table 4.6 are plotted as a function of Q^2.

Proton inefficiency on the π^+ side for the majority of kinematic points is below 0.5 % with only two settings exceeding the inefficiency threshold of 1.0 %. Extending δ_{TOF} cuts above $2\,\text{GeV}^2$ made it possible to keep the inefficiency below 0.6 %

at the cost of an increased π^+ contamination. At low and moderate Q^2, contamination was significantly reduced to the level of 0.1 % and below. As Q^2 increases and TOF cuts are opened to include full π^+ contribution, contamination grows up to about 2.0 %, which is predominantly observed at larger $\theta_{\rm HMS}$ settings. At small proton scattering angles (small ε) contamination is typically less than 0.5 %. The error bars included in Fig 4.26 comes from the combined uncertainty shown at the bottom of Fig. 4.25 by a black solid line.

Proton inefficiency obtained from the deuteron side has noticeably better internal consistency in the ε behavior but exhibit much more pronounced Q^2 dependence. A sharp drop in $\epsilon^{\rm R}_{\rm TOF}$ at $Q^2 = 1.91\,{\rm GeV}^2$ is again related to expansion of the TOF cuts. However, in this case, due to the dummy subtraction removing most of the deuteron contribution, contamination remains at negligible levels of ~ 0.1 % and can be treated as systematic uncertainty rather than an additional correction.

4.6 Simulation

As discussed in Sec. 4.1, the MC simulation of the E05-017 experimental conditions serves two purposes: (a) it models the elastic scattering process which is used for cross section extraction through the MC ratio method (Sec. 4.1), (b) it is used to reproduce components of the background events contributing to the observed spectrum (Fig. 4.1) in order to isolate elastically scattered protons.

The software package which was used to perform both elastic and inelastic scattering simulation is called SIMC. It is the standard Hall C simulation program which grew out of a similar MC program designed to describe the $(e, e'p)$ reaction for the SLAC NE18 experiment. The package can be exploited in the coincidence $(e, e'p)$ or inclusive (e, e'), (e, p) reaction mode.

For this analysis, the SIMC event generator was extended to include generation in terms of the scattered proton, instead of the standard electron, kinematics, which significantly reduced the phase space that had to be populated and corresponding CPU run-time. The parameters necessary to uniquely define the event are generated uniformly (as a flat distribution) to fill the phase space that slightly exceeds the true experimental acceptance. The interaction vertex position is randomized within the volume defined by the target length (see Table 3.3), transverse size ($\sim 100\,\mu$m) of the electron beam and the size (± 1 mm) and the form (triangle waveform of the driving magnets) of the raster pattern. The direction of the outgoing proton is specified by generating angular variables $x'_{\rm fp}$ and $y'_{\rm fp}$ (Sec. 4.2.2), which, combined with kinematic specific spectrometer angle, $\theta_{\rm HMS}$, are then translated into the physical angles in the laboratory frame. The beam energy is generated around the measured, for a given kinematics, value taking into account fluctuations observed in the real beam spread (~ 0.05 %). The remaining quantities used in the simulation are determined by the two-body reaction kinematics.

Once an event is generated, the SIMC package simulates propagation of the proton from the target through the spectrometer magnets to the detector hut. It contains detailed description of the geometry and materials used for the target cell and

scattering chamber, models of the HMS physical apertures, including collimator, magnet bore, and vacuum pipe configurations, as well as all materials traversed by the proton inside of the detector stack. The HMS optical properties and resolution are modeled by a built-in software package called COSY which produces forward and backward matrix elements for transporting the proton through the HMS. While SIMC does not incorporate simulation of the individual detector element response or its efficiency, it accounts for a tracking per-plane resolution of the drift chambers.

At every stage, from creating a proton vector and tracing it to the detector hut, the following processes contributing to the changes in proton (and incoming electron) kinematics are considered: internal and external radiative corrections (that follows the recipes of Ref. [9, 141]), ionization energy losses, multiple scattering and decay of unstable particles. The energy losses and multiple scattering corrections are applied for all materials in the path of both incoming and outgoing particles. However, the simulation of the proton absorption due to the interaction with traversed materials is not included in the package and the calculations for associated losses are applied as a separate correction (see Sec. 4.4.4). When the proton vector passes through each limiting aperture in the spectrometer and hits all hodoscope planes required to form a trigger, the event is recorded as successful. For each successful event, a specific weight parameter is calculated which incorporates information about the relevant reaction cross section model, the luminosity and the covered phase space for a given kinematic setting. Since the detailed detector response, on ADC and TDC level, is not simulated, the reconstruction part is included in the package and uses reverse COSY matrix elements to obtain target quantities (y_{trg}, x'_{trg}, y'_{trg}, Δ_{p}), while taking into account detector resolution and multiple scattering. The more detailed description of the SIMC software package can be found on Ref. [163].

4.6.1 Elastic simulation

The cross section model for elastic scattering was parametrized by using the Rosenbluth formula and an empirical fit, Eq. 1.21 and 1.22, to the world form factor data performed by Bosted [24]. The simulation was performed for each kinematic setting listed in Table 3.1. Once the MC ntuples, in the format identical to the data files, were obtained, the distributions similar to the one shown in Fig. 4.1 were filled for further processing. The example of the resulting $\delta\theta$ spectrum that was used in the actual analysis is shown in Fig. 4.27.

The comparison of the position and the shape of the $\delta\theta$ elastic peak revealed a mismatch between the simulated and the observed spectra. The position shift, that can be attributed to the insufficient knowledge in determining the spectrometer angle, the beam energy, or the spectrometer central momentum, was resolved by applying correction, $c_{\delta\theta}$, to the observed data $\delta\theta_{\mathrm{data}}$. The shape differences manifest in a slightly smaller width of the simulated distributions and the presence of the non-Gaussian tails in the measured spectra. Although the data is fairly well reproduced by the simulation, the imperfections in the MC description of the op-

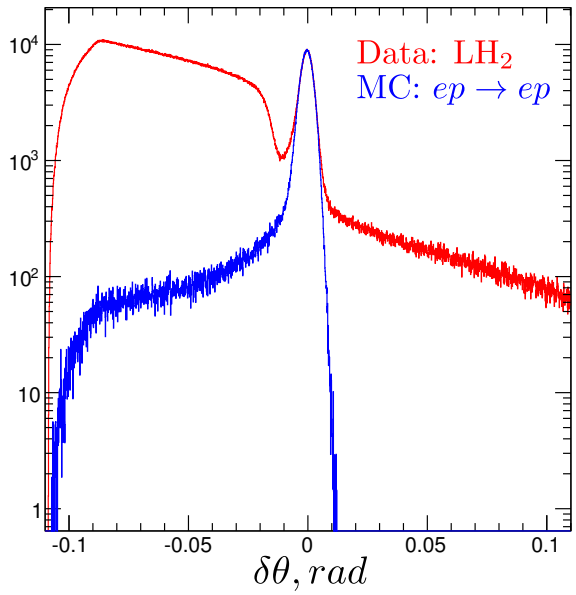

Figure 4.27: Example of the effective charge normalized $\delta\theta$ distribution for $Q^2 = 2.29\,\mathrm{GeV}^2$ and $\varepsilon = 0.07$ obtained from the MC simulation of the elastically scattered proton, $\delta\theta_{\mathrm{prot}}$ (blue), and from the data runs on the LH_2 target, $\delta\theta_{\mathrm{lhyd}}$ (red). The red symbols represent the $\delta\theta_{\mathrm{lhyd}}$ after the $c_{\delta\theta}$ correction was applied. The $\delta\theta_{\mathrm{prot}}$ distribution underwent only preliminary, one-Gaussian, smearing. The presence of non-Gaussian tail in the data spectrum can be seen at $\delta\theta \sim 10\,\mathrm{mrad}$.

tical transport system, drift chambers resolution and multiple scattering give rise to the resolution mismatch effects. The shape reproducibility was seen to improve when employing a two-Gaussian smearing of the particle's in-plane angle, y'_{trg}. The sum of two Gaussians with different widths and weights used in the smearing procedure reproduced the longer tails much better. Fig. 4.27 shows the effect of the preliminary, one-Gaussian, smearing with the $c_{\delta\theta}$ correction included. In the range of $\delta\theta_{\mathrm{lhyd}} \sim 5\,\mathrm{mrad} - 12\,\mathrm{mrad}$ ($\delta\theta_{\mathrm{lhyd}}$ denotes the LH_2 target runs distribution), the deviation from the Gaussian shape can be seen in the data peak tail that resides on the flat homogeneous quasi-elastic background from the target endcaps. The methods used to calculate the correction factor $c_{\delta\theta}$ and the parameters necessary for the smearing procedure are discussed in Sec. 4.7.

4.6.2 Background simulation

As it is clearly seen in Fig. 4.27, there is a significant overlap between the radiative tail of the elastic peak and the dominating background shoulder in the inelastic zone. As was discussed earlier, two major background reactions initiated by the bremsstrahlung photons created in the upstream target window and LH_2 are pion photoproduction ($\gamma p \rightarrow \pi^0 p$) and Compton scattering ($\gamma p \rightarrow \gamma p$). Since SIMC does not reproduce detector inefficiencies, only the detailed background shape was simulated to separate elastic events in the region where the elastic selection cut is applied, while the overall normalization factor was obtained by matching simulated and observed spectra.

The background production rate is proportional to the bremsstrahlung photon flux while the kinematics of the reaction depends on the energy of the incoming photon. Both, the upstream aluminum target window and the liquid hydrogen in the target can act as a radiators with slightly different properties and radiation lengths. The flux dependence on the radiation length and the photon energy spectrum, E_γ, was calculated in the thin target approximation [166] to be used as an input for simulation package. The bremsstrahlung energy spectrum for liquid hydrogen was obtained as function of the position (for forty increasing radiation lengths) along the target and was summed with a separately generated spectrum for aluminum radiator (Fig. 4.28). After the reaction vertex position is generated, the photon energy spectrum with the appropriate radiator length is selected and the photon energy is randomized according to the selected distribution.

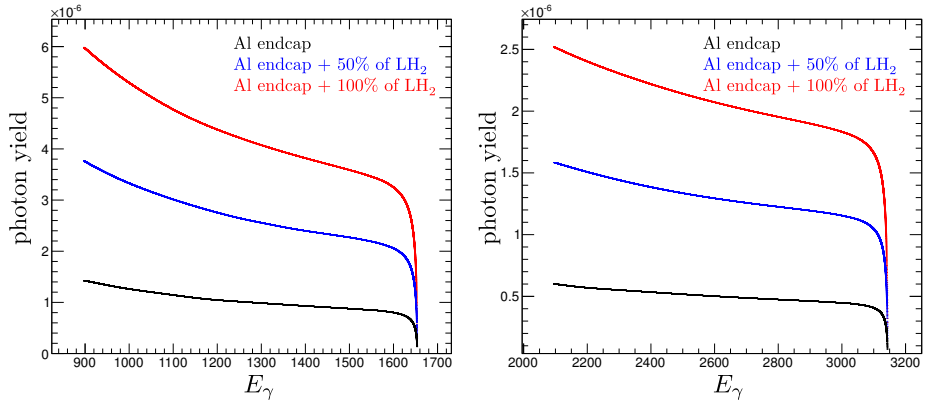

Figure 4.28: Fractional photon yield is plotted as a function of photon energy E_γ for two values of the electron beam energy $E_{\text{beam}} = 1.657\,\text{GeV}$ (left) and $E_{\text{beam}} = 3.147\,\text{GeV}$ (right). For each electron beam energy setting the photon energy spectrum is plotted for three different values of the radiator length: thickness of the Al window (black), Al window combined with a half of the LH_2 target diameter (blue), Al window combined with a full diameter of the LH_2 target (red).

The details of the proton vector propagation through the spectrometer and its reconstruction back to the target coordinate system is identical to that of the elastic proton. The only difference between elastic and background simulation was that no radiative corrections were applied to the background cross sections. The empirical model which is used to described the pion photoproduction cross section is parametrized in terms of the Mandelstam variable s based on the results of Ref. [167]

$$\left(\frac{d\sigma}{dt}\right)_{\gamma p\to\pi^0 p} \propto s^{-7}(1-\cos\theta^*)^{-5}(1+\cos\theta^*)^{-4}, \tag{4.40}$$

where θ^* is the π^0 scattering angle in the center-of-mass frame. The expression used to describe the real compton scattering (RCS) is parametrized by the product of Klein-Nishina point-like Compton scattering cross section σ_{KN} and the combination of the RCS form factors R_{V} and R_{A} as follows:

$$\left(\frac{d\sigma}{dt}\right)_{\gamma p\to\gamma p} \propto \sigma_{\mathrm{KN}}\left[f_{\mathrm{V}}R_{\mathrm{V}}^2(t) + (1-f_{\mathrm{V}})R_{\mathrm{A}}^2(t)\right], \tag{4.41}$$

where f_{V} is a kinematic factor which for the E05-017 settings was approximately equal to one and, thus, only the first term in Eq. 4.41 contributed to the cross section. R_{V} was parametrized based on the measurements in Ref. [168, 169].

An overall normalization factor has to be applied in order to match each simulated background $\delta\theta$ distribution to the observed spectrum. Since Compton scattering is overpowered by the dominant simulated background contribution from π^0 photoproduction, it cannot be reasonably normalized as a standalone component. Instead, it was first scaled by a factor obtained from the parametrization of the measured cross section ratio between Compton scattering and π^0 photoproduction. The data reported in Ref. [64] covered a range of the incoming photon energy of $\sim$ 2 GeV − 6 GeV while the ratio for low E_γ kinematics available during this experiment was extracted from Ref. [63] (Fig. 4.29). The angular dependence of the exiting data on the cross section ratio was significantly limited by the available measurements for Compton scattering so the scaling factor was obtained from a second order polynomial fit to the cross section ratio:

$$\frac{\sigma_{\gamma p\to\gamma p}}{\sigma_{\gamma p\to\pi^0 p}} = 0.03299 - 0.01838E_{\mathrm{beam}} + 0.00379E_{\mathrm{beam}}^2. \tag{4.42}$$

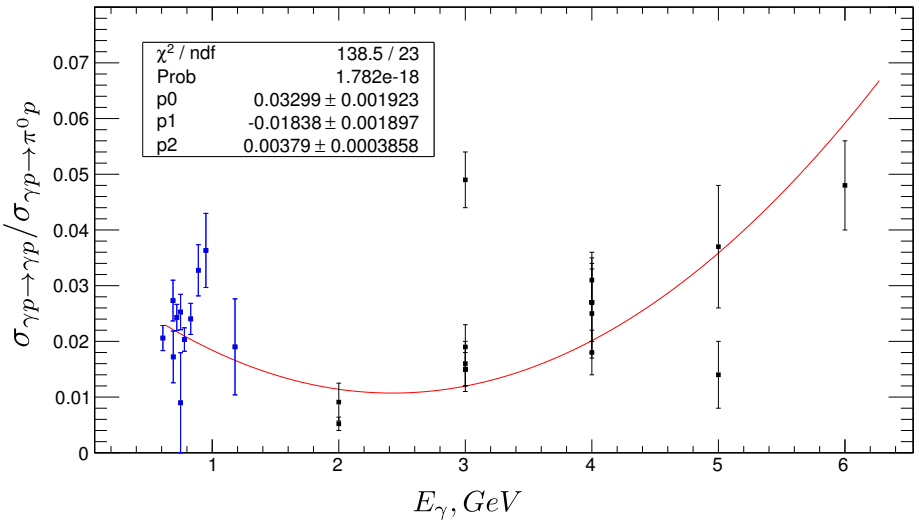

Figure 4.29: Cross section ratio between Compton scattering and π^0 photoproduction is plotted as a function of the central incident photon energy: blue squares [63], black squares [64], red line - quadratic fit.

The combined simulated background contribution $\delta\theta_{\mathrm{pico}}$ is given by the sum of π^0 photoproduction and Compton scattering distributions. This total background distribution is scaled again as discussed in Sec. 4.7 to reproduce data:

$$s_{\text{pico}}\delta\theta_{\text{pico}} = s_{\text{pico}}(\delta\theta_{\text{pion}} + s_{\text{comp}}\delta\theta_{\text{comp}}), \tag{4.43}$$

where $\delta\theta_{\text{pion}}$ ($\delta\theta_{\text{comp}}$) is π^0 photoproduction (Compton scattering) distribution, s_{pico} is the scaling factor for the sum and s_{comp} is the scaling factor determined according to Eq. 4.42 and the relative yield of the $\delta\theta_{\text{pion}}$ and $\delta\theta_{\text{comp}}$ histograms in the inelastic zone. An example of the corresponding individual distributions is shown in Fig. 4.30. The resolution of both $\delta\theta_{\text{pion}}$ and $\delta\theta_{\text{comp}}$ distributions was smeared according to the methods used in, and parameters obtained from, the procedure used in the elastic scattering simulation (Sec. 4.6.1).

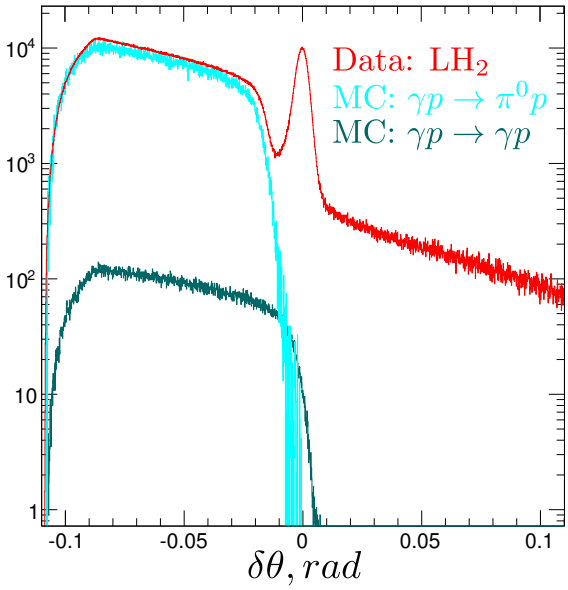

Figure 4.30: Example of the effective charge normalized $\delta\theta$ distribution for $Q^2 = 2.29\,\text{GeV}^2$ and $\varepsilon = 0.07$ obtained from the MC simulation of the pion photoproduction process, $\delta\theta_{\text{pion}}$ (cyan), Compton scattering, $\delta\theta_{\text{comp}}$ (dark cyan), and from the data runs on the LH_2 target, $\delta\theta_{\text{lhyd}}$ (red). The $\delta\theta_{\text{pion}}$ and $\delta\theta_{\text{comp}}$ distributions (the sum is not shown) were scaled by s_{pico} and $s_{\text{pico}}s_{\text{comp}}$ factors respectively as defined by Eq. 4.43.

4.7 Cross section extraction

The cross section (Eq. 4.3) extraction procedure follows the general recipe outlined in Sec. 4.1. Once the clean proton sample is obtained through PID procedures described in Sec. 4.5, the separation of elastic reaction is achieved by fitting the observed spectrum $\delta\theta_{\text{lhyd}}$ (data obtained on a liquid hydrogen target) with the sum of the major contributing components $\delta\theta_{\text{comb}}$ (combined distribution) as

$$\begin{aligned}\delta\theta_{\text{lhyd}} &\approx \delta\theta_{\text{comb}} \\ &= s_{\text{prot}}\delta\theta_{\text{prot}} + s_{\text{alum}}\delta\theta_{\text{alum}} + s_{\text{pico}}(\delta\theta_{\text{pion}} + s_{\text{comp}}\delta\theta_{\text{comp}}).\end{aligned} \tag{4.44}$$

Here, $\delta\theta$ terms listed on the second line of Eq. 4.44 represent MC simulation of elastically scattered proton; background originating from aluminum windows of the actual target, which was measured with a dummy target; MC simulation of the proton resulting from the pion photoproduction reaction; and MC simulation of the proton resulting from the Compton scattering reaction; while s terms stand for the scaling parameters obtained from the iterative fitting procedure. The $\delta\theta$ distribution of pure elastic events is then extracted as

$$\begin{aligned} \delta\theta_{\text{elas}} &\approx \delta\theta_{\text{lhyd}} - s_{\text{alum}}\delta\theta_{\text{alum}} - s_{\text{pico}}\delta\theta_{\text{pico}} \\ &\approx s_{\text{prot}}\delta\theta_{\text{prot}}, \end{aligned} \tag{4.45}$$

where $\delta\theta_{\text{pico}} = \delta\theta_{\text{pion}} + s_{\text{comp}}\delta\theta_{\text{comp}}$. Each $\delta\theta$ distribution is normalized by effective charge defined by Eq. 4.7. The comparison of Eq. 4.45 and 4.3 gives

$$\sigma_{\text{R}} = \sigma_{\text{R}}^{\text{MC}} s_{\text{prot}} = \left[\tau G_{\text{M}_\text{p}}^2(Q^2) + \varepsilon G_{\text{E}_\text{p}}^2(Q^2)\right] s_{\text{prot}}, \tag{4.46}$$

where the scaling factor s_{prot} is determined by the ratio of integrals of the $\delta\theta_{\text{elas}}$ and $\delta\theta_{\text{prot}}$ distributions over the identical $\delta\theta$ window (elastic cut) around the elastic peak. The model cross section $\sigma_{\text{R}}^{\text{MC}}$ is given by the Rosenbluth formula where the electromagnetic form factors are parametrized by the empirical fit of Bosted [24].

The following sections provide details on the data selection used to fill each $\delta\theta$ histogram listed in Eq. 4.44, the adjustment of the MC simulation, and extraction of scaling parameters in the fitting procedure defined by Eq. 4.44.

4.7.1 Data selection

Prior to the beginning of the elastic separation routine, a specific event selection process has to be performed to suppress accidental hits and poorly reconstructed tracks. A set of acceptance cuts is applied to the reconstructed variables y_{trg}, x'_{trg}, y'_{trg}, and Δ_{p}. A loose cut was applied to the reconstructed vertex position y_{trg}

$$|y_{\text{trg}}| < 5.0\,\text{cm} \tag{4.47}$$

which eliminates particles whose initial trajectory is reconstructed to be far outside of the physical dimensions of the target. This can happen when particles hit one of the magnet apertures and are then re-scattered back to the focal plane imitating a valid track. The angular acceptance is determined by the cuts applied to the reconstructed out-of-plane and in-plane angles x'_{trg} and y'_{trg} relative to the spectrometer central ray as

$$\left|x'_{\text{trg}}\right| < 40.0\,\text{mrad}, \quad \left|y'_{\text{trg}}\right| < 10.0\,\text{mrad}. \tag{4.48}$$

In this case, the cuts define the region which is notably smaller than the geometrical angular acceptance of the spectrometer. This is done to ensure that the elastic peak remains within the region where the reconstruction is not affected by the efficiency losses at the edge of acceptance – for all ε settings at given Q^2. Finally, the cut on the Δ_{p}, the deviation from the central HMS momentum, provides a well-defined momentum acceptance

$$|\Delta_{\mathrm{p}}| < 5.0\,\%. \tag{4.49}$$

A typical $\delta\theta_{\mathrm{lhyd}}$ distribution is shown in Fig. 4.31 demonstrating the progression of the effects of these cuts. The combined impact of the cuts given by Eq. 4.47, 4.48, and 4.49, henceforth the BASIC cuts, is represented by the red symbols. The BASIC cuts are used together with the PID$^{\mathrm{s}}$ cuts (Table 4.6) to obtain a set of final $\delta\theta$ distributions for the fitting procedure. The PID$^{\mathrm{s}}$ cuts typically have a negligible effect on the shape of the $\delta\theta$ spectrum as both deuteron and π^+ contributions are distributed rather homogeneously in the $\delta\theta$ plane as can be seen in Fig. 4.21 (right column).

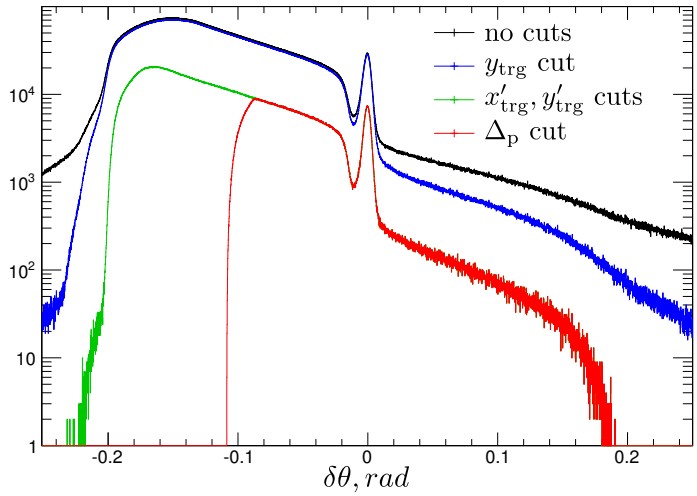

Figure 4.31: Example of the $\delta\theta_{\mathrm{lhyd}}$ distribution for $Q^2 = 2.29\,\mathrm{GeV}^2$ and $\varepsilon = 0.07$. Each histogram corresponds to the sequentially applied cuts defined by Eq. 4.47, 4.48, and 4.49.

4.7.2 Measured background subtraction

The quasi-elastic and inelastic scattering events on nucleons of the aluminum nuclei in the target windows populate the entire range of the $\delta\theta$ spectrum. The difference in the thickness between the aluminum of the LH_2 can and the blank target foils used for the measurement of this background led to the scaling mismatch of the $\delta\theta_{\mathrm{lhyd}}$ and $\delta\theta_{\mathrm{alum}}$ distributions. The appropriate scaling factor, s_{alum} (Eq. 4.45), depends on the nominal geometrical thickness difference, given by direct comparison of the target survey data (Table 3.3), the difference in the radiative corrections and

the difference in the number of bremsstrahlung photons created in the upstream target window and dummy foil. While in the inelastic and elastic zones the $\delta\theta_{\mathrm{lhyd}}$ distribution is dominated by other reactions, the super-elastic zone is assumed to have only target endcap events. The s_{alum} was extracted by normalizing the number of events of the $\delta\theta_{\mathrm{alum}}$ and $\delta\theta_{\mathrm{lhyd}}$ spectra in the far super-elastic zone as

$$s_{\mathrm{alum}} = \frac{A_{\mathrm{LH_2}} + C_{\mathrm{LH_2}}}{A_{\mathrm{dummy}} + C_{\mathrm{dummy}}} s_{\mathrm{rad}} = \frac{\int \delta\theta_{\mathrm{lhyd}}(\mathrm{SuZ^h})}{\int \delta\theta_{\mathrm{alum}}(\mathrm{SuZ^h})}, \tag{4.50}$$

where A and C are the nominal thickness measurements defined in Table 3.3, s_{rad} signifies the difference in the external radiative corrections, and the hard $\mathrm{SuZ^h}$ denotes a more restrictive super-elastic zone ($\sim 5\sigma$ away from elastic peak while excluding the far right edge of acceptance). The procedure is illustrated in Fig. 4.32 where the light green symbols indicate the scaled $\delta\theta_{\mathrm{alum}}$ spectrum.

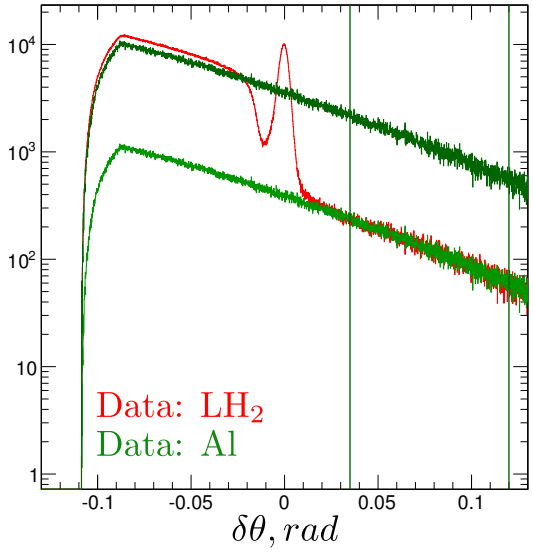

Figure 4.32: Example of the $\delta\theta_{\mathrm{lhyd}}$ (red), $\delta\theta_{\mathrm{alum}}$ (dark green), and scaled $\delta\theta_{\mathrm{alum}}$ (light green) distributions for $Q^2 = 2.29\,\mathrm{GeV}^2$ and $\varepsilon = 0.07$. The vertical green lines indicate the hard, $\mathrm{SuZ^h}$, super-elastic zone.

In principle, several iterations can be conducted to improve the quality of the extraction, however the fast convergence of s_{alum} showed that it was unnecessary. The first iteration of the measured background subtraction determines only the preliminary scaling factor s'_{alum}. In this iteration, there is a probability that elastic events may leak into the $\mathrm{SuZ^h}$ zone and affect s_{alum} extraction. In the next stage, the semi-clean elastic peak is extracted as $\delta\theta'_{\mathrm{elas}} = \delta\theta_{\mathrm{lhyd}} - s'_{\mathrm{alum}}\delta\theta_{\mathrm{alum}}$ and is used to normalize the elastic proton simulation as $s'_{\mathrm{prot}}\delta\theta_{\mathrm{prot}}$. It makes it possible to obtain the target endcap contribution free of elastic events in the $\mathrm{SuZ^h}$ zone as $(\delta\theta_{\mathrm{lhyd}} - s'_{\mathrm{prot}}\delta\theta_{\mathrm{prot}})$. The determination of the s_{alum} factor is then repeated according to Eq. 4.50. The schematics of the procedure is illustrated in Fig. 4.33.

The fraction of the background from the target endcaps in the elastic zone with respect to the elastic yield was estimated for each kinematic setting. The results,

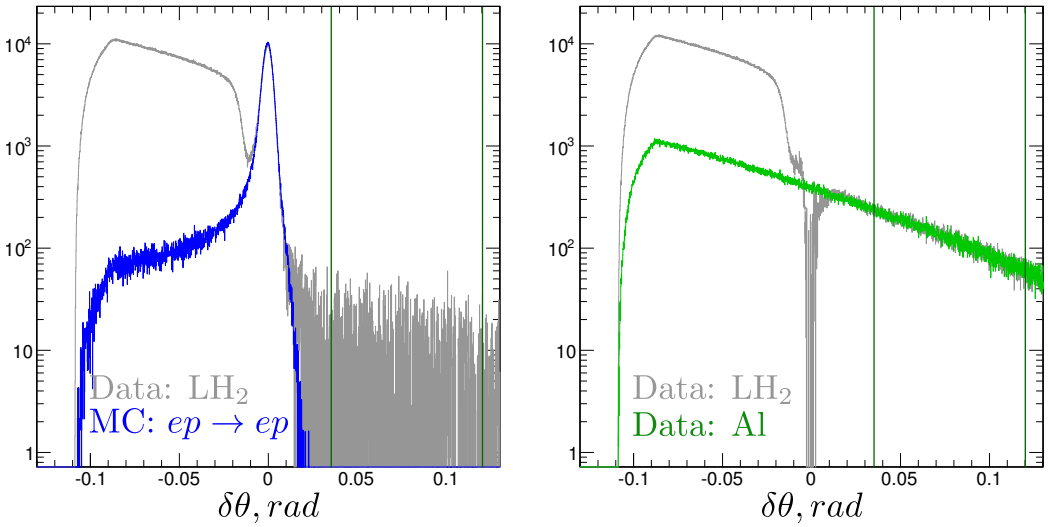

Figure 4.33: Example of the second iteration of the measured background subtraction for $Q^2 = 2.29\,\mathrm{GeV}^2$ and $\varepsilon = 0.07$. Left: $\delta\theta_{\mathrm{prot}}$ (blue) and dummy subtracted $\delta\theta_{\mathrm{lhyd}}$ (gray) distributions used for $\delta\theta_{\mathrm{prot}}$ scaling. Right: final scaled $\delta\theta_{\mathrm{alum}}$ (light green) and $\delta\theta_{\mathrm{prot}}$ subtracted $\delta\theta_{\mathrm{lhyd}}$ (gray) distributions. The vertical green lines indicate the hard, SuZ$^{\mathrm{h}}$, super-elastic zone. For this kinematic setting elastic events do not contribute to the counts in the super-elastic zone.

which vary from $\sim$ 11 % at small Q^2 to up to $\sim$ 33 % at large Q^2, are plotted in Fig. 4.34 as function of Q^2.

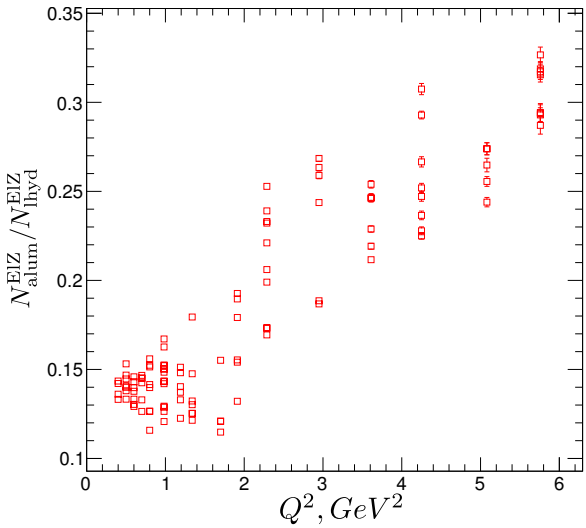

Figure 4.34: Fraction of the target endcaps background in elastic zone is plotted as a function of Q^2.

The comparison of the nominal thickness difference between the dummy and LH_2 targets and the effective thickness difference extracted as a scaling parameter $1/s_{\mathrm{alum}}$ is shown in Fig. 4.35. The nominal thickness difference shown by the horizontal black line is based on the target survey data and is calculated as $(A_{\mathrm{dummy}} + C_{\mathrm{dummy}})/(A_{\mathrm{LH_2}} + C_{\mathrm{LH_2}})$ (Sec. 3.4).

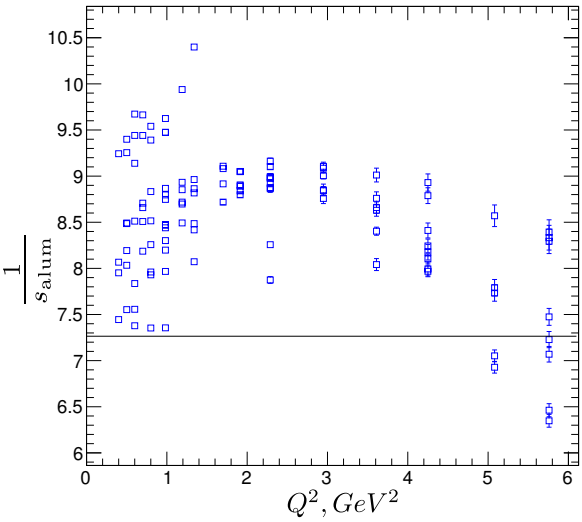

Figure 4.35: Ratio of the effective thickness of Al target to the thickness of LH_2 target is plotted as a function of Q^2. The horizontal black line indicates the nominal ratio determined by the geometrical size of the targets.

4.7.3 Simulated background subtraction

The overall amplitude of the combined inelastic background, $\delta\theta_{\text{pico}}$, discussed in Sec. 4.6.2 and the size of its intrusion in the elastic zone vary significantly over the covered kinematics. Since the MC simulation reproduces only the relative shape of the distribution and the scaling factor s_{pico} has to be obtained by normalizing simulated spectra to data, it was necessary to extract a clean sample of inelastic events from data unaffected by radiative elastic tail or dummy contribution.

The extraction procedure continues and builds upon the results of the measured background subtraction (Sec. 4.7.2). At this stage the scaled aluminum and preliminary elastic spectra are known, so the inelastic component is recovered as $\delta\theta_{\text{inel}} = \delta\theta_{\text{lhyd}} - s_{\text{alum}}\delta\theta_{\text{alum}} - s'_{\text{prot}}\delta\theta_{\text{prot}}$. Similar to the approach exploited in Sec. 4.7.2, the s_{pico} is calculated by comparing the number of events of the simulated $\delta\theta_{\text{pico}}$ and proton and dummy subtracted $\delta\theta_{\text{lhyd}}$ spectra in the far inelastic zone as

$$s_{\text{pico}} = \frac{\int \delta\theta_{\text{inel}}(\text{InZ}^{\text{h}})}{\int \delta\theta_{\text{pico}}(\text{InZ}^{\text{h}})}, \tag{4.51}$$

the hard InZ^{h} denotes a more restrictive inelastic zone ($\sim 5\sigma$ away from elastic peak while excluding the far left edge of acceptance). The relevant spectra are depicted in Fig. 4.36.

The fraction of the combined inelastic background that contributes to the yield in the elastic zone is plotted in Fig. 4.37.

4.7.4 Simulation adjustments

The discussion of the MC tuning (Sec. 4.6.1), which is performed prior to background subtraction, had to be postponed as it exploits the subtraction approach

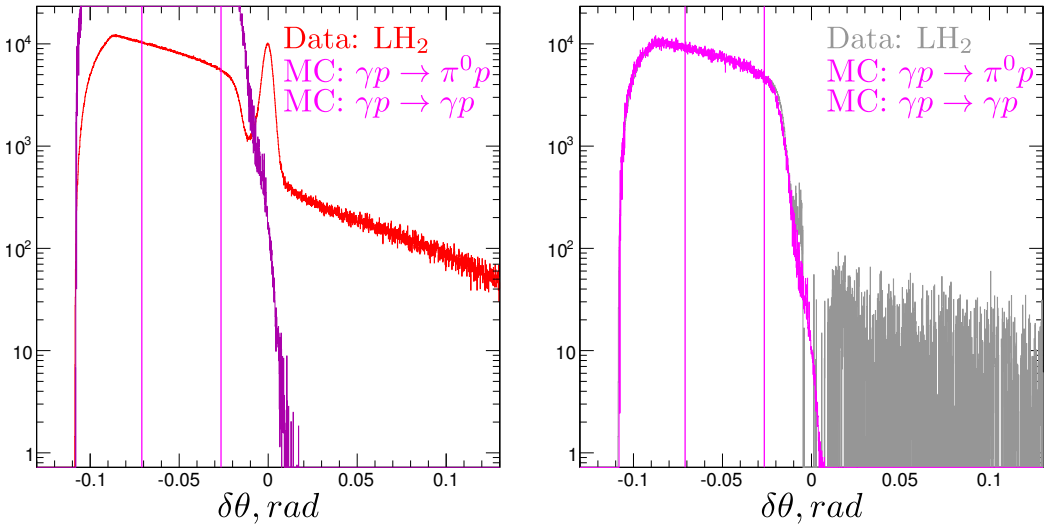

Figure 4.36: Example of the simulated background subtraction for $Q^2 = 2.29\,\mathrm{GeV}^2$ and $\varepsilon = 0.07$. Left: $\delta\theta_{\mathrm{lhyd}}$ (red) and $\delta\theta_{\mathrm{pico}}$ (dark pink) distributions. Right: scaled $\delta\theta_{\mathrm{pico}}$ (pink) and $\delta\theta^{\mathrm{data}}_{\mathrm{pico}}$ (gray) distributions. The vertical pink lines indicate the hard, $\mathrm{InZ}^{\mathrm{h}}$, inelastic zone.

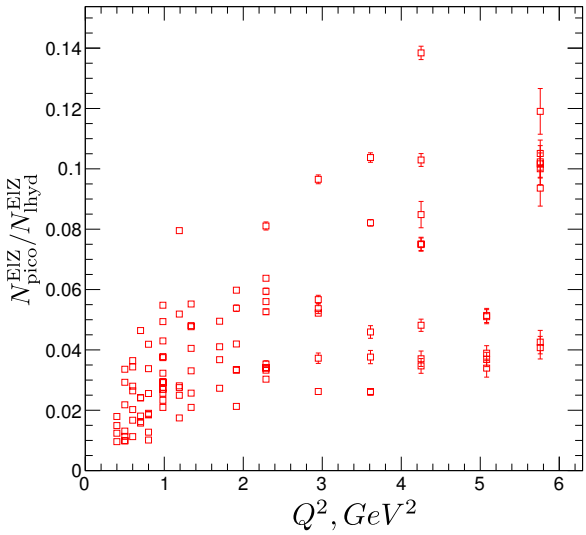

Figure 4.37: Fraction of the inelastic background in elastic zone is plotted as a function of Q^2.

introduced in previous Sec. 4.7.2 and 4.7.3. To reduce computational costs, the elastic peak shift correction $c_{\delta\theta}$ and two-Gaussian smearing were applied outside of the SIMC package on a histogram level.

It is crucial to have a proper alignment of the experimental and simulated elastic peaks to insure that the elastic cut (Sec. 4.7.5) selects an equivalent part of the peak and tail region in both cases. The $c_{\delta\theta}$ is calculated as the difference between the means of the Gaussian fit to the $\delta\theta_{\mathrm{lhyd}}$ and $\delta\theta_{\mathrm{prot}}$ distribution. The extracted value is then applied as a correction to the θ_{HMS} for each kinematic setting (Fig. 4.38). For a majority of the settings, the correction was contained within $|c_{\delta\theta}| \lesssim 1\,\mathrm{mrad}$ limits. While $c_{\delta\theta}$ is calculated by matching the $\delta\theta_{\mathrm{lhyd}}$ and $\delta\theta_{\mathrm{prot}}$ dis-

tributions, the results of the correction are applied to both measured spectra, $\delta\theta_{\rm lhyd}$ and $\delta\theta_{\rm alum}$.

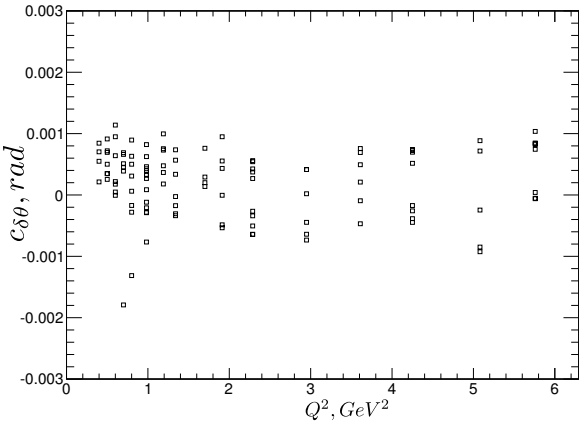

Figure 4.38: Elastic peak shift correction $c_{\delta\theta}$ is plotted as a function of Q^2.

The identification of the smearing parameters requires at least two iterations in order to match the non-Gaussian part of the elastic peak tails. First, a preliminary one-Gaussian smearing of the $\delta\theta_{\rm prot}$ distribution is performed (Fig. 4.27) with the smearing factor deduced as

$$\sigma^{\rm 1G}_{\rm smear} = \sqrt{\sigma^2_{\rm lhyd} - \sigma^2_{\rm prot}}, \tag{4.52}$$

where $\sigma_{\rm lhyd}$ ($\sigma_{\rm prot}$) is the width parameter of the Gaussian fit to the elastic peak of $\delta\theta_{\rm lhyd}$ ($\delta\theta_{\rm prot}$) distribution. Since the one-Gaussian smearing reproduces the resolution of the elastic peak within $\approx \pm 2\sigma$ fairly well, it is then possible to extract an intermediate sample of the clean elastic events, $\delta\theta^{\rm 1G}_{\rm elas}$, using the subtraction techniques described in Sec. 4.7.2 and 4.7.3. The $\delta\theta^{\rm 1G}_{\rm elas}$ distribution is fitted to a sum of two co-centered Gaussian functions for which the mean parameter is forced to be identical and, thus, reducing the number of the fit function parameters to five. The fitting is focused on the right side (positive $\delta\theta$) of the distribution since it is not affected by radiative effects and is less dependent on the background subtraction (Fig. 4.39).

In the second iteration, the following smearing parameters are determined through comparison of the original $\delta\theta_{\rm prot}$ and experimental $\delta\theta^{\rm 1G}_{\rm elas}$ distributions: $\sigma^{\rm 2G}_{\rm peak}$, $\sigma^{\rm 2G}_{\rm tail}$, $\sigma^{\rm 2G}_{\rm weight}$. The $\sigma^{\rm 2G}_{\rm peak}$ ($\sigma^{\rm 2G}_{\rm tail}$) is calculated similarly to Eq. 4.52 and represents the smearing parameter of the peak (tail) width while the $\sigma^{\rm 2G}_{\rm weight}$ defines the relative strength of two Gaussians and is found as the $\pm 3\sigma$ integral ratio of the tail Gaussian function to the peak Gaussian function. The summary of the smearing results in terms of the extracted parameters is given in Fig. 4.40 where they are plotted as a function of $p_{\rm HMS}$. The lower edge of the $\sigma^{\rm 2G}_{\rm peak}$ parameter has a very well pronounced $1/p_{\rm HMS}$ behavior indicating that additional smearing is most likely related to the multiple scattering effects unaccounted for in SIMC. Both the $\sigma^{\rm 2G}_{\rm peak}$ and the $\sigma^{\rm 2G}_{\rm tail}$ parameters have noticeable $\theta_{\rm HMS}$ dependence for kinematics with $p_{\rm HMS} < 1.5\,{\rm GeV}$.

The contribution of the tail fraction is growing with increasing momentum from $\sim 6\,\%$ to $\sim 19\,\%$ as indicated by σ^{2G}_{weight}. The second step is concluded by applying a 3-parameter smearing to the originally generated $\delta\theta_{prot}$ distribution which is consequently used as an input distribution for background subtraction procedures of Sec. 4.7.2 and 4.7.3.

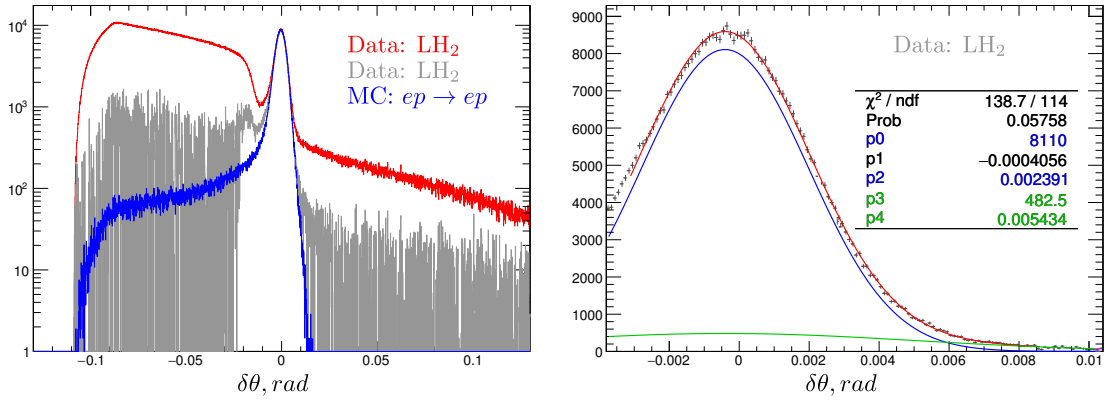

Figure 4.39: Example of the background subtraction and two-Gaussian fitting for $Q^2 = 2.29\,\mathrm{GeV}^2$ and $\varepsilon = 0.07$. Left: $\delta\theta_{\mathrm{lhyd}}$ (red), background subtracted $\delta\theta^{1G}_{\mathrm{elas}}$ (gray), and two-Gaussian smeared $\delta\theta_{\mathrm{prot}}$ (blue) distributions. The $\delta\theta_{\mathrm{prot}}$ distribution reproduces fairly well the right side of the $\delta\theta^{1G}_{\mathrm{elas}}$ spectrum while the left side of the experimental spectrum remains slightly wider and indicates a mismatch in the background subtraction of inelastic zone. Right: $\delta\theta^{1G}_{\mathrm{elas}}$ (zoomed-in) is fitted with the sum (red) of two Gaussian functions (blue, green). $p1$ represents the mean parameter of both functions while $p0$ and $p2$ ($p3$ and $p4$) stand for normalization and width parameters of the peak (tail) function.

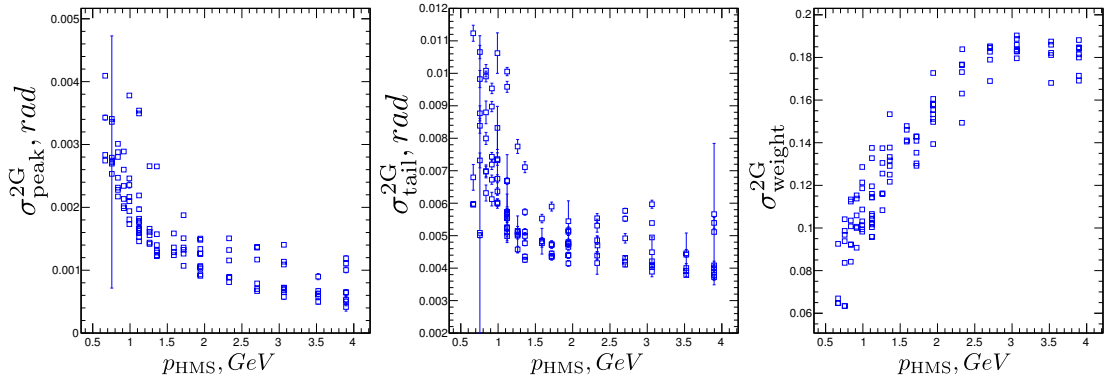

Figure 4.40: Parameters of the smearing procedure are plotted as a function of spectrometer central momentum setting. Left: the smearing parameter of the Gaussian function reproducing resolution of the main elastic peak. Middle: smearing parameter of the Gaussian function reproducing resolution of the non-Gaussian tails. Right: the weighting parameter specifying the magnitude of each component contribution.

Whereas the smearing parameters were identified based on the elastic proton simulation, the identical two-Gaussian smearing was applied when generating neutral pion photoproduction and Compton scattering spectra.

4.7.5 Reduced cross section

Combining the prescriptions for both components of the background subtraction makes it possible to select a clean sample of elastic events $\delta\theta_{\text{elas}}$ according to Eq. 4.45. The scaling parameter s_{prot} which determines reduced cross section (Eq. 4.46) is calculated as

$$s_{\text{prot}} = \frac{\int \delta\theta_{\text{elas}}(\text{ElZ})}{\int \delta\theta_{\text{prot}}(\text{ElZ})}, \tag{4.53}$$

where the $\delta\theta_{\text{prot}}$ is the original unscaled simulated elastic proton distribution. The summary of the fitting process as well as the extracted $\delta\theta_{\text{elas}}$ is shown in Fig. 4.41. The integration limits of Eq. 4.53 are defined by elastic cuts (the blue vertical lines in Fig. 4.41), ELAS, which are listed in Table 4.7 for each kinematic setting.

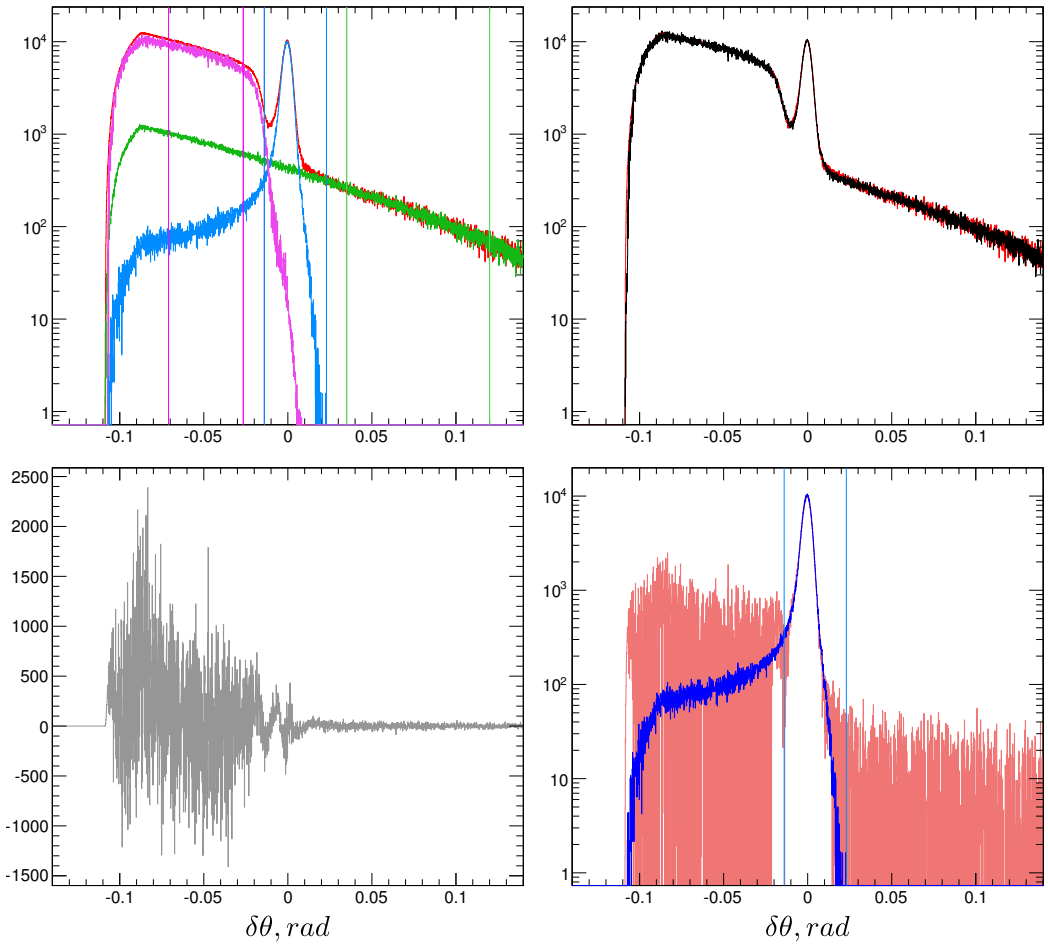

Figure 4.41: Example of the fitting process for $Q^2 = 2.29\,\text{GeV}^2$ and $\varepsilon = 0.07$. Top left: $\delta\theta_{\text{lhyd}}$ (red) and scaled $\delta\theta_{\text{prot}}$ (light blue), $\delta\theta_{\text{alum}}$ (green), $\delta\theta_{\text{pico}}$ (pink) distributions; vertical lines from left to right define InZ$^{\text{h}}$ (Sec. 4.7.3), ElZ, and SuZ$^{\text{h}}$(Sec. 4.7.2) zones. Top right: $\delta\theta_{\text{lhyd}}$ (red) and the combined sum of components $\delta\theta_{\text{comb}}$ (black) distributions. Bottom left: residual of $\delta\theta_{\text{lhyd}} - \delta\theta_{\text{comb}}$ (gray). Bottom right: original unscaled $\delta\theta_{\text{prot}}$ (blue) and defined by Eq. 4.45 $\delta\theta_{\text{elas}}$ (brick red) distributions.

#	ELAS, [rad]
1	(−0.0540, 0.0510)
2	(−0.0355, 0.0300)
3	(−0.0300, 0.0265)
4	(−0.0300, 0.0250)
5	(−0.0300, 0.0300)
6	(−0.0500, 0.0520)
7	(−0.0500, 0.0520)
8	(−0.0300, 0.0300)
9	(−0.0250, 0.0230)
10	(−0.0250, 0.0245)
11	(−0.0280, 0.0250)
12	(−0.0325, 0.0400)
13	(−0.0225, 0.0260)
14	(−0.0185, 0.0250)
15	(−0.0240, 0.0220)
16	(−0.0300, 0.0275)
17	(−0.0175, 0.0225)
18	(−0.0135, 0.0235)
19	(−0.0155, 0.0250)
20	(−0.0115, 0.0165)
21	(−0.0115, 0.0190)
22	(−0.0120, 0.0200)
23	(−0.0150, 0.0200)
24	(−0.0155, 0.0210)
25	(−0.0230, 0.0210)
26	(−0.0230, 0.0210)
27	(−0.0280, 0.0230)
28	(−0.0300, 0.0250)
29	(−0.0140, 0.0230)
30	(−0.0085, 0.0155)
31	(−0.0100, 0.0160)
32	(−0.0100, 0.0160)
33	(−0.0095, 0.0190)
34	(−0.0130, 0.0200)
35	(−0.0130, 0.0200)
36	(−0.0200, 0.0210)
37	(−0.0250, 0.0220)
38	(−0.0105, 0.0210)
39	(−0.0085, 0.0190)
40	(−0.0170, 0.0200)
41	(−0.0200, 0.0210)
42	(−0.0220, 0.0190)
43	(−0.0105, 0.0170)
44	(−0.0090, 0.0170)
45	(−0.0085, 0.0160)
46	(−0.0085, 0.0175)
47	(−0.0170, 0.0190)
48	(−0.0100, 0.0160)
49	(−0.0090, 0.0135)
50	(−0.0085, 0.0180)
51	(−0.0110, 0.0180)
52	(−0.0170, 0.0170)
53	(−0.0200, 0.0190)
54	(−0.0235, 0.0200)
55	(−0.0080, 0.0145)
56	(−0.0080, 0.0150)
57	(−0.0125, 0.0140)
58	(−0.0080, 0.0160)
59	(−0.0140, 0.0190)
60	(−0.0060, 0.0130)
61	(−0.0090, 0.0150)
62	(−0.0130, 0.0150)
63	(−0.0045, 0.0100)
64	(−0.0045, 0.0100)
65	(−0.0060, 0.0120)
66	(−0.0060, 0.0120)
67	(−0.0060, 0.0125)
68	(−0.0130, 0.0150)
69	(−0.0165, 0.0150)
70	(−0.0100, 0.0140)
71	(−0.0100, 0.0170)
72	(−0.0140, 0.0190)
73	(−0.0170, 0.0190)
74	(−0.0180, 0.0190)
75	(−0.0050, 0.0100)
76	(−0.0050, 0.0100)
77	(−0.0100, 0.0180)
78	(−0.0075, 0.0165)
79	(−0.0110, 0.0180)
80	(−0.0170, 0.0190)
81	(−0.0160, 0.0190)
82	(−0.0215, 0.0200)
83	(−0.0210, 0.0185)
84	(−0.0035, 0.0100)
85	(−0.0090, 0.0135)
86	(−0.0140, 0.0135)
87	(−0.0090, 0.0150)
88	(−0.0110, 0.0180)
89	(−0.0220, 0.0180)
90	(−0.0065, 0.0090)
91	(−0.0065, 0.0090)
92	(−0.0055, 0.0100)
93	(−0.0055, 0.0100)
94	(−0.0125, 0.0110)
95	(−0.0095, 0.0125)
96	(−0.0100, 0.0180)
97	(−0.0170, 0.0190)
98	(−0.0170, 0.0190)
99	(−0.0150, 0.0180)
100	(−0.0130, 0.0130)
101	(−0.0100, 0.0150)
102	(−0.0090, 0.0150)
103	(−0.0150, 0.0175)
104	(−0.0050, 0.0100)
105	(−0.0050, 0.0100)
106	(−0.0050, 0.0100)
107	(−0.0060, 0.0100)
108	(−0.0080, 0.0110)
109	(−0.0080, 0.0110)
110	(−0.0095, 0.0120)
111	(−0.0120, 0.0190)
112	(−0.0200, 0.0200)

Table 4.7: List of $\delta\theta$ elastic cuts, ELAS, used to define elastically scattered proton zone. The kinematic setting number is defined according to Table 3.1.

The extracted parameter s_{prot} along with the parametrized electromagnetic form factors are used to extract the reduced elastic scattering cross section for each combination of the Q^2 and ε values (Eq. 4.46). The results are listed in Table 4.8. The calculation of the statistical uncertainty, $\delta^{\text{stat}}_{\sigma_{\text{R}}}$, takes into account statistical fluctuations of the measured and simulated background yields at every stage of the fitting procedure (Eq. 4.45). The statistical uncertainty values are well below 0.3 % for $Q^2 < 2\,\text{GeV}^2$, while at larger Q^2 they vary from 0.2 % up to ~ 1.8 %.

Q^2	ε	σ_{R}
0.40	0.570	0.226 178(48)
	0.884	0.274 933(57)
	0.984	0.278 167(62)
	0.985	0.273 562(60)
0.50	0.445	0.174 711(43)
	0.566	0.187 915(52)
	0.847	0.223 497(63)
	0.884	0.226 638(54)
	0.949	0.230 438(56)
	0.979	0.230 255(58)
	0.989	0.223 382(80)
0.60	0.320	0.138 799(43)
	0.463	0.151 679(46)
	0.591	0.159 830(48)
	0.809	0.177 646(60)
	0.881	0.180 094(57)
	0.966	0.187 577(53)
	0.981	0.191 925(51)
0.70	0.191	0.111 032(42)
	0.357	0.122 721(45)
	0.767	0.145 354(56)
	0.824	0.151 109(52)
	0.922	0.157 491(55)
	0.968	0.159 601(48)
0.80	0.068	0.093 292(42)
	0.248	0.100 010(46)
	0.417	0.107 502(44)
	0.505	0.110 190(42)
	0.723	0.121 241(48)
	0.828	0.126 202(54)
	0.952	0.131 462(49)
	0.973	0.136 845(50)
0.98	0.051	0.072 420(47)
	0.051	0.072 386(47)
	0.251	0.077 613(47)
	0.359	0.079 391(46)
	0.635	0.088 673(49)
	0.723	0.090 722(46)

Q^2,	ε	σ_{R}
0.98	0.772	0.090 944(50)
	0.823	0.091 810(47)
	0.878	0.097 001(48)
	0.911	0.098 120(49)
	0.937	0.097 252(52)
	0.951	0.100 172(56)
	0.965	0.101 369(58)
	0.974	0.099 817(55)
1.19	0.058	0.054 363(45)
	0.526	0.063 750(47)
	0.638	0.065 301(58)
	0.841	0.069 263(46)
	0.936	0.071 972(50)
	0.941	0.072 651(50)
1.34	0.058	0.046 051(46)
	0.441	0.050 742(44)
	0.571	0.052 771(50)
	0.647	0.053 598(49)
	0.725	0.046 467(38)
	0.903	0.056 418(45)
	0.959	0.058 519(58)
1.70	0.223	0.031 963(40)
	0.395	0.033 424(40)
	0.395	0.033 170(41)
	0.893	0.036 339(42)
1.91	0.089	0.024 373(48)
	0.283	0.025 439(36)
	0.530	0.028 267(47)
	0.834	0.028 298(44)
	0.881	0.028 537(43)
	0.931	0.029 517(46)
2.29	0.077	0.017 296(41)
	0.222	0.017 608(36)
	0.380	0.018 291(36)
	0.570	0.019 232(43)
	0.685	0.018 687(39)
	0.745	0.018 186(45)
	0.779	0.018 339(54)

Q^2,	ε	σ_{R}
2.29	0.829	0.019 261(44)
	0.882	0.019 754(47)
	0.909	0.019 475(45)
2.95	0.090	0.009 714(30)
	0.351	0.010 590(33)
	0.519	0.010 010(39)
	0.662	0.010 520(43)
	0.759	0.010 542(43)
	0.861	0.010 726(45)
3.61	0.106	0.006 057(29)
	0.324	0.006 255(33)
	0.448	0.006 902(34)
	0.520	0.006 493(30)
	0.744	0.006 556(36)
	0.812	0.006 632(35)
4.25	0.116	0.003 805(28)
	0.270	0.004 087(29)
	0.361	0.004 140(30)
	0.361	0.004 289(31)
	0.538	0.004 126(32)
	0.655	0.004 224(39)
	0.747	0.004 243(30)
	0.747	0.004 328(30)
5.08	0.133	0.002 409(23)
	0.133	0.002 362(23)
	0.520	0.002 662(25)
	0.520	0.002 682(25)
	0.647	0.002 647(26)
5.76	0.145	0.001 611(24)
	0.145	0.001 608(25)
	0.203	0.001 711(28)
	0.394	0.001 802(28)
	0.394	0.001 819(28)
	0.552	0.001 893(25)
	0.552	0.001 843(24)
	0.552	0.001 636(30)

Table 4.8: The list of the Q^2, [GeV^2] and ε settings along with values of the reduced elastic scattering cross section σ_{R} and its statistical uncertainty.

4.8 Systematic uncertainties

Since the primary goal of this analysis is the extraction of the form factors ratio and limits on nonlinear in ε behavior of the elastic cross section, it is important to estimate systematic effects that modify these quantities. The normalization, or scale, systematic uncertainties $\delta^{\mathrm{norm}}_{\sigma_{\mathrm{R}}}$ alter the cross section for ε points at a given

Q^2 setting by the same factor. Thus, the extraction of the G_{E_p}/G_{M_p} ratio or the curvature parameter P_2 (Eq. 2.5) will be unaffected by these normalization uncertainties; however, they have an impact on the extraction of individual electromagnetic form factors. Another group of uncertainties, called point-to-point, or random $\delta^{\text{rand}}_{\sigma_R}$, uncertainties, modifies the cross section differently from one ε point to another at selected Q^2. Their effect is similar to that of statistical uncertainties as they affect extraction of all physics quantities. The summary of the normalization and point-to-point uncertainties associated with a particular efficiency calculation, correction estimation or specific analysis procedure is given in Table 4.9.

Source	$\delta^{\text{rand}}_{\sigma_R}$, [%]	$\delta^{\text{norm}}_{\sigma_R}$, [%]
BCM calibration	0.1	0.3
Target boiling	0.05	0.4
Target length	0.05	0.2
Acceptance	0.0	3.0
E_{beam}, θ_{HMS} and p_{HMS} offset	0.3	0.4
Trigger efficiency	0.02	0.1
DC tracking efficiency	0.2	0.5
Missing TOF	0.1	0.1
Proton absorption	0.0	1.0
PID efficiency	0.05-0.02	0.5
$\delta\theta_{\text{alum}}$ subtraction	0.15-0.3	0.0
$\delta\theta_{\text{pico}}$ subtraction	0.15-0.3	0.0
Elastic cut variation	0.2-0.3	0.0
Radiative correction	0.5	1.0

Table 4.9: Summary of the systematic uncertainties.

5 Results

Extraction of the physics quantities, G_{E_p}, G_{M_p}, $\mu_p G_{E_p}/G_{M_p}$, and P_2, was performed on the reduced data set. Although the majority of the sources of systematic uncertainties were estimated, there are several specific kinematic settings for which the elastic cut ELAS (Table 4.7) still has to be optimized. These settings mostly reside in the high end of the ε range. In order to avoid possible bias in the form factor ratio or nonlinearity extraction, all measurements with $\varepsilon > 0.95$ were temporarily excluded from further analysis. In addition, three other kinematic settings (#45, #46, and #61) were also excluded as apparent outliers which have to be investigated more carefully. At the current stage of analysis, a total of 96 out 112 reduced cross section measurements listed in Table 4.8 were included in the calculation of the above-mentioned quantities.

5.1 Form Factors extraction

The extraction of the individual electromagnetic form factors G_{E_p} and G_{M_p} follows the standard Rosenbluth procedure where the linear fit is performed to the ε dependence of the reduced cross section σ_R given by Eq. 1.13. The following functional form is used to extract fitting parameters:

$$\sigma_R = \tau p_0^2 + \varepsilon p_1^2, \tag{5.1}$$

where p_0 (p_1) represents $G_{M_p}(Q^2)$ ($G_{E_p}(Q^2)$). The statistical and point-to-point systematic uncertainties discussed in Sec. 4.7 and 4.8 are added in quadrature to form combined σ_R uncertainty as

$$\delta_{\sigma_R} = \sqrt{(\delta_{\sigma_R}^{\text{stat}})^2 + (\delta_{\sigma_R}^{\text{rand}})^2}. \tag{5.2}$$

Once the fitting procedure is performed the partial uncertainties for $G_{M_p}(Q^2)$ and $G_{E_p}(Q^2)$ are obtained from the fit uncertainties in p_0 and p_1. The $\delta G_{M_p}^{\text{fit}}$ and $\delta G_{E_p}^{\text{fit}}$,

thus, represent contributions from statistical and point-to-point uncertainties. In order to determine the contribution of the normalization uncertainty $\delta^{\text{norm}}_{\sigma_{\text{R}}}$, another linear fit was performed while varying σ_{R} as

$$\sigma^{\text{norm}}_{\text{R}} = \sigma_{\text{R}}(1.0 + \delta^{\text{norm}}_{\sigma_{\text{R}}}). \tag{5.3}$$

The new values of $G^{\text{norm}}_{\text{M}_\text{p}}$ and $G^{\text{norm}}_{\text{E}_\text{p}}$ retrieved from the fit are then used to estimate normalization uncertainty contribution as

$$\delta G^{\text{norm}}_{\text{M}_\text{p}} = \left| G^{\text{norm}}_{\text{M}_\text{p}} - G_{\text{M}_\text{p}} \right|, \quad \delta G^{\text{norm}}_{\text{E}_\text{p}} = \left| G^{\text{norm}}_{\text{E}_\text{p}} - G_{\text{E}_\text{p}} \right|. \tag{5.4}$$

The total uncertainty is calculated by adding the fit and normalization uncertainties in quadrature. Fig. 5.1 gives a summary of the Rosenbluth extraction of electromagnetic form factors for sixteen Q^2 settings. The reduced cross section in Fig. 5.1 is normalized by a $\tau\mu_\text{p}^2 G_\text{D}^2$ term, where the G_D represents the dipole form factor (Eq. 1.14).

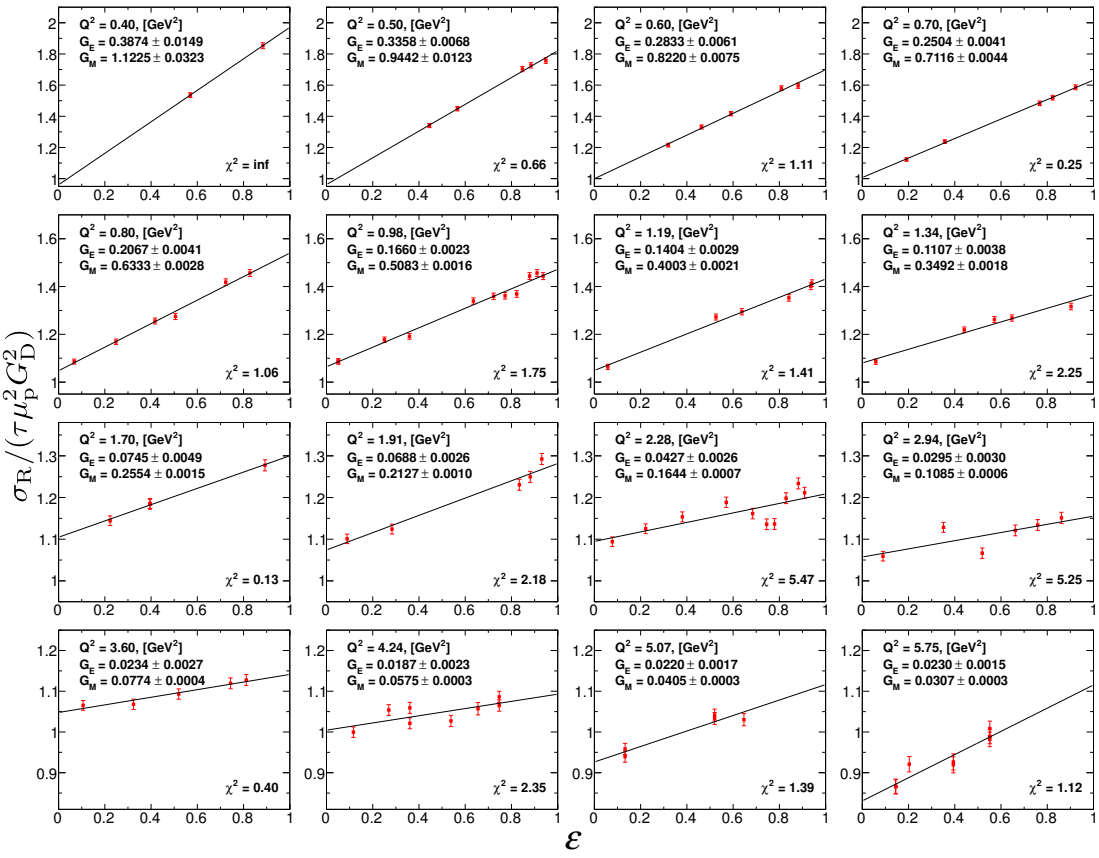

Figure 5.1: The $\tau\mu_\text{p}^2 G_\text{D}^2$ normalized reduced cross section σ_R (red symbols) is plotted as a function of ε for sixteen Q^2 settings. The linear fit (black line) represents the Rosenbluth separation procedure for each setting. The quoted G_{E_p} (G_{M_p}) values include the contribution of the statistical and point-to-point systematic uncertainties $\delta G^{\text{fit}}_{\text{E}_\text{p}}$ ($\delta G^{\text{fit}}_{\text{M}_\text{p}}$) only.

The values of extracted form factors as well as the dipole-normalized G_{E_p}/G_D and G_{M_p}/G_D ratios are plotted as a function of Q^2 in Fig. 5.2. The uncertainties presented in Fig. 5.2 include the contributions from statistical and point-to-point and normalization systematic uncertainties in σ_R. The corresponding values are given in Table 5.1 and 5.2. The bottom plots in Fig. 5.2 compare results of this analysis with world's data showing the scope of the E05-017 data and the improvements in the uncertainties with respect to the global results.

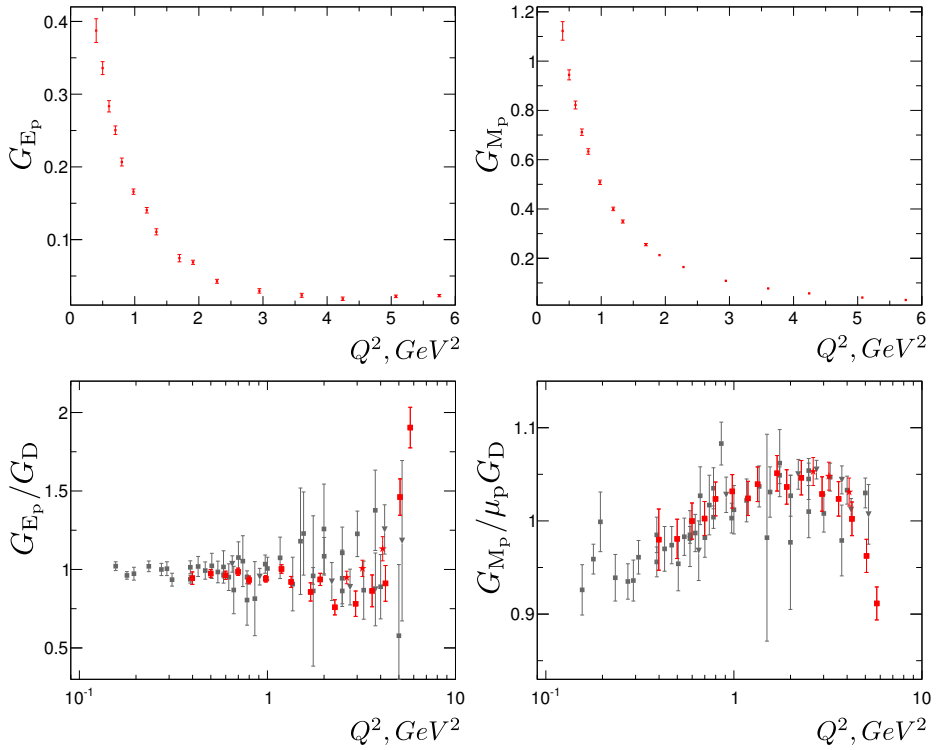

Figure 5.2: The proton electromagnetic form factors (top) as well as G_{E_p}/G_D and G_{M_p}/G_D ratios (bottom) are plotted as a function of Q^2. The bottom plots also include the compilation of the world's data on the dipole-normalized form factors: red stars - Super-Rosenbluth extraction from Ref. [12]; gray (conventional Rosenbluth extraction) squares - from Ref. [25] (combines [4, 5, 9, 10]) and triangles - from Ref. [11].

5.2 Form Factors ratio

As was discussed in Sec. 4.8 and 5.1 the extraction of the form factors ratio is unaffected by normalization uncertainties. Therefore, in this case, it is more convenient to rewrite Eq. 1.13 in the form

$$\begin{aligned}\sigma_R &= \tau(G_{M_p}(Q^2))^2\left(1.0+\frac{\varepsilon}{\tau}\left(\frac{G_{E_p}(Q^2)}{G_{M_p}(Q^2)}\right)^2\right)\\ &= \tau p_0^2\left(1.0+\frac{\varepsilon}{\tau}p_1^2\right),\end{aligned} \tag{5.5}$$

Q^2, [GeV^2]	$G_{\mathrm{E_p}}$	$\delta G^{\mathrm{fit}}_{\mathrm{E_p}}$	$\delta G^{\mathrm{norm}}_{\mathrm{E_p}}$	$\delta G^{\mathrm{total}}_{\mathrm{E_p}}$	$G_{\mathrm{E_p}}/G_{\mathrm{D}}$	$\delta(G_{\mathrm{E_p}}/G_{\mathrm{D}})$
0.40	0.3495	0.0074	0.0060	0.0095	0.853	0.018
0.50	0.3205	0.0041	0.0055	0.0069	0.932	0.012
0.60	0.2793	0.0032	0.0048	0.0058	0.951	0.011
0.70	0.2495	0.0026	0.0043	0.0050	0.984	0.010
0.80	0.2112	0.0021	0.0036	0.0042	0.956	0.009
0.98	0.1695	0.0014	0.0029	0.0032	0.963	0.008
1.19	0.1404	0.0021	0.0024	0.0032	1.006	0.015
1.34	0.1021	0.0024	0.0018	0.0030	0.851	0.020
1.70	0.0745	0.0035	0.0013	0.0037	0.859	0.040
1.91	0.0685	0.0019	0.0012	0.0022	0.935	0.025
2.29	0.0427	0.0019	0.0007	0.0020	0.761	0.034
2.95	0.0295	0.0022	0.0005	0.0023	0.783	0.059
3.61	0.0236	0.0021	0.0004	0.0021	0.874	0.077
4.25	0.0188	0.0019	0.0003	0.0019	0.916	0.092
5.08	0.0220	0.0015	0.0004	0.0015	1.466	0.097
5.76	0.0230	0.0014	0.0004	0.0014	1.912	0.115

Table 5.1: The summary of the proton electric form factor extraction.

Q^2, [GeV^2]	$G_{\mathrm{M_p}}$	$\delta G^{\mathrm{fit}}_{\mathrm{M_p}}$	$\delta G^{\mathrm{norm}}_{\mathrm{M_p}}$	$\delta G^{\mathrm{total}}_{\mathrm{M_p}}$	$G_{\mathrm{M_p}}/G_{\mathrm{D}}$	$\delta(G_{\mathrm{M_p}}/G_{\mathrm{D}})$
0.40	1.1882	0.0161	0.0204	0.0260	1.039	0.014
0.50	0.9647	0.0076	0.0165	0.0182	1.004	0.008
0.60	0.8257	0.0045	0.0142	0.0149	1.006	0.005
0.70	0.7121	0.0030	0.0122	0.0126	1.006	0.004
0.80	0.6314	0.0018	0.0108	0.0110	1.023	0.003
0.98	0.5073	0.0011	0.0087	0.0088	1.032	0.002
1.19	0.4003	0.0015	0.0069	0.0070	1.027	0.004
1.34	0.3489	0.0012	0.0060	0.0061	1.041	0.004
1.70	0.2554	0.0011	0.0044	0.0045	1.054	0.004
1.91	0.2137	0.0007	0.0037	0.0037	1.044	0.003
2.29	0.1644	0.0005	0.0028	0.0029	1.049	0.003
2.95	0.1085	0.0004	0.0019	0.0019	1.032	0.004
3.61	0.0772	0.0003	0.0013	0.0014	1.024	0.004
4.25	0.0575	0.0003	0.0010	0.0010	1.005	0.005
5.08	0.0405	0.0002	0.0007	0.0007	0.965	0.006
5.76	0.0307	0.0003	0.0005	0.0006	0.914	0.008

Table 5.2: The summary of the proton magnetic form factor extraction.

such that the uncertainty of $G_{\mathrm{E_p}}(Q^2)/G_{\mathrm{M_p}}(Q^2)$ can be obtained directly from the fit. The reduced cross section ε dependence at each Q^2 was fit to the functional form shown in the second line of Eq. 5.5. The fitting procedure yielded the fit line and $G_{\mathrm{M_p}}$ values identical to those shown in Fig. 5.1. The Q^2 dependence of the ratio $G_{\mathrm{E_p}}(Q^2)/G_{\mathrm{M_p}}(Q^2)$ extraction is shown in Fig. 5.3 while the corresponding values are given in Table 5.3.

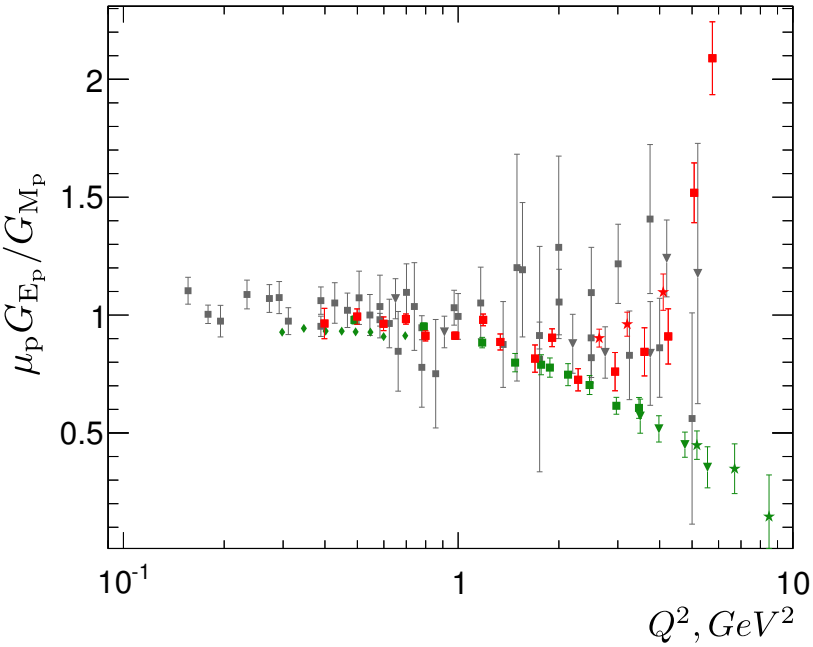

Figure 5.3: The $G_{E_p}(Q^2)/G_{M_p}(Q^2)$ ratio is plotted as a function Q^2: Super-Rosenbluth extractions (red squares) this experiment and (red stars) [12]; conventional Rosenbluth extractions (gray squares) [25] (combines [4,5,9,10]) and (gray triangles) [11]; polarization transfer measurements (green diamonds) [65], (green squares) [19], (green triangles) [21], (green stars) [66].

Q^2, [GeV^2]	G_{E_p}/G_{M_p}	$\delta(G_{E_p}/G_{M_p})$	$\mu_P G_{E_p}/G_{M_p}$	$\delta(\mu_P G_{E_p}/G_{M_p})$
0.40	0.2941	0.0102	0.8214	0.0284
0.50	0.3323	0.0068	0.9279	0.0191
0.60	0.3383	0.0057	0.9447	0.0158
0.70	0.3504	0.0049	0.9786	0.0138
0.80	0.3346	0.0042	0.9344	0.0117
0.98	0.3341	0.0034	0.9330	0.0095
1.19	0.3506	0.0063	0.9793	0.0175
1.34	0.2926	0.0078	0.8172	0.0218
1.70	0.2919	0.0147	0.8151	0.0410
1.91	0.3206	0.0096	0.8954	0.0269
2.29	0.2598	0.0122	0.7256	0.0339
2.95	0.2717	0.0215	0.7588	0.0602
3.61	0.3059	0.0283	0.8542	0.0789
4.25	0.3264	0.0342	0.9116	0.0956
5.08	0.5440	0.0388	1.5194	0.1085
5.76	0.7489	0.0508	2.0916	0.1418

Table 5.3: The summary of the proton magnetic form factor ratios extraction.

5.3 Nonlinearities extraction

The analysis of nonlinear behavior of the ε dependence of the reduced cross section followed the recipe provided in Ref. [51] where a fit function of the form of Eq. 2.4 was used to estimate the deviation from linearity in the global analysis combining

several data sets. The curvature parameter P_2 and its uncertainty were extracted from the second-order degree polynomial fit of the reduced cross section. In Fig. 5.4 two fit functions are shown for each Q^2 setting depicting the variation of the curve when the P_2 term was modified by $\pm 1\sigma$ of extracted uncertainty (central value is not shown) while other parameters remain fixed. The uncertainty δP_2 obtained from the fit accounts for statistical and point-to-point variations in σ_{R} while the normalization systematic uncertainty does not modify possible nonlinearity of the σ_{R} ε dependence.

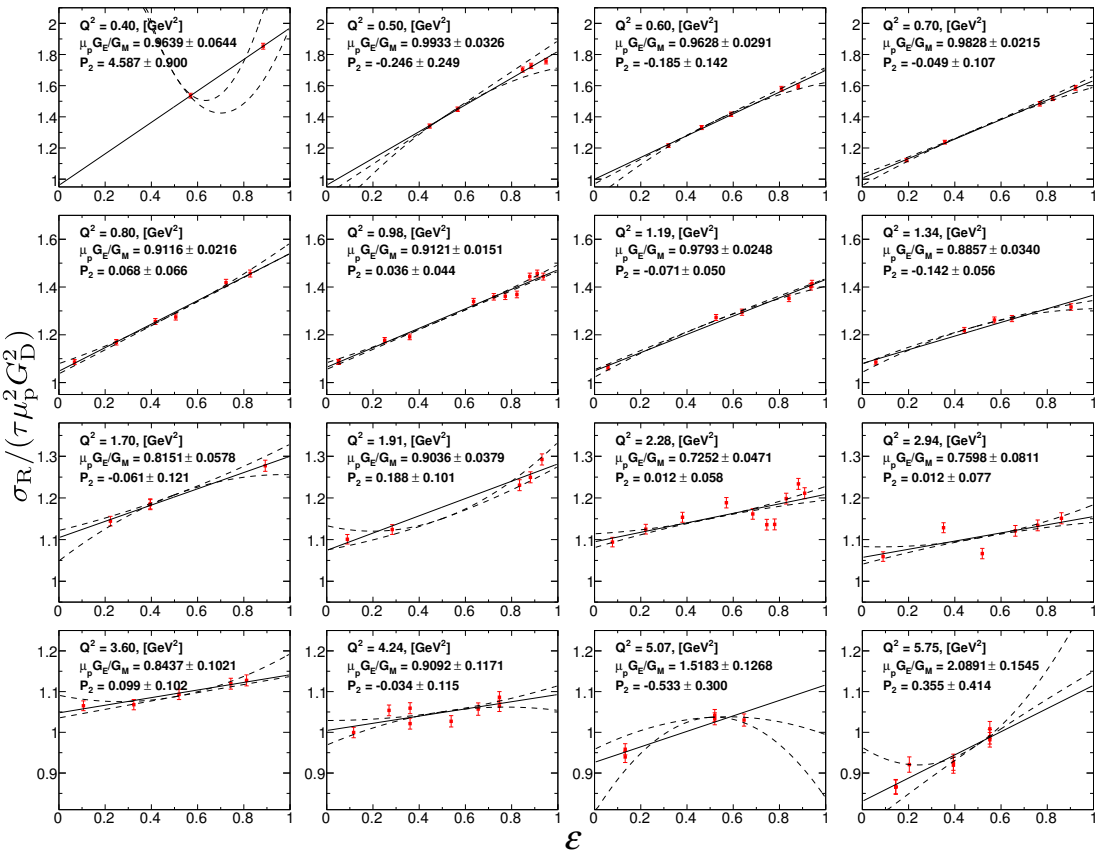

Figure 5.4: The $\tau\mu_{\mathrm{p}}^2 G_{\mathrm{D}}^2$ normalized reduced cross section σ_{R} (red symbols) is plotted as a function of ε for sixteen Q^2 settings. The linear fit (solid black line) represents the Rosenbluth separation procedure (Eq. 5.5) for each setting as described in Sec. 5.2. The quoted $G_{\mathrm{E_p}}(Q^2)/G_{\mathrm{M_p}}(Q^2)$ values include the contributions of the statistical and point-to-point systematic uncertainties and correspond to the values in Table 5.3. The second-order degree polynomial fit (dashed black lines) represents the extraction of P_2. Two lines correspond to the $\pm 1\sigma$ variation in parameter P_2. The $Q^2 = 0.4$ is excluded from P_2 analysis as there are currently only two σ_{R} measurements contributing to this setting.

A summary of the P_2 extraction is shown in Fig. 5.5 and Table 5.4.

5.4 Conclusion

The JLab Hall C Experiment E05-017 followed the methodology of the high precision Super-Rosenbluth Experiment E01-001 (JLab Hall A), namely, the detection

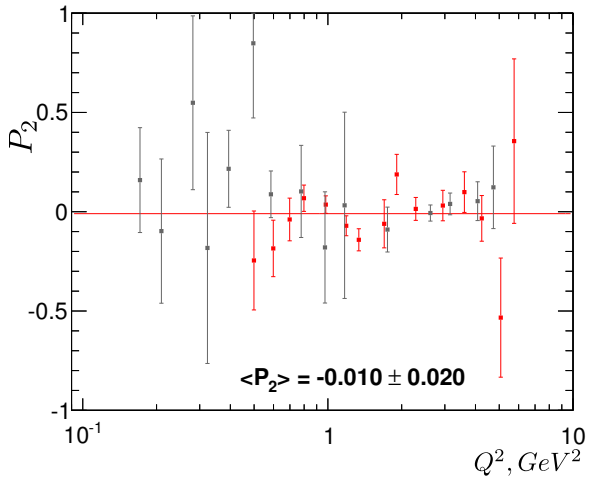

Figure 5.5: The extracted curvature parameter P_2 (red squares) is plotted as a function of Q^2. The red line is the zero-order polynomial fit performed to obtain the global average value quoted as $< P_2 >$. The gray squares show the P_2 world's data analysis from Ref. [51].

Q^2, [GeV^2]	P_2	δP_2
0.50	-0.628	0.130
0.60	-0.153	0.069
0.70	-0.049	0.062
0.80	0.088	0.031
0.98	0.087	0.026
1.19	-0.071	0.035
1.34	0.048	0.033
1.70	-0.061	0.086
1.91	-0.101	0.046
2.29	0.014	0.042
2.95	0.026	0.057
3.61	0.172	0.071
4.25	-0.036	0.094
5.08	-0.533	0.258
5.76	0.351	0.384

Table 5.4: The summary of the curvature parameter extraction. The $Q^2 = 0.4\,\mathrm{GeV}^2$ is excluded from P_2 analysis as there are currently only two σ_R measurements contributing to this setting.

of the recoil proton instead of the typically detected scattered electron. The main feature of this approach is a significantly reduced, compared to the conventional electron Rosenbluth separation, effect of the ε-dependent corrections which, in turn, leads to a high precision in the extraction of the $G_{\mathrm{E_p}}/G_{\mathrm{M_p}}$ ratio, while offering a better or comparable extraction of individual form factors. The experiment focused on the precise $G_{\mathrm{E_p}}/G_{\mathrm{M_p}}$ extraction with the goal of estimating the size of TPE corrections to elastic electron-proton scattering cross section. The nonlinearity in the ε dependence of the reduced cross section (the deviation from Rosenbluth formalism) was another focal point of the E05-017 measurements. The uniqueness of the experiment is reflected in distinctly broad Q^2 coverage and extended ε range (reaching

out to the extremes of ε and including many points at selected Q^2).

The analysis of the E05-017 data set is nearly complete. While all necessary analysis steps along with the procedures to estimate systematic uncertainties have been implemented, several tasks, such as verification of the background fitting robustness and alternative radiative corrections treatment, still require attention. The current results are obtained from the truncated data set that excluded several kinematic settings indicating temporarily unresolved issues.

The experiment measured the elastic scattering cross section at a total of 112 (with 98 points contributing to presented results) kinematic settings in the range of Q^2 from $0.40\,\mathrm{GeV}^2$ to $5.76\,\mathrm{GeV}^2$. The proton electromagnetic form factors, their ratio, and the limits on deviation from linearity in the Rosenbluth plot were estimated at sixteen values of Q^2.

For $Q^2 < 2.5\,\mathrm{GeV}^2$, preliminary results on the form factors ratio yields much better precision than prior global Rosenbluth extractions. The total uncertainty of the $G_{\mathrm{E_p}}/G_{\mathrm{M_p}}$ ratio in the $2.5<Q^2<4.5\,\mathrm{GeV}^2$ range are comparable to the E01-001 extraction while the systematic effects at two highest Q^2 settings are possibly underestimated. Although the form factor ratio uncertainty is unlikely to significantly change upon inclusion of the entire data set, the uncertainty analysis has to be completed by splitting the systematic point-to-point uncertainty in two more finely defined groups: uncorrelated and ε-correlated uncertainty. This will ensure that the final uncertainty on the physics quantities are properly represented: for example, the slope (ε-correlated) uncertainty would have the biggest impact on the form factor ratio, while leaving the nonlinearity extraction almost unaffected. The comparison of the $G_{\mathrm{E_p}}/G_{\mathrm{M_p}}$ results presented in this thesis to the global PT extractions in the $0.4<Q^2<2.5\,\mathrm{GeV}^2$ range shows that they are in agreement within 3σ except for two Q^2 settings. This behavior implies that TPE corrections are small in this Q^2 region where the previous Rosenbluth results were inconclusive. At $Q^2\sim 3.0\,\mathrm{GeV}^2$, the E05-017 data starts to deviate from PT measurements but not to the extent observed in the E01-011 run. The two highest Q^2 settings ($> 5.0\,\mathrm{GeV}^2$) are in strong disagreement with high Q^2 PT results. It has to be noted that the ε range for these two measurements was kinematically limited by the maximum available beam energy.

Unlike the nonlinearity extraction in the previous global multi-experiment analysis, which is potentially biased due to the combination of data sets with different normalization factors, the E05-017 linearity test are performed as a single extraction with typically better low-ε coverage. Although the analysis of the curvature parameter P_2 did not reveal an obvious non-zero signature of TPE effects, extracted δP_2 values already provide better averaged limits on nonlinearity than the combined global extraction. The final uncertainty can further be improved by inclusion of the truncated kinematics and by completion of the aforementioned separation of systematic uncertainties into ε-correlated and uncorrelated groups.

Future E05-017 analysis work includes several comprehensive tasks. First, once the physics extraction on the full data set is available, the detailed comparison to the world's data has to be conducted. Most importantly, given new constraints from the P_2 analysis and the new precision achieved in the measurements of the

discrepancy between Rosenbluth and PT methods, the extraction of the Q^2 dependence of the TPE amplitudes will be possible in a wide Q^2 range. Finally, this new level of precision on TPE amplitudes will make it possible to correct the measured form factors and reanalyze existing form factor fits.

In addition to the primary E05-017 goals, it is also possible to perform an analysis similar to the one presented here for the extraction of the pion photoproduction cross section based on the background scaling obtained in the subtraction procedures.

Bibliography

[1] L. N. Hand, D. G. Miller, and R. Wilson. Electric and magnetic form factors of the nucleon. *Rev. Mod. Phys.*, 35:335, 1963.

[2] T. Janssens, R. Hofstadter, E. B. Hughes, and M. R. Yearian. Proton form factors from elastic electron-proton scattering. *Phys. Rev.*, 142:922, 1966.

[3] L. E. Price, J. R. Dunning, M. Goitein, et al. Backward-angle electron-proton elastic scattering and proton electromagnetic form factors. *Phys. Lett. D*, 4:45, 1971.

[4] J. Litt, G. Buschhorn, D. H. Coward, et al. Measurement of the ratio of the proton form factors, G_E/G_M, at high momentum transfers and the question of scaling. *Phys. Lett. B*, 31:40, 1970.

[5] C. Berger, V. Burkert, G. Knop, B. Langenbeck, and K. Rith. Electromagnetic form factors of the proton at squared four-momentum transfers between 10 and 50 fm^{-2}. *Phys. Lett. B*, 35:87, 1971.

[6] W. Bartel, F. W. Busser, W. R. Dix, et al. Measurement of proton and neutron electromagnetic form factors at squared four-momentum transfers up to 3 $(GeV/c)^2$. *Nucl. Phys. B*, 58:429, 1973.

[7] F. Borkowski, P. Peuser, G. G. Simon, V. H. Walther, and R. D. Wendling. Electromagnetic form factors of the peoton at low four-momentum transfer (ii). *Nucl. Phys. B*, 93:461, 1975.

[8] G. G. Simon, C. Schmitt, F. Borkowski, and V. H. Walther. Absolute electron-proton cross sections at low momentum transfer measured with a high pressure gas target system. *Nucl. Phys. A*, 333:381, 1980.

[9] R. C. Walker, B. W. Filippone, J. Jourdan, et al. Measurements of the proton elastic form factors for $1 \leq Q^2 \leq 3(GeV/c)^2$. *Phys. Rev. D*, 49:5671, 1994.

[10] L. Andivahis, P. E. Bosted, A. Lung, et al. Measurements of the electric and magnetic form factors of the proton from $Q^2 = 1.75$ to $8.83(GeV/c)^2$. *Phys. Rev. D*, 50:5491, 1994.

[11] M. E. Christy, A. Ahmidouch, C. S. Armstrong, A. J., et al. Measurements of electron-proton elastic cross sections for $0.4 < Q^2 < 5.5(GeV/c)^2$. *Phys. Rev. C*, 70:015206, 2004.

[12] I. A. Qattan, J. Arrington, R. E. Segel, et al. Precision rosenbluth measurement of the proton elastic form factors. *Phys. Rev. Lett.*, 94:142301, 2005.

[13] P. N. Kirk, M. Breidenbach, J. I. Friedman, G. C. Hartmann, et al. Elastic electron-proton scattering at large four-momentum transfer. *Phys. Lett. D*, 8:63, 1973.

[14] A. F. Sill, R. G. Arnold, P. E. Bosted, et al. Measurements of elastic electron-proton scattering at large momentum transfer. *Phys. Rev. D*, 48:29, 1993.

[15] J. J. Kelly. Simple parametrization of nucleon form factors. *Phys. Rev. C*, 70:068202, 2004.

[16] E. J. Brash, A. Kozlov, S. Li, and G. M. Huber. New empirical fits to the proton electromagnetic form factors. *Phys. Rev. C*, 65:051001, 2002.

[17] V. Punjabi, C. F. Perdrisat, M. K. Jones, E. J. Brash, and C. E. Carlson. The structure of the nucleon: Elastic electromagnetic form factors. *Eur. Phys. J. A*, 51:79, 2015.

[18] M. K. Jones et al. G_{E_p}/G_{M_p} ratio by polarization transfer in $\vec{e}p \rightarrow e\vec{p}$. *Phys. Rev. Lett.*, 84:1398, 2000.

[19] V. Punjabi and other. Proton elastic form factor ratios to $Q^2 = 3.5GeV^2$ by polarization transfer. *Phys. Rev. C*, 71:055202, 2005.

[20] O. Gayou et al. Measurement of G_{E_p}/G_{M_p} in $\vec{e}p \rightarrow e\vec{p}$ to $Q^2 = 5.6GeV^2$. *Phys. Rev. Lett.*, 88:092301, 2002.

[21] A. Puckett, E. Brash, O. Gayou, M. Jones, and L. Pentchev. Final analysis of proton form factor ratio data at $Q^2 = 4.0, 4.8$ and $5.6GeV^2$. *Phys. Lett. C*, 85:045203, 2012.

[22] M. Meziane et al. Search for effects beyond the born approximation in polarization transfer observables in $\vec{e}p$ elastic scattering. *Phys. Rev. Lett.*, 106:132501, 2011.

[23] A. Puckett, E. Brash, M. Jones, W. Luo, and M. Meziane. Recoil polarization measurements of the proton electromagnetic form factor ratio to $Q^2 = 8.5(GeV/c)^2$. *Phys. Rev. Lett.*, 104:242301, 2010.

[24] P. E. Bosted. Empirical fit to the nucleon electromagnetic form factors. *Phys. Rev. C*, 51:409, 1995.

[25] J. Arrington. How well do we know the electromagnetic form factors of the proton? *Phys. Rev. C*, 68:034325, 2003.

[26] J. Arrington. Implications of the discrepancy between proton form factor measurements. *Phys. Rev. C*, 69:022201, 2004.

[27] I. A. Qattan. Precision rosenbluth measurement of the proton elastic electromagnetic form factors and their ratio at $Q^2 = 2.64, 3.20$ and $4.10GeV^2$. *Ph.D. thesis*, 2005.

[28] R. L. Anderson, B. Borgia, G. L. Cassiday, et al. Positron-proton elastic scattering at 800 and 1200 mev. *Phys. Rev.*, 166:1336–1342, Feb 1968.

[29] B. Bouquet, D. Benaksas, B. Grossette, et al. Backward scattering of positrons and electrons on protons. *Phys. Lett. B*, 26(3):178 – 180, 1968.

[30] J. Mar, B. C. Barish, J. Pine, et al. Comparison of electron-proton and positron-proton elastic scattering at four-momentum transfers up to 5.0 $(\mathrm{GeV}/c)^2$. *Phys. Rev. Lett.*, 21:482–484, Aug 1968.

[31] W. Bartel, B. Dudelzak, H. Krehbiel, et al. Scattering of positrons and electrons from protons. *Phys. Lett. B*, 25(3):242 – 245, 1967.

[32] R. L. Anderson, B. Borgia, G. L. Cassiday, et al. Scattering of positrons and electrons from protons. *Phys. Rev. Lett.*, 17:407–409, Aug 1966.

[33] A. Browman, F. Liu, and C. Schaerf. Positron-proton scattering. *Phys. Rev.*, 139:B1079–B1085, Aug 1965.

[34] D. Yount and J. Pine. Scattering of high-energy positrons from protons. *Phys. Rev.*, 128:1842–1849, Nov 1962.

[35] J. Arrington. Evidence for two-photon exchange contributions in electron-proton and positron-proton elastic scattering. *Phys. Rev. C*, 69:032201, Mar 2004.

[36] I. A. Rachek, J. Arrington, V. F. Dmitriev, et al. Measurement of the two-photon exchange contribution to the elastic $e^{\pm}p$ scattering cross sections at the vepp-3 storage ring. *Phys. Rev. Lett.*, 114:062005, Feb 2015.

[37] M. Moteabbed, M. Niroula, B. A. Raue, et al. Demonstration of a novel technique to measure two-photon exchange effects in elastic $e^{\pm}p$ scattering. *Phys. Rev. C*, 88:025210, Aug 2013.

[38] D. Adikaram, D. Rimal, L. B. Weinstein, et al. Towards a resolution of the proton form factor problem: New electron and positron scattering data. *Phys. Rev. Lett.*, 114:062003, Feb 2015.

[39] D. Rimal, D. Adikaram, B. A. Raue, et al. Measurement of two-photon exchange effect by comparing elastic $e^{\pm}p$ cross sections. *Phys. Rev. C*, 95:065201, Jun 2017.

[40] H. Zhou and S. Yang. $\Delta(1232)$ resonance contribution to two-photon exchange in electron-proton scattering revisited. *The European Physical Journal A*, 51(8):105, Aug 2015.

[41] P. G. Blunden, W. Melnitchouk, and J. A. Tjon. Two-photon exchange in elastic electron-nucleon scattering. *Phys. Rev. C*, 72:034612, Sep 2005.

[42] J. Arrington, P. Blunden, and W. Melnitchouk. Review of two-photon exchange in electron scattering. *Prog. in Part. and Nucl. Phys.*, 66(4):782 – 833, 2011.

[43] B. S. Henderson, L. D. Ice, D. Khaneft, et al. Hard two-photon contribution to elastic lepton-proton scattering determined by the olympus experiment. *Phys. Rev. Lett.*, 118:092501, Mar 2017.

[44] S. Kondratyuk, P. G. Blunden, W. Melnitchouk, and J. A. Tjon. Δ resonance contribution to two-photon exchange in electron-proton scattering. *Phys. Rev. Lett.*, 95:172503, Oct 2005.

[45] J. C. Bernauer, M. O. Distler, J. Friedrich, et al. Electric and magnetic form factors of the proton. *Phys. Rev. C*, 90:015206, Jul 2014.

[46] O. Tomalak and M. Vanderhaeghen. Subtracted dispersion relation formalism for the two-photon exchange correction to elastic electron-proton scattering: comparison with data. *The European Physical Journal A*, 51(2):24, Feb 2015.

[47] A. V. Afanasev, S. J. Brodsky, C. E. Carlson, Y. Chen, and M. Vanderhaeghen. Two-photon exchange contribution to elastic electron-nucleonscattering at large momentum transfer. *Phys. Rev. D*, 72:013008, Jul 2005.

[48] N. Kivel and M. Vanderhaeghen. Two-photon exchange in elastic electron-proton scattering: a qcd factorization approach. *Phys. Rev. Lett.*, 103:092004, Aug 2009.

[49] Y. M. Bystritskiy, E. A. Kuraev, and E. Tomasi-Gustafsson. Structure function method applied to polarized and unpolarized electron-proton scattering: A solution of the $G_E(p)/G_M(p)$ discrepancy. *Phys. Rev. C*, 75:015207, Jan 2007.

[50] H. Kirkman, R. Railton, J. Rutherglen, et al. Measurements of the polarisation of the recoil proton in elastic electron proton scattering at $Q^2 = 1.3, 1.5$ and $1.9(GeV/c)^2$. *Phys. Lett. B*, 32(6):519 – 522, 1970.

[51] V. Tvaskis, J. Arrington, M. E. Christy, et al. Experimental constraints on nonlinearities induced by two-photon effects in elastic and inelastic rosenbluth separations. *Phys. Rev. C*, 73:025206, Feb 2006.

[52] A. Afanasev, P. G. Blunden, D. Hasell, and B. A. Raue. Two-photon exchange in elastic electronproton scattering. *Prog. Part. Nucl. Phys.*, 95:245–278, 2017.

[53] F. Weissbach, K. H., D. T., and I. Sick. Improved radiative corrections and proton charge form factor from the rosenbluth separation technique. *Phys. Rev. C*, 80:064605, Dec 2009.

[54] P. G. Blunden, W. Melnitchouk, and J. A. Tjon. Two-photon exchange and elastic electron-proton scattering. *Phys. Rev. Lett.*, 91:142304, Oct 2003.

[55] S. Kondratyuk and P. G. Blunden. Contribution of spin 1/2 and 3/2 resonances to two-photon exchange effects in elastic electron-proton scattering. *Phys. Rev. C*, 75:038201, Mar 2007.

[56] C. E. Carlson and M. Vanderhaeghen. Two-photon physics in hadronic processes. *Annual Review of Nuclear and Particle Science*, 57(1):171–204, 2007.

[57] O. Gayou et al. Measurements of the elastic electromagnetic form factor ratio $\mu_p G_{E_p}/G_{M_p}$ via polarization transfer. *Phys. Rev. C*, 64:038202, 2001.

[58] D. Borisyuk and A. Kobushkin. Perturbative qcd predictions for two-photon exchange. *Phys. Rev. D*, 79:034001, Feb 2009.

[59] J. Arrington, W. Melnitchouk, and J. A. Tjon. Global analysis of proton elastic form factor data with two-photon exchange corrections. *Phys. Rev. C*, 76:035205, Sep 2007.

[60] V. Mamyan. Measurements of F_2 and $R = \sigma_{\mathrm{L}}/\sigma_{\mathrm{T}}$ on nuclear targets in the nucleon resonance region. *Ph.D. thesis*, 2010.

[61] I. Albayrak. Measurements of R in the nucleon resonance region on deuterium and the non-singlet moments of the nucleon. *Ph.D. thesis*, 2011.

[62] M. Johnson. Two-photon exchange effects in elastic electron-proton scattering. *Ph.D. thesis*, 2013.

[63] H. Genzel and W. Pfeil. *Photoproduction of Elementary Particles*, pages 1–5. Springer Berlin Heidelberg, Berlin, Heidelberg, 1973.

[64] M. A. Shupe, R. H. Milburn, D. J. Quinn, et al. Neutral-pion photoproduction and proton compton scattering at large angles. *Phys. Rev. D*, 19:1921–1930, Apr 1979.

[65] X. Zhan, K. Allada, D. Armstrong, J. Arrington, and W. Bertozzi. High-precision measurement of the proton elastic form factor ratio $\mu_p G_{E_p}/G_{M_p}$ at low Q^2. *Phys. Lett. B*, 705:59, 2011.

[66] A. J. R. Puckett, E. J. Brash, M. K. Jones, et al. Polarization transfer observables in elastic electron-proton scattering at $Q^2 = 2.5$, 5.2, 6.8, and 8.5GeV^2. *Phys. Rev. C*, 96:055203, Nov 2017.

[67] O. Stern et al. Magnetic moment of the proton. *Nature*, 132:169–170, 1933.

[68] R. Hofstadter, H. R. Fechter, and J. A. McIntyre. High-energy electron scattering and nuclear structure determinations. *Phys. Rev.*, 92:978, 1953.

[69] D. R. Yennie, M. M. Levy, and D. G. Ravenhall. Electromagnetic structure of nucleons. *Rev. Mod. Phys.*, 29:144, 1957.

[70] F. J. Ernst, R. G. Sachs, and K. C. Wali. Electromagnetic form factors of the nucleon. *Phys. Rev.*, 119:1105, 1960.

[71] M. N. Rosenbluth. High energy elastic scattering of electrons on protons. *Phys. Rev.*, 79:615, 1950.

[72] M. Goitein, R. J. Budnitz, L. Carroll, J. R. Chen, et al. Elastic electron-proton scattering cross sections measured by a coincidence technique. *Phys. Rev. D*, 1:2449, 1970.

[73] J. J. Murphy, Y. M. Shin, and D. M. Skopik. Proton form factor from 0.15 and 0.79 fm^{-2}. *Phys. Lett. C*, 9:2125, 1974.

[74] F. Borkowski, P. Peuser, G. G. Simon, V. H. Walther, and R. D. Wendling. Electromagnetic form factors of the proton at low four-momentum transfer. *Nucl. Phys. A*, 222:269, 1974.

[75] R. G. Arnold, P. E. Bosted, C. C. Chang, J. Gomez, et al. Measurement of elastic electron scattering from the proton at high momentum transfer. *Phys. Rev. Lett.*, 57:174, 1986.

[76] P. E. Bosted, A. T. Katramatou, R. G. Arnold, D. Benton, et al. Measurements of the deuteron and proton magnetic form factors at large momentum transfers. *Phys. Rev. C*, 42:38, 1990.

[77] S. Rock, R. G. Arnold, P. E. Bosted, B. T. Chertok, et al. Measurement of elastic electron-neutron scattering and inelastic electron-deuteron scattering cross sections at high momentum transfer. *Phys. Rev. D*, 46:24, 1992.

[78] J. C. Bernauer, P. Achenbach, C. Ayerbe Gayoso, et al. High-precision determination of the electric and magnetic form factors of the proton. *Phys. Rev. Lett.*, 105:242001, Dec 2010.

[79] R. R. Wilson and J. S. Levinger. Structure of the proton. *Ann. Rev. Nucl. Sci.*, 14:135, 1964.

[80] C. Hyde-Wright and K. de Jager. Electromagnetic form factors of the nucleon and compton scattering. *Ann. Rev. Nucl. Part. Sci.*, 54:217, 2004.

[81] J. Arrington, C. Roberts, and J. Zanotti. Nucleon electromagnetic form factors. *J. Phys. G*, 34:S23, 2007.

[82] C. Perdrisat, V. Punjabi, and M. Vanderhaeghen. Progress in particle and nuclear physics. *Prog. Part. Nucl. Phys.*, 59:694, 2007.

[83] J. Arrington, K. de Jager, and C. Perdrisat. Nucleon form factors a jefferson lab perspective. *J. Phys. Conf. Ser.*, 299:012002, 2011.

[84] S. Pacetti, R. Baldini Ferroli, and E. Tomasi-Gustafsson. Proton electromagnetic form factors: Basic notions, present achievements and future perspectives. *Phys. Rep.*, 550-551:1, 2014.

[85] A. I. Akhiezer, L. N. Rozentsweig, and I. M. Shmuskevich. Scattering of electrons by protons. *Sov. Phys. JETP*, 6:588, 1958.

[86] A. I. Akhiezer and M. P. Rekalo. Polarization phenomena in electron scattering by protons in the high energy region. *Sov. Phys. Dokl (Dokl.Akad.Nauk Ser.Fiz.)*, 13:572, 1968.

[87] A. I. Akhiezer and M. P. Rekalo. Polarization effects in the scattering of leptons by hadrons. *Fiz. Elem. Chast. Atom. Yadra*, 4:662, 1973.

[88] N. Dombey. Scattering of polarized leptons at high energy. *Rev. Mod. Phys.*, 41:236, 1969.

[89] R. G. Arnold, C. E. Carlson, and F. Gross. Polarization transfer in elastic electron scattering from nucleons and deuterons. *Phys. Rev. C*, 23:363, 1981.

[90] B. Milbrath et al. Comparison of polarization observables in electron scattering from the proton and deuteron. *Phys. Rev. Lett.*, 80:452, 1998.

[91] B. Milbrath et al. Erratum: Comparison of polarization observables in electron scattering from the proton and deuteron. *Phys. Rev. Lett.*, 82:2221, 1999.

[92] T. Pospischil et al. Measurement of G_{E_p}/G_{M_p} via polarization transfer at $Q^2 = 0.4(GeV/c)^2$. *Eur. Phys. J. A*, 12:125, 2001.

[93] G. MacLachlan et al. The ratio of proton electromagnetic form factors via recoil polarimetry at $Q^2 = 1.13(GeV/c)^2$. *Nucl. Phys. A*, 764:261, 2006.

[94] B. Hu et al. Polarization transfer in the $2H(\vec{e}, e'\vec{p})n$ reaction up to $Q^2 = 1.61(GeV/c)^2$. *Phys. Rev. C*, 73:064004, 2006.

[95] M. Paolone, S. Malace, S. Strauch, I. Albayrak, and J. Arrington. Polarization transfer in the $4He(\vec{e}, e'\vec{p})3H$ reaction at $Q^2 = 0.8(GeV/c)^2$ and $1.3(GeV/c)^2$. *Phys. Rev. Lett.*, 105:072001, 2010.

[96] G. Ron et al. Low-Q^2 measurements of the proton form factor ratio $\mu_p G_{E_p}/G_{M_p}$. *Phys. Rev. C*, 84:055204, 2011.

[97] M. K. Jones et al. Proton G_E/G_M from beam-target asymmetry. *Phys. Rev. C*, 74:035201, 2006.

[98] C. Crawford et al. Measurement of the proton's electric to magnetic form factor ratio from $1\vec{H}(\vec{e}, e'p)$. *Phys. Rev. Lett.*, 98:052301, 2007.

[99] J. C. Bizot, J. M. Buon, et al. Polarization of recoil protons from electron-proton scattering at 950 mev. *Phys. Rev.*, 140:B1387–B1402, Dec 1965.

[100] G. V. Di Giorgio, E. Ganssauge, R. Gomez, et al. Polarization of recoil protons in e-p elastic scattering at 20 fm^{-2}. *Il Nuovo Cimento (1955-1965)*, 39(2):474–485, Sep 1965.

[101] D. E. Lundquist, R. L. Anderson, J. V. Allaby, and D. M. Ritson. Polarization of recoil protons from neutral pion photoproduction. *Phys. Rev.*, 168:1527–1533, Apr 1968.

[102] J. R. Chen, J. Sanderson, J. A. Appel, et al. Test of time-reversal invariance in electroproduction interactions using a polarized proton target. *Phys. Rev. Lett.*, 21:1279–1282, Oct 1968.

[103] J. A. Appel, J. R. Chen, J. Sanderson, et al. Search for violation of time-reversal invariance in inelastic $e - p$ scattering. *Phys. Rev. D*, 1:1285–1303, Mar 1970.

[104] S. Rock, M. Borghini, O. Chamberlain, et al. Search for T-invariance violation in the inelastic scattering of electrons from a polarized proton target. *Phys. Rev. Lett.*, 24:748–753, Mar 1970.

[105] T. Powell, M. Borghini, O. Chamberlain, et al. Measurement of the polarization in elastic electron-proton scattering. *Phys. Rev. Lett.*, 24:753–756, Mar 1970.

[106] A. Airapetian et al. Search for a two-photon exchange contribution to inclusive deep-inelastic scattering. *Phys. Lett. B*, 682(4):351 – 354, 2010.

[107] J. Katich, X. Qian, Y. X. Zhao, et al. Measurement of the target-normal single-spin asymmetry in deep-inelastic scattering from the reaction $^3\mathrm{He}^{\uparrow}(e, e')X$. *Phys. Rev. Lett.*, 113:022502, Jul 2014.

[108] Y.-W. Zhang, E. Long, M. Mihovilovič, et al. Measurement of the target-normal single-spin asymmetry in quasielastic scattering from the reaction $^3\mathrm{He}^{\uparrow}(e, e')$. *Phys. Rev. Lett.*, 115:172502, Oct 2015.

[109] S. P. Wells, T. Averett, D. Barkhuff, et al. Measurement of the vector analyzing power in elastic electron-proton scattering as a probe of the double virtual compton amplitude. *Phys. Rev. C*, 63:064001, May 2001.

[110] F. E. Maas, K. Aulenbacher, S. Baunack, et al. Measurement of the transverse beam spin asymmetry in elastic electron-proton scattering and the inelastic contribution to the imaginary part of the two-photon exchange amplitude. *Phys. Rev. Lett.*, 94:082001, Mar 2005.

[111] D. S. Armstrong, J. Arvieux, R. Asaturyan, et al. Transverse beam spin asymmetries in forward-angle elastic electron-proton scattering. *Phys. Rev. Lett.*, 99:092301, Aug 2007.

[112] P. LaViolette et al. E158 transverse asymmetries. 2009. E158 Tech. Rep. No. 70.

[113] D. Androić, D. S. Armstrong, J. Arvieux, et al. Transverse beam spin asymmetries at backward angles in elastic electron-proton and quasielastic electron-deuteron scattering. *Phys. Rev. Lett.*, 107:022501, Jul 2011.

[114] S. Abrahamyan, A. Acha, A. Afanasev, et al. New measurements of the transverse beam asymmetry for elastic electron scattering from selected nuclei. *Phys. Rev. Lett.*, 109:192501, Nov 2012.

[115] B. P. Waidyawansa et al. Beam normal single spin asymmetry measurements from qweak. 2016.

[116] D. B. Ríos, K. Aulenbacher, S. Baunack, et al. New measurements of the beam normal spin asymmetries at large backward angles with hydrogen and deuterium targets. *Phys. Rev. Lett.*, 119:012501, Jul 2017.

[117] E. Tomasi-Gustafsson and G. I. Gakh. Search for evidence of two-photon contribution in elastic electron-proton data. *Phys. Rev. C*, 72:015209, Jul 2005.

[118] Y. C. Chen, C. W. Kao, and S. N. Yang. Is there model-independent evidence of the two-photon-exchange effect in the electron-proton elastic scattering cross section? *Physics Letters B*, 652(5):269 – 274, 2007.

[119] M. P. Rekalo, E. Tomasi-Gustafsson, and D. Prout. Search for evidence of two-photon exchange in new experimental high momentum transfer data on electron deuteron elastic scattering. *Phys. Rev. C*, 60:042202, Sep 1999.

[120] J. Arrington. Extraction of two-photon contributions to the proton form factors. *Phys. Rev. C*, 71:015202, Jan 2005.

[121] D. Borisyuk and A. Kobushkin. Phenomenological analysis of two-photon exchange effects in proton form factor measurements. *Phys. Rev. C*, 76:022201, Aug 2007.

[122] D. Borisyuk and A. Kobushkin. Two-photon exchange amplitudes for elastic *ep* scattering at $Q^2 = 2.5$ GeV^2 from experimental data. *Phys. Rev. D*, 83:057501, Mar 2011.

[123] I. A. Qattan and A. Alsaad. Empirical parametrization of the two-photon-exchange effect contributions to the electron-proton elastic scattering cross section. *Phys. Rev. C*, 83:054307, May 2011.

[124] J. Guttmann, N. Kivel, M. Meziane, and M. Vanderhaeghen. Determination of two-photon exchange amplitudes from elastic electron-proton scattering data. *The European Physical Journal A*, 47(6), Jun 2011.

[125] K. M. Graczyk. Two-photon exchange effect studied with neural networks. *Phys. Rev. C*, 84:034314, Sep 2011.

[126] I. A. Qattan, A. Alsaad, and J. Arrington. Reexamination of phenomenological two-photon exchange corrections to the proton form factors and $e^{\pm}p$ scattering. *Phys. Rev. C*, 84:054317, Nov 2011.

[127] I. A. Qattan. Phenomenological extraction of two-photon exchange amplitudes from elastic electron-proton scattering cross section data. *Phys. Rev. C*, 95:055205, May 2017.

[128] W. A. McKinley and H. Feshbach. The coulomb scattering of relativistic electrons by nuclei. *Phys. Rev.*, 74:1759–1763, Dec 1948.

[129] R. R. Lewis. Potential scattering of high-energy electrons in second born approximation. *Phys. Rev.*, 102:537–543, Apr 1956.

[130] S. D. Drell and M. A. Ruderman. Proton polarizability correction to electron-proton scattering. *Phys. Rev.*, 106:561–563, May 1957.

[131] S. D. Drell and S. Fubini. Higher electromagnetic corrections to electron-proton scattering. *Phys. Rev.*, 113:741–744, Jan 1959.

[132] N. R. Werthamer and M. A. Ruderman. Nucleon polarizability correction to high-energy electron-nucleon scattering. *Phys. Rev.*, 123:1005–1013, Aug 1961.

[133] J. A. Campbell. Algebraic computation of radiative corrections for electron-proton scattering. *Nuclear Physics B*, 1(5):283 – 300, 1967.

[134] J. A. Campbell. Accuracy of radiative corrections to electromagnetic scattering from protons. *Phys. Rev.*, 180:1541–1546, Apr 1969.

[135] G. K. Greenhut. Two-photon exchange in electron-proton scattering. *Phys. Rev.*, 184:1860–1867, Aug 1969.

[136] R. W. Brown. Comparison of the scattering of electrons and positrons from protons at small angles. *Phys. Rev. D*, 1:1432–1444, Mar 1970.

[137] Y.-S. Tsai. Radiative corrections to electron-proton scattering. *Phys. Rev.*, 122:1898–1907, Jun 1961.

[138] N. Meister and D. R. Yennie. Radiative corrections to high-energy scattering processes. *Phys. Rev.*, 130:1210, 1963.

[139] L. W. Mo and Y. S. Tsai. Radiative corrections to elastic and inelastic *ep* and μp scattering. *Rev. Mod. Phys.*, 41:205, 1969.

[140] L. C. Maximon and J. A. Tjon. Radiative corrections to electron-proton scattering. *Phys. Rev. C*, 62:054320, 2000.

[141] R. Ent, B. W. Filippone, N. C. R. Makins, et al. Radiative corrections for $(e, e^{'} p)$ reactions at gev energies. *Phys. Rev. C*, 64:054610, Oct 2001.

[142] Y. M. Bystritskiy, E. A. Kuraev, and E. Tomasi-Gustafsson. Structure function method applied to polarized and unpolarized electron-proton scattering: A solution of the $G_E(p)/G_M(p)$ discrepancy. *Phys. Rev. C*, 75:015207, Jan 2007.

[143] G. I. Gakh, M. I. Konchatnij, N. P. Merenkov, and E. Tomasi-Gustafsson. Radiative corrections to elastic proton-electron scattering measured in coincidence. *Phys. Rev. C*, 95:055207, 2017.

[144] P. A. M. Guichon and M. Vanderhaeghen. How to reconcile the rosenbluth and the polarization transfer methods in the measurement of the proton form factors. *Phys. Rev. Lett.*, 91:142303, Oct 2003.

[145] M. Meziane. Search for effects beyond the born approximation in polarization transfer observables in $\vec{e}p$ elastic scattering. *Ph.D. thesis*, 2011.

[146] M. Gorchtein. Dispersive contributions to e+p/ep cross section ratio in forward regime. *Phys. Lett. B*, 644(5):322 – 330, 2007.

[147] D. Borisyuk and A. Kobushkin. Two-photon exchange in a dispersion approach. *Phys. Rev. C*, 78:025208, Aug 2008.

[148] P. G. Blunden and W. Melnitchouk. Dispersive approach to two-photon exchange in elastic electron-proton scattering. *Phys. Rev. C*, 95:065209, Jun 2017.

[149] B. Pasquini and M. Vanderhaeghen. Resonance estimates for single spin asymmetries in elastic electron-nucleon scattering. *Phys. Rev. C*, 70:045206, Oct 2004.

[150] K. M. Graczyk. Comparison of neural network and hadronic model predictions of the two-photon exchange effect. *Phys. Rev. C*, 88:065205, Dec 2013.

[151] I. T. Lorenz, U.-G. Meißner, H.-W. Hammer, and Y.-B. Dong. Theoretical constraints and systematic effects in the determination of the proton form factors. *Phys. Rev. D*, 91:014023, Jan 2015.

[152] Y.-C. Chen, A. Afanasev, S. J. Brodsky, C. E. Carlson, and M. Vanderhaeghen. Partonic calculation of the two-photon exchange contribution to elastic electron-proton scattering at large momentum transfer. *Phys. Rev. Lett.*, 93:122301, Sep 2004.

[153] P. van Nieuwenhuizen. Muon-electron scattering cross section to order α^3. *Nuclear Physics B*, 28(2):429 – 454, 1971.

[154] G. Grammer and D. R. Yennie. Improved treatment for the infrared-divergence problem in quantum electrodynamics. *Phys. Rev. D*, 8:4332–4344, Dec 1973.

[155] N. Kivel and M. Vanderhaeghen. Soft spectator scattering in the nucleon form factors at large Q^2 within the soft collinear effective theory approach. *Phys. Rev. D*, 83:093005, May 2011.

[156] N. Kivel and M. Vanderhaeghen. Two-photon exchange corrections to elastic electron-proton scattering at large momentum transfer within the scet approach. *Journal of High Energy Physics*, 2013(4):29, Apr 2013.

[157] J. Arrington et al. A measurement of two-photon effects in upolarized electron-proton scattering. *PAC26 Hall-C proposal*, 2005.

[158] C. W. Leemann, D. R. Douglas, and G. A. Krafft. The continuous electron beam accelerator facility: CEBAF at the Jefferson Laboratory. *Ann. Rev. Nucl. Part. Sci.*, 51(1):413–450, 2001.

[159] C. Yan, P. Adderley, D. Barker, et al. Superharp - a wire scanner with absolute position readout for beam energy measurement at CEBAF. *Nucl. Instrum. Meth.*, 365(2):261 – 267, 1995.

[160] P. Gueye. Status of the actual beam position monitors in the hall c beamline. *CEBAF Internal Report*, 1995.

[161] K. B. Unser. The parametric current transformer, a beam current monitor developed for lep. *AIP Conf. Proc.*, 252(1):266–275, 1992.

[162] C. Yan, R. Carlini, and D. Neuffer. Beam energy measurement using the arc beam line as a spectrometer. *CEBAF-PR-93-004*, 1993.

[163] J. R. Arrington. Inclusive electron scattering from nuclei at $x > 1$ and high Q^2. *Ph.D. thesis*, 1998.

[164] C. Yan, P. Adderley, R. Carlini, et al. Target raster system at CEBAF. *Nucl. Instrum. Meth.*, 365(1):46 – 48, 1995.

[165] K. Makino and M. Berz. Cosy infinity version 8. *Nucl. Instrum. Meth.*, 427(1):338 – 343, 1999.

[166] E. C. Schulte. High energy measurements of the deuteron photodisintegration differential cross section. *Ph.D. thesis*, 2002.

[167] R. L. Anderson, D. B. Gustavson, D. M. Ritson, et al. Measurements of exclusive photoproduction processes at large values of t and u from 4 to 7.5 gev. *Phys. Rev. D*, 14:679–697, Aug 1976.

[168] A. I. Danagoulian. Measurements of compton scattering on the proton at $2 - 6GeV^2$. *Ph.D. thesis*, 2006.

[169] A. Danagoulian, V. H. Mamyan, M. Roedelbronn, et al. Compton-scattering cross section on the proton at high momentum transfer. *Phys. Rev. Lett.*, 98:152001, Apr 2007.